FLOW AND HEAT TRANSFER CHARACTERISTICS OF BACKWARD-FACING STEP FLOW IN A RECTANGULAR DUCT

BY

Hiroshi IWAI

1998

Contents

Acknowledgments

I would like to express my sincere thanks and gratitude to Professor Kenjiro Suzuki for his invaluable guidance and experienced advice on my research work throughout my six years with the Heat Transfer Laboratory of Kyoto University.

I would also like to show my appreciation to Associate Professor Kazuyoshi Nakabe and Dr. Kyoji Inaoka for their encouragement, generous assistance and suggestions.

I must also thank Dr. G.N. Xi, Dr. K. Suga, Associate Professor H. Suzuki, Dr. K. Matsubara and Mr. H. Onishi for their kindness and patience in answering to all my queries on numerical methods in CFD. My sincere thanks are also due to members and ex-members of the Heat Transfer Laboratory of Kyoto University, particularly Messrs. E.C. Neo and Y. Aoki for their collaboration.

Special thanks go to Messrs. J. Yamamoto, K. Omae and K. Tatsumi who were the administrators of the computer system in the Heat Transfer Laboratory of Kyoto University.

Finally, I would like to thank my family for their understanding, constant confidence and support throughout my study. I would also like to take this opportunity to express my heartfelt thanks to my fiancée Ms. Mariko Hamaji for her patience, encouragement and support.

Chapter 1

Introduction

1.1 Background

Flow separation and reattachment phenomena are encountered in many engineering devices; heat exchangers, electric module assembles etc. Although flow separation and reattachment phenomena cause energy loss due to pressure drops, it is sometimes intentionally used for heat transfer enhancement. Flows in some practical applications, such as heat exchangers for instance, are often modified with vortex generators [1,2] or ribs [3,4] in order to establish a favorable heat exchange. Such flow modification often includes the flow separation and reattachment. Consequently the modified flows tend to have quite complicated flow structures. In order to improve the performance of heat exchangers, understanding the details of such complicated flow and thermal structures is very important. Therefore, attention was paid in this study to one of the flows in such category, namely a separating and reattaching flow. In particular, as the most typical geometry to generate separation and reattachment of flows, the fundamental characteristics of a backward-facing step flow have been investigated experimentally and also numerically.

There have been many experimental investigations for flow separation and reattachment phenomena in turbulent flows. The early works were reviewed by Eaton and Johnston [5]. Recently, both flow measurements and heat transfer measurements were carried out by

researchers, including Ötügen [6],Ötügen and Muckenthaler [7],Vogel and Eaton [8], Driver et al. [9] and Adams and Eaton [10]. In most of these experimental investigations, a considerably large aspect ratio was adopted in order to assume the two-dimensionality of the flow and thermal fields around the centerline of the duct, following the conclusion of de Brederode and Bradshaw [11] that the side wall effects on the flow along the centerplane were negligible for aspect ratios greater than 10 in turbulent flow cases. More recently, Ötügen et al. [12],Papadopoulos and Ötügen [13] and Shih and Ho [14] attempted to reveal the three-dimensional structure of flow field and reported the existence of highly three-dimensional flow structure near the wall immediately after the step. However these investigations basically focused on the three-dimensionality only of flow field and few investigations are yet available concerning the three-dimensionality of the thermal fields.

There have also been many numerical investigations on turbulent flows over a backward-facing step. Although the development of computer hardware made a DNS (Direct Numerical Simulation) of three-dimensional turbulent flow possible [15], it still certainly requires a considerable CPU time and memory. Therefore some kinds of turbulent model are often employed in the turbulent flow simulations. Numerical studies on turbulent backward-facing step flows and various types of turbulent models were reviewed by Lasher and Taulbee [16] and Launder [17]. However almost all numerical computations of the turbulent backward-facing step flow using turbulent models assume that the flow is two-dimensional.

In the laminar and transition flow cases, the two-dimensional assumption for flow and thermal fields in the duct center region is also often adopted. Goldstein et al. [18],Denham and Patrick [19] and Armaly et al. [20] measured the flow field using hot-wire anemometry or laser Doppler anemometry, while Aung [21], Abu-Mulaweh et al. [22,23] and Baek et al. [24] carried out heat transfer measurement. All of these studies basically assume the two-dimensionality of flow and thermal field and neglect the effects of side wall. Although Armaly mentioned in his literature the possibility of flow three-dimensionality even in the laminar flows, the details of three-dimensional flow and thermal structures in a backward-

facing step laminar flows are still unknown.

In the numerical simulations of laminar backward-facing step flows, two-dimensional assumption for flow and thermal fields has often been adopted neglecting the side wall effects. Kondoh et al. [25], Ichinose et al. [26], Lin et al. [27,28], Hong et al. [29], Sparrow et al. [30] and Sparrow and Chuck [31] carried out two-dimensional simulations and studied the effects of various parameters such as Reynolds number, expansion ratio, Prandtl number and buoyancy on flow and thermal fields. Beskok and Karniadakis [32] also carried out two-dimensional simulations for microscale backward-facing step flows. Kaiktsis et al. [33] recently performed three-dimensional simulations and studied the three-dimensionality of the flow field but no discussion was made for the thermal field.

Considering that the actual flow and thermal fields in heat exchangers are expected to be three-dimensional, it is necessary to understand the details of such flow and thermal structures. The main objective of this study is to investigate systematically the flow structures and the related heat transfer characteristics of flows over a backward-facing step in a rectangular duct for a wide range of Reynolds number. Three-dimensionality of the flow and thermal fields is a particular interest. Since the fluid velocity component in duct spanwise direction is expected to be small, an accurate measurement of three-dimensional flow structure is not easy. This is especially so in laminar flow cases. On the other hand, numerical approach could give a whole information of the flow and thermal fields once a proper computation is established. Therefore numerical approach is employed in this study. Reflecting recent requirements of compact high-performance heat exchanger, laminar flow cases will be intensively studied.

1.2 Outline of the Thesis

Chapter 2 presents the outline of the fundamental procedure of the numerical simulation adopted in this study.

Chapter 3 presents the results of three-dimensional numerical simulations for forced convective laminar flows over a backward-facing step in a rectangular duct. The Reynolds number and the duct aspect ratio are changed and their effects on the flow and thermal fields are discussed.

Chapter 4 presents the results of two- and three-dimensional simulations for mixed convective upward flows over a backward-facing step at low Reynolds number. The buoyancy level is changed to see its effects on the flow and thermal fields. How the two-dimensional simulation can model the actual three-dimensional flow is also discussed.

Chapter 5 presents the results of three-dimensional simulations for mixed convective flows over a backward-facing step at low Reynolds number. Two kinds of inclination angles are introduced to describe the duct posture. Those inclination angles are changed and their effects on the flow and thermal fields are discussed.

Chapter 6 presents the results of two- and three-dimensional simulations for turbulent flows over a backward-facing step in a rectangular duct. Two types of turbulent models are tested. Three-dimensional structures of the flow and thermal fields are discussed for two cases of different aspect ratio through the results obtained by three-dimensional numerical simulations.

Chapter 7 presents the results of two- and three- dimensional simulations for laminar backward-facing step flows in a microscale duct. The effects of rarefaction(the velocity slip and temperature jump conditions) on the microscale flows with flow separation and reattachment are discussed. The effect of compressibility is also discussed.

Chapter 8 summarizes the major conclusions of this study and offers suggestions for future work.

References

[1] Fiebig, M., Kallweit, P. and Mitra, N.K., *Wing Type Vortex Generators for Heat Transfer Enhancement*, Proc. 8th Int. Heat Transfer Conf., Vol. 6 , pp. 2909-2913, (1986).

[2] Fiebig, M., *Vortex Generators for Compact Heat Exchangers*, J. Enhanced Heat Transfer, Vol. 2, Nos. 1-2 , pp. 43-61, (1995).

[3] Webb, R.L., Eckert, E.R.G. and Goldstein, R.J., *Heat Transfer and Friction in Tubes with Repeated-Rib Roughness*, Int. J. Heat Mass Transfer, Vol. 14 , pp. 601-617, (1971).

[4] Lehmann, G.L. and Wirtz, R.A., *Effect of Variations in Streamwise Spacing and Length on Convection from Surface-Mounted Rectangular Components*, Heat Transfer Engng, Vol. 9, No. 3, pp. 66-75, (1988).

[5] Eaton, J.K. and Johnston, J.P., *A Review of Research on Subsonic Turbulent Flow Reattachment*, AIAA Journal, Vol. 19, No. 9, pp. 1093-1100, (1981).

[6] Ötügen, M.V., *Expansion Ratio Effects on the Separated Shear Layer and Reattachment Downstream of a Backward-Facing Step*, Exp. Fluids, Vol. 10, pp. 273-280 (1991).

[7] Ötügen, M. V. and Muckenthaler, G., *Study of Separated Shear Layer in Moderate Reynolds Number Plane Sudden Expansion Flows*, AIAA journal, Vol. 30, No. 7, pp. 1807-1814 (1992).

[8] Vogel, J.C. and Eaton, J.K., *Combined Heat Transfer and Fluid Dynamic Measurements Downstream of a Backward-Facing Step*, J. Heat Transfer, Vol. 107, pp. 922-929, (1985).

[9] Driver, D.M., Seegmiller, H.L. and Marvin, J.G., *Time-Dependent Behavior of a Reattaching Shear Layer*, AIAA journal, Vol. 25, No. 7, pp. 914-919 (1987).

[10] Adams, E.W. and Eaton J.K., *An LDA Study of the Backward-Facing Step Flow, Including the Effects of Velocity Bias*, J. Fluids Engng., Vol. 110, pp. 275-282, (1988).

[11] Brederode, V. de, and Bradshaw, P., *Three-Dimensional Flow in Nominally Two-Dimensional Separation Bubbles; I. Flow Behind a Rearward-Facing Step*, Imperial College of Science and Technology, Aero Report 72-19, (1972).

[12] Ötügen, M.V., Papadopoulos, G., Vradis, G. and Muckenthaler, G., *Spanwise Characteristics of the Separated Flow in a Suddenly Expanding Duct*, Experiments in fluids, Vol. 14, pp. 213-216, (1992).

[13] Papadopoulos, G., Ötügen, M.V., *Separating and Reattaching Flow Structure in a Suddenly Expanding Rectangular Duct*, J. Fluids Engng., Vol.117, pp. 17-23, (1995).

[14] Shih, C. and Ho, C.M., *Three-Dimensional Recirculation Flow in a Backward Facing Step*, J. Fluids Engng., Vol.116, pp. 228-232, (1994).

[15] Le, H., Moin, P. and Kim, J., *Direct Numerical Simulation of Turbulent Flow Over a Backward-Facing Step*, Proceedings of The 9th International Symposium on Turbulent Shear Flows, pp. 13.2.1-13.2.5, (1993).

[16] Lasher, W.C. and Taulbee, D.B., *On the Computation of Turbulent Backstep Flow*, Int. J. Heat and Fluid Flow, Vol. 13, No. 1, pp. 30-40, (1992).

[17] Launder, B.E. *On the Computation of Convective Heat Transfer in Complex Turbulent Flows*, J. Heat Transfer, Vol. 110, pp. 1112-1128, (1988).

[18] Goldstein, R.J., Ericsen, V.L., Olson, R.M. and Eckert, E.R.G., *Laminar Separation,Reattachment,and Transition of the Flow Over a Downstream-Facing Step*, J. Basic Engng., pp 732-741, (1970).

[19] Denham, M.K. and Patrick, M.A., *Laminar Flow Over a Downstream-Facing Step in a Two-Dimensional Flow Channel*, Trans.INSTN CHEM.ENGRS,, Vol 52, pp 361-367, (1974).

[20] Armaly, B. F., Durst, F., Pereira, J. C. F. and Schonung, B., *Experimental and Theoretical Investigation of Backward-Facing Step Flow*, Journal of Fluid Mechanics, Vol.127, pp. 473-496, (1983).

[21] Aung, W., *An Experimental Study on Laminar Heat Transfer Downstream of Backsteps*, J. Heat Transfer, Vol.105, pp. 823-829, (1983).

[22] Abu-Mulaweh, H.I., Armaly, B.F. and Chen, T.S., *Measurements of Laminar Mixed Convection in Boundary-Layer Flow over Horizontal and Inclined Backward-Facing Steps*, Int. J. Heat Mass Transfer, Vol.36-7, pp. 1883-1895, (1993).

[23] Abu-Mulaweh, H.I., Armaly, B.F. and Chen, T.S., *Measurements in Buoyancy-Opposing Laminar Flow over a Vertical Backward-Facing Step*, J. Heat Transfer, Vol.116, pp. 247-249, (1994).

[24] Baek, B.J., Armaly, B.F. and Chen, T.S., *Measurements in Buoyancy-Assisting Separated Flow Behind a Vertical Backward-Facing Step*, Trans.ASME: J.Heat Trans., Vol. 115, pp.403-408, (1993).

[25] Kondoh,T.,Nagano,Y. and Tsuji,T., *Computational Study of Laminar Heat Transfer Downstream of a Backward-Facing Step* , Int.J.Heat Mass Transfer, vol.36-3, pp.577-591 (1993).

[26] Ichinose, K., Tokunaga, H. and Satofuka, N., *Numerical Simulation of Two-dimensional Backward-Facing Step Flows* , Trans.JSME B, vol.57-543, pp.3715-3721 (1991)(in Japanese).

[27] Lin J.T.,Armaly, B.F. and Chen, T.S., *Mixed Convection in Buoyancy-Assisting, Vertical Backward-Facing Step Flows*, Int. J. Heat Mass Transfer, Vol.33-10, pp. 2121-2132, (1990).

[28] Lin J.T.,Armaly, B.F. and Chen, T.S.,*Mixed Convection Heat Transfer in Inclined Backward-Facing Step Flows*, Int. J. Heat Mass Transfer, Vol.34-6, pp. 1568-1571,

(1991).

[29] Hong B.,Armaly, B.F. and Chen, T.S., *Laminar Mixed Convection in a Duct with a Backward-Facing Step: the Effects of Inclination Angle and Prandtl Number* , Int.J.Heat Mass Trans., vol.36-12, pp.3059-3067 (1993).

[30] Sparrow, E.M., Kang, S. and Chuck W., *Relation between the Points of Flow Reattachment and Maximum Heat Transfer for Regions of Flow Separation*, Int.J. Heat Mass Transfer, Vol. 30-7, pp.1237-1246, (1987).

[31] Sparrow, E.M. and Chuck, W., *PC Solutions for Heat Transfer and Fluid Flow Downstream of an Abrupt, Asymmetric Enlargement in a Channel*, Num. Heat Transfer, Vol. 12, pp. 19-40, (1987).

[32] Beskok, A. and Karniadakis, G.E., *Modeling Separation in Rarefied Gas Flows*, AIAA 97-1883, (1997).

[33] Kaiktsis, L., Karniadakis, G.E. and Orszag, S.A., *Onset of Three-Dimensionality, Equilibria, and Early Transition in Flow over a Backward-Facing Step*, J. Fluid Mech., Vol 231, pp 501-528, (1991).

Chapter 2

Numerical Procedure

2.1 Introduction

Recent development of computer hardware enabled the numerical approach to various types of heat and mass transfer problems and a number of computational methods have been proposed by many researchers. Finite-Volume Method (FVM) adopted in the present study is one of the most commonly used methods.

The computational code used in the present study originates in the two-dimensional steady code (2/E/FIX) by Pun and Spalding [1]. With continuous efforts by researchers such as Kang [2,3], Suzuki [4], Xi [5] and Matsubara [6], this primary code had been developed into three-dimensional unsteady code in the Heat Transfer laboratory of Kyoto University. In the present study, further development was made to the three-dimensional unsteady code by applying the higher-order finite difference method [7] in order to perform three dimensional computations effectively with relatively small number of grid points. In this chapter, the outline of the numerical procedure used in the present study is discussed.

2.2 Governing Equations

The following assumptions were basically adopted in the numerical computations.

1. The working fluid is an incompressible Newtonian fluid

2. Physical properties of fluid are constant

3. Viscous dissipation is neglected

The working fluid is basically assumed to be air and its fluid properties are evaluated at the duct inlet. Prandtl number is taken to be 0.71. Only in Chapter 7, the fluid is assumed to be Nitrogen. The governing equations are written as follows:

Continuity equation

$$\frac{\partial \rho}{\partial t} + \frac{\partial}{\partial x}(\rho U) + \frac{\partial}{\partial y}(\rho V) + \frac{\partial}{\partial z}(\rho W) = 0 \tag{2.1}$$

Navier-Stokes equations

$$\begin{aligned} &\frac{\partial}{\partial t}(\rho U) + \frac{\partial}{\partial x}(\rho U^2) + \frac{\partial}{\partial y}(\rho VU) + \frac{\partial}{\partial z}(\rho WU) \\ = \; &-\frac{\partial P}{\partial x} + \frac{\partial}{\partial x}\left(\mu \frac{\partial U}{\partial x}\right) + \frac{\partial}{\partial y}\left(\mu \frac{\partial U}{\partial y}\right) + \frac{\partial}{\partial z}\left(\mu \frac{\partial U}{\partial z}\right) \end{aligned} \tag{2.2}$$

$$\begin{aligned} &\frac{\partial}{\partial t}(\rho V) + \frac{\partial}{\partial x}(\rho UV) + \frac{\partial}{\partial y}(\rho V^2) + \frac{\partial}{\partial z}(\rho WV) \\ = \; &-\frac{\partial P}{\partial y} + \frac{\partial}{\partial x}\left(\mu \frac{\partial V}{\partial x}\right) + \frac{\partial}{\partial y}\left(\mu \frac{\partial V}{\partial y}\right) + \frac{\partial}{\partial z}\left(\mu \frac{\partial V}{\partial z}\right) \end{aligned} \tag{2.3}$$

$$\begin{aligned} &\frac{\partial}{\partial t}(\rho W) + \frac{\partial}{\partial x}(\rho UW) + \frac{\partial}{\partial y}(\rho VW) + \frac{\partial}{\partial z}(\rho W^2) \\ = \; &-\frac{\partial P}{\partial z} + \frac{\partial}{\partial x}\left(\mu \frac{\partial W}{\partial x}\right) + \frac{\partial}{\partial y}\left(\mu \frac{\partial W}{\partial y}\right) + \frac{\partial}{\partial z}\left(\mu \frac{\partial W}{\partial z}\right) \end{aligned} \tag{2.4}$$

Energy equation

$$\begin{aligned} &\frac{\partial}{\partial t}(\rho h) + \frac{\partial}{\partial x}(\rho Uh) + \frac{\partial}{\partial y}(\rho Vh) + \frac{\partial}{\partial z}(\rho Wh) \\ = \; &\frac{\partial}{\partial x}\left(\frac{\lambda}{C_P}\frac{\partial h}{\partial x}\right) + \frac{\partial}{\partial y}\left(\frac{\lambda}{C_P}\frac{\partial h}{\partial y}\right) + \frac{\partial}{\partial z}\left(\frac{\lambda}{C_P}\frac{\partial h}{\partial z}\right) \end{aligned} \tag{2.5}$$

where x,y and z are the streamwise, normal and spanwise directions respectively, to be specified later. The symbols U,V,W,P and h denote the fluid velocity components in the x,y and z directions, pressure and enthalpy, respectively, while ρ,μ,λ and C_P stand for the fluid density, viscosity, thermal conductivity and specific heat, respectively.

2.3 Computational Domain and Coordinate System

Figure 2.1 schematically illustrates the computational domain presently adopted for three-dimensional computations. The duct is made up of a stepped (heated) wall, a straight wall and two side walls. The origin of the coordinate system is located at the center of the bottom line of the backward-facing wall. x-coordinate is set for the streamwise direction, y for the transverse direction and z for the spanwise direction. The computational domain is set to cover the streamwise positions of $-1 \leq x/S \leq 30$, where S is the step height, in most of the present calculations. It is confirmed in a preliminary stage of the study that the effects of domain size on final results are small enough with this arrangement for the computational domain.

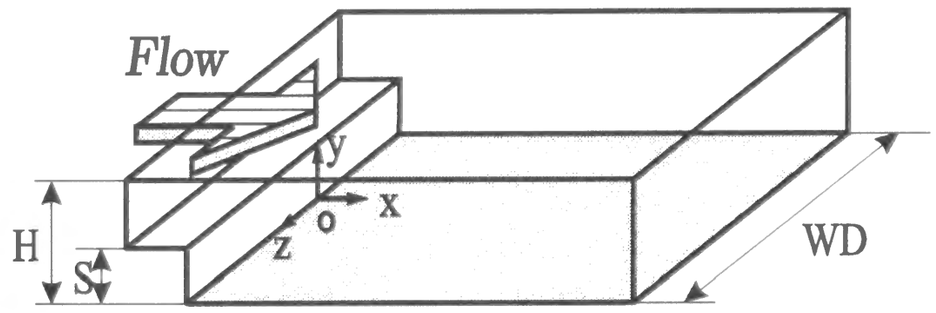

Figure 2.1: Computational domain.

Although most of the computations are three-dimensional in this study, some two-dimensional computations are also carried out. Those 2-D computations are conducted in the plane where z=0. Since the computational method adopted is basically the same for both 2-D and 3-D simulations, the method for the 3-D simulation will only be explained here.

2.4 Grid System

A staggered grid arrangement is employed as the grid system in this study. A typical grid system in $x-y$ plane is illustrated in Fig. 2.2 as an example. In this grid system, scalar variables such as pressure and temperature are evaluated and stored at main grid points while velocity components are calculated and stored at the velocity grid points staggered from the main grid points. The velocity grid points are centered in the faces of the main grid cells. There are two major advantages for the use of this staggered grid system. One is that calculated velocity components are directly available at the faces of the control-volume for scalar variables, where the velocity components are needed for the calculation of the scalar convection flux crossing the boundaries of control-volume. The other one is that the pressure difference between two adjacent main grid points can directly be used as a source to drive the velocity component stored at a velocity grid point located between the two main grid points.

In addition, to save computational time and cost, a non-uniform grid system is employed whereby grid points are allocated densely near the walls, the corners of the rectangular duct and the edge of the step where large gradients of velocity and temperature are expected to be established. The maximum expansion ratio of grid spacing adopted in this study is 1.1.

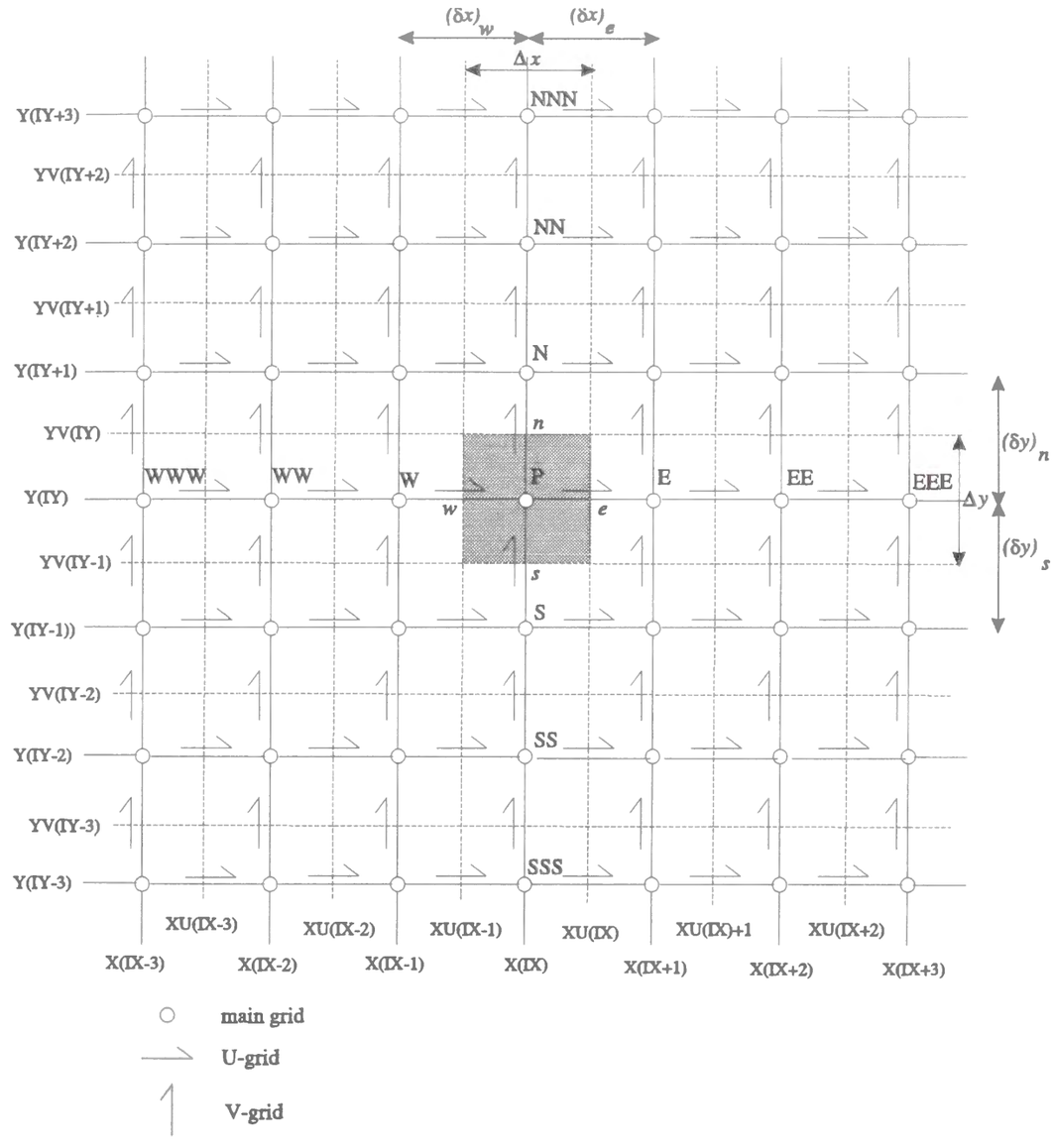

Figure 2.2: Staggered grid system ($x-y$ plane)

2.5 Discretisation Method

The Finite-Volume Method is adopted in the present study. In this method, the governing equations are integrated over each control volume and discretised with the values of velocity and other variables at the grid points inside and on the faces of the control volume.

A general form of all the governing equations mentioned above can be written as

$$\begin{aligned} &\frac{\partial}{\partial t}(\rho\phi) + \frac{\partial}{\partial x}(\rho U\phi) + \frac{\partial}{\partial y}(\rho V\phi) + \frac{\partial}{\partial z}(\rho W\phi) \\ = \; &\frac{\partial}{\partial x}\left(\Gamma_\phi \frac{\partial \phi}{\partial x}\right) + \frac{\partial}{\partial y}\left(\Gamma_\phi \frac{\partial \phi}{\partial y}\right) + \frac{\partial}{\partial z}\left(\Gamma_\phi \frac{\partial \phi}{\partial z}\right) + S_\phi \end{aligned} \tag{2.6}$$

where ϕ represents any transport variable, Γ_ϕ the diffusion coefficient and $S_\phi = S_c + S_p\phi$ the source term respectively. Attention is now paid to a control volume surrounding the main grid point P as is shown as the shaded part in Fig. 2.2 . The general form of all governing equations, Eq. (2.6), is now integrated over the control volume in the x-direction from the point w to the point e, in the y direction from s to n and in the z direction from b to t. The points b and t are not shown in Fig. 2.2 but are the grid points on both sides of the point P aligned in the direction normal to the $x-y$ plane passing through the paper. Here, e, w, n, s, t, b denote the east, west, north, south, top, bottom faces of the control-volume respectively. A further integration over a finite time step, Δt, is carried out over a time period from t to $t + \Delta t$. In this process, the fully implicit scheme is adopted for the unsteady term; a scheme where the value of the variable ϕ at the time $t + \Delta t$ is assumed to persist over the time period Δt. The time step, Δt, is kept constant during each computation and is selected such that the Courant number defined below is equal to unity, i.e.

$$\text{Courant number, } C = \frac{U_{max}\Delta t}{\Delta x_{min}} = 1$$

where U_{max} is the maximum value of fluid velocity and Δx_{min} is the minimum grid spacing.

The result of the entire integration process gives,

$$\begin{aligned} &\{(\rho\phi)_P - (\rho\phi)_P^o\}\,\Delta x\Delta y\Delta z + \{(\rho U\phi)_e - (\rho U\phi)_w\}\,\Delta y\Delta z\Delta t \\ &+ \{(\rho V\phi)_n - (\rho V\phi)_s\}\,\Delta x\Delta z\Delta t + \{(\rho W\phi)_t - (\rho W\phi)_b\}\,\Delta x\Delta y\Delta t \\ = \; &\left\{\left(\Gamma\frac{\partial\phi}{\partial x}\right)_e - \left(\Gamma\frac{\partial\phi}{\partial x}\right)_w\right\}\Delta y\Delta z\Delta t + \left\{\left(\Gamma\frac{\partial\phi}{\partial y}\right)_n - \left(\Gamma\frac{\partial\phi}{\partial y}\right)_s\right\}\Delta x\Delta z\Delta t \\ &+ \left\{\left(\Gamma\frac{\partial\phi}{\partial z}\right)_t - \left(\Gamma\frac{\partial\phi}{\partial z}\right)_b\right\}\Delta x\Delta y\Delta t + S_\phi\Delta x\Delta y\Delta z\Delta t \end{aligned} \tag{2.7}$$

The superscript 'o' here refers to the values of ϕ at the old time level t while values at the new time level $t + \Delta t$ are not superscripted.

The above equation, Eq. (2.7) represents the balance of ϕ in a control volume. The left hand side comprises the unsteady term and the net convective flux. The right hand side contains the net diffusive flux and the generation or destruction of the property ϕ within the control volume.

To relate the face values specified with lower case suffices e, w, n, s, b and t in Eq. (2.7) to the grid values, some form of interpolation polynomial is required for approximation of ϕ between grid nodes. In the present study, the 5th-order upwind scheme is employed for the convection terms while the 4th-order central-difference scheme is employed [7] for the diffusion terms. Figure 2.3 shows the one-dimensional grid system as the simplest example. In the 5th-order upwind scheme, a five-point upstream-weighted 4th-order polynomial interpolation is used to evaluate the cell face values. The cell face value of ϕ is obtained from a polynomial function passing through total 5 nodes along the line crossing the cell face, 3 nodes on the upstream side and 2 on the downstream side. The combination of the nodes used in this scheme changes depending on the flow direction at the cell face. For instance, the value of ϕ at the e-face of the control volume,ϕ_e, is determined from $(\phi_{WW}, \phi_W, \phi_P, \phi_E, \phi_{EE})$ when $U_e > 0$, while it is determined from $(\phi_W, \phi_P, \phi_E, \phi_{EE}, \phi_{EEE})$ when $U_e < 0$. The value of ϕ at the w-face of the control volume,ϕ_w, is also determined in the same way.

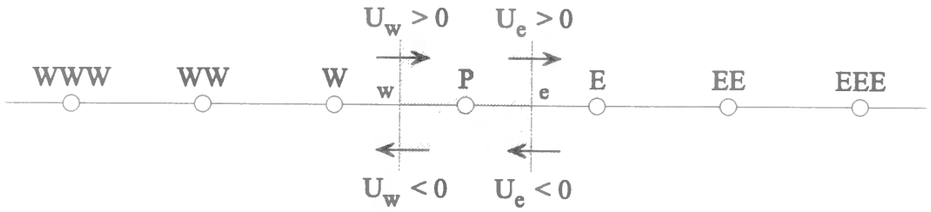

Figure 2.3: One dimensional grid system.

Then the value of ϕ at e and w faces of the control volume can be written as follows:

$$\phi_e = f_P^6\phi_{WW} + f_P^7\phi_W + f_P^8\phi_P + f_P^9\phi_E + f_P^{10}\phi_{EE} \quad (if\ \ U_e < 0) \tag{2.8}$$

$$\phi_e = f_E^1\phi_{WWW} + f_E^2\phi_{WW} + f_E^3\phi_W + f_E^4\phi_P + f_E^5\phi_E \quad (if\ \ U_e > 0) \tag{2.9}$$

$$\phi_w = f_P^1\phi_{WW} + f_P^2\phi_W + f_P^3\phi_P + f_P^4\phi_E + f_P^5\phi_{EE} \quad (if\ \ U_w < 0) \tag{2.10}$$

$$\phi_w = f_W^6\phi_{WWW} + f_W^7\phi_{WW} + f_W^8\phi_W + f_W^9\phi_P + f_W^{10}\phi_E \quad (if\ \ U_w > 0) \tag{2.11}$$

where f is the coefficient which can be determined from a geometrical analysis once the grid system is determined. $f_P^1 \sim f_P^5$ are used when fluid is directed in a way to flow out from the w-side of the control volume around the grid point P, while $f_P^6 \sim f_P^{10}$ are used when fluid flows out from the e-side of the control volume around P. This is schematically illustrated in Fig. 2.4.

The 4th-order central-difference scheme is just an extension of the lower-order central-difference scheme. More neighboring points are used to approximate the diffusion terms with this scheme. Considering the mathematical convenience, the ϕ gradients at e and w surfaces are written as:

$$(\delta x)_e \left(\frac{\partial\phi}{\partial x}\right)_e = d_e^1\phi_W + d_e^2\phi_P + d_e^3\phi_E + d_e^4\phi_{EE} \quad (e-side) \tag{2.12}$$

$$(\delta x)_w \left(\frac{\partial\phi}{\partial x}\right)_w = d_w^1\phi_{WW} + d_w^2\phi_W + d_w^3\phi_P + d_w^4\phi_E \quad (w-side) \tag{2.13}$$

where $d_e^1 \sim d_e^4$ and $d_w^1 \sim d_w^4$ are the coefficients obtained from the geometrical analysis similar to the one referred to for $f_P^1 \sim f_P^5$ and $f_P^6 \sim f_P^{10}$.

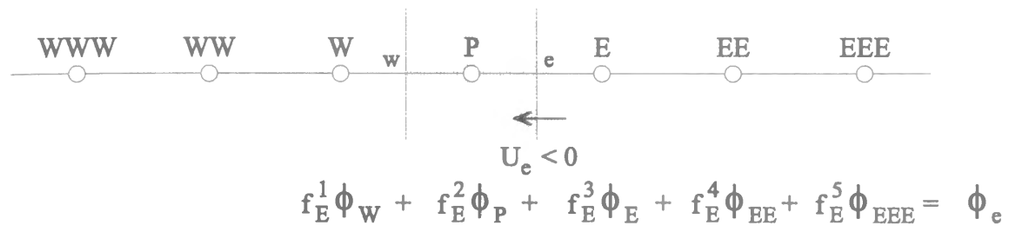

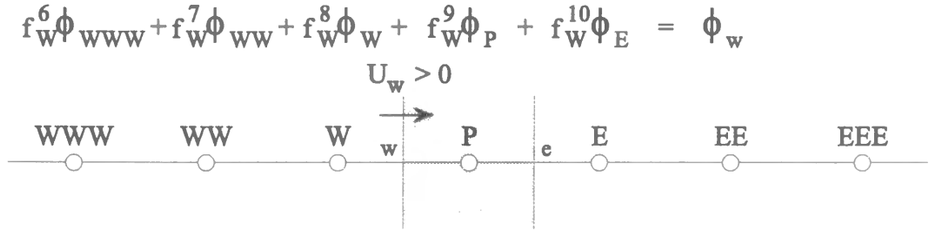

Figure 2.4: Fifth order upwind scheme.

Higher-order scheme involves more neighboring points and reduces discretisation errors, particularly numerical diffusion errors, which could be a disadvantage in terms of computational stability though. In addition, it possibly reduces the CPU time needed for the computation since a change given at a boundary could propagate to the grid points inside the computational domain faster.

Adoption of the 5th-order upwind and 4th-order central-difference approximations leads finally to the following discretised equation:

$$\begin{aligned} a_P\phi_P &= a_{WWW}\phi_{WWW} + a_{WW}\phi_{WW} + a_W\phi_W + a_E\phi_E + a_{EE}\phi_{EE} + a_{EEE}\phi_{EEE} \\ &\quad + a_{SSS}\phi_{SSS} + a_{SS}\phi_{SS} + a_S\phi_S + a_N\phi_N + a_{NN}\phi_{NN} + a_{NNN}\phi_{NNN} \\ &\quad + a_{BBB}\phi_{BBB} + a_{BB}\phi_{BB} + a_B\phi_B + a_T\phi_T + a_{TT}\phi_{TT} + a_{TTT}\phi_{TTT} \\ &\quad + b \end{aligned} \tag{2.14}$$

where,

$$\begin{aligned} a_{WWW} &= f^6_{xW}[\![F_w, 0]\!] \\ a_{WW} &= -f^6_{xP}[\![F_e, 0]\!] + f^7_{xW}[\![F_w, 0]\!] - f^1_{xP}[\![-F_w, 0]\!] - d^1_w D_w \\ a_W &= -f^7_{xP}[\![F_e, 0]\!] + f^1_{xE}[\![-F_e, 0]\!] + f^8_{xW}[\![F_w, 0]\!] - f^2_{xP}[\![-F_w, 0]\!] + d^1_e D_e - d^2_w D_w \\ a_E &= -f^9_{xP}[\![F_e, 0]\!] + f^3_{xE}[\![-F_e, 0]\!] + f^{10}_{xW}[\![F_w, 0]\!] - f^4_{xP}[\![-F_w, 0]\!] + d^3_e D_e - d^4_w D_w \\ a_{EE} &= -f^{10}_{xP}[\![F_e, 0]\!] + f^4_{xE}[\![-F_e, 0]\!] - f^5_{xP}[\![-F_w, 0]\!] + d^4_e D_e \\ a_{EEE} &= f^5_{xE}[\![-F_e, 0]\!] \\ a_{SSS} &= f^6_{yS}[\![F_s, 0]\!] \\ a_{SS} &= -f^6_{yP}[\![F_e, 0]\!] + f^7_{yS}[\![F_s, 0]\!] - f^1_{yP}[\![-F_s, 0]\!] - d^1_s D_s \\ a_S &= -f^7_{yP}[\![F_n, 0]\!] + f^1_{yN}[\![-F_n, 0]\!] + f^8_{yS}[\![F_s, 0]\!] - f^2_{yP}[\![-F_s, 0]\!] + d^1_n D_n - d^2_s D_s \\ a_N &= -f^9_{yP}[\![F_n, 0]\!] + f^3_{yN}[\![-F_n, 0]\!] + f^{10}_{yS}[\![F_s, 0]\!] - f^4_{yP}[\![-F_s, 0]\!] + d^3_n D_n - d^4_s D_s \\ a_{NN} &= -f^{10}_{yP}[\![F_n, 0]\!] + f^4_{yN}[\![-F_n, 0]\!] - f^5_{yP}[\![-F_s, 0]\!] + d^4_n D_n \\ a_{NNN} &= f^5_{yN}[\![-F_n, 0]\!] \\ a_{BBB} &= f^6_{zB}[\![F_b, 0]\!] \\ a_{BB} &= -f^6_{zP}[\![F_e, 0]\!] + f^7_{zB}[\![F_b, 0]\!] - f^1_{zP}[\![-F_b, 0]\!] - d^1_b D_b \\ a_B &= -f^7_{zP}[\![F_t, 0]\!] + f^1_{zT}[\![-F_t, 0]\!] + f^8_{zB}[\![F_b, 0]\!] - f^2_{zP}[\![-F_b, 0]\!] + d^1_t D_t - d^2_b D_b \\ a_T &= -f^9_{zP}[\![F_t, 0]\!] + f^3_{zT}[\![-F_t, 0]\!] + f^{10}_{zB}[\![F_b, 0]\!] - f^4_{zP}[\![-F_b, 0]\!] + d^3_t D_t - d^4_b D_b \\ a_{TT} &= -f^{10}_{zP}[\![F_t, 0]\!] + f^4_{zT}[\![-F_t, 0]\!] - f^5_{zP}[\![-F_b, 0]\!] + d^4_t D_t \\ a_{TTT} &= f^5_{zT}[\![-F_t, 0]\!] \end{aligned}$$

$$\begin{aligned} a^o_P &= \frac{\rho^o_P \Delta x \Delta y \Delta z}{\Delta t} \\ b &= S_C \Delta x \Delta y \Delta z + a^o_P \phi^o_P \\ a_P &= a_{WWW} + a_{WW} + a_W + a_E + a_{EE} + a_{EEE} \\ &\quad + a_{SSS} + a_{SS} + a_S + a_N + a_{NN} + a_{NNN} \\ &\quad + a_{BBB} + a_{BB} + a_B + a_T + a_{TT} + a_{TTT} + a^o_P - S_P \Delta x \Delta y \Delta z \end{aligned}$$

Here, $[\![\ ,\ ]\!]$ is a symbol selecting the larger one from the two values written on both sides of comma. F and D represent the convective mass flux and diffusion conductance at the cell face specified by the suffix and are defined as follows:

$$\begin{aligned} F_e &= (\rho U)_e \Delta y \Delta z \quad , \quad D_e = \frac{\Gamma_e \Delta y \Delta z}{(\delta x)_e} \\ F_w &= (\rho U)_w \Delta y \Delta z \quad , \quad D_w = \frac{\Gamma_w \Delta y \Delta z}{(\delta x)_w} \\ F_n &= (\rho V)_n \Delta z \Delta x \quad , \quad D_n = \frac{\Gamma_n \Delta z \Delta x}{(\delta y)_n} \\ F_s &= (\rho U)_s \Delta z \Delta x \quad , \quad D_s = \frac{\Gamma_s \Delta z \Delta x}{(\delta y)_s} \\ F_t &= (\rho W)_t \Delta x \Delta y \quad , \quad D_t = \frac{\Gamma_t \Delta x \Delta y}{(\delta z)_t} \\ F_b &= (\rho W)_b \Delta x \Delta y \quad , \quad D_b = \frac{\Gamma_b \Delta x \Delta y}{(\delta z)_b} \end{aligned}$$

2.6 Revisions of the Coefficients

Near the boundaries of the computational domain

The higher-order schemes used in the present study involve more neighboring points than the lower-order schemes. In the fifth order upwind scheme, for example, the values of ϕ at three grid points away from P (ϕ_{WWW} and ϕ_{EEE} in Fig. 2.4) are needed. Such higher-order schemes cannot be adopted for the cells near the boundaries of the computational domain simply because the number of the neighboring grid points available are not enough for the scheme. In those cases, the lower-order schemes such as QUICK (Quadratic Upstream Interpolation for Convective Kinematics) [8] and the second order central scheme are used in the present study.

Near the step surfaces

The lower-order schemes are also used for the cells near the step surfaces. In addition to this, the discretised equations for the cells near the step surfaces need to be revised because of the staggered grid system adopted in this study. The coefficients of the discretised equations are revised before the computation is executed. An outline of the revisions of the coefficients will be presented below. The case for the U velocity component is discussed as an example. The same principle is applied to the equations of V,W velocity components and of enthalpy.

Figure 2.5 shows a cell adjoining the up-facing surface of the step. The lower boundary (south side) of this control volume is the step surface. Thus, the coefficient for the south side of this cell should not include the contribution from the convection. Only the diffusion from the south side of this control volume is taken into account.

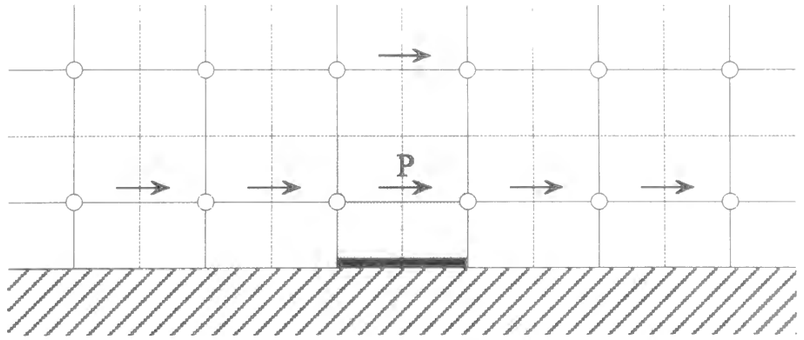

Figure 2.5: Staggered grid cells adjoining to a up-facing surface of the step

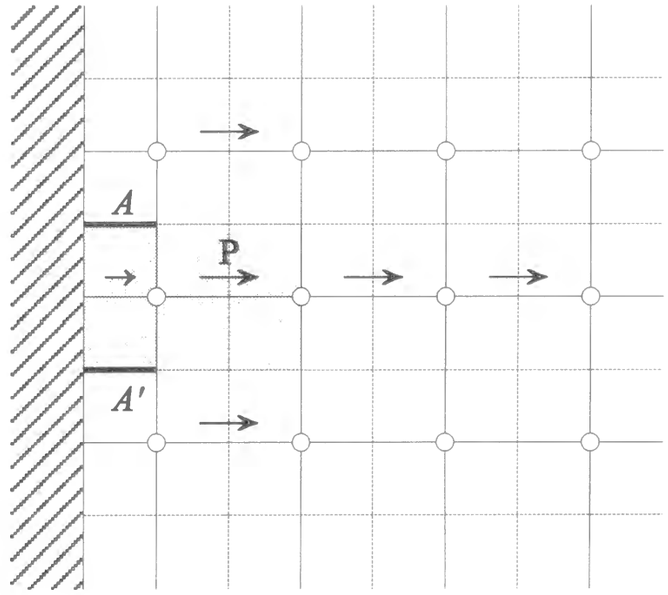

Figure 2.6: Staggered grid cells adjoining to a rear surface of the step

In the case of a cell attaching to the rear surface of the step shown in Fig. 2.6, the coefficients based on the convection and diffusion fluxes through the additional area of the boundary surfaces A and A' (north side and south side) should be taken into account in the calculation of the coefficients. Velocity component V at the boundary surface A is

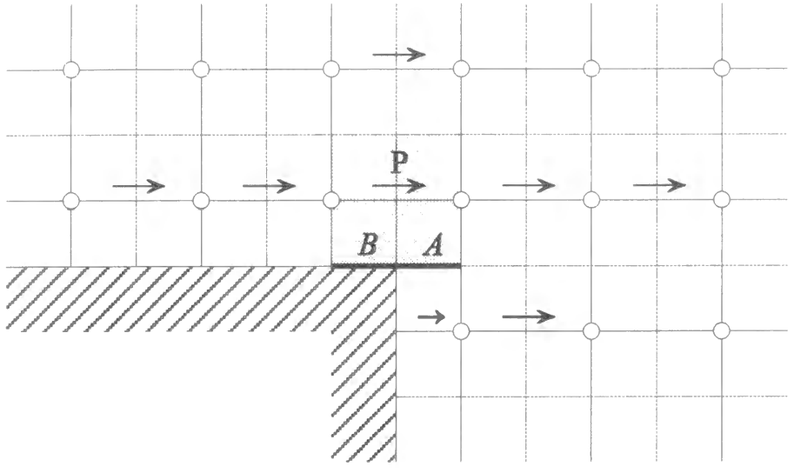

Figure 2.7: Staggered grid cells on the corner of the step

determined by linear interpolation between its value at the first grid from the step surface and that at the wall, which is zero. The same treatment is also used for the evaluation of V at the surface A'. The west side of the cell illustrated in Fig. 2.6 is a solid boundary. Thus the coefficient for the west side of the cell a_W is determined in a similar way to that described above for the south side of a cell adjoining to the up-facing surface of the step.

In the case of a cell on the corner of the step shown in Fig. 2.7, the coefficients of the discretised equations for the south side of the cell are described by the sum of the coefficients based on the convection and diffusion through the additional part A of the south boundary surface and those based on the diffusion through the part B of the south boundary surface.

2.7 Algorithm

The solution algorithm used in the present study is an iterative solution strategy called SIMPLE (Semi-Implicit Method for Pressure-Linked Equations) by Patankar and Spalding [9]. In this algorithm, the convective fluxes through cell faces F are first evaluated from the so-called guess velocity components. Furthermore, a guess pressure field is used to solve the momentum equations. Then a pressure correction equation, which is derived from the continuity equation, is solved to obtain a pressure correction at each grid point. The corrected pressure is in turn used to update the velocity and pressure fields. To start the iteration process, initial guesses for the velocity and pressure fields are used. As the algorithm proceeds, these guess fields are progressively improved. The process is iterated until convergence of the velocity and pressure field is achieved.

The discretised pressure correction equation derived from the continuity equation can be expressed as follows:

$$a_P P'_P = a_E P'_E + a_W P'_W + a_N P'_N + a_S P'_S + a_T P'_T + a_B P'_B + b \tag{2.15}$$

where

$$\begin{aligned}
a_E &= \rho_e d_e \Delta y \Delta z \\
a_W &= \rho_w d_w \Delta y \Delta z \\
a_N &= \rho_n d_n \Delta z \Delta x \\
a_S &= \rho_s d_s \Delta z \Delta x \\
a_T &= \rho_t d_t \Delta x \Delta y \\
a_B &= \rho_b d_b \Delta x \Delta y \\
b &= \frac{(\rho^o_P - \rho_P)\Delta x \Delta y \Delta z}{\Delta t} \\
&\quad + (\rho U^*_w - \rho U^*_e)\Delta y \Delta z \\
&\quad + (\rho V^*_s - \rho V^*_n)\Delta z \Delta x \\
&\quad + (\rho W^*_b - \rho W^*_t)\Delta x \Delta y
\end{aligned}$$

$$a_P = a_E + a_W + a_N + a_S + a_T + a_B$$

and

$$d_w = \frac{\Delta y \Delta z}{a_{P_{U_w}}}$$
$$d_e = \frac{\Delta y \Delta z}{a_{P_{U_e}}}$$
$$d_s = \frac{\Delta z \Delta x}{a_{P_{U_s}}}$$
$$d_n = \frac{\Delta z \Delta x}{a_{P_{U_n}}}$$
$$d_b = \frac{\Delta x \Delta y}{a_{P_{U_b}}}$$
$$d_t = \frac{\Delta x \Delta y}{a_{P_{U_t}}}$$

P' here denotes the pressure correction. The SIMPLE is iterative. When the governing equations of other scalars are coupled to the momentum equations, the calculation needs to be done in a sequential operations summarized as below:

1. Guess initial pressure field, P^*
2. Solve the momentum equations to yield the intermediate velocity field (U^*, V^*, W^*)
3. Solve the continuity equation in the form of an equation for pressure correction P'
4. Correct pressure and velocity by means of the following equations:

$$P = P^* + P'$$
$$U_e = U_e^* + d_e(P'_P - P'_E)$$
$$V_n = V_n^* + d_n(P'_P - P'_N)$$
$$W_t = W_t^* + d_t(P'_P - P'_T)$$

5. Solve all other discretised transport equations for scalars ϕ.
6. Repeat the process from 2 to 5 until the fields P, U, V, W, ϕ have all converged.

For unsteady flow calculations which are employed in the present study, the iterative procedures described above are applied at each time level until convergence is achieved. The main algorithm steps for the time-marching procedure are as follows:

A. Set initial values for U^o, V^o, W^o, ϕ^o

B. Carry out the iterative procedure described above, i.e. the one from step 1 to step 6.

C. The newly obtained converged values are used as initial values for the next time step and go back to the step B.

At every time step, a maximum number of 10 iterations were carried out. The complete algorithm structure for the present code is shown in Fig. 2.8.

To solve the discretised equations described above, a linear-iterative method using the modified Tri-Diagonal Matrix Algorithm (TDMA) [10] combined with the alternation of sweep directions is employed. Such an Alternating Direction Implicit Method [11] (ADI) coupled with the TDMA method is used to enhance an isotropic propagation of a change of variables occurring at one point to the surroundings. In such a procedure, the line-by-line TDMA method is applied along $e - w$ (east-west) lines (x-direction), $n - s$ (north-south) lines (y-direction),$t - b$ (top-bottom) lines (z-direction) alternately in one iteration. This procedure is applied twice in one iteration for the pressure correction.

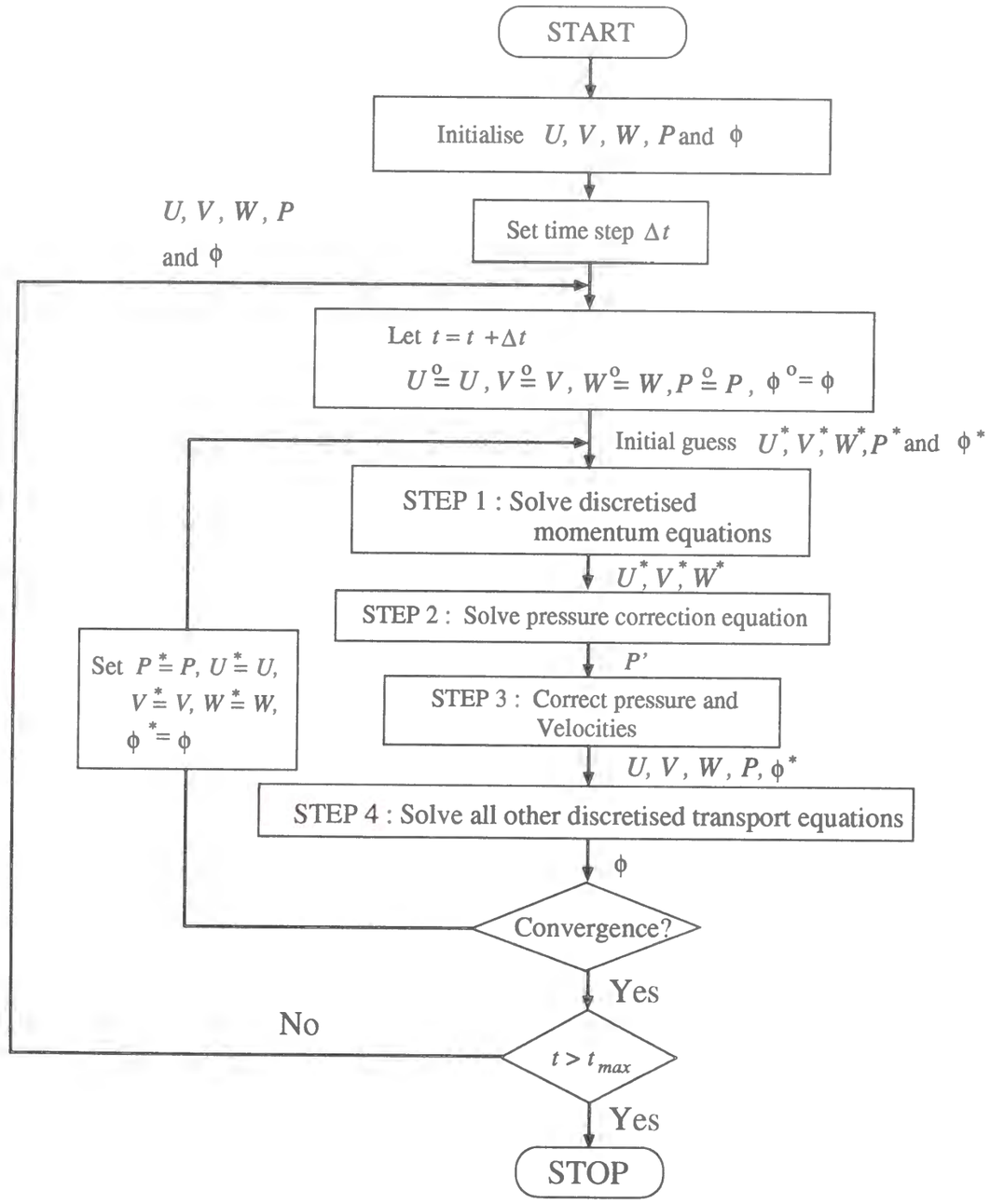

Figure 2.8: Flow Chart : Transient flow SIMPLE algorithm and its variants

2.8 Initial Conditions

Computations are started with tentative flow and thermal fields. The calculated flow and thermal fields depend on the adopted initial condition only at an early stage of the calculation and become independent of it after a certain number of time steps has been proceeded. The number of time steps needed then is subject to the computational (or boundary) conditions but is around 2×10^4. The values of velocity and temperature are monitored at several grid points during the calculations to check the influence of the initial condition as well as to decide if the calculated flow can be considered steady or not. All the discussions will be made to those results independent of initial conditions hereafter.

2.9 Boundary Conditions

Details of the adopted boundary conditions will be shown in each chapter. Only the basic conditions which often appear in the present study are listed here. Most of the calculations are made on a combination of these basic boundary conditions.

Inlet:

Fully developed flow

Uniform temperature

Wall surfaces:

No-slip condition for the normal scale flow, and slip condition for the microscale flow

Constant heat flux, Constant temperature or Adiabatic for the normal scale flow, and Temperature jump condition for the microscale flow.

Exit:

Boundary layer approximation [12] or Neumann condition

2.10 Summary

In this chapter the fundamental procedure of numerical simulation adopted in the present study has been outlined. Its basic feature can be summarized as follows:

1. The governing equations are discretised using Finite-Volume Method.
2. Staggered grid system is used.
3. Higher-order finite difference methods are used.
4. SIMPLE algorithm is adopted for the calculation of pressure.

Higher-order finite difference methods employed in the present study reduce discretisation errors, particularly numerical diffusion errors. The details of the boundary conditions will be described in each chapter.

References

[1] Pun, W.M. and Spalding, D.B., *A general Computer Program for Two Dimensional Elliptic Flows*, Impereial College Mechanical Engineering Department Report HTS/76/2, (1976).

[2] Kang, Y. and Suzuki, K., *Numerical Computation of the Heat Transfer in Confined Jets*, Trans. JSME, Vol. 48B, No. 425, pp. 122-129, (1982).

[3] Kang, Y., Suzuki, K., Sato, T. and Nishino, J., *Experiments and Numerical Computation of the Heat Transfer in Confined Jets*, Trans. JSME, Vol. 49B, No. 433, pp. 1513-1520, (1983).

[4] Suzuki, H., Inoue, Y., Nishihara, A. and Suzuki, K., *Unsteady Flow and Heat Transfer in a Channel Obstructed by a Square Rod (1st. Report, Validation of Numerical Calculation and Flow Visualization of Vortex Street)*, Trans. JSME, Vol. 57B, No. 536, pp. 1390-1395, (1991).

[5] Xi, G.N., Futagami, S., Hagiwara, Y. and Suzuki K., *Flow and Heat Transfer Characteristics of Fin Arrays in the Middle Range of Reynolds Number (1st. Report, Statistical Characteristics of Unsteady Flow and Temperature Fields)*, Trans. JSME, Vol. 59B, No. 560, pp. 1318-1323, (1993).

[6] Matsubara, K., Nakabe, K. and Suzuki, K. *Flow and Heat Transfer in a Channel with Fins Attached to One Wall*, Trans. JSME, Vol. 62B, No. 602, pp. 3675-3682, (1996).

[7] Miyauchi, T., Hirata, T. and Tanahashi, M., *Direct Numerical Simulation of Two-Dimensional Homogeneous Isotropic Turbulence by Higher-Order Finite Difference Scheme(Comparison with the Spectral Method)*, Trans. JSME, Vol. 60B, No. 574, pp. 1999-2006, (1994).

[8] Leonard, B.P., *A Stable and Accurate Convective Modelling Procedure Based on Quadratic Upstream Interpolation*, Comput. Method Appl. Mech. Eng., Vol.19, pp.

59-98, (1979).

[9] Patankar, S.V. and Spalding, D.B., *A Calculation Procedure for Heat, Mass and Momentum Transfer in Three-Dimensional Parabolic Flows*, Int. J. Heat Mass Transfer, Vol.15, no.10, pp.1787-1806, (1972).

[10] Patankar, S.V., *Numerical Heat Transfer and Fluid Flow*, (1980), Hemisphere.

[11] Rocache P.J. *Computational Fluid Dynamics*, (1976), Hermosa Publishers.

[12] Kieda, S. and Suzuki, K., *Numerical Study of the Flow Passing a Flat Plate of Finite Length*, Trans. JSME, Vol. 46B, No. 409, pp. 1655-1661, (1984).

Chapter 3

The Effects of Aspect Ratio on Laminar Flows over a Backward-Facing Step

3.1 Introduction

Recent requirement for the downsizing of heat exchanger brought the Reynolds number of the flows inside the heat exchangers relatively low. When Reynolds number is low enough the flows become laminar. Heat transfer enhancement due to the turbulence cannot be expected under such conditions. In order to establish a favorable heat exchange at low Reynolds number, it is necessary to modify the flow structure appropriately, for instance, with vortex generators [1,2] or ribs [3,4]. Such flow modification often includes the flow separation and reattachment. Consequently the modified flows tend to have quite complicated flow structures. In order to improve the performance of heat exchangers, understanding the details of such complicated flow structures is very important. Therefore, attention has been paid to one of the flows in such category, namely a separating and reattaching flow. In particular, as the most typical problem, backward-facing step flows under laminar conditions have been investigated both experimentally [5,6,7] and numerically [8,9,10] to obtain the basic information of the flow separation and reattachment phenomena in laminar flow

regime.

In most of the experimental investigations a considerably large aspect ratio of the duct was adopted in order to assume the two-dimensionality of the flow around the duct center region. Armaly [7] adopted the duct aspect ratio of 36 and ensured that the oncoming flow was two-dimensional. He measured quite successfully the distributions of the streamwise velocity for backward-facing step flows in a wide Reynolds number range, including laminar cases, using Laser-Doppler anemometer. Nevertheless it was reported in his paper that the flow downstream of the step only remained two-dimensional at low and high Reynolds numbers.

In numerical calculation the flows are often assumed to be two-dimensional since two-dimensional simulations require less CPU time and consume less memory compared to three-dimensional simulations. Although two-dimensional simulation is useful to obtain the basic idea of the flow and thermal fields, it is reported that the results of the two-dimensional computations sometimes show larger discrepancy from the experimental results as Reynolds number is increased, even in its range where the flow remains laminar [7~10]. This discrepancy is claimed to be a result of three-dimensional flow structures in experiments. Kaiktsis [10] performed three-dimensional simulations employing periodic boundary condition in the spanwise direction. However his numerical results still show noticeable discrepancy from the experimental results. One of the possible reason for this discrepancy is the three-dimensional structure of flow and thermal fields due to the existence of side walls.

In this chapter, three-dimensional numerical computation is performed for both flow and thermal fields over a backward-facing step in a rectangular duct in order to investigate the three-dimensional side wall effects on the flow and thermal fields.

3.2 Computational Conditions

3.2.1 Computational Domain

The computational domain is schematically illustrated in Fig. 3.1. The computational domain is set to cover the streamwise positions of $-1 \leq x/S \leq 30$, where S is the step height. It was confirmed that the effects of domain size on final results are small enough with this arrangement for the computational domain. The duct expansion ratio,$ER = H/(H-S)$, is kept constant at two.

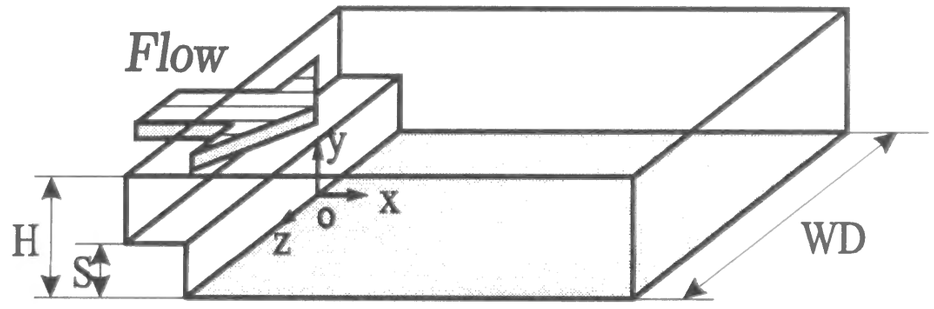

Figure 3.1: Computational domain.

3.2.2 Boundary Conditions

At the upstream boundary, inlet flow is assumed to be hydrodynamically steady and fully developed. The profile of the streamwise velocity U is given by the following approximation [11] which represents a fully developed laminar flow in a rectangular duct:

$$\frac{U}{U_{in}} = \left(\frac{m+1}{m}\right)\left(\frac{n+1}{n}\right)\left(1-\left(\frac{(y-S)-(H-S)/2}{(H-S)/2}\right)^{n}\right)\left(1-\left(\frac{z}{WD/2}\right)^{m}\right) \quad (3.1)$$

$$m = 1.7 + 0.5(\alpha^*)^{-1.4}$$

$$n = \begin{cases} 2 & for \quad \alpha^* \leq \frac{1}{3} \\ 2 + 0.3\left(\alpha^* - \frac{1}{3}\right) & for \quad \frac{1}{3} \leq \alpha^* \leq \frac{1}{2} \end{cases}$$

$$\alpha^* = \frac{H-S}{WD}$$

where U_{in} is the cross-sectional mean velocity at the inlet. S,H and WD are the step height, the duct height downstream of the step and the duct width, respectively. Other velocity components V and W are set to zero at the inlet, while the fluid is assumed to have a uniform temperature at the inlet. No-slip condition is applied at all wall surfaces. The side walls are treated adiabatic, while the other walls are kept at constant temperature higher than the inlet fluid temperature. At the downstream boundary, velocity and temperature profiles are assumed to obey the boundary layer approximation [12]. Discretised equations are derived from the following modified governing equations taking account of the boundary layer approximation:

$$\frac{\partial}{\partial t}(\rho U) + \frac{\partial}{\partial x}(\rho U^2) + \frac{\partial}{\partial y}(\rho VU) + \frac{\partial}{\partial z}(\rho WU) = -\frac{\partial P}{\partial x} + \frac{\partial}{\partial y}\left(\mu\frac{\partial U}{\partial y}\right) + \frac{\partial}{\partial z}\left(\mu\frac{\partial U}{\partial z}\right) \tag{3.2}$$

$$\frac{\partial}{\partial t}(\rho V) + \frac{\partial}{\partial x}(\rho UV) + \frac{\partial}{\partial y}(\rho V^2) + \frac{\partial}{\partial z}(\rho WV) = \frac{\partial}{\partial y}\left(\mu\frac{\partial V}{\partial y}\right) + \frac{\partial}{\partial z}\left(\mu\frac{\partial V}{\partial z}\right) \tag{3.3}$$

$$\frac{\partial}{\partial t}(\rho W) + \frac{\partial}{\partial x}(\rho UW) + \frac{\partial}{\partial y}(\rho VW) + \frac{\partial}{\partial z}(\rho W^2) = \frac{\partial}{\partial y}\left(\mu\frac{\partial W}{\partial y}\right) + \frac{\partial}{\partial z}\left(\mu\frac{\partial W}{\partial z}\right) \tag{3.4}$$

$$\frac{\partial}{\partial t}(\rho h) + \frac{\partial}{\partial x}(\rho Uh) + \frac{\partial}{\partial y}(\rho Vh) + \frac{\partial}{\partial z}(\rho Wh) = \frac{\partial}{\partial y}\left(\frac{\lambda}{C_P}\frac{\partial h}{\partial y}\right) + \frac{\partial}{\partial z}\left(\frac{\lambda}{C_P}\frac{\partial h}{\partial z}\right) \tag{3.5}$$

3.2.3 Computational Conditions

Calculations are carried out for several cases of different aspect ratios,AR, i.e. the duct width to the step height ratio, and of different Reynolds numbers,Re, based on the step height and the mean velocity at the inlet. The expansion ratio of the duct height to the inlet height is kept constant at 2.0. The computational conditions are summarized in Table 3.1. Numerical results are shown in the following sections for both of laminar and transitional flows in the Reynolds number range of $125 \leq Re \leq 375$. The computed flows were found to remain steady in all the cases calculated here, except in the case of $Re = 375$, in which the flow was found to be periodically unsteady. Distribution will be shown of the time averaged result for the case of $Re = 375$.

Table 3.1 : Computational conditions.

AR	$Re = 125$	$Re = 250$	$Re = 300$	$Re = 375$
4		○		
8		○		
16	○	○	○	○
24		○		

- Reynolds number, $Re = \frac{U_{in}S}{\nu}$
- Expansion Ratio, $ER = \frac{H}{H-S} = 2$
- Aspect Ratio, $AR = \frac{WD}{S}$

Close attention is paid to the distribution patterns of both skin friction coefficient and Nusselt number on the heated wall. They are defined as below:

$$\text{Skin friction coefficient}, C_f = \frac{2\tau_w}{\rho U_{in}^2} \tag{3.6}$$

$$\text{Nusselt number}, Nu = \frac{q_w S}{\lambda(T_w - T_{in})} \tag{3.7}$$

τ_w, q_w, T_w and T_{in} used here refer to the values of the wall shear stress, wall heat flux, wall temperature and inlet temperature respectively.

3.3 Results and Discussion

In experimental studies, various characteristic quantities of the fluid flow including Nusselt number,Nu, and skin friction coefficient,C_f, in the duct are often measured along the streamwise centerline of the bottom wall. A large aspect ratio is often adopted to ensure the two-dimensionality of flow field. Thus, in this chapter, first will be discussed the effects of the aspect ratio, AR, on the distribution patterns both of Nu and C_f along the centerline. Figure 3.2 shows the Nu distributions along the centerline in the cases of $AR = 4$, 8 and 16, compared with the one in the case of $AR = 24$ in which three-dimensionality is expected to be minimum among these four cases. The Reynolds number,Re, is fixed at

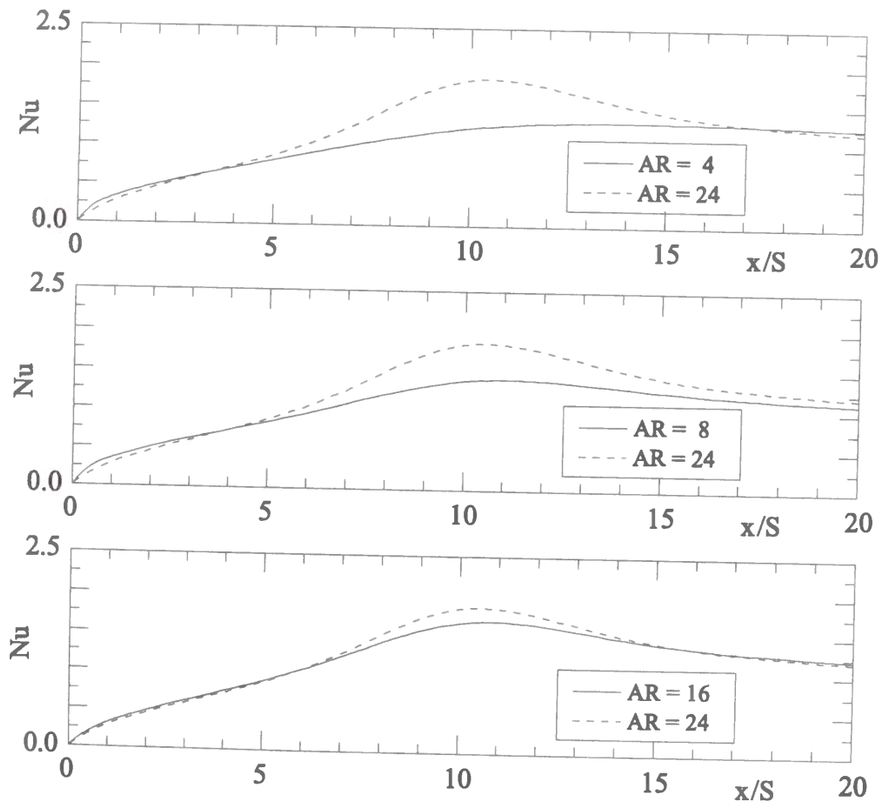

Figure 3.2: Nu distribution along the centerline.

250 in these cases. Although the case of $AR = 16$ shows better agreement with the case of $AR = 24$ than the rest of the cases, it still shows innegligible deviation in the region of $7 \leq x/S \leq 15$. The maximum difference of 11% between the case of $AR = 16$ and the case of $AR = 24$ is observed in the values of Nu. Figure 3.3 shows C_f distributions along the centerline similar to Fig. 3.2. C_f distribution also shows the dependency on the value of AR similar to the distribution of Nu. The shape of C_f distribution becomes closer to the one for $AR = 24$ as AR increases. However, maximum 10% of difference is still observed between the two cases $AR = 16$ and $AR = 24$ in the value of C_f. This result suggests that a considerably large aspect ratio is actually needed in order to assume the

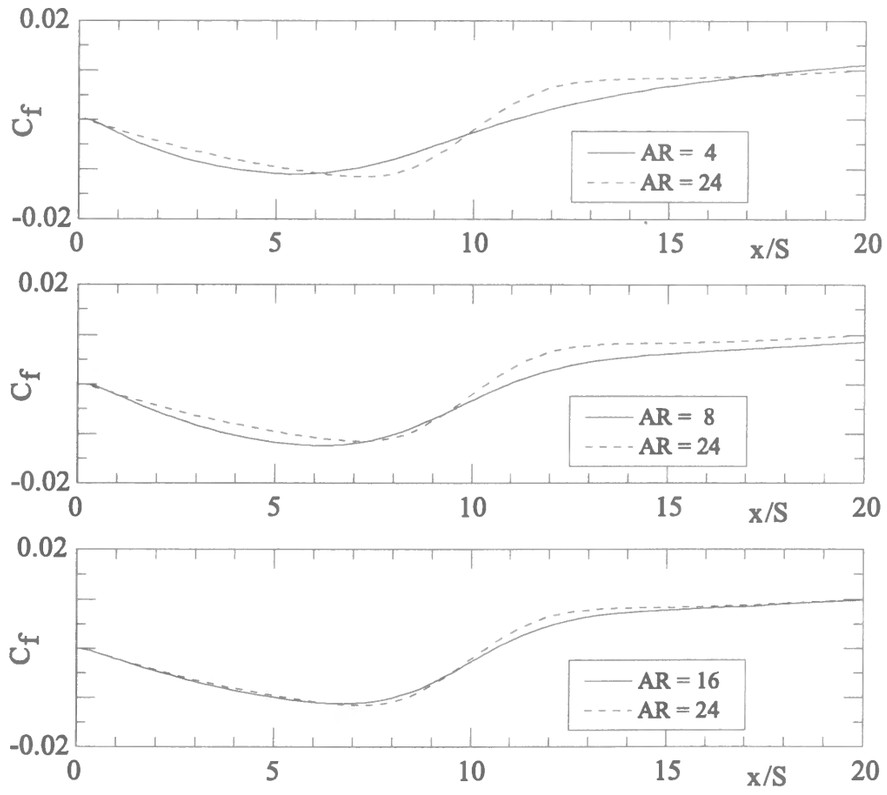

Figure 3.3: C_f distribution along the centerline.

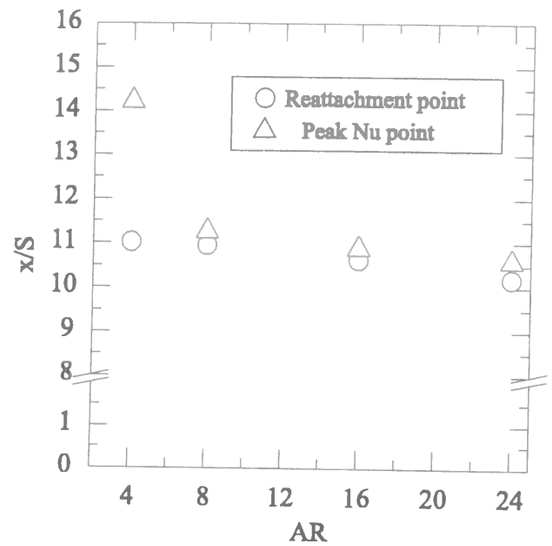

Figure 3.4: The effect of AR on the positions of Reattachment point and peak Nu point.

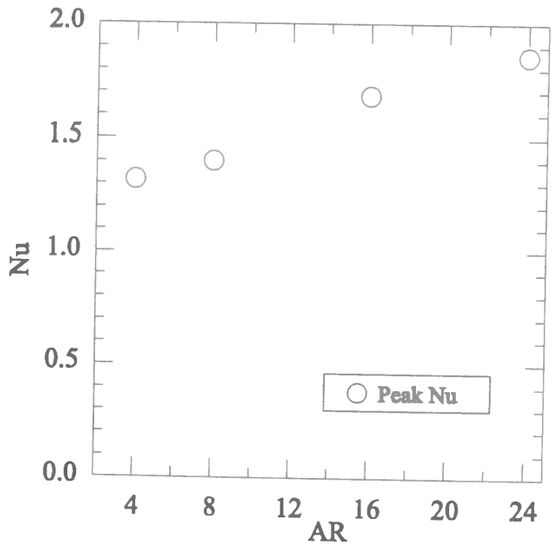

Figure 3.5: The effect of AR on the value of peak Nu.

two-dimensionality of the flow. It is also found in Fig. 3.2 that the peak Nusselt number, the highest value of Nusselt number along the centerline of the bottom face, becomes larger and its location moves upstream, as the aspect ratio is increased.

The positions of the peak Nu point and the reattachment point are plotted in Fig. 3.4. Reattachment point is defined as the point at which the skin friction coefficient changes its sign from negative to positive. Spatial relation of these two points has frequently been discussed in turbulent separating and reattaching flows but it has little been discussed in laminar backward-facing step flow. Figure 3.4 reveals that both positions shift upstream as AR increases and that the peak Nu position always appears downstream of the reattachment point. The distance between the peak Nu position and the reattachment point is relatively smaller for a larger aspect ratio, although the distance between the two points remains finite even in the case of $AR = 24$. Figure 3.5 shows the effect of AR on the value of peak Nusselt number. It is seen that the peak Nusselt number increases as AR is increased.

The evolvement of velocity profiles along the duct centerline, in particular the position of reattachment point, obtained from the present calculations agrees well with the experimental counterpart obtained by other researchers [7]. Figure 3.6 shows the position of the reattachment point plotted against the Reynolds number. Aspect ratio is set equal to 16 commonly in the present three-dimensional simulations. The position of the reattachment point for $Re = 375$ is its time-averaged value, since the flow in that case became periodically changing unsteady one. As clearly shown here, for a Reynolds number range of $Re < 200$, the present results as well as all the other numerical results reported by Ichinose [8], Kim and Moin [9] and Kaiktsis [10] show good agreement with the experimental results obtained by Armaly [7]. As Reynolds number increases, underestimation of the numerically calculated reattachment length gradually becomes more noticeable, except for the numerical results of the present 3-D computation. Results by Kaiktsis [10] plotted in Fig. 3.6 was obtained by 3-D simulations by making use of periodical boundary condition in the spanwise direction, not taking account of the side wall effects. Neglecting the side

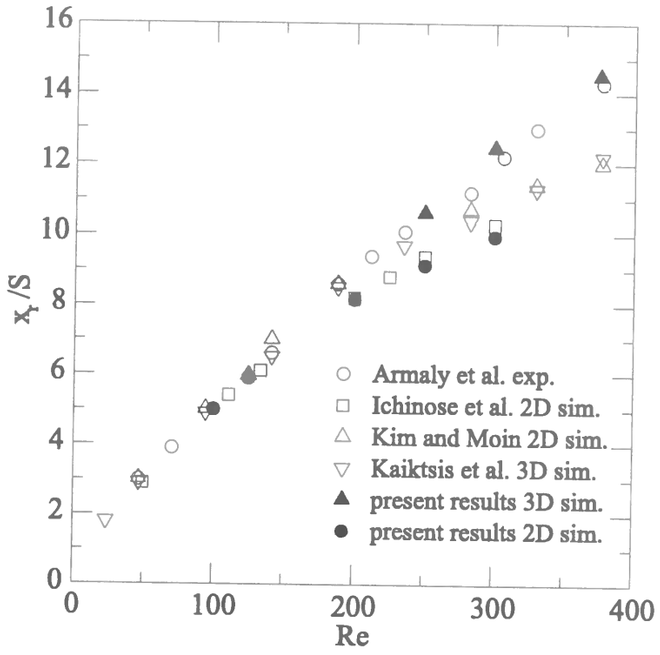

Figure 3.6: Reattachment points.

wall effects must be one of the reason for their similar tendency to the ones of other two-dimensional simulations.

Close attention is paid to the distribution patterns of both the Nusselt number and the skin friction coefficient at the bottom wall surface. Figure 3.7 shows the Nusselt number distributions at the bottom wall surface for the cases of different aspect ratios at the same Reynolds number, $Re = 250$. The gray tone level corresponds to the level of the calculated Nusselt number. This figure reveals that the aspect ratio has a great influence on the Nusselt number distribution pattern. An aspect ratio as large as AR=16 at least is needed to obtain a two-dimensional area around the center line of the bottom wall in the case of $Re = 250$. The two-dimensional area mentioned here is defined as the area where the Nu

or C_f contour lines lie parallel to the spanwise direction (z-axis). The two-dimensional area covers 30% of the spanwise width of the bottom wall in the middle at $x/S = 8.0$ for the case of $AR = 16$ and 50% for the case of $AR = 24$. At the positions of $x/S > 10$, however, a three-dimensionality is observed to exist over the whole duct width even for the case of $AR = 16$ as seen in Fig. 3.7. It is also found that the maximum Nusselt number, Nu_{max} appears near the both side walls, not on the centerline of the bottom wall, in all the cases studied here. With a change of the aspect ratio, change occurs in the location where Nu_{max} is obtained and its value. The locations and values of Nu_{max} calculated in each case are tabulated in Table 3.2. It is found that Nu_{max} shifts upstream and its value increases as AR increases, while its spanwise location remains approximately 0.9 step height away from the both side walls.

Table 3.2 Locations and values of Nu_{max}.

AR	x_{max}/S	$\lvert z_{max}/WD \rvert$	Nu_{max}
4	9.5	0.31	1.9
8	8.9	0.39	2.7
16	8.1	0.44	3.4
24	7.5	0.46	3.6

Distributions of skin friction coefficient are shown in Fig. 3.8, corresponding to ones of Nu shown in Fig. 3.7. Shaded area in the figure corresponds to the area where the skin friction coefficient is positive in sign. Being analogous to the case of the Nusselt number distributions mentioned above, an aspect ratio as large as AR=16 at least is needed to assume the two-dimensionality for the distribution of skin friction coefficient in the central region of the duct. The spanwise width of two-dimensional area is about 30% of the duct width at $x/S = 8.0$ for the case of $AR = 16$, and 50% for the case of AR =24.

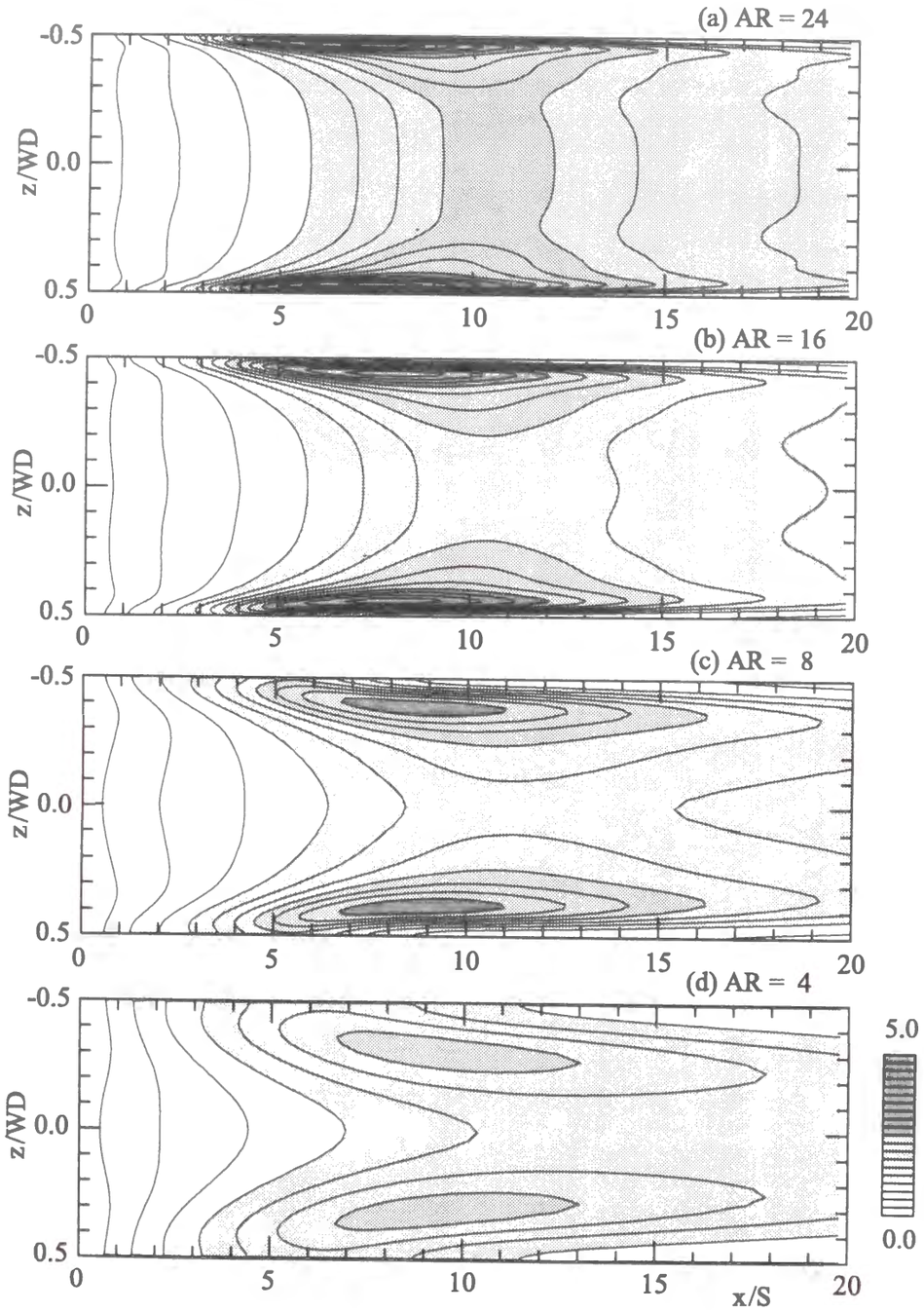

Figure 3.7: Nusselt number contours on the bottom wall.

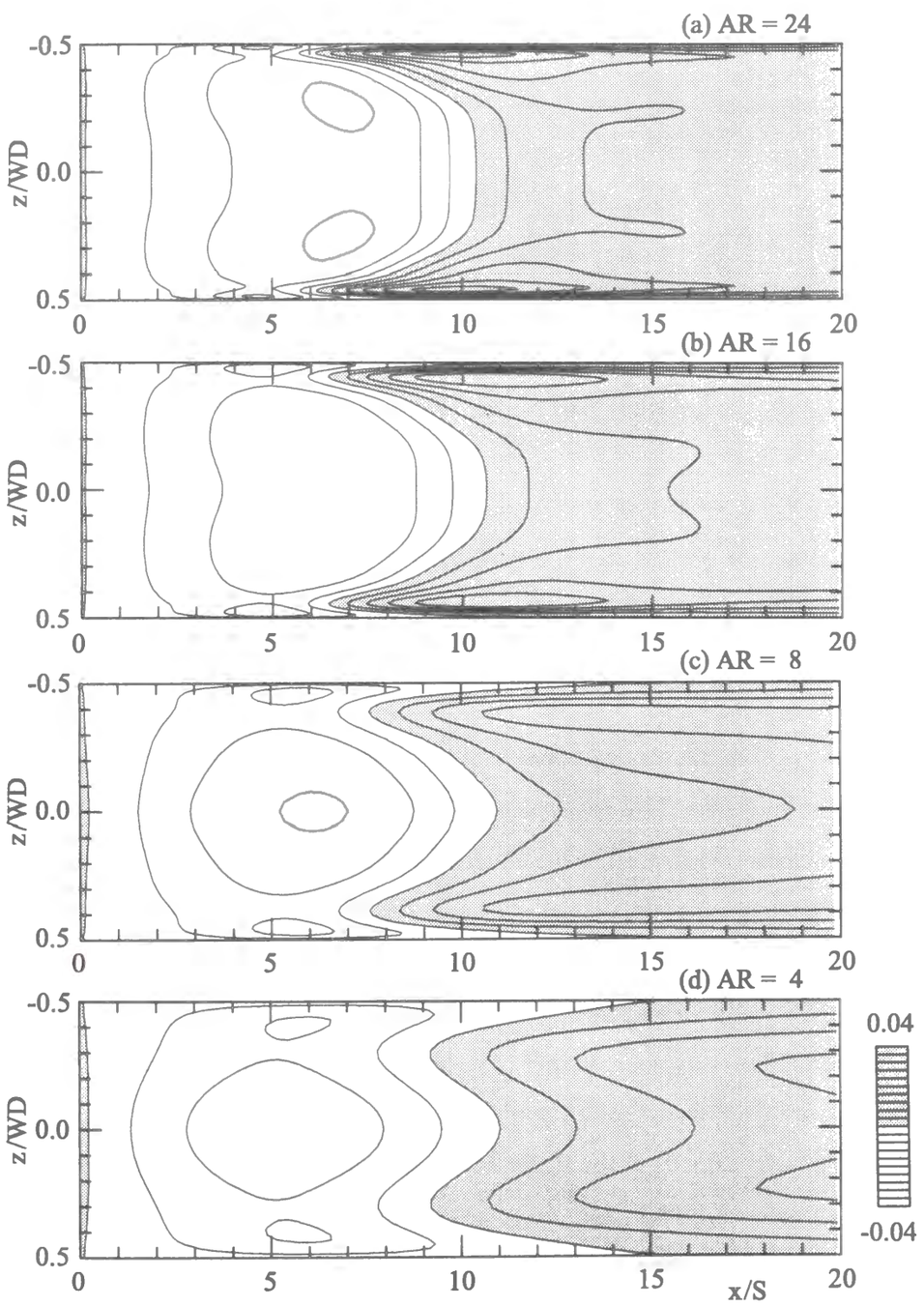

Figure 3.8: C_f contours on the bottom wall.

To discuss the three-dimensionality of the flow and thermal fields in detail, profiles of the flow velocity and temperature in the y-z cross-sections of the duct are examined at six streamwise locations for the case of $AR = 8$ and 16 at $Re = 250$. Figures 3.9 and 3.11 show the upstream view of the velocity vectors (V,W) together with the contours of the streamwise velocity U in six cross-sections of different streamwise positions. Shaded areas in the figures correspond to the positive U velocity regions and white areas to negative U. Figures 3.10 and 3.12, on the other hand, show the profiles of the temperature contours similar to those for velocity contours shown in Figures 3.9 and 3.11. The level of gray tone corresponds to the temperature level in these figures.

In Figures 3.9 and 3.11, it is seen that main flow bends toward the bottom wall after passing the step. Its manner is not uniform in spanwise direction. U contours protrude toward the bottom wall around $|z/WD| = 0.4$ when $AR = 8$, and $|z/WD| = 0.45$ when $AR = 16$. These spanwise positions are approximately 0.8 times the step height away from the side walls in both cases. This certainly matches the distribution pattern of the skin friction coefficient. In Fig. 3.8, upstream indent is observed in its zero value contour at the same spanwise positions. This spanwise non-uniformity of U contours is produced by the downwash flow observed to exist in the middle height region of the channel at such spanwise positions. This is ascribed to the superposition of the secondary flows to the spanwisely uniform downward flow toward the bottom wall. The existence of the secondary flows is clearly confirmed by the upstream view of the velocity vectors (V,W). In the case of AR=8 shown in Fig. 3.9 for example, existence of a counter-clockwise rotating flow is observed by the appearance of the flow directed toward the duct center near the bottom wall on the left hand side ($z/WD > 0$) of the figure at $x/S = 3.0$, while another longitudinal vortex like flow rotating clockwise is observed at around $z/WD = 0.42$ at $x/S = 12.0$.

The contours of fluid temperature also protrude toward the bottom wall at positions around $|z/WD| = 0.4$ when $AR = 8$ and $|z/WD| = 0.45$ when $AR = 16$, respectively. This corresponds to the velocity profiles shown in Fig. 3.9 and Fig. 3.11. Higher spatial density of the contours observed at such spanwise positions near the bottom wall leads to larger temperature gradient there, and therefore to larger Nusselt number observed in Fig. 3.7. Although the secondary flows become less obvious at $x/S = 18.0$ in Fig. 3.9 and Fig. 3.11, the above mentioned secondary flow still exists and produces the high Nusselt number areas on both sides of the centerline of the bottom wall.

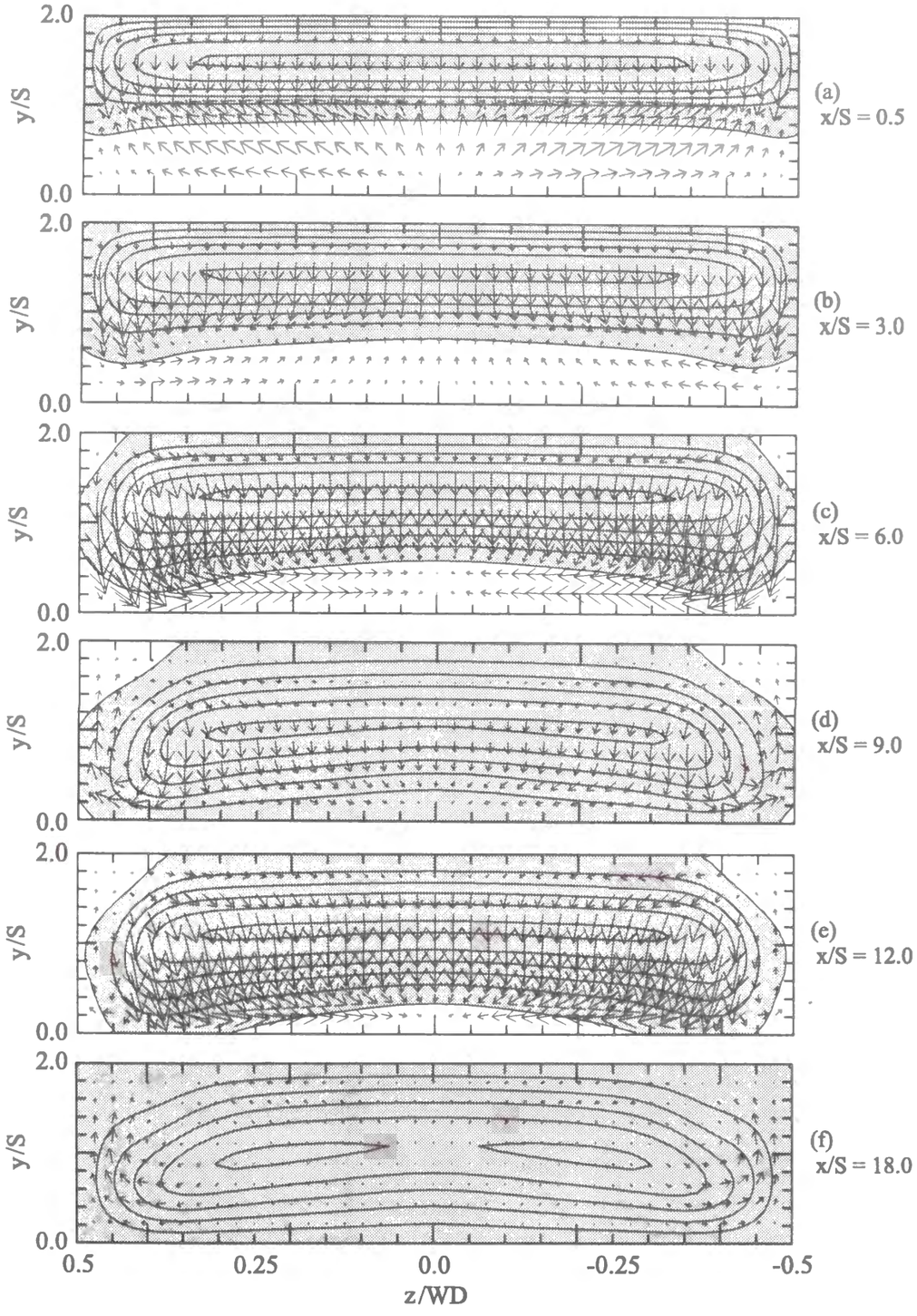

Figure 3.9: U contour and V-W vector plots (AR=8).

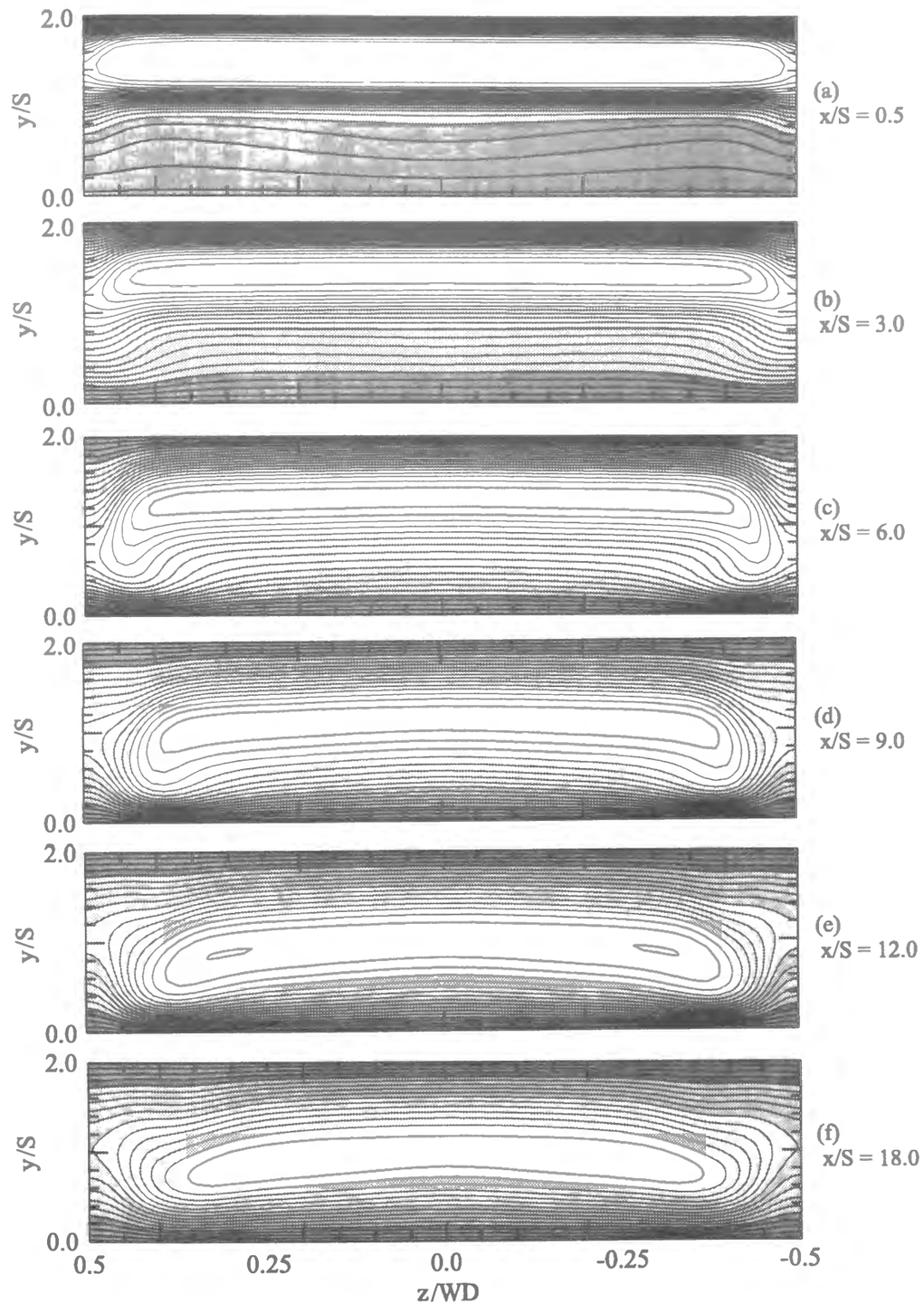

Figure 3.10: Temperature contour (AR=8).

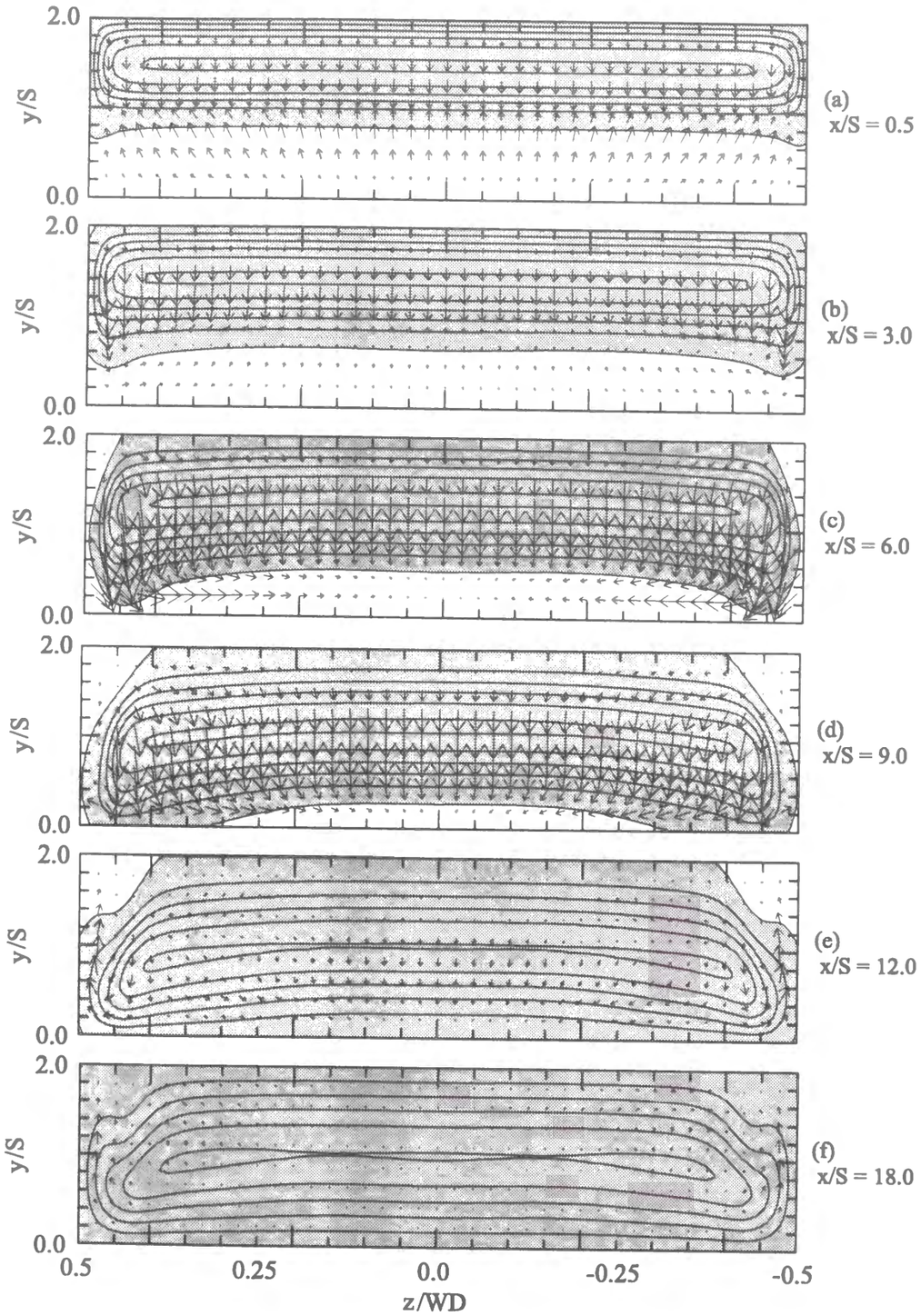

Figure 3.11: U contour and V-W vector plots (AR=16).

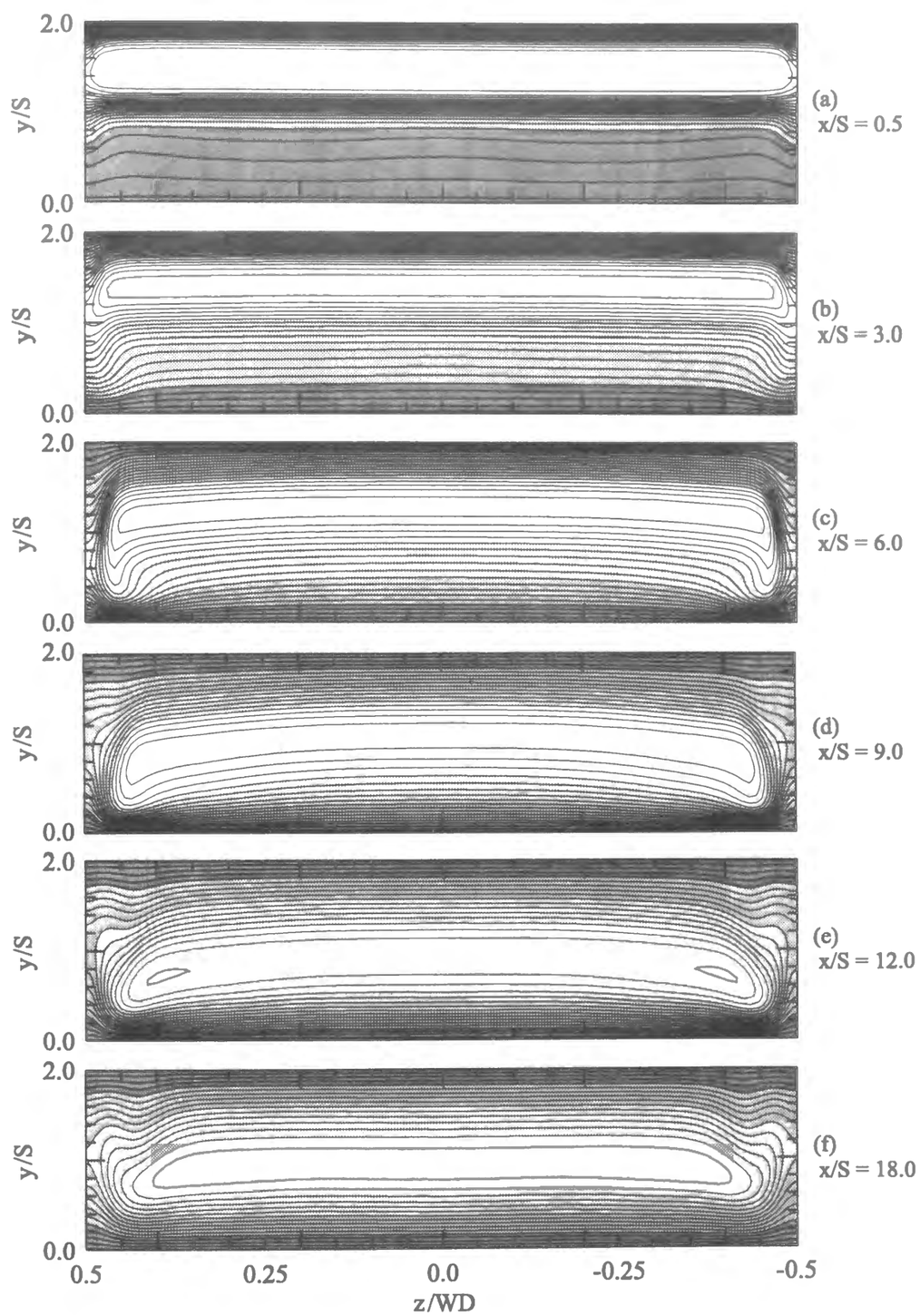

Figure 3.12: Temperature contour (AR=16).

In order to examine the effect of the secondary flows on the heat transfer enhancement from the bottom wall, the value of Wy at the bottom wall surface defined below is calculated.

$$Wy = \frac{2\mu \frac{\partial W}{\partial y}|_{y=0}}{\rho U_{in}^2}$$

where W is the spanwise velocity component. Figure 3.13 shows the distribution of Wy contours on the bottom wall. Shaded parts correspond to the regions where the value of Wy is positive in sign while white parts to negative. Wy changes its sign at the centerline of the duct,z=0. This reflects the spanwise symmetry of the flow with respect the duct centerline. $|W_y|$ are observed to take two pairs of peaks around the positions $(x/S,\ z/WD)$ = (6.5, $\pm$0.35) and (11.0, $\pm$0.4) in the cases of AR=8. The former peaks correspond to the inward flow produced by the rotating secondary flow observed in Fig. 3.9(c). The latter peaks, on the other hand, correspond to the longitudinal vortex like flow observed at such spanwise positions in Fig. 3.9(e). Boundary between the shaded and white areas extending from the both side rim of the bottom wall around $x/S = 4$ is observed between these two peaks. The position of this boundary in the area of $5 < x/S < 10$ coincide with the area where relatively larger value of Nusselt number is observed in Fig. 3.7. The contour lines of Wy around this boundary become more closely located as the aspect ratio is increased. This means the intensification of the secondary flows, which directly affects the value of Nu_{max} as can be seen in Table 3.2.

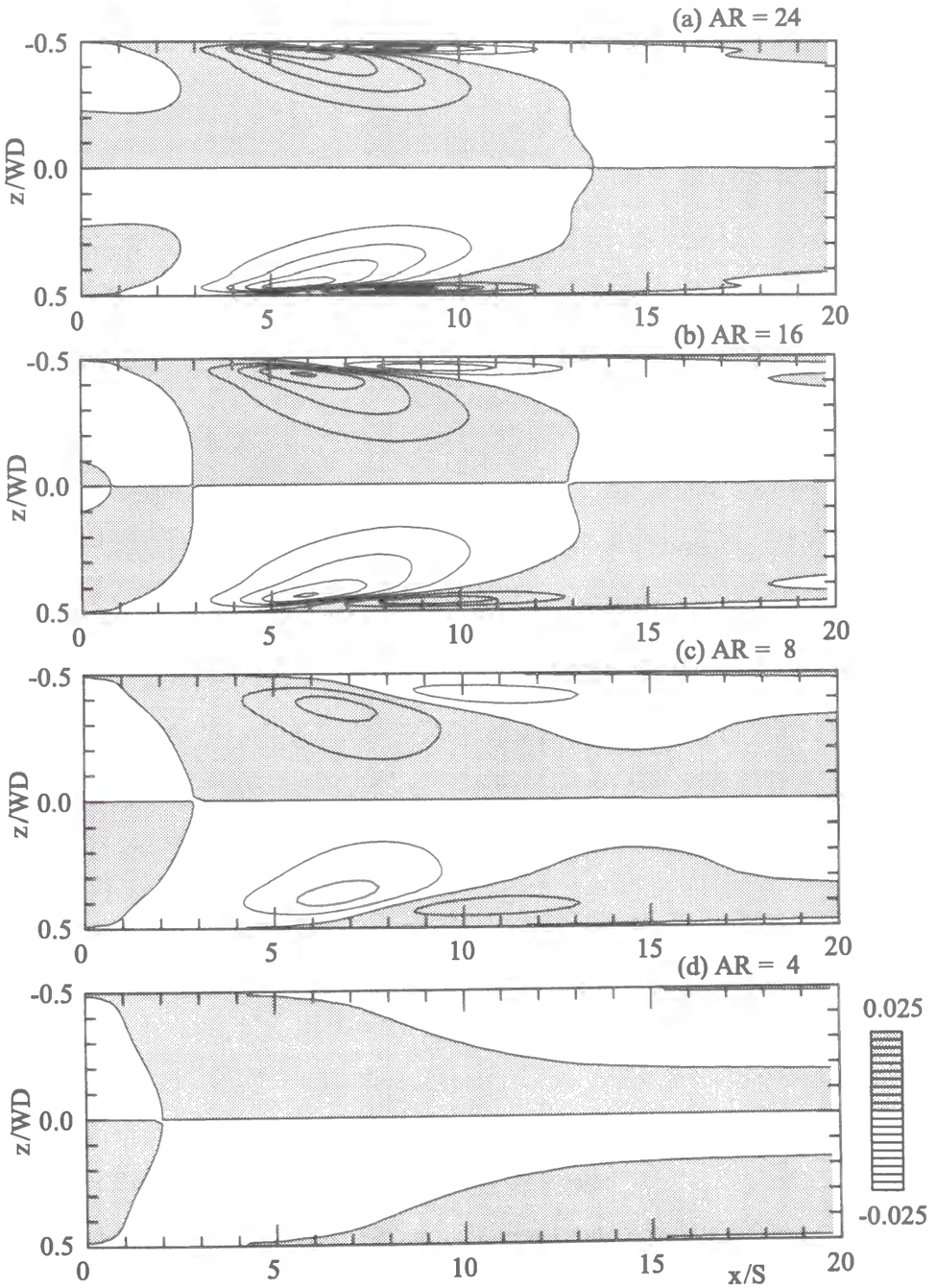

Figure 3.13: Wy contours on the bottom wall.

The intersection points of the boundaries in Fig. 3.8 and the boundaries in Fig. 3.13 are the stagnation points on the bottom wall where both the streamwise velocity,U, and the spanwise velocity,W, are zero. In all the cases studied, a pair of stagnation points is symmetrically obtained with respect to the duct centerline near the both side walls. This is clearly seen in Fig. 3.14 which shows the velocity vectors (U, W) together with the contours of the absolute value of the local velocity at $y/S = 1.25 \times 10^{-3}$ for the case of $AR = 8$. Figure 3.14(b) is a partial enlarged view over region of $5 \leq x/S \leq 15$ and $0 \leq z/WD \leq 0.5$ of Fig. 3.14(a). Thicker tone correspond to the higher velocity area. Low velocity regions are symmetrically observed near both side walls. The positions of these near side wall stagnation points are calculated in each case and are tabulated in Table 3.3. Comparison of Table 3.2 and Table 3.3 reveals that the positions of the stagnation points do not match the positions of the maximum Nusselt number points. Nu_{max} are obtained downstream of the stagnation points.

Table 3.3 Locations of near side wall stagnation points.

AR	x/S	$\|z/WD\|$
4	9.2	0.31
8	7.9	0.42
16	6.7	0.46
24	6.4	0.48

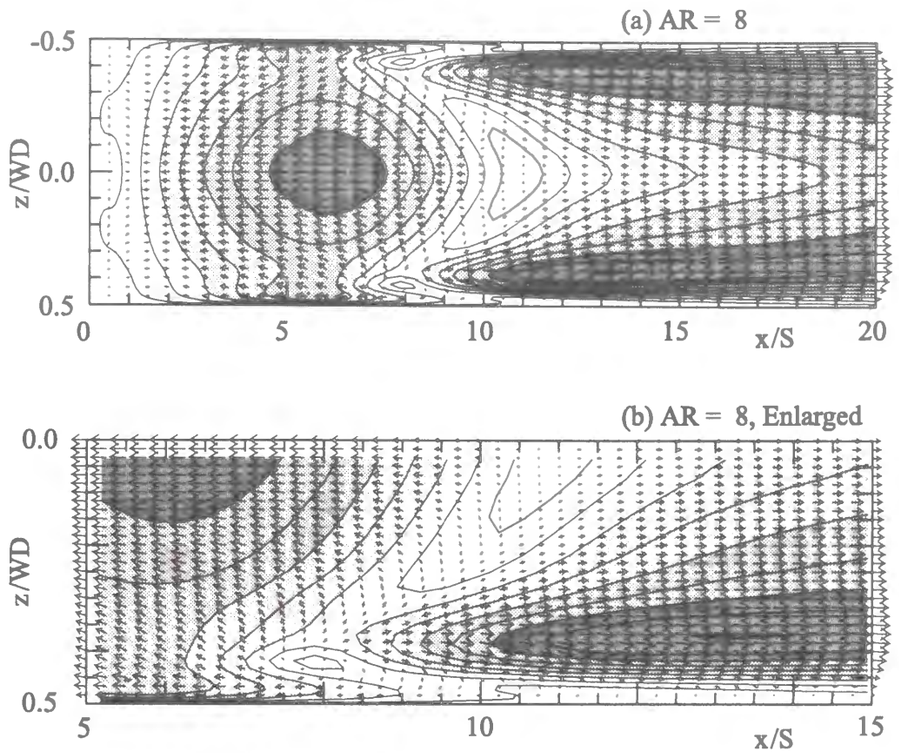

Figure 3.14: U-W vector plots with absolute velocity contours(AR=8,$y/S = 1.25 \times 10^{-3}$).

Figure 3.15 shows the influence of the Reynolds number on the Nusselt number distribution. Aspect ratio is kept constant at 16. The spanwise width of the region where two-dimensionality of the thermal field is expected to exist becomes smaller as the Reynolds number is increased. At $x/S = 8.0$, for example, the two-dimensionality is estimated to exist in the middle 50% and 30% of the total spanwise width of the bottom wall, respectively, for the cases of $Re = 125$ and 250. For $Re \geq 300$, however, the two-dimensional region cannot be identified from the distributions of Nusselt number. The locations and its value of the maximum Nusselt number are summarized in Table 3.4. As the Reynolds number is increased, the maximum Nusselt number becomes larger and its streamwise location shifts downstream. The spanwise location of Nu_{max}, however, does not move so much. This

is ascribed to the characteristics of the secondary flows. Its cross-sectional size does not change but its intensity changes as the Reynolds number is increased.

Table 3.4 Locations and values of Nu_{max}.

Re	x_{max}/S	$\lvert z_{max}/WD \rvert$	Nu_{max}
125	4.7	0.45	2.1
250	8.1	0.44	3.4
300	9.1	0.44	3.9
375	10.8	0.44	4.7

Figure 3.16 shows the C_f distribution for the cases corresponding to those of Fig. 3.15. Again the spanwise width of the two-dimensional region becomes smaller as Re is increased. In all the cases, the near side wall stagnation points are symmetrically obtained near the positions of Nu_{max} similar to the cases when AR is changed at a constant Re. The positions of the near side wall stagnation points are summarized in Table 3.5. Here again the positions of the near wall stagnation points do not match the positions of the maximum Nusselt number points. Nu_{max} are obtained downstream of the stagnating positions.

Although the reattachment point shifts downstream at almost all spanwise positions as Re is increased, this is more noticeable near the duct central region than near the side walls. This indicates that the effect of changing Re appears non-uniformly in spanwise direction leading to the change in the three-dimensional flow structure.

Table 3.5 Locations of near side wall stagnation points.

Re	x/S	$\lvert z/WD \rvert$
125	4.5	0.46
250	6.7	0.46
300	7.4	0.46
375	8.3	0.46

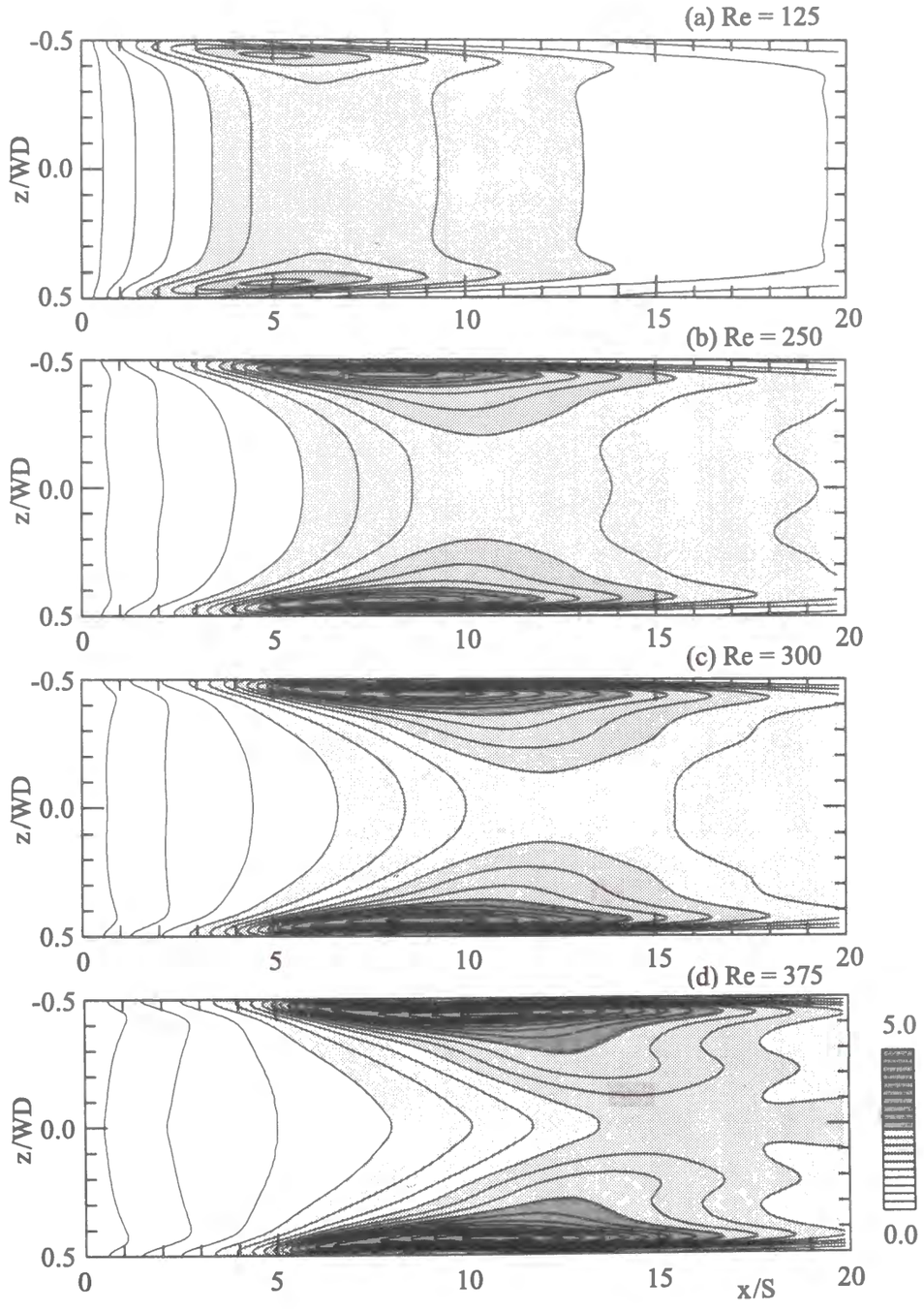

Figure 3.15: Nusselt number contours on the bottom wall.

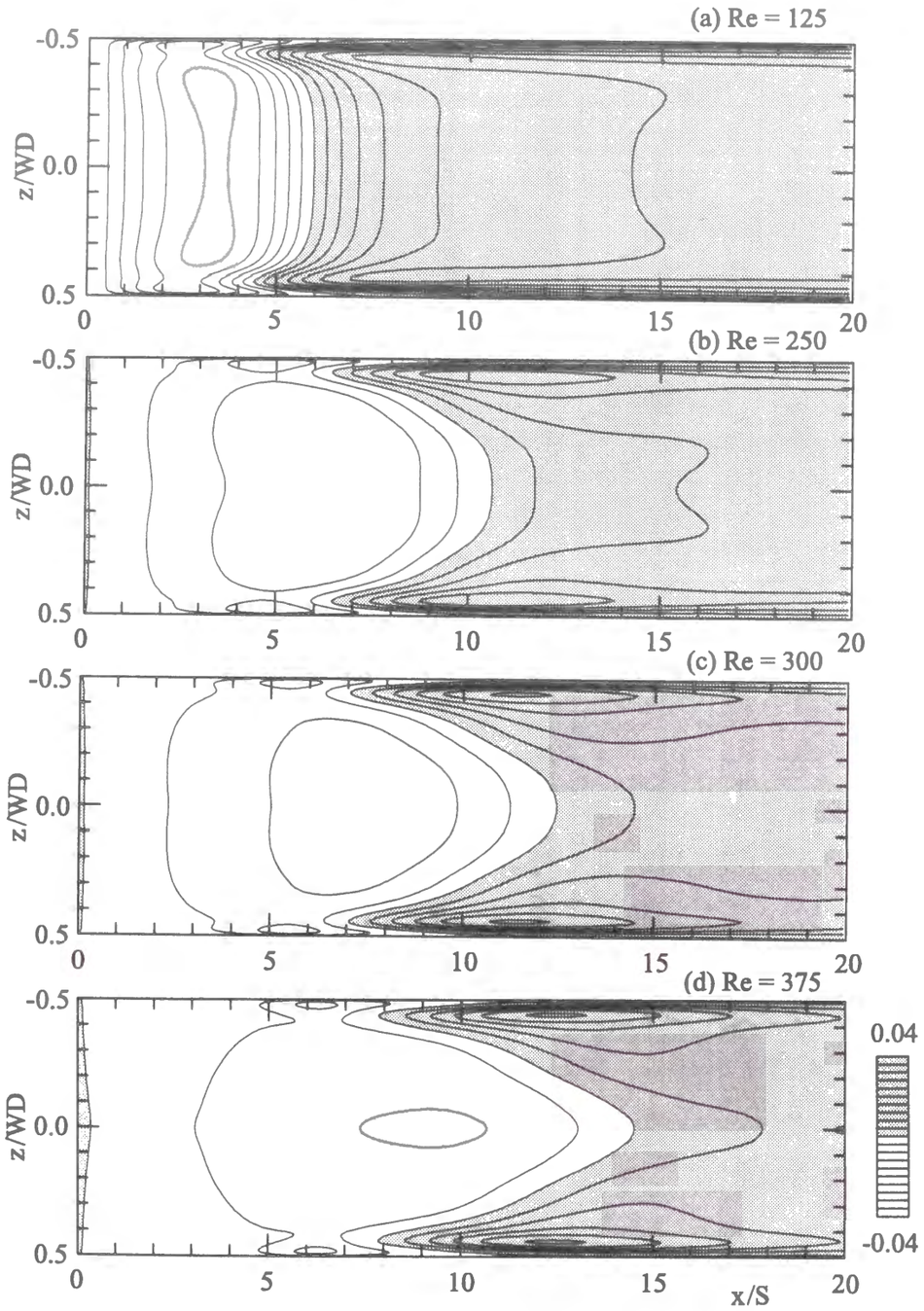

Figure 3.16: C_f contours on the bottom wall.

In order to visualize the three-dimensional flow pattern, the trajectories of fluid particles tracking the flow are sampled at every constant time interval. Figure 3.17 shows a bird's-eye upstream view of the results for the case of $AR = 16$ and $Re = 250$. The top and both side walls of the computational domain are not described in this figure. The initial x and y locations of the studied particles are shown in Table 3.6. Some of the particles starting from the vicinity of a side wall are found to recirculate spirally in the recirculating zone behind the step and to move toward the center of the duct, and finally to flow out toward further downstream. The streamwise stroke of the particle extends downstream as the particle approaches the centerline. Therefore, time period for one stroke of particle recirculation becomes longer. This numerical result agrees well with the experimental results obtained by Goldstein [5]. The trajectory patterns and the number of the spiral recirculation strongly depend on the initial location of the particles. This method of presentation of the results was proven effective to visually examine the three-dimensionality of the flow.

Table 3.6 Starting x-y locations of particles.

No.	1	2	3	4	5	6	7	8	9	10
x/S	0.0									
y/S	1.04	1.14	1.24	1.34	1.44	1.54	1.64	1.74	1.84	1.94

(a) z/WD = 0.0

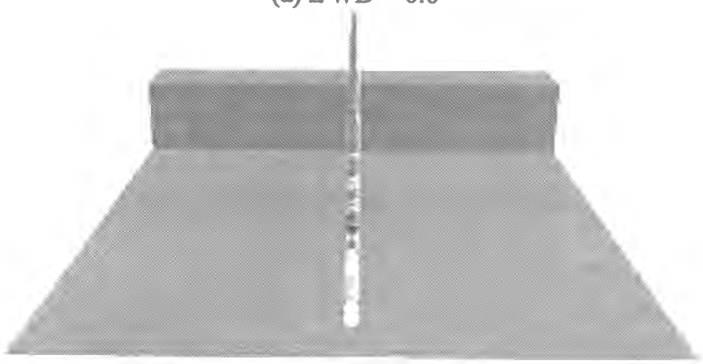

(b) z/WD = 0.2

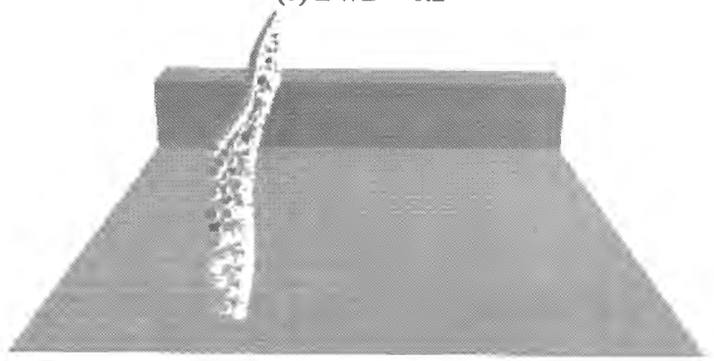

(c) z/WD = 0.3

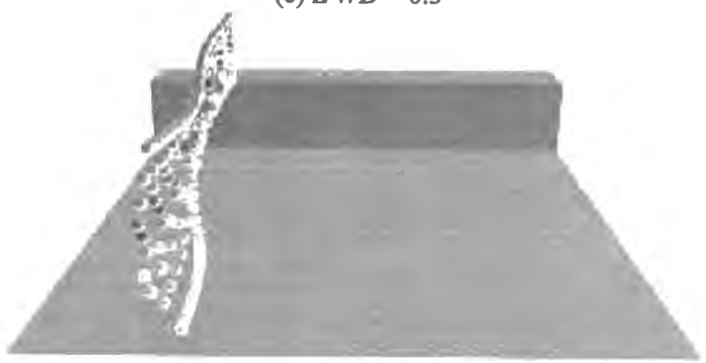

(d) z/WD = 0.4

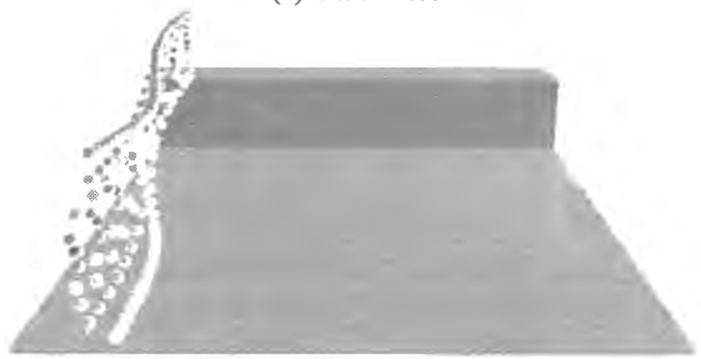

(e) z/WD = 0.45

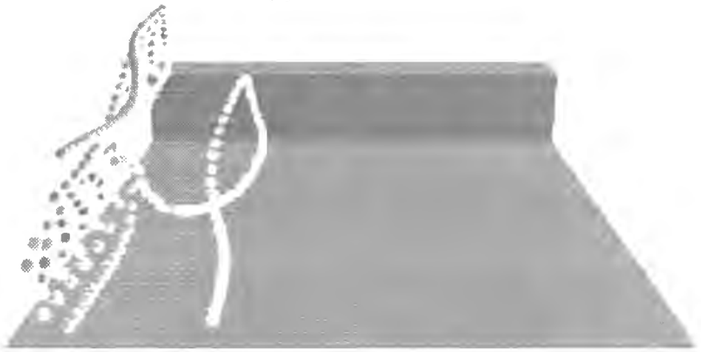

(f) z/WD = 0.48

Figure 3.17: Behavior of fluid particles (Re=250,AR=16).

In relation with the above mentioned interesting spiral motion of the particles, pressure distributions are calculated in the vicinity of the bottom wall. Figure 3.18 shows the pressure coefficients along the centerline of the bottom wall in the case of $AR = 16$ and $Re = 250$. The reference pressure is its value at a position near the origin of the coordinate system. Spanwise non-uniformity of pressure coefficient is also calculated using the centerline pressure at respective streamwise position as its reference value. The results are shown in Fig. 3.19. Shaded areas indicate that the coefficient is positive in sign. The pressure coefficient is zero along the boundary between the shaded area and the neighboring white area, and also along the centerline. Spanwise pressure gradient is noticeable near the side wall, although less profound in the middle 40% region of the duct width. The spiral fluid motion in the recirculating flow region was found in the above to approach toward the center of the duct. This is caused by this spanwise pressure nonuniformity decreasing toward the centerline. The maxima of the pressure coefficients are symmetrically located near the both side walls at approximately $x/S = 6.7$ and $|z/WD| = 0.45$.

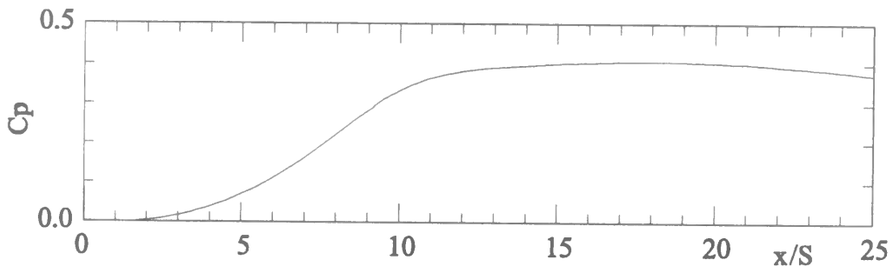

Figure 3.18: Cp distribution along the centerline.

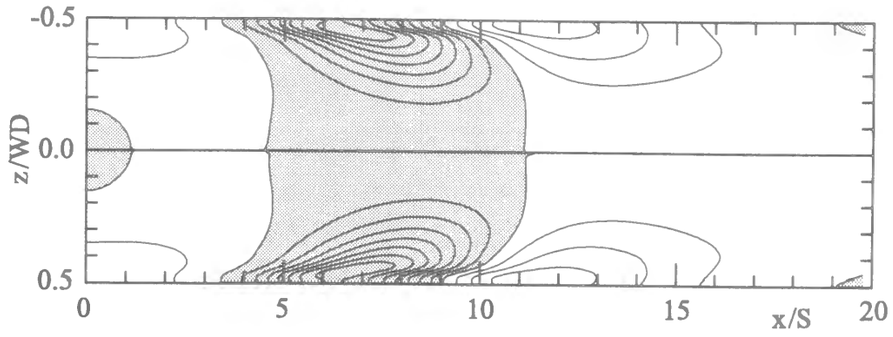

Figure 3.19: Cp contour on the bottom wall.

3.4 Conclusions

Three-dimensional numerical simulation has been performed for the laminar flows over a backward-facing step in a rectangular duct. The results obtained in the present study are summarized as follows:

(1) Reattachment points calculated in the present study agree well with the existing experimental results.

(2) The flow is found to remain steady under all calculated conditions, except for $Re = 375$ (the maximum Reynolds number adopted in the present study), in which the flow becomes periodically changing unsteady one.

(3) An aspect ratio of as large as AR=16 is needed at least to secure two-dimensional region in the central part of the duct at Re=250.

(4) In the case of constant aspect ratio, the area of the two-dimensional region becomes larger, as Re number is decreased. It is also found that the maximum Nusselt number increases with an increase of the aspect ratio and/or Re number.

(5) The maximum Nusselt number on the bottom wall is obtained at two positions near the side walls located symmetrically with respect to the duct centerline, and not on the centerline in all the cases studied here.

(6) Some of the particles starting from the vicinity of a side wall are found to recirculate

spirally in the recirculating zone behind the step. This spiral fluid motion in the recirculating flow region approaches toward the center of the duct because of the spanwise pressure nonuniformity decreasing toward the centerline.

References

[1] Fiebig, M., Kallweit, P. and Mitra, N.K., *Wing Type Vortex Generators for Heat Transfer Enhancement*, Proc. 8th Int. Heat Transfer Conf., Vol. 6 , pp. 2909-2913, (1986).

[2] Fiebig, M., *Vortex Generators for Compact Heat Exchangers*, J. Enhanced Heat Transfer, Vol. 2, Nos. 1-2 , pp. 43-61, (1995).

[3] Webb, R.L., Eckert, E.R.G. and Goldstein, R.J., *Heat Transfer and Friction in Tubes with Repeated-Rib Roughness*, Int. J. Heat Mass Transfer, Vol. 14 , pp. 601-617, (1971).

[4] Lehmann, G.L. and Wirtz, R.A., *Effect of Variations in Streamwise Spacing and Length on Convection from Surface-Mounted Rectangular Components*, Heat Transfer Engng, Vol. 9, No. 3, pp. 66-75, (1988).

[5] Goldstein, R.J., Ericsen, V.L., Olson, R.M. and Eckert, E.R.G., *Laminar Separation,Reattachment,and Transition of the Flow over a Downstream-Facing Step*, J. Basic Engng., pp 732-741, (1970).

[6] Denham, M.K. and Patrick, M.A., *Laminar Flow over a Downstream-Facing Step in a Two-Dimensional Flow Channel*, Trans.INSTN CHEM.ENGRS,, Vol 52, pp 361-367, (1974).

[7] Armaly, B. F., Durst, F., Pereira, J. C. F. and Schonung, B., *Experimental and Theoretical Investigation of Backward-Facing Step Flow*, Journal of Fluid Mechanics, Vol.127, pp. 473-496, (1983).

[8] Ichinose, K., Tokunaga, H. and Satofuka, N., *Numerical Simulation of Two-dimensional Backward-Facing Step Flows* , Trans.JSME B, vol.57-543, pp.3715-3721 (1991)(in Japanese).

[9] Kim, J. and Moin, P., *Application of a Fractional-Step Method to Incompressible Navier-Stokes Equations* , J. Computational Physics, Vol.59, pp. 308-323 (1985).

[10] Kaiktsis, L., Karniadakis, G.E. and Orszag, S.A., *Onset of Three-Dimensionality, Equilibria, and Early Transition in Flow over a Backward-Facing Step*, J. Fluid Mech., Vol 231, pp 501-528, (1991).

[11] Shah, R.K. and London, A.L., *Laminar Forced Convection in Ducts*, (1978), Academic Press.

[12] Kieda, S. and Suzuki, K., *Numerical Study of the Flow Passing a Flat Plate of Finite Length*, Trans. JSME, Vol. 46B, No. 409, pp. 1655-1661, (1984).

Chapter 4

The Effects of Buoyancy Level on Buoyancy Assisting Laminar Flows over a Backward-Facing Step

4.1 Introduction

The flows inside the recent compact heat exchangers can be laminar. In such heat exchangers, flow separation and reattachment phenomena are often used to modify the flow field, for establishing a favorable heat exchange. Therefore it is very important to understand the details of the flow separation and reattchment phenomena. As the most typical problem, flows over a backward-facing step have attracted considerable attention. In the previous chapter the influence of the duct aspect ratio on the flow and thermal fields was investigated at low Reynolds numbers for the flows in a rectangular duct with a sudden expansion. Although the buoyancy effects were not taken into consideration in the previous chapter, it should become significant when the temperature difference between fluid and wall is set relatively large and the flow becomes one of the mixed convection regime [1,2,3]. Considering that a low Reynolds number flow is sensitive to the buoyancy effects, it is important to study how its effect is.

Recently, Baek [4] and Abu-Mulaweh [5,6] measured experimentally the velocity and

temperature distributions in buoyancy affected backward-facing step flows. Lin [7,8] and Hong [9] performed 2-D simulations for similar flows, varying the buoyancy level, inclination angle of the duct and Prandtl number. However, there are many parameters in this system and the details of flows are not clear yet. Especially only few researchers dealt with the three-dimensionality of the flow and thermal fields. This is the motivation for the 3-D simulations carried out in this chapter.

Since 2-D calculations can be carried out with smaller CPU time and at lower cost, they are also used here to discuss a general feature of the flow fields. Therefore, it is essential to know how far the results of 2-D simulations sufficiently predict the real flow phenomena in a duct of finite value of aspect ratio, which should be under 3-D effects to some extent.

In this chapter, both 2-D and 3-D numerical simulations are performed for mixed convective flows over a backward-facing step in a duct. Special attention is paid to the effect of buoyancy on the flow and thermal fields. According to Hong [9], the effects of buoyancy are expected to be relatively bigger when the flow direction is parallel to the direction of gravity. The upward flow heated from the duct wall is chosen as a case to be studied in this chapter. How the 2-D simulation can model the actual flow will be also discussed. The effects of the duct posture will be studied in Chapter 5.

4.2 Computational Conditions

4.2.1 Computational Domain

The computational domain for the three-dimensional simulations made in this chapter is schematically illustrated in Fig. 4.1. Two-dimensional simulations are carried out in a plane where z/WD=0.0. The expansion ratio,$ER = H/(H - S)$, and the aspect ratio (in the 3-D cases),$AR = WD/S$, are kept constant at 2 and 16 respectively throughout this chapter. The computational domain covers $-1 \leq x/S \leq 30$ in the streamwise direction.

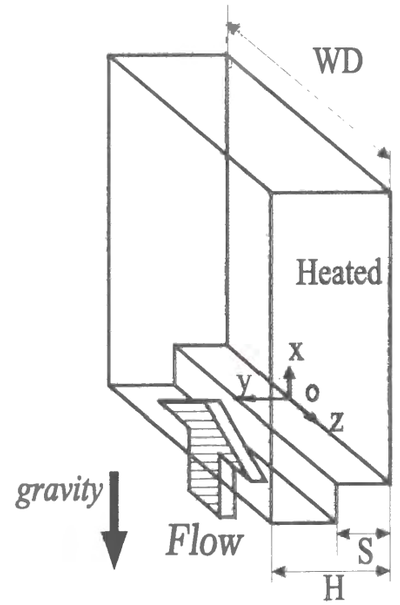

Figure 4.1: Computational domain.

4.2.2 Governing Equations

To take into account the buoyancy effects, the momentum equations should include the buoyancy term. The equation for the streamwise velocity U is written as:

$$\begin{aligned} &\frac{\partial}{\partial t}(\rho U) + \frac{\partial}{\partial x}(\rho U^2) + \frac{\partial}{\partial y}(\rho VU) + \frac{\partial}{\partial z}(\rho WU) \\ = \; &-\frac{\partial P}{\partial x} + \frac{\partial}{\partial x}\left(\mu\frac{\partial U}{\partial x}\right) + \frac{\partial}{\partial y}\left(\mu\frac{\partial U}{\partial y}\right) + \frac{\partial}{\partial z}\left(\mu\frac{\partial U}{\partial z}\right) - \rho g \end{aligned} \tag{4.1}$$

The last term in Eq. (4.1) is the buoyancy term. Boussinesq approximation [2] is used to evaluate this term.

4.2.3 Boussinesq Approximation

The sum of the pressure term and the buoyancy term in Eq. (4.1) is written as:

$$S = -\frac{\partial P}{\partial x} - \rho g \tag{4.2}$$

When the domain is filled with the fluid having the density ρ_{in}, which is taken as the reference density, and there is no flow, the following equation holds.

$$-\frac{\partial P'}{\partial x} - \rho_{in} g = 0 \tag{4.3}$$

where P' is pressure. Supposing that ρ_{in} is equal to the fluid density at the inlet temperature, Eq. (4.3) is equivalent to the momentum equation for the system in which fluid is at rest. Subtracting Eq. (4.3) from Eq. (4.1) yields:

$$S = -\frac{\partial P^*}{\partial x} - (\rho_{in} - \rho)g \tag{4.4}$$

where $P^* = P - P'$. When Boussinesq approximation is applied, the local density ρ is expressed in terms of the local temperature T as:

$$\rho = \rho_{in}\{1 - \beta(T - T_{in})\} \tag{4.5}$$

where β is the cubic expansion coefficient. It is evaluated at the inlet temperature. Combining this equation, Eq. (4.2) can be written as:

$$S = -\frac{\partial P^*}{\partial x} + \rho_{in} g\beta(T - T_{in}) \tag{4.6}$$

Finally the momentum equation in the streamwise direction is written as:

$$\begin{aligned} &\frac{\partial}{\partial t}(\rho U) + \frac{\partial}{\partial x}(\rho U^2) + \frac{\partial}{\partial y}(\rho VU) + \frac{\partial}{\partial z}(\rho WU) \\ = \; &-\frac{\partial P^*}{\partial x} + \frac{\partial}{\partial x}\left(\mu\frac{\partial U}{\partial x}\right) + \frac{\partial}{\partial y}\left(\mu\frac{\partial U}{\partial y}\right) + \frac{\partial}{\partial z}\left(\mu\frac{\partial U}{\partial z}\right) + \rho_{in}\beta g(T - T_{in}) \end{aligned} \tag{4.7}$$

Other governing equations are the momentum equations in both transverse and spanwise directions, energy equation and continuity equation. They are the same as ones described in Chapter 3. All properties of the working fluid (air) appearing in Eq. (4.7) are assumed to be constant in the following computation and they are evaluated at the inlet condition. Thus ρ in the left hand side of the Eq. (4.7) is treated equal to ρ_{in}.

4.2.4 Boundary Conditions

The inlet flow at the upstream boundary is assumed to be hydrodynamically steady and fully developed with uniform temperature,T_{in}. In 3-D calculations, U velocity profile there is set according to the approximation proposed by Shah [10], while a parabolic U profile is given at the inlet in the 2-D computations. V and W were set equal to zero. No-slip boundary conditions (U=V=W=0) are adopted at all wall surfaces. These boundary conditions are the same as the ones adopted in the previous chapter. The wall downstream of the step is assumed to be heated at a uniform heat flux,, while the top wall ($y/S = 2.0$), the bottom wall upstream of the step ($y/S = 1.0$, $x/S < 0$), the backward-facing wall and the side walls (in the 3-D cases) are assumed to be thermally adiabatic. Streamwise gradients of all quantities at the duct exit are set to be zero.

4.2.5 Computational Conditions

Duct flow Reynolds number defined with the step height and the cross-sectional mean velocity at the inlet is kept constant at 125.

$Re = \frac{U_{in}S}{\nu} = 125$

It was confirmed in the previous chapter that both the flow and thermal fields of this Reynolds number can be considered as two-dimensional in the central region in the duct, if buoyancy is neglected. Since the main objective of this chapter is to investigate the effects of buoyancy on the flow and thermal fields, calculations are carried out for several cases of different values of modified Richardson number, Ri^*, ranging from zero to 0.12. Modified Richardson number is defined here as follows:

$$Ri^* = \frac{Gr^*}{Re^2} \tag{4.8}$$

where Gr^* is the modified Grashof number defined below.

$$Gr^* = \frac{g\beta q_w S^4}{\nu^2 \lambda} \tag{4.9}$$

Variation of Ri^* is equivalent to varying heat flux while keeping the step height constant. The computational conditions are chosen so that when the step height was 10mm the temperature difference between main flow and the heated wall remain in the range of $10 \sim 30K$, which can be achieved without difficulty in the laboratory.

Close attention is paid to the distribution patterns of both skin friction coefficient and Nusselt number on the heated wall. They are defined as below:

$$\text{Skin friction coefficient}, C_f = \frac{2\tau_w}{\rho U_{in}^2} \tag{4.10}$$

$$\text{Nusselt number}, Nu = \frac{q_w S}{\lambda(T_w - T_{in})} \tag{4.11}$$

τ_w, q_w, T_w, T_{in} and U_{in} used here refer to the values of the wall shear stress, wall heat flux, wall temperature, inlet temperature and the cross-sectional mean velocity at the inlet respectively.

4.3 Results and Discussion

Figure 4.2 compares the presently calculated Nusselt number distributions on the heated wall with the experimental data obtained by Baek [4]. The experiment by Baek was carried out introducing a boundary layer type upward flow to the step and measurements were taken for the thermal field. The wall downstream of the step was heated at a constant temperature. The difference between the wall temperature and the inlet flow temperature was kept constant at $10K$. The aspect ratio was also fixed at 48 to ensure two-dimensionality of the flow. The Reynolds number was 230. For the purpose to compare with the experiment by Baek, a two-dimensional calculation was performed with the boundary conditions equivalent to those of their experiment. As shown in Fig. 4.2, the present 2-D numerical result show excellent agreement with the experimental data. This validates the Boussinesq Approximation adopted to evaluate the buoyancy term in the present numerical computation.

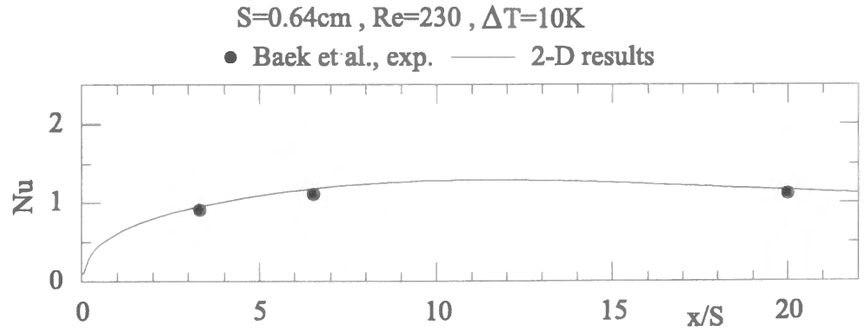

Figure 4.2: Nu distribution on the heated wall.

A typical buoyancy-affected case (Ri^*=0.06) is compared with another case in which buoyancy is neglected (gravity=0) in order to get a general idea of the buoyancy effect on an upward flow over a backward-facing step. In both cases, 2-D computations are carried out since both of the flow and thermal fields can be considered as two-dimensional in the central part of the duct at Re=125 if the aspect ratio is sufficiently large. The adopted

boundary conditions are the same for both cases including the constant heat flux given at the heated wall. Figure 4.3 shows the distributions of the skin friction coefficient and Nusselt number for both of these cases with and without buoyancy effect. It is clearly seen in this figure that buoyancy affects both of the flow and thermal fields. As can be observed in Fig. 4.3, the values of the skin friction coefficient are bigger in the entire range of the x-location when buoyancy is considered. This is due to the larger velocity gradients produced in the near-wall region in the buoyancy-affected case, where the heated fluid is accelerated upward by buoyancy force. This flow acceleration is clearly observed in Fig. 4.4 where the profiles of the streamwise velocity (U) at several x-locations are plotted. Apparently, the buoyancy-affected velocity gradients at y/S=0 are larger than the non-buoyant ones.

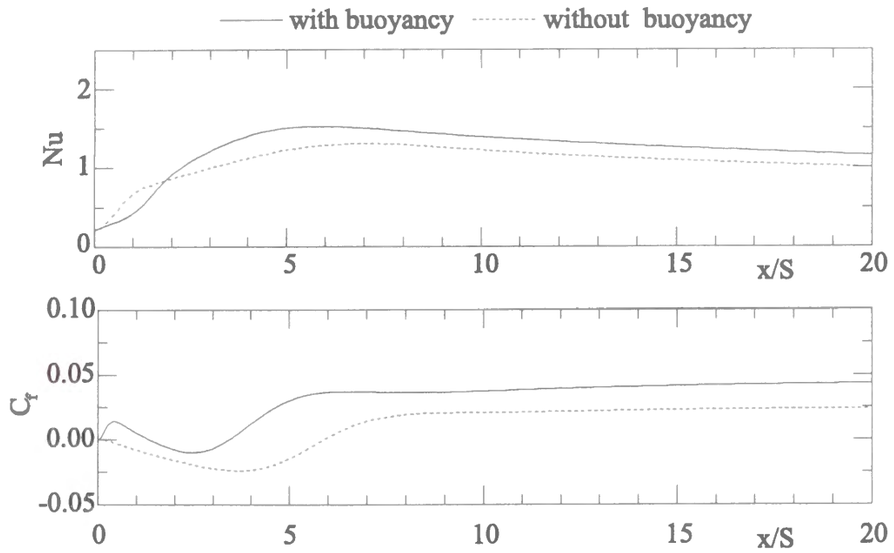

Figure 4.3: Effect of buoyancy.

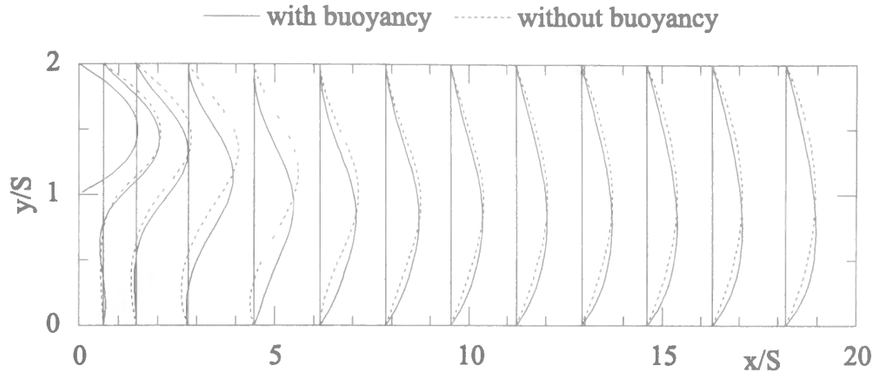

Figure 4.4: U profiles at several x-locations.

The distribution patterns both of the Nusselt number, Nu, and skin friction coefficient, C_f, at several buoyancy levels are shown in Fig. 4.5. It can be observed in Fig. 4.5 that C_f increases in the entire range of the x-location as Ri^* increases. This is caused by the above-mentioned buoyancy driven acceleration near the heated wall. The y-locations of the maximum streamwise velocity were sampled at x/S=20 and are plotted against the modified Richardson number, Ri^* in Fig. 4.6. The maximum U appears closer to the heated wall as Ri^* increases, resulting a large C_f at the wall. Another interesting feature can be observed in Fig. 4.5: the formation of secondary recirculation region. The secondary recirculation region mentioned here is a recirculation region having an opposite direction of recirculation which appears at the corner of the step, inside of the main recirculation zone . Its streamwise size, x_o is defined in this study as the length from the step to a point where the skin friction coefficients change sign from positive to negative. It can be seen in Fig. 4.5(a) that the size of the secondary recirculation region increases with an increase in Ri^*. Due to the formation of such a secondary recirculation region, Nusselt number distributions also change in shape at the positions of $x/S < 2$ as observed in Fig. 4.5. It should also be noted that the value of the peak Nu increases and the shape becomes more peaky as Ri^* increases.

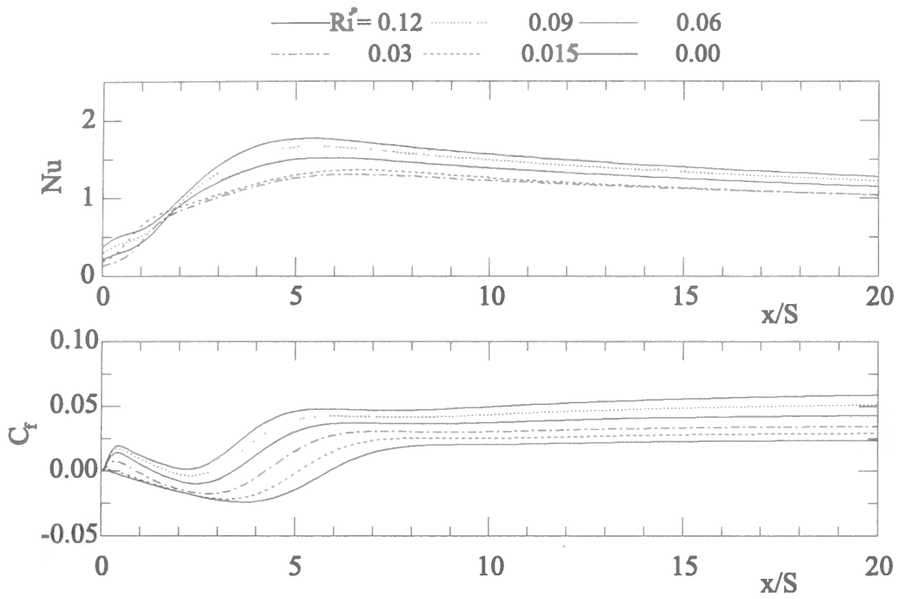

Figure 4.5: C_f and Nu distributions(2-D).

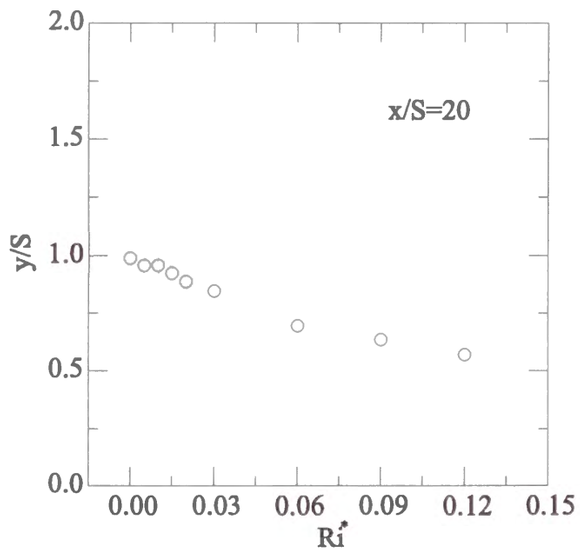

Figure 4.6: y-position of maximum U.

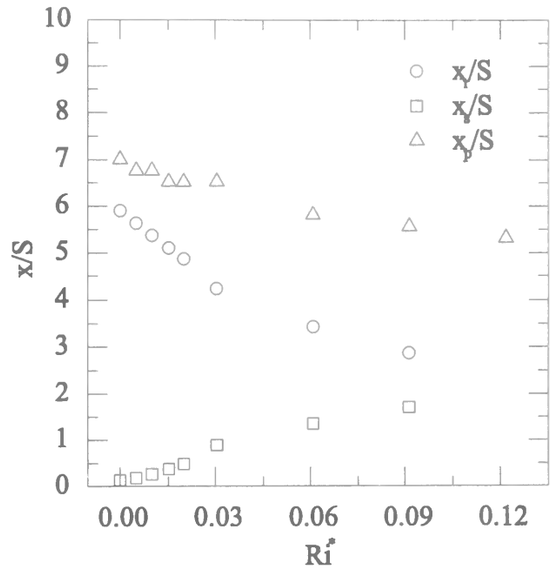

Figure 4.7: Effect of Ri^* on x_r, x_p and x_s.

Figure 4.7 shows the effect of Ri^* on the positions of the reattachment point x_r, the peak Nusselt number location x_p and the size of the secondary recirculation region x_s. The reattachment point and the peak Nusselt number point move upstream as Ri^* increases, while the secondary recirculation region extends further downstream. The peak Nusselt number position is always located downstream of the reattachment point and the distance between x_r and x_p increases as Ri^* increases. Baek [4]. and Lin [7]. obtained similar results under a constant temperature condition. x_r and x_s are expected to merge beyond Ri^*=0.09, where detachment of the main recirculation region from the heated wall occurs as will be confirmed soon.

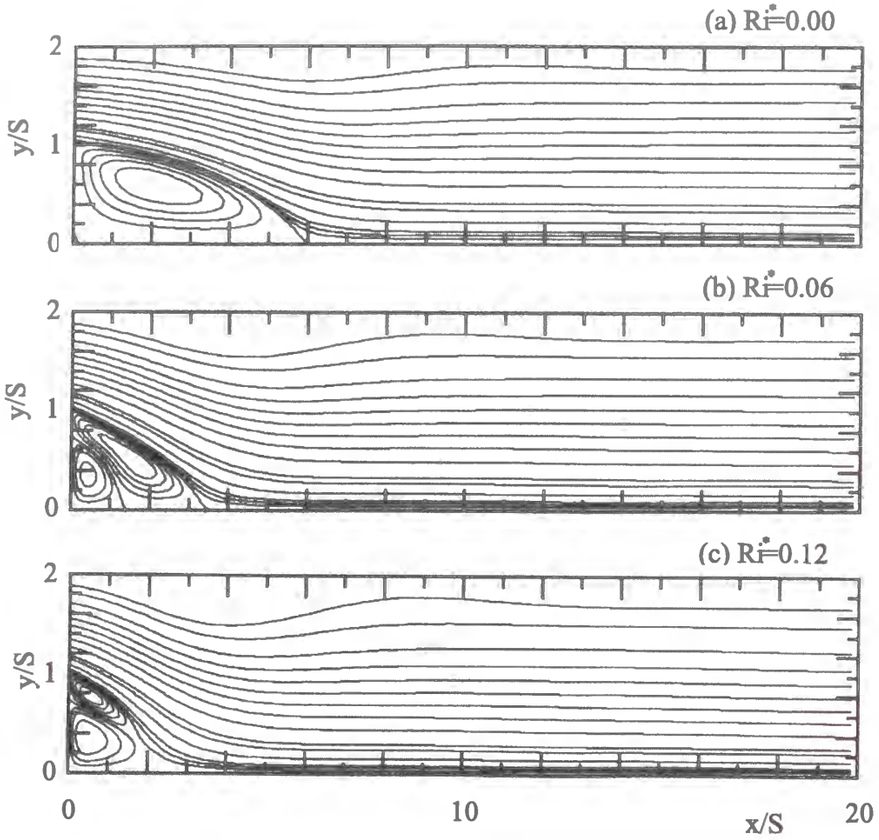

Figure 4.8: Streamlines.

Figure 4.8 shows the streamlines for the cases of Ri^*= 0.00, 0.06 and 0.12. The main recirculation region, which extends downstream after the step, clearly decreases in size as Ri^* increases, while the secondary recirculation region becomes larger. At Ri^*=0.12 the main recirculation region detaches from the heated wall, as mentioned above.

Fundamental characteristics of buoyancy-assisting backward-facing step flow have been discussed so far using the 2-D calculation results in the above. The results of the 3-D calculations are now discussed to study the three dimensional effect of buoyancy (modified Richardson number) on the flow and thermal fields. In particular, three different cases of Ri^*,i.e. Ri^*=0.00 (no gravity), 0.06, 0.12 will be closely examined. Note that the bottom

wall is heated even in the case of Ri^*=0.00 in order to compare with the other two cases but under very small heat flux. Incidentally, it may be worthwhile to note that for the case when Ri^*=0.06, the heat flux is as approximately 7 times large as that of Baek's experiment [4].

In experimental studies, characteristic values are often measured along the centerline of the duct where both flow and thermal fields are assumed to be two-dimensional if the aspect ratio is sufficiently large. Figure 4.9 shows the skin friction coefficient and Nusselt number distributions along the centerline obtained from 3-D calculations. A careful comparison between Fig. 4.9 and Fig. 4.5 reveals that although the results of 2-D and 3-D simulations are similar when Ri^*=0.00, their distribution patterns of C_f show discrepancy in the region $x/S < 5$ when Ri^*=0.06 and 0.12. This suggests that three dimensionality cannot be neglected even around the center region of the duct for the cases of Ri^*=0.06 and 0.12.

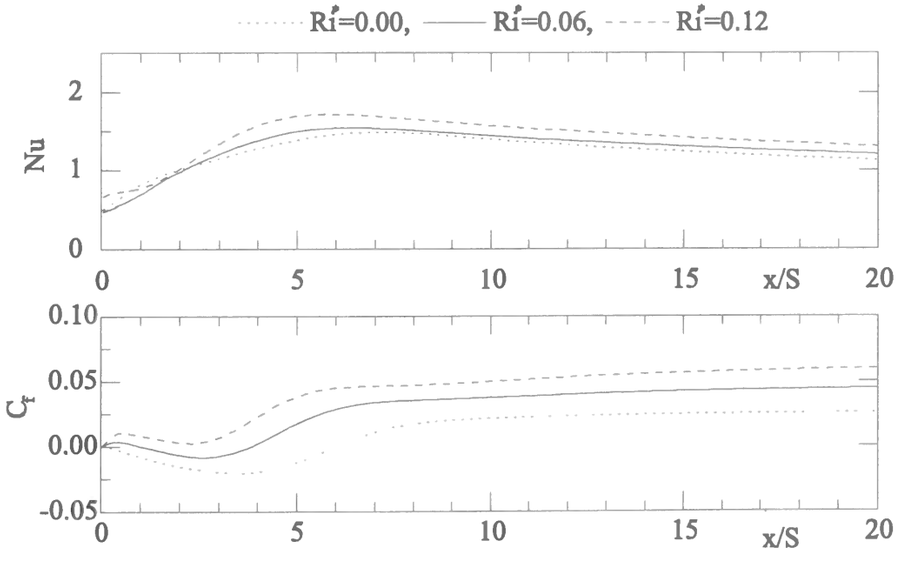

Figure 4.9: C_f and Nu distributions(3-D).

Figure 4.10 shows the skin friction coefficient C_f contour on the heated wall for three different values of Ri^*. The shaded area corresponds to the area where the skin friction coefficients are positive in sign. In the case of Ri^*=0.06 shown in Fig. 4.10, borderlines between the shaded area and the white area are observed around x/S =1 and 4 corresponding to the positions of $x = x_s$ and $x = x_r$ respectively. A comparison among the three figures in Fig. 4.10 indicates that as Ri^* increases, the borderline indicating the position of $x = x_r$ shifts upstream throughout the entire span of the heated bottom wall, while the position of $x = x_s$ moves downstream. In the case of Ri^*=0.00, a two-dimensional region exists in the middle of the heated wall. The two-dimensional region mentioned here is defined as the region where almost all the skin friction contours lie parallel to the z-axis. Spanwise area fraction of the two-dimensional region is estimated to be more than 50% of the heated wall. On the other hand, for Ri^*=0.06 and 0.12, such two-dimensional regions cannot be identified. This suggests that three-dimensionality of the flow field is reinforced by buoyancy. In the case of Ri^*=0.12 shown in Fig. 4.10, the shaded area exists along the entire x-axis indicating that positive skin friction prevails everywhere. This confirms that the main recirculation zone detaches from the heated wall as mentioned in the previous section. Small white regions are still observed near both side walls indicating the appearance of reverse flow regions . This phenomenon could not be predicted by 2-D calculations.

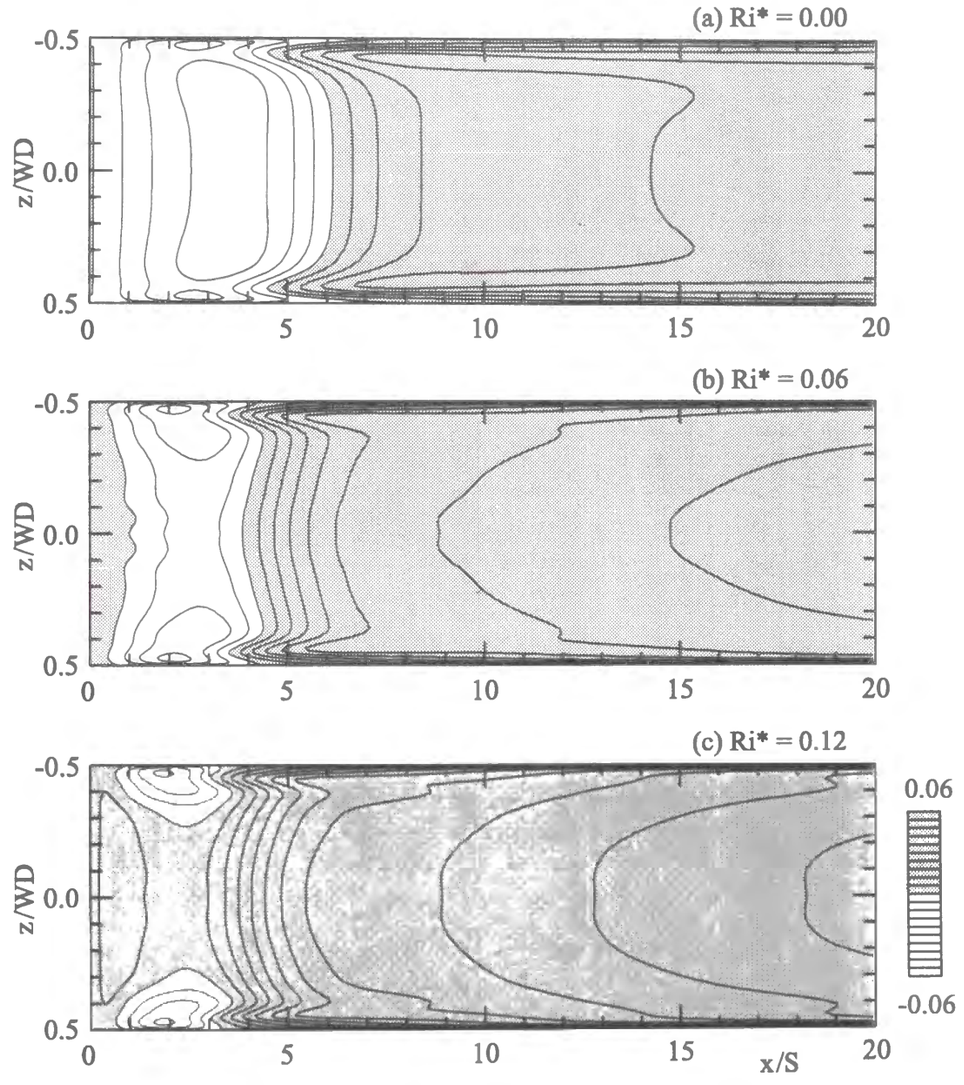

Figure 4.10: C_f contours on the heated wall.

Figure 4.11 shows the distribution pattern of the Nusselt number Nu contours on the heated wall for the same three values of Ri^*. Gray tone levels correspond to the values of Nusselt numbers. Maximum Nusselt numbers,Nu_{max}, appear symmetrically near the both side walls and not on the centerline of the heated wall, similar to the pure forced convection case. As Ri^* increases, the maximum Nusselt number becomes larger and its streamwise location shifts upstream. The spanwise location of Nu_{max}, however, remains in the vicinity of the side walls. The value of Nu_{max} and its streamwise and spanwise locations are summarized in Table 4.1.

Table 4.1 Locations and values of Nu_{max}.

Ri^*	x_{max}/S	z_{max}/WD	Nu_{max}
0.00	4.9	0.45	2.2
0.06	4.1	0.45	2.8
0.12	3.7	0.45	3.0

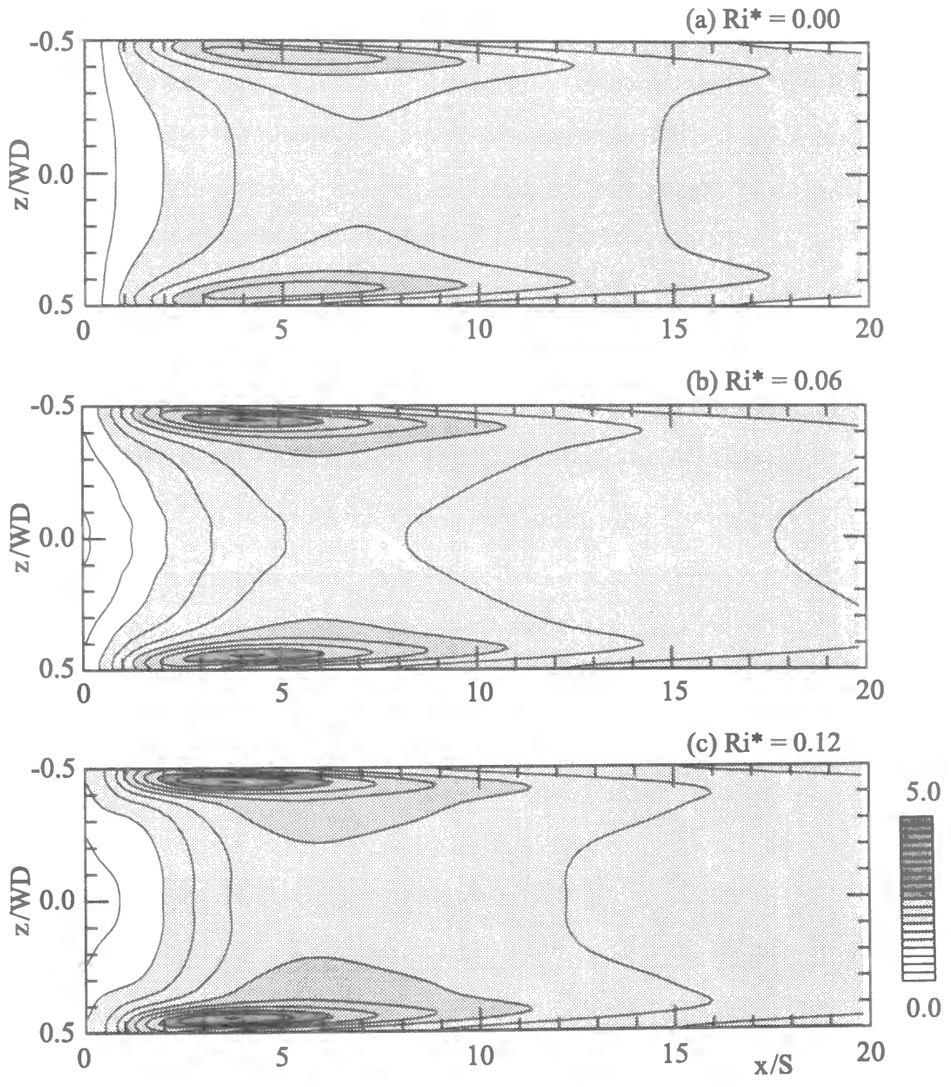

Figure 4.11: Nu contours on the heated wall.

In order to examine the three-dimensionality of the flow and thermal fields in detail, profiles of the flow velocity in the y-z cross-sections of the duct were examined at two different streamwise locations for each case of different values of Ri^*. The resultant velocity vectors of V and W and the contours of the streamwise velocity U in the two streamwise cross-sectional planes are shown in Fig. 4.12. The shaded areas here correspond to the region where positive U velocity exists. Figure 4.13, on the other hand, shows a similar view of the temperature contours. The level of the gray tone corresponds to the temperature level here.

In general, the distribution patterns both of the cross-sectional velocity vectors and the U contours of buoyancy-affected flow are observed to be quite similar to those of pure forced convective flow. In Fig. 4.12(b-2,c-2), for instance, U contours protrude toward the heated wall at positions around $|z/WD| = 0.45$, similar to the case of the flow without buoyancy (a-2). This is caused by the downwash flow observed at such spanwise positions. It can also be found that buoyancy effects become more noticeable as Ri^* increases. In the cross section of x/S=0.5, the fractional area of positive U region increases in the vicinity of the heated bottom wall as Ri^* increases.

It is clearly seen in Fig. 4.12 that the downward deflection of the positive U main flow region toward the heated wall is affected by Ri^*. In the case of Ri^*=0.00, U contours in the cross-section of $x/S = 3.0$ are almost uniform in the spanwise direction in the region of $|z/WD| < 0.3$. In this spanwise region, the boundary between the shaded and white area is parallel to the z-axis in this case. However, this spanwise uniformity in the duct center region does not hold in the cases of buoyancy affected flows. In the case of Ri^*=0.06 for example, the positive U main flow region projects toward the heated wall around the duct center region in the cross-section of $x/S = 3.0$. The boundary between the shaded and white area is obviously not parallel to the z-axis. It should also be noted in Fig. 4.12(c-1) that there exists a flow directed toward the center region of the duct in the region $0< y/S <1$ and $0.2< |z/WD| <0.4$. This flow is not observed in the pure forced convection case (a-1) and becomes more intense as Ri^* increases. The flow field gains its

three-dimensionality right after the step (x/S =0.5) as Ri^* increases.

As can be seen in Fig. 4.13, maximum wall temperature appears around duct center region at x/S =0.5. The effects of the previously mentioned duct inward flow right after the step (x/S =0.5) on the thermal field are not clear. At x/S =3.0, relatively cold fluid approaches the heated wall at around $|z/WD|$=0.45 in all the cases studied here, where the downwash flows are observed in Fig. 4.12. This corresponds well with Nu distribution on the heated wall shown in Fig. 4.11, in which larger Nu areas are symmetrically observed at such spanwise positions.

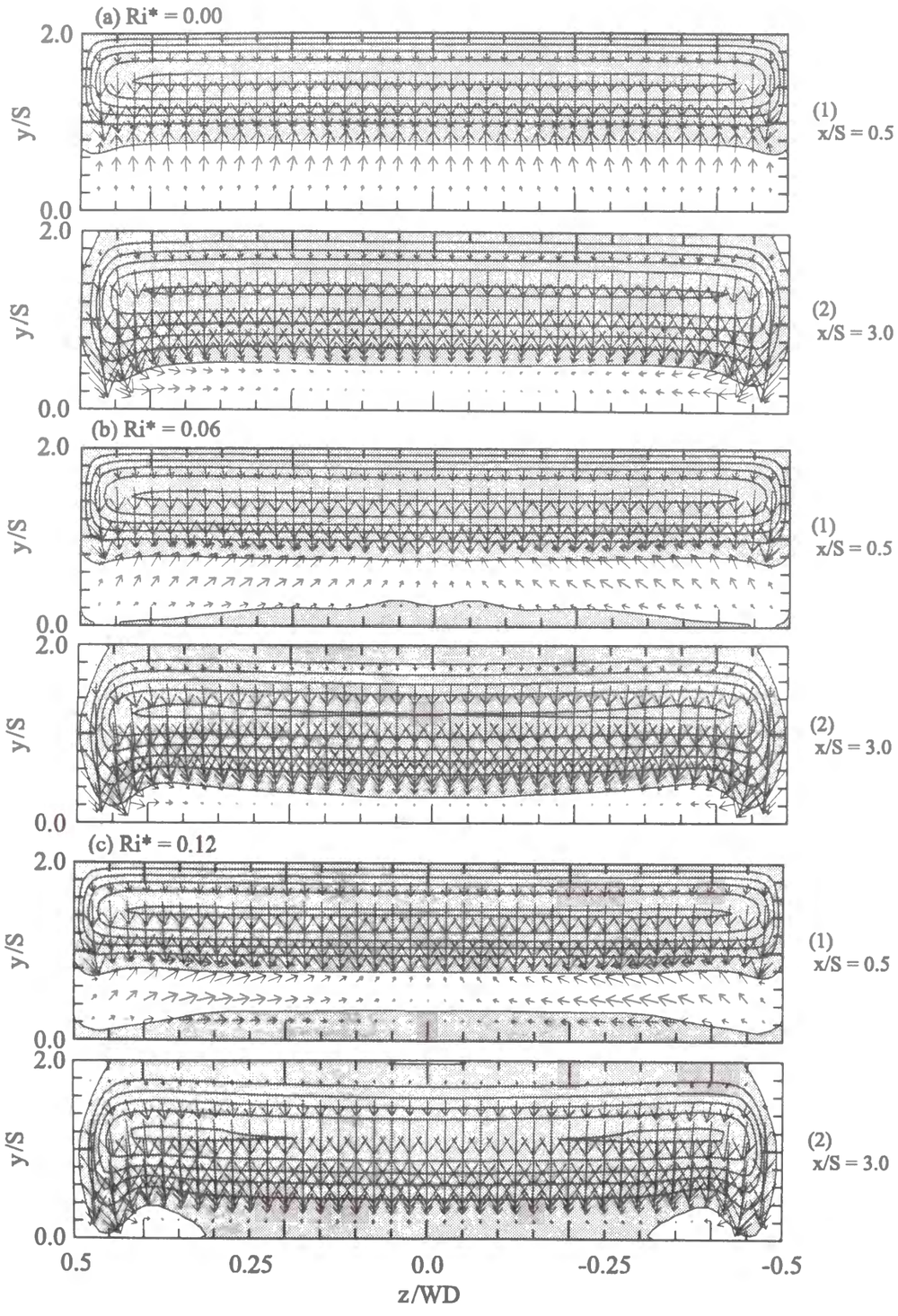

Figure 4.12: U contours and V-W vector plots.

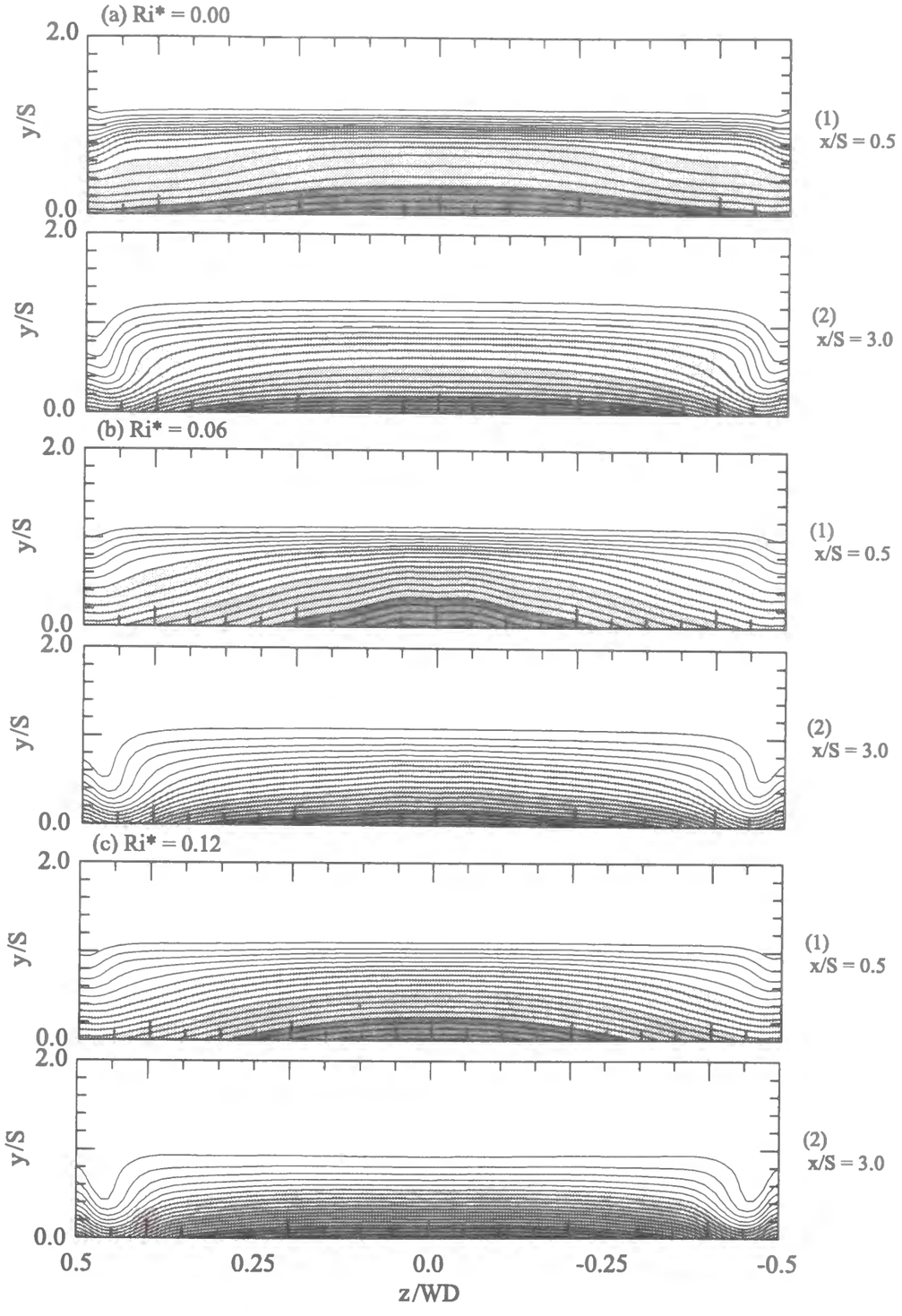

Figure 4.13: Temperature contours.

The value of W_y defined below is calculated at the bottom wall surface and its contours are shown in Fig. 4.14 for different values of Ri^*.

$$Wy = \frac{2\mu \frac{\partial W}{\partial y}|_{y=0}}{\rho U_{in}^2}$$

where W is the spanwise velocity component. In this figure, the shaded parts correspond to the regions where the value of Wy is positive in sign, while the white parts to the negative Wy regions. This figure features inward flow more intensely appearing right after the step in the cases of Ri^*=0.06 and 0.12. $|Wy|$ are observed to take peaks around x/S=0.5, $|z/WD|$=0.3 in the cases of Ri^*=0.06 and 0.12, while such peaks are not observed in the case without buoyancy. These peaks reflect the existence of strong inward flow there seen in Fig. 4.12. Spatial density of Wy contourlines become higher around the peaks as Ri^* increases. This implies that this inward flow right after the step is reinforced more intensively with an increase of buoyancy level.

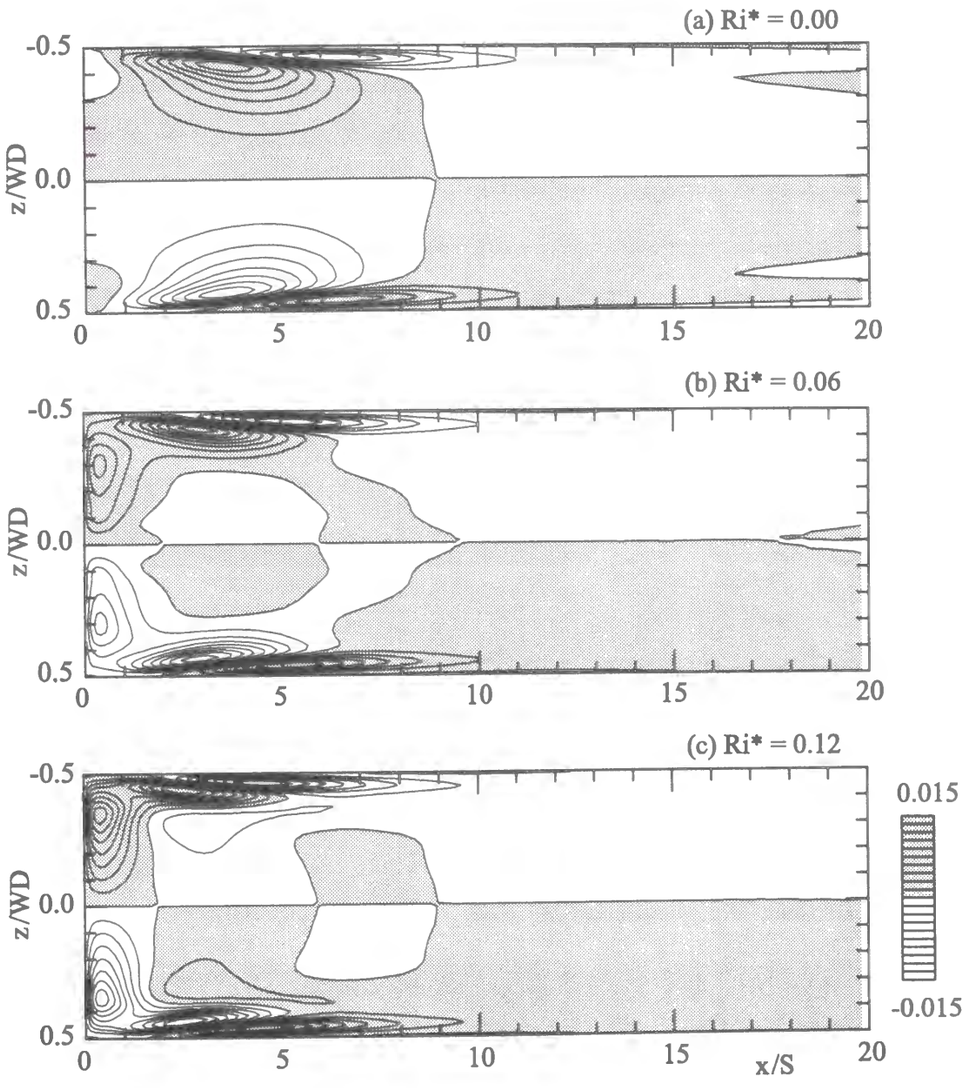

Figure 4.14: Wy contours on the heated wall.

Pressure distributions are calculated for all three values of Ri^* in the cross section x/S=0.5 where the previously mentioned inward flow near the heated wall is observed. Contours of pressure coefficient calculated for the same conditions are illustrated in Fig. 4.15. The reference value of the pressure is its value at z/WD=0 near the heated wall in the cross-section. Shaded areas here indicate that the coefficient is positive in sign. Spanwise pressure non-uniformity becomes more pronounced as Ri^* increases in the region $y/S <$ 1.0, reflecting the more pronounced three-dimensionality of the flow field. In the case of Ri^*=0.12, in particular, the contourlines are closely located to each other at positions around 0.3< z/WD <0.4, corresponding well to the reinforcement of the inward flow near the heated wall observed in Fig. 4.12.

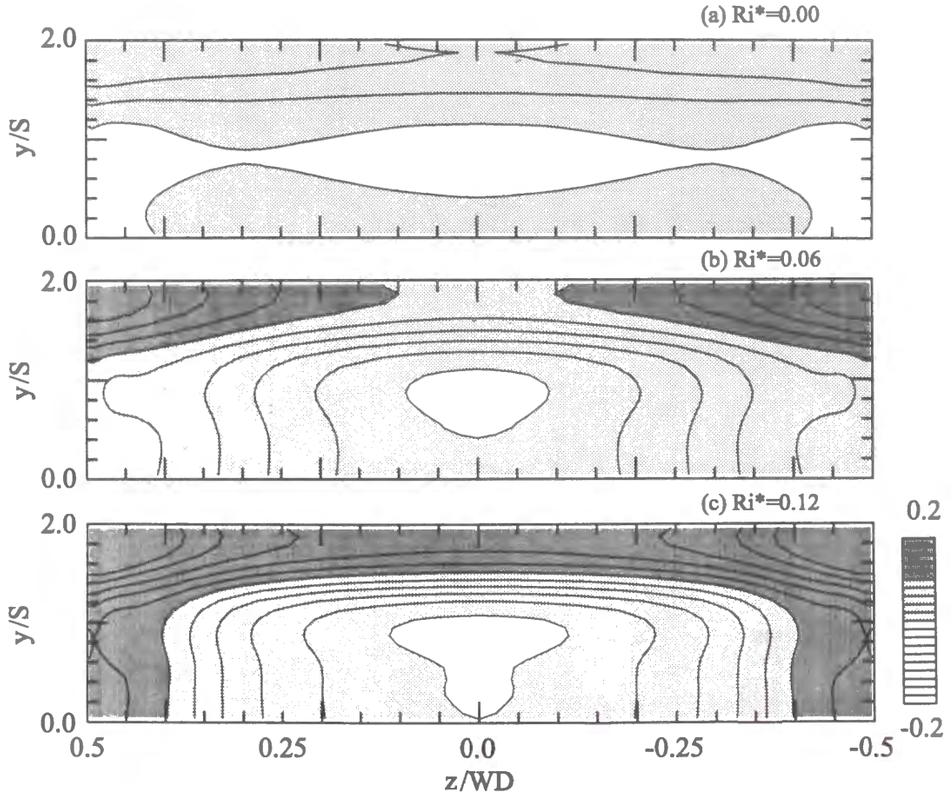

Figure 4.15: Pressure coefficient contours in y-z cross section right after the step.

All the above calculations discussed so far were performed at a constant Reynolds number equal to 125. In the remaining part of this chapter, the effect of the Reynolds number is now discussed based on 2-D calculations carried out for three different Reynolds number equal to 100,125 and 150 keeping the buoyancy level constant at Ri^*=0.12. Figure 4.16 compares the streamwise distributions of skin friction coefficient and the Nusselt number distribution for different Reynolds numbers. It is seen in Fig. 4.16 that the value of C_f decreases along a large portion of the entire x-axis with an increase of Re, while Nusselt number increases generally. However the manner how buoyancy affects the flow and thermal fields remains unchanged disregarding the change of Reynolds number. At all three values of Re, the main recirculation region detaches from the heated wall, resulting in positive skin friction coefficient values along the entire x-axis. From these results, it can be expected that there should not be any big differences in the influence of buoyancy effects due to the change of Re as far as the flow remains steady. This is the background of why the discussions of present chapter were mainly devoted to the effects of buoyancy level instead to the effects of the Reynolds number.

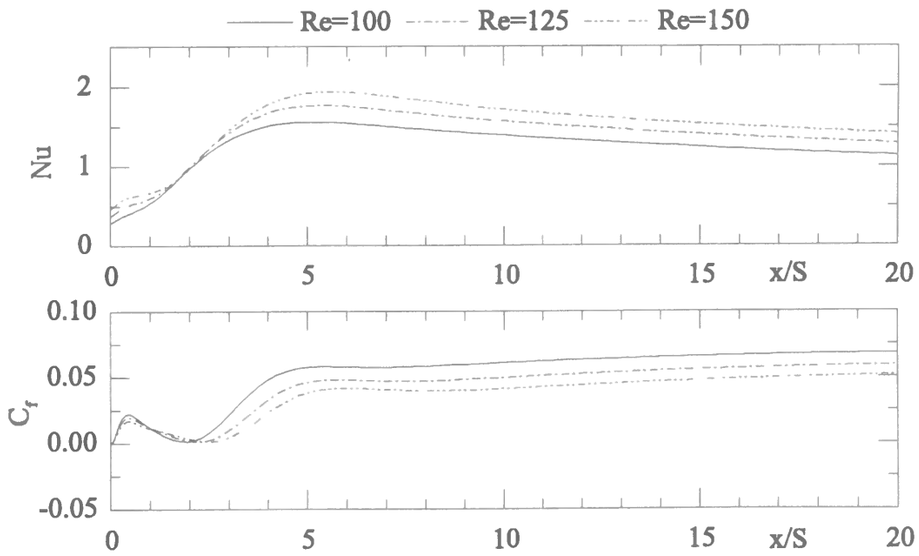

Figure 4.16: Effect of Re at the same Ri^*.

4.4 Conclusions

In this chapter, the effects of buoyancy on the flow and thermal fields over a backward-facing step were studied. For this purpose 2-D and 3-D numerical computations were carried out for mixed convective upward flows under the conditions such that the flow remains steady if buoyancy is being neglected. The following conclusions were obtained.

(1) Both of the reattachment point and the peak Nusselt number point move upstream as Ri^* increases, while the secondary recirculation region, formed at the corner of the step becomes larger in size. The main recirculation region detaches from the heated wall at Ri^*=0.12. Moreover, the peak Nusselt number point always appear downstream of the reattachment point and the distance between them increases as Ri^* increases.

(2) Maximum Nusselt number positions on the heated wall are located near the side walls symmetrically with respect to the duct center plane, in a similar manner to the cases of pure forced convection and their positions shift upstream as Ri^* increases. There also exists an inward flow near the heated wall right after the step, where flow is directed toward the center of the duct. Such flow becomes more intensive as Ri^* increases.

(3) 2-D computations are effective in predicting the phenomena mentioned in (1). However, when three-dimensionality of the flow and thermal fields becomes prominent, (e.g. $Ri^* > 0.06$, as reported in this paper) a 3-D computation becomes necessary.

(4) The manner how buoyancy affects the flow and thermal fields remains unchanged disregarding the change of Reynolds number as far as the flow remains steady.

References

[1] Worsoe-Schmidt, P.M. and Leppert, G., *Heat Transfer and Friction for Laminar Flow of Gas in a Circular Tube at High Heating Rate*, Int. J. Heat Mass Transfer, Vol. 8, pp. 1281-1301, (1965).

[2] Patankar, S.V., Ramadhyani, S. and Sparrow, E.M., *Effect of Circumferentially Nonuniform Heating on Laminar Combined Convection in a Horizontal Tube*, Trans.ASME: J.Heat Trans., Vol. 100, pp.63-70, (1978).

[3] Ramachandran, N., Armaly, B.F. and Chen, T.S., *Measurements and Predictions of Laminar Mixed Convection Flow Adjacent to a Vertical Surface*, Trans.ASME: J.Heat Trans., Vol. 107, pp.636-641, (1985).

[4] Baek, B.J., Armaly, B.F. and Chen, T.S., *Measurements in Buoyancy-Assisting Separated Flow Behind a Vertical Backward-Facing Step*, Trans.ASME: J.Heat Trans., Vol. 115, pp.403-408, (1993).

[5] Abu-Mulaweh, H.I., Armaly, B.F. and Chen, T.S., *Measurements of Laminar Mixed Convection in Boundary-Layer Flow over Horizontal and Inclined Backward-Facing Steps*, Int.J.Heat Mass Trans., Vol.36-7, pp. 1883-1895, (1993).

[6] Abu-Mulaweh, H.I., Armaly, B.F. and Chen, T.S., *Measurements in Buoyancy-Opposing Laminar Flow over a Vertical Backward-Facing Step*, Trans.ASME: J.Heat Trans., Vol.116, pp. 247-249, (1994).

[7] Lin J.T.,Armaly, B.F. and Chen, T.S., *Mixed Convection in Buoyancy-Assisting, Vertical Backward-Facing Step Flows*, Int.J.Heat Mass Trans., Vol.33-10, pp. 2121-2132, (1990).

[8] Lin J.T.,Armaly, B.F. and Chen, T.S.,*Mixed Convection Heat Transfer in Inclined Backward-Facing Step Flows*, Int.J.Heat Mass Trans., Vol.34-6, pp. 1568-1571, (1991).

[9] Hong B.,Armaly, B.F. and Chen, T.S., *Laminar Mixed Convection in a Duct with a Backward-Facing Step: the Effects of Inclination Angle and Prandtl Number* , Int.J.Heat Mass Trans., vol.36-12, pp.3059-3067 (1993).

[10] Shah, R.K. and London, A.L., *Laminar Forced Convection in Ducts*, (1978), Academic Press.

Chapter 5

The Effects of Duct Inclination Angle on Laminar Mixed Convective Flows over a Backward-Facing Step

5.1 Introduction

In the previous chapter, the effects of buoyancy level on the mixed convective laminar flows over a backward-facing step are discussed, taking upward flows as an example. In practical applications, the flow separation and reattachment phenomena could happen in ducts of various positions. However there is not many investigations [1] dealing with the effects of duct inclination angles on the flow and thermal fields for mixed convective flows with flow separation and reattachment. Especially no three-dimensional study on the effects of inclination angles has been previously reported in the literature, to the author's knowledge.

In this chapter, three-dimensional simulations are carried out for mixed convective flows over a backward-facing step in a duct. Attention is paid in particular to the effects of the two inclination angles of the flow configuration: one is the pitch angle and the other is the rolling angle to be defined later.

5.2 Computational Conditions

5.2.1 Computational Domain

The computational domain is schematically illustrated in Fig. 5.1. The aspect ratio,AR, and the expansion ratio,ER, were kept constant at 16 and 2 respectively in this chapter. The computational domain covers $-1 \leq x/S \leq 30$. It is confirmed that adoption of a longer streamwise size of computational domain does not change the final results.

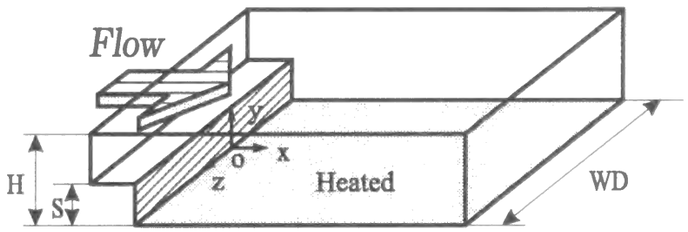

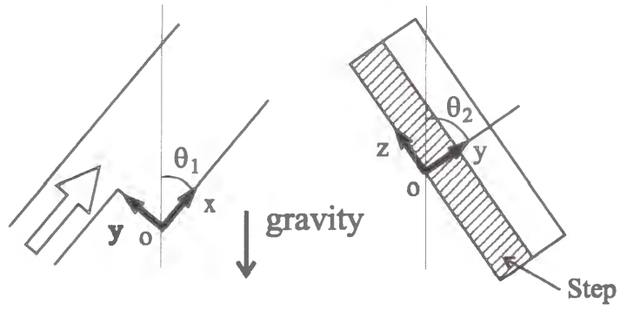

Figure 5.1: Computational domain.

- Expansion Ratio, $ER = \frac{H}{H-S} = 2$
- Aspect Ratio, $AR = \frac{WD}{S} = 16$

The duct posture is determined by specifying two inclination angles θ_1 and θ_2 described in Fig. 5.1. The two inclination angles of the flow configuration are defined as below:

- θ_1 : pitch angle : an angle between the streamwise direction and vertical upward direction and its changing range is $0° \leq \theta_1 \leq 360°$
- θ_2 : rolling angle : an angle between the normal direction and vertical upward direction, $0° \leq \theta_2 \leq 180°$

In the next section, how the heat transfer characteristics are affected by the change of θ_1 will be first examined followed by the discussion about the effects of θ_2. When θ_1 is changed the value of θ_2 is kept constant at θ_2=0°, where θ_1=0° corresponds to the upward flow case, θ_1=180° to the downward flow case. On the other hand, when θ_2 is changed the value of θ_1 is kept constant at θ_1=90°.

5.2.2 Governing Equations

The continuity equation and the energy equation used in this chapter are the same as the ones shown in Chapter 2. However the momentum equations should be modified appropriately to study the effects of the two inclination angles θ_1 and θ_2. The momentum equations adopted in this chapter contain the buoyancy term in order to take account of the buoyancy effects. Buoyancy term is evaluated by making use of Boussinesq approximation [2] as was explained in Chapter 4. The momentum equations can be written as follows:

$$\begin{aligned} &\frac{\partial}{\partial t}(\rho U) + \frac{\partial}{\partial x}(\rho U^2) + \frac{\partial}{\partial y}(\rho VU) + \frac{\partial}{\partial z}(\rho WU) \\ = \; &-\frac{\partial P}{\partial x} + \frac{\partial}{\partial x}\left(\mu\frac{\partial U}{\partial x}\right) + \frac{\partial}{\partial y}\left(\mu\frac{\partial U}{\partial y}\right) + \frac{\partial}{\partial z}\left(\mu\frac{\partial U}{\partial z}\right) + \rho_{in}\beta g(T - T_{in})\cos\theta_1 \end{aligned} \tag{5.1}$$

$$\begin{aligned} &\frac{\partial}{\partial t}(\rho V) + \frac{\partial}{\partial x}(\rho UV) + \frac{\partial}{\partial y}(\rho V^2) + \frac{\partial}{\partial z}(\rho WV) \\ = \; &-\frac{\partial P}{\partial y} + \frac{\partial}{\partial x}\left(\mu\frac{\partial V}{\partial x}\right) + \frac{\partial}{\partial y}\left(\mu\frac{\partial V}{\partial y}\right) + \frac{\partial}{\partial z}\left(\mu\frac{\partial V}{\partial z}\right) + \rho_{in}\beta g(T - T_{in})\sin\theta_1\cos\theta_2 \end{aligned} \tag{5.2}$$

$$\frac{\partial}{\partial t}(\rho W) + \frac{\partial}{\partial x}(\rho UW) + \frac{\partial}{\partial y}(\rho VW) + \frac{\partial}{\partial z}(\rho W^2)$$
$$= -\frac{\partial P}{\partial z} + \frac{\partial}{\partial x}\left(\mu\frac{\partial W}{\partial x}\right) + \frac{\partial}{\partial y}\left(\mu\frac{\partial W}{\partial y}\right) + \frac{\partial}{\partial z}\left(\mu\frac{\partial W}{\partial z}\right) + \rho_{in}\beta g(T - T_{in})\sin\theta_2 \qquad (5.3)$$

5.2.3 Boundary Conditions

At the upstream boundary, inlet flow is assumed to be hydrodynamically steady and fully developed and to have a uniform temperature profile. U profile is assumed to obey the approximation proposed by Shah [3], while V and W are set to be zero. No-slip condition is applied at the all wall surfaces. The heated wall downstream of the step is maintained at a uniform heat flux, while the top and bottom straight walls, the backward-facing wall and the side walls are assumed to be thermally adiabatic. Streamwise gradients of all quantities at the duct exit are set to be zero.

5.2.4 Computational Conditions

Reynolds number, the expansion ratio and the aspect ratio are kept constant at Re=125, ER=2 and AR=16 respectively.

- Reynolds number, $Re = \frac{U_{in}S}{\nu} = 125$
- Expansion Ratio, $ER = \frac{H}{H-S} = 2$
- Aspect Ratio, $AR = \frac{WD}{S} = 16$

From the discussions in Chapter 3, it is known that the flow and thermal fields can be considered as two-dimensional under these conditions around the center region of the heated wall, if buoyancy is neglected. The main interest in this chapter is the effects of two inclination angles over the flow and thermal fields. Calculations are carried out in the first stage of this chapter for several cases of different modified Richardson number, Ri^*, for the two extreme cases, upward and downward flows, in order to select the buoyancy level at which the effects of inclination angles should be investigated. Variation of Ri^* is equivalent

to varying the heat flux for a given step height. The computational conditions are chosen so that the temperature difference between the main flow and the heated wall ranges from $10K$ to $30K$ for the case of $10mm$ step height, which should be a normal size to be adopted in experiments. The effects of inclination angles, θ_1 and θ_2, are studied, keeping Ri^* at a constant value to be chosen as the results of the first stage computation. θ_1 is first changed in the range of $0° \leq \theta_1 \leq 360°$ with θ_2 kept at 0°. The case of $\theta_1 = 0°$ (=360°) is equivalent to the upward flow case while $\theta_1 = 180°$ to the downward flow. Finally θ_2 will be changed in the range of $0° \leq \theta_2 \leq 180°$ keeping θ_1 constant at 90° and its effects will be studied. The case of (θ_1, θ_2) = (270°, 0°) and (90°, 180°) are the same posture to each other.

Close attention is paid to the distribution patterns of both skin friction coefficient and Nusselt number on the heated wall. They are defined as below:

$$\text{Skin friction coefficient}, C_f = \frac{2\tau_w}{\rho U_{in}^2} \qquad (5.4)$$

$$\text{Nusselt number}, Nu = \frac{q_w S}{\lambda(T_w - T_{in})} \qquad (5.5)$$

τ_w, q_w, T_w, T_{in} and U_{in} used here refer to the values of the wall shear stress, wall heat flux, wall temperature, inlet temperature and the cross-sectional mean velocity at the inlet respectively.

5.3 Results and Discussion

5.3.1 Ri^* effects on up/downward flows

The effects of Ri^* on the three positions of the reattachment point x_r, the peak Nusselt number point x_p and the downstream end of the secondary recirculation region x_s are discussed here. Their positions obtained along the centerline of the heated wall are presented in Fig. 5.2 for both upward ($Ri^* > 0$) and downward ($Ri^* < 0$) flows. The peak Nusselt number here means the maximum Nusselt number along the centerline of the heated wall. The secondary recirculation region is defined as the recirculation region which appears at the corner of the step, inside of the main recirculation zone with an opposite direction of recirculating flow and is schematically illustrated in Fig. 5.3. The value of x_s is defined as the distance from the step to a position where the sign of skin friction coefficient changes from positive to negative. Although the value of Ri^* should be always positive in nature, negative value is assigned for convenience in Fig. 5.2 for downward flows heated from the wall.

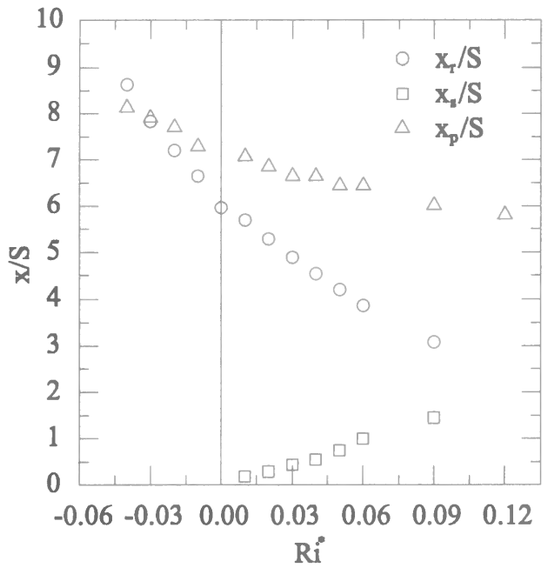

Figure 5.2: Effect of Ri^* on x_r, x_p and x_s.

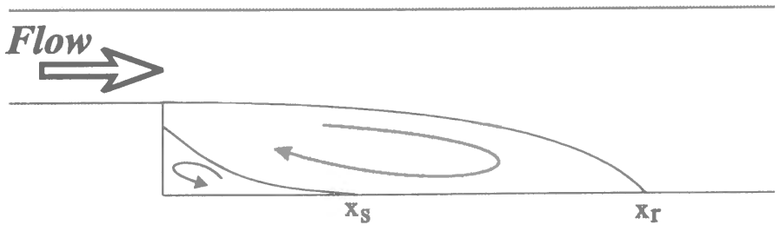

Figure 5.3: Main and secondary recirculation regions.

The buoyancy level, or the value of Ri^*, clearly affects the positions plotted in Fig. 5.2. As the absolute value of Ri^* is increased, the reattachment position,x_r, and the peak Nusselt number position,x_p, move upstream in the upward flow case ($Ri^* > 0$) and move downstream in the downward flow case ($Ri^* < 0$). x_r is located downstream of x_p when $Ri^* = -0.04$. When $Ri^* = -0.03$, they are closely located to each other. For $Ri^* \geq -0.02$, x_r always appears upstream of x_p. The distance of between x_r and x_p becomes longer as Ri^* increases. The secondary recirculation region exists only in the upward flow cases ($Ri^* > 0$). x_s moves downstream as Ri^* increases. x_r and x_s are expected to merge in when Ri^* is increased above 0.09. In that case the main recirculation region detaches from the heated wall [4].

Abu-Mulaweh [5] reported that x_r increased considerably with a small increase of Ri^* in the downward flow case ($Ri^* <0$), or in the present manner of description, with a small decrease of Ri^* from zero. The same tendency is observed in the present simulation. The value of x_r increases with decrease of Ri^* in downward flow cases, resulting a stronger and longer main recirculation region downstream of the step. This results from the reinforcement of the reverse flow inside the main recirculation region produced by the buoyancy acting on the relatively high temperature fluid existing near the heated wall. At Ri^*=–0.05, the calculation was no longer stable. Considering the above results, the effects of θ_1 and θ_2 will be studied in the following by keeping Ri^* equal to 0.03.

5.3.2 Effects of the pitch angle θ_1

The effects of θ_1 is examined first. θ_1 is changed from 0° to 360° while θ_2 is kept constant at 0°. This is schematically illustrated in Fig. 5.4. θ_1=0° and θ_1=180° correspond to the upward and downward flows respectively. The flow is accelerated in the x-direction by the buoyancy at the pitch angle in the ranges $0° \leq \theta_1 < 90°$ and $270° < \theta_1 \leq 360°$. Hong [1] studied a similar case by conducting a 2-D simulation. They did a computation for the condition of Re=100 and Gr^*=609, where the buoyancy level,Ri^*, is expected to be twice as large as than that of the present study.

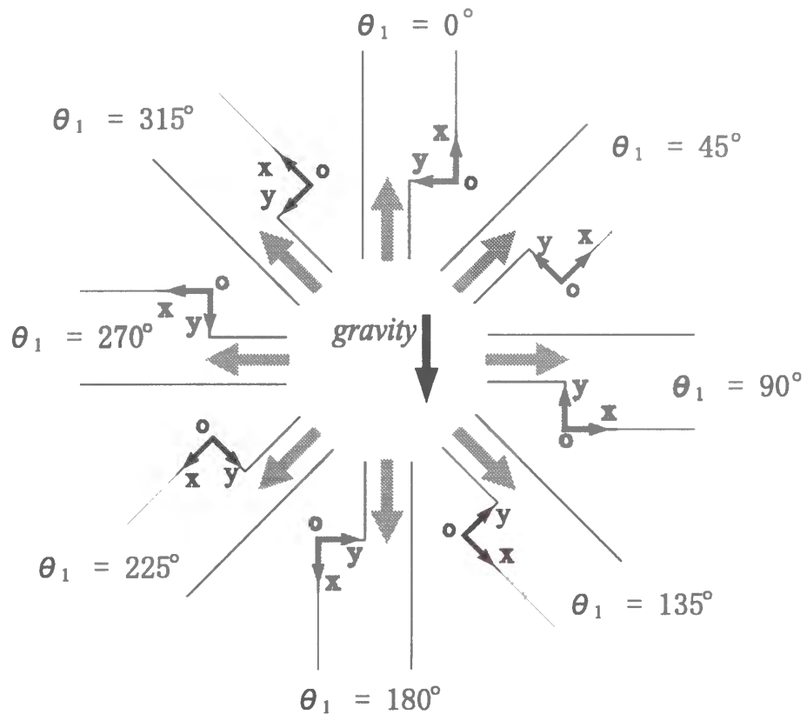

Figure 5.4: Change of duct posture with θ_1.

The effects of θ_1 on the positions of the reattachment point,x_r, the peak Nusselt number point,x_p and the secondary recirculation region,x_s along the centerline of the heated wall are shown in Fig. 5.5. The results qualitatively matches the results obtained by Hong [1].

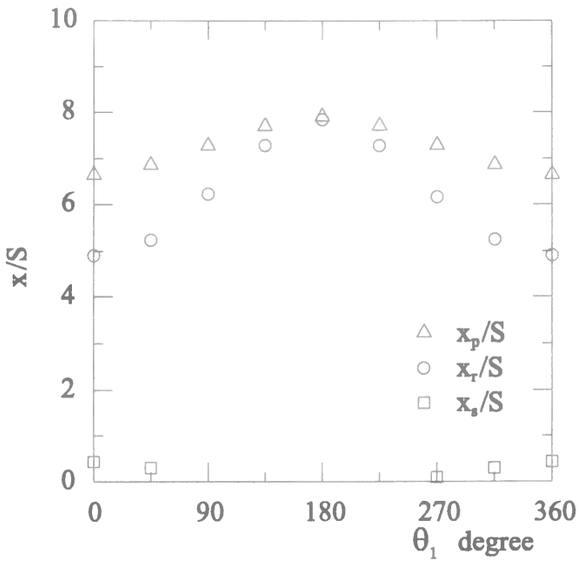

Figure 5.5: Effect of θ_1 on x_r, x_p and x_s(3-D).

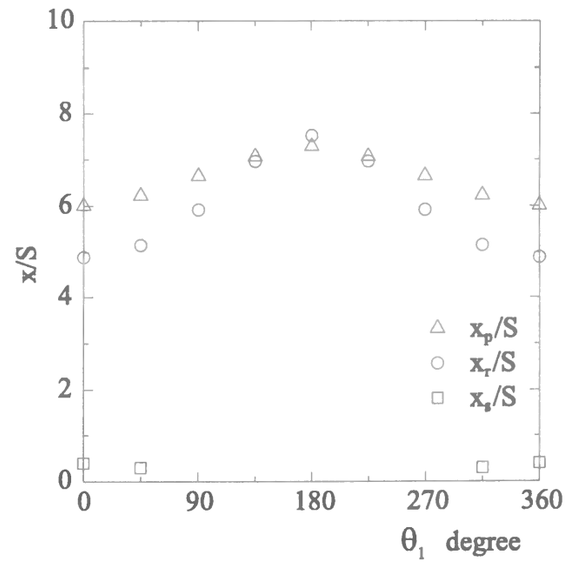

Figure 5.6: Effect of θ_1 on x_r, x_p and x_s(2-D).

As θ_1 increases, the value of x_r and x_p increase when $0° \leq \theta_1 \leq 180°$ and decrease when $180° \leq \theta_1 \leq 360°$. Hong [1] reported that the relative positions of x_r and x_p switched at a certain pitch angle and that in the range of $120° < \theta_1 < 240°$ x_r was located downstream of x_p. This phenomenon is not observed in the present 3-D simulations. The peak Nusselt number point x_p always appears at a position further downstream of the reattachment point x_r in Fig. 5.5. The distance between the two points is found to reach a maximum value at θ_1=0° (360°) and a minimum value at θ_1=180°. Hong [1] also reported that the changing pattern of the three positions with a change of θ_1 was asymmetric about θ_1=180°. However this asymmetry is smaller in Fig. 5.5 compared to Hong's results [1]. Figure 5.5 shows that the end position of the secondary recirculation region,x_s, marks its maximum value at θ_1=0°. No secondary recirculation is observed in the range of the pitch angle $90° < \theta_1 < 225°$.

Two-dimensional simulations under the same computational conditions as the ones shown in Fig. 5.5 are performed to be compared with the results of three-dimensional simulations. The results of 2-D simulations are shown in Fig. 5.6. The switching phenomenon of the positions of x_r and x_p is observed at $\theta_1 = 180°$ in Fig. 5.6. It implies that two-dimensional assumption can affect the relative position of x_r and x_p. The relative spatial positions of these two points should be discussed carefully. The asymmetry of the changing patterns of x_r,x_p and x_s positions about $\theta_1 = 180°$ in the 2-D simulations shown in Fig. 5.6 is even smaller than that of present 3-D simulations shown in Fig. 5.5. This suggests that the stronger asymmetry reported by Hong [1] is not due to the two-dimensional assumption but probably related to the larger buoyancy level employed in his study.

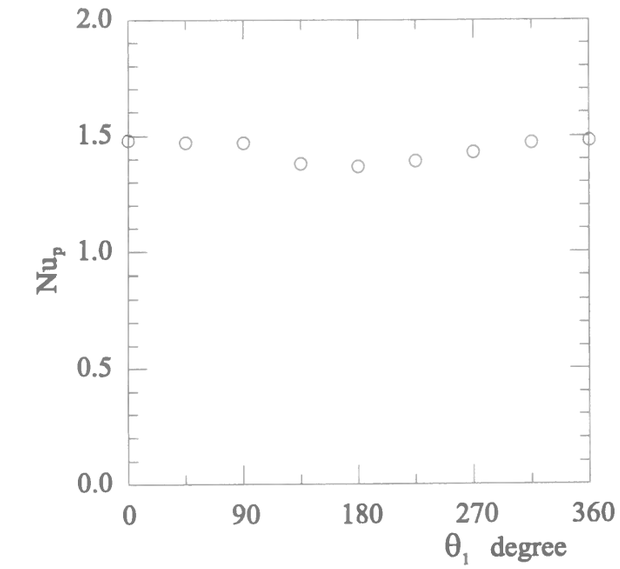

Figure 5.7: Effect of θ_1 on the peak Nu along the centerline(3-D).

Figure 5.7 shows the effect of θ_1 on the value of peak Nusselt number,Nu_p, for the results of 3-D simulations. Peak Nusselt number marks its maximum at θ_1=0° and minimum at θ_1=180°. The difference between the maximum and minimum is approximately 7% of the average value of Nu_p.

The contours of the skin friction coefficient C_f on the heated wall are shown in Fig. 5.8 for four different values of θ_1 (0°,90°,180°,270°). The shaded area corresponds to the area where the skin friction coefficient is positive in sign. The borderlines between the shaded area and the white area correspond to the positions of x_s and x_r. In all the cases, a two-dimensional region can be observed in the middle of the heated wall, where the contourlines are almost parallel to the z-axis. The two-dimensional region seems to be narrower in the case of θ_1=180° compared to other three cases. It is obviously seen in Fig. 5.8 that the cases of θ_1=90° and 270° have C_f distribution patterns on the entire heated wall quite similar to each other. This suggests that buoyancy effect is not large for horizontal flow at the buoyancy level of $Ri^* = 0.03$.

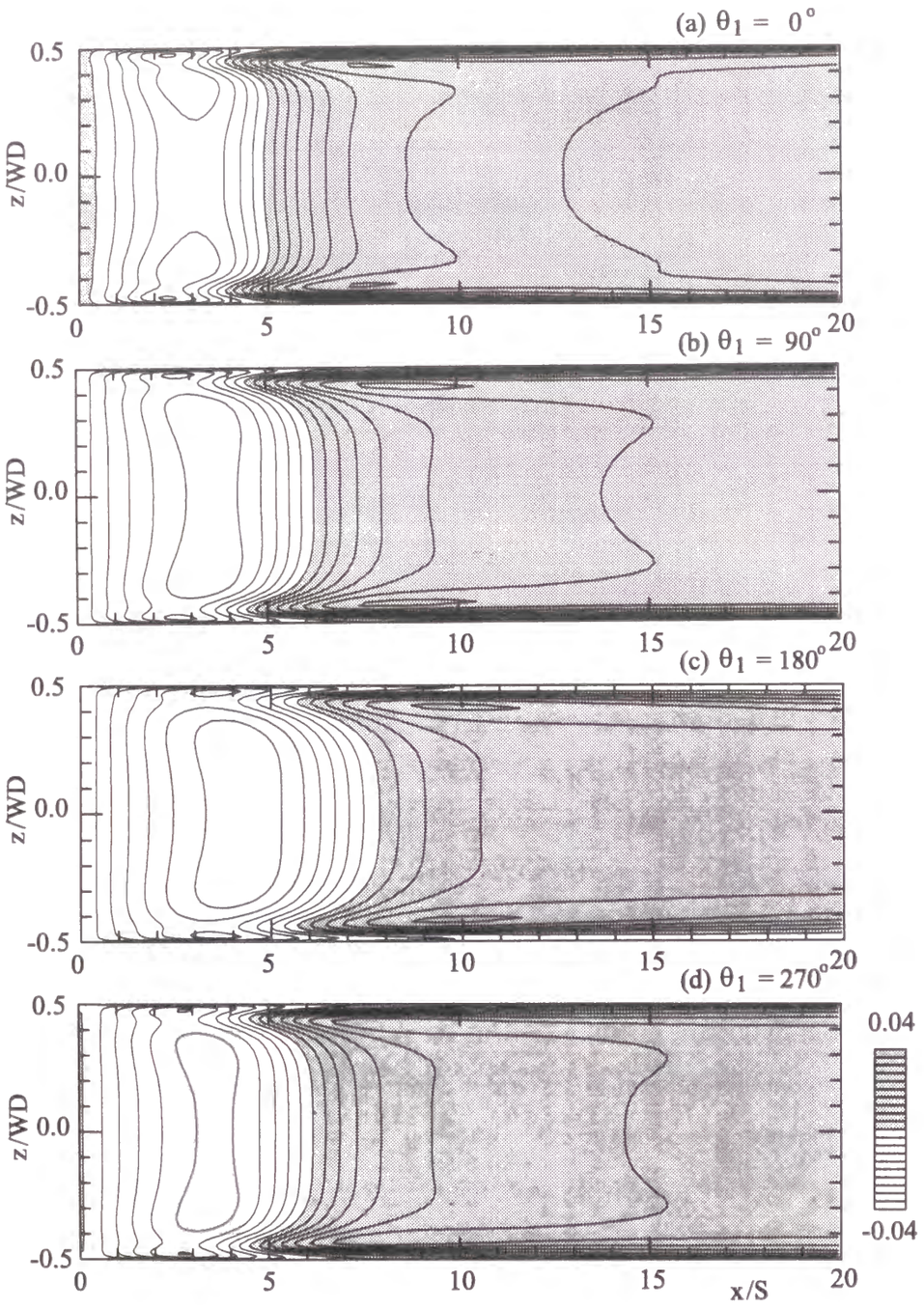

Figure 5.8: C_f contours on the heated wall.

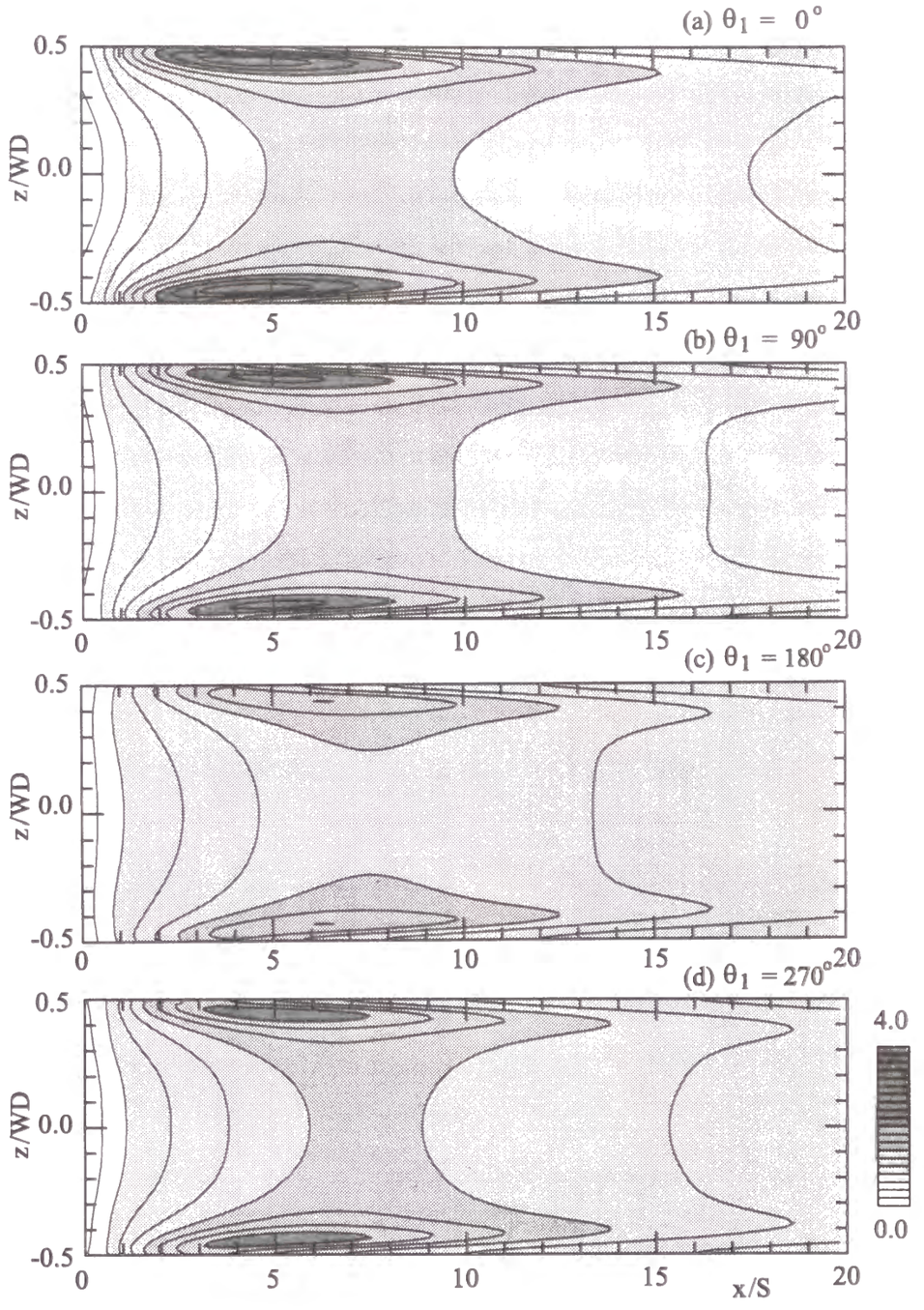

Figure 5.9: Nu contours on the heated wall.

The contours of the Nusselt number Nu on the heated wall corresponding to those of C_f plotted in Fig. 5.8 are shown in Fig. 5.9. The gray tone level corresponds to the level of Nusselt number. The calculated thermal fields are symmetric with respect to the duct centerline. Again,, the two-dimensional region can be observed in the middle region of the heated wall. Maximum Nusselt numbers,Nu_{max}, are located symmetrically near both side walls and not on the centerline of the heated wall similar to the cases of pure forced convection discussed in Chapter 3.

The value of Nu_{max} and its streamwise and spanwise locations are shown in Fig. 5.10 $\sim$ Fig. 5.12. In Fig. 5.10, Nu_{max} exhibits its highest value at θ_1=0° (=360°) and lowest value at 180°. Figure 5.11 shows that Nu_{max} appears at the most upstream position for the case θ_1=0°. On the other hand, Nu_{max} is located at the most downstream position for the case θ_1=180°. Figure 5.12 shows that the spanwise position of Nu_{max} appears slightly closer to the duct center at θ_1=180° than θ_1=0°. However, it remains in any case close to the side walls.

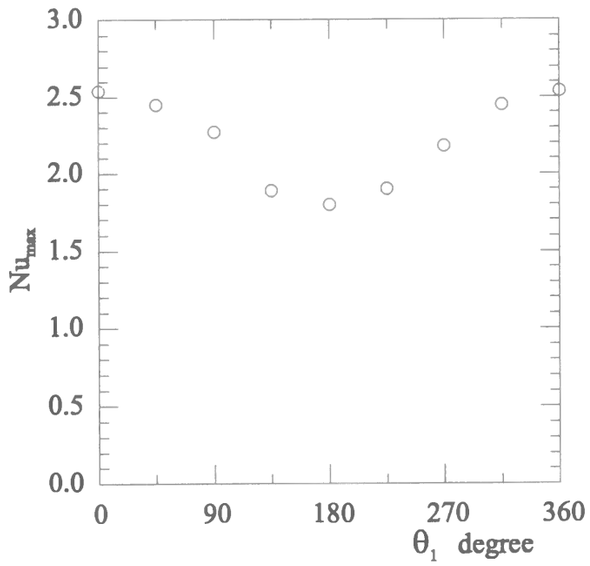

Figure 5.10: Effect of θ_1 on Nu_{max}.

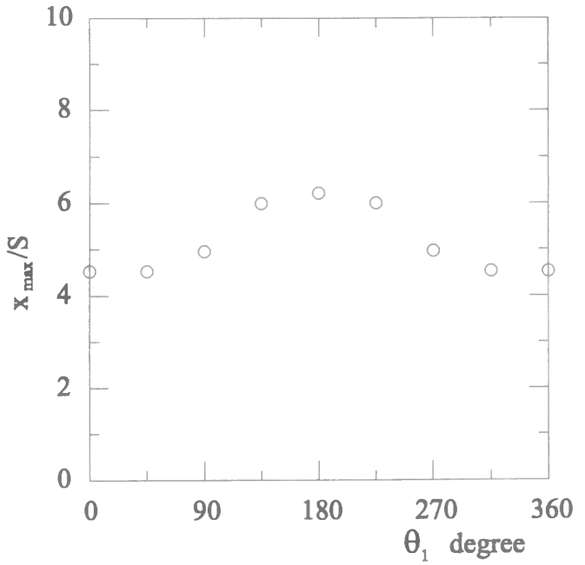

Figure 5.11: Effect of θ_1 on the streamwise position of Nu_{max}.

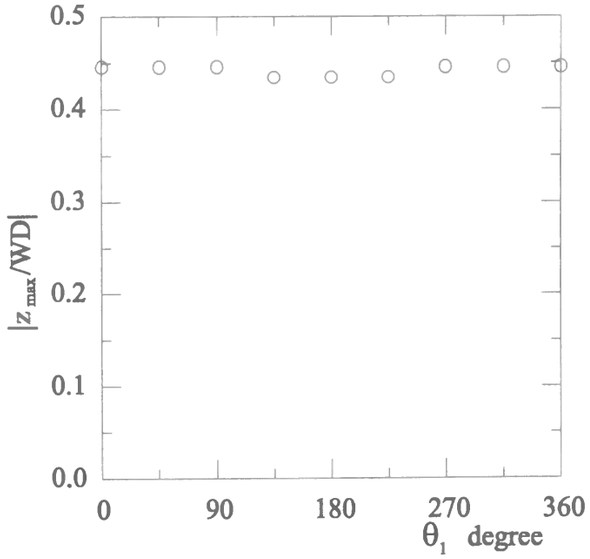

Figure 5.12: Effect of θ_1 on the spanwise position of Nu_{max}.

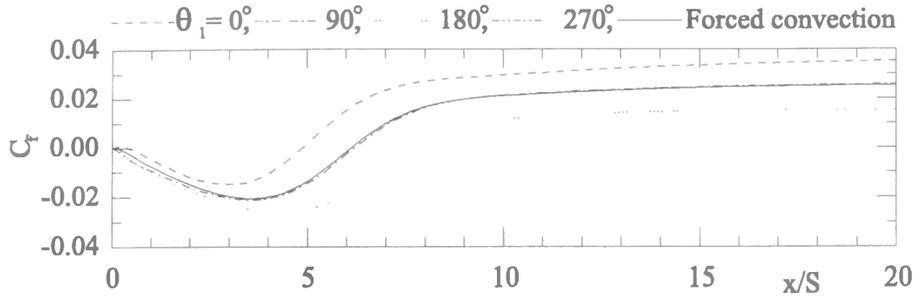

Figure 5.13: C_f distributions along the centerline.

The skin friction coefficient distribution along the centerline are compared among the studied four cases in Fig. 5.13. Result of a pure forced convection case (unheated case) is also shown in this figure as a reference. C_f values are particularly bigger over the entire range of the x-location when θ_1=0°, and smaller when θ_1=180°, compared to the pure forced convection case. The reason for this is that the main flow direction (x-direction) is exactly parallel to the buoyancy direction in these two cases, which affects the U profile near the wall. Hence, the buoyancy driven acceleration near the heated wall becomes maximum, when θ_1=0° and minimum when θ_1=180°. Two horizontal cases (θ_1=90°,270°) show little deviation from the pure forced convection case. This again suggests that the buoyancy level Ri^*=0.03 is not large enough to alter the velocity field noticeably in the cases of horizontal flows. A careful observation indicates that even in such cases a slight deviation can be found near the step ($0< x/S <3$) where fluid velocity is quite small (refer to Fig. 5.5).

Figure 5.14 shows the fluid temperature contours in the duct center plane calculated for the two cases of θ_1=90° and 270°. The temperature difference between two neighboring contourlines in Fig. 5.14 corresponds to 0.8 K if the step height,S, is presumed to be 10 mm. There is no noticeable difference between the two distribution patterns downstream of the reattachment point ($x_r/S \simeq 6.2$). However inside the main recirculation region, especially near the origin of the coordinate system, slight difference is observed between

these two cases. This difference may be related to the fact that the secondary recirculation region exists only in the case of θ_1=270° but not in the case of θ_1=90° as is seen in Fig. 5.5.

In experimental studies, flow direction is often set to be horizontal like such cases as θ_1=90° and 270°, in order to minimize the effects of buoyancy to the flow field. Considering the above figures and discussions, keeping the flow direction horizontal seems to be effective for this purpose. Especially if one focuses to the downstream of the reattachment point, buoyancy effects are small enough for the cases of θ_1=90° and 270° at $Ri^* = 0.03$ in which flow can be regarded to be a pure forced convective flow. Yet in the main recirculation region, where the flow is very slow, flow and temperature fields can be affected even at this relatively low buoyancy level. Experimental results must be examined very carefully there.

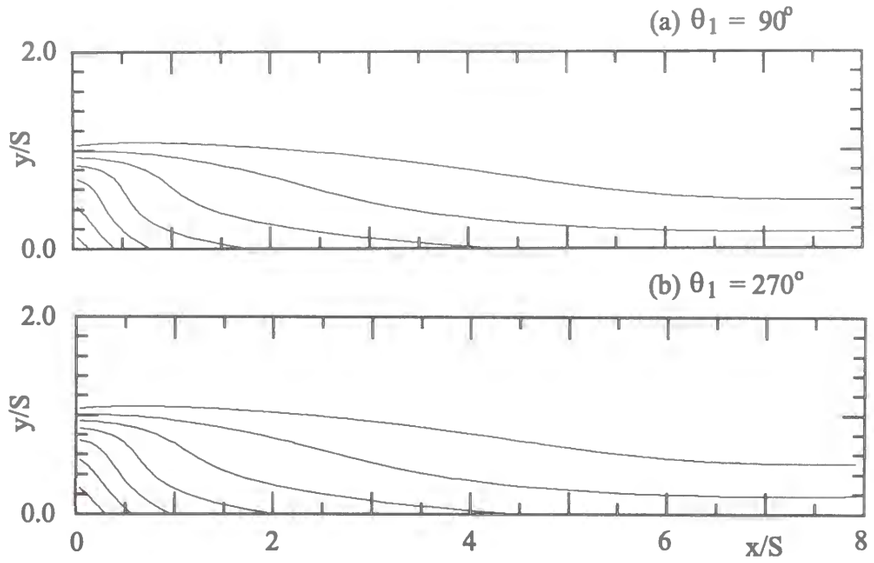

Figure 5.14: Temperature contours in the central plane z/WD=0.

5.3.3 Effects of the rolling angle θ_2

The effects of the rolling angle,θ_2, is studied here. θ_2 shown in Fig. 5.1 is changed from 0° to 180° while θ_1 is kept constant at 90°. This is schematically illustrated in Fig. 5.15. It should be noted that the side wall at $z/WD = 0.5$ is always on the higher level than the other side wall at $z/WD = -0.5$ in the range of $0° < \theta_2 < 180°$. The side wall at $z/WD = 0.5$ will then be called as the 'upper side wall' while the side wall at $z/WD = -0.5$ as the 'lower side wall' in this section. The cases of $\theta_2 = 0°$, 180° at $\theta_1 = 90°$ are equivalent to the cases of $\theta_1 = 90°$, 270° at $\theta_2 = 0°$. The flow and thermal fields in these two cases were found to be symmetric about the duct centerline. The results for other values of the rolling angle in the range $0° < \theta_2 < 180°$, on the other hand, show strong asymmetry. Therefore, the discussion will basically be focused on the cases in which the asymmetric flow and thermal fields are observed.

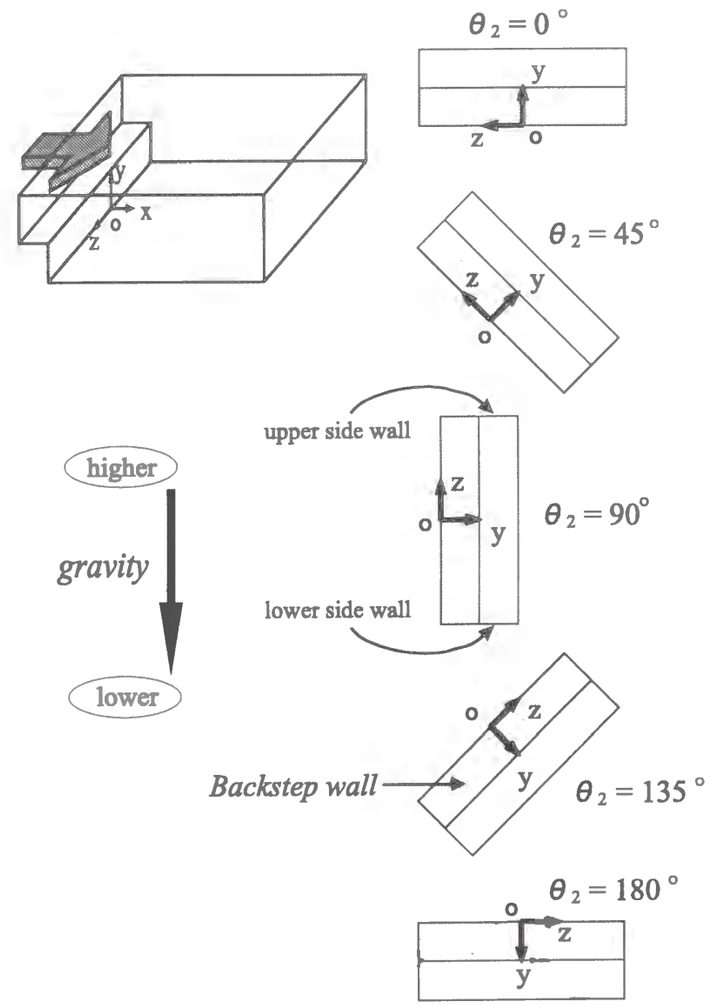

Figure 5.15: Change of duct posture with θ_2.

The contours of the skin friction coefficient,C_f, on the heated wall are presented in Fig. 5.16 for four cases of different values of θ_2 namely $\theta_2 = 15°$, $45°$, $90°$, $135°$. The upper side wall is drawn on the upper side of the paper in each figure so that an upper location in the figure corresponds to a higher location. Asymmetry of the contours about the duct centerline is evident in these figures. The borderline between the shaded area and the white area around $x/S \simeq 5$ corresponds to the position of reattachment point. It can be seen in Fig. 5.16 that the main flow reattaches the heated wall at a more upstream location in lower half of the duct ($z/WD < 0$) than in the other half.

The contours of the Nusselt number,Nu, on the heated wall corresponding to those of C_f illustrated in Fig. 5.16 are shown in Fig. 5.17. The gray tone level corresponds to the level of Nusselt number. Maximum Nusselt number,Nu_{max}, are obtained at two positions lying symmetrically with respect to the centerline only when θ_2=0°, 180° as has been observed in Fig. 5.9(b),(d). In all the other cases plotted in Fig. 5.17 Nu_{max} can be obtained only at one position, near z/WD=−0.5. Although a clear peak of Nusselt number is still observed near upper side wall (z/WD=0.5) in the case of θ_2=15°, no peak can be detected in other cases as is observed in Fig. 5.17.

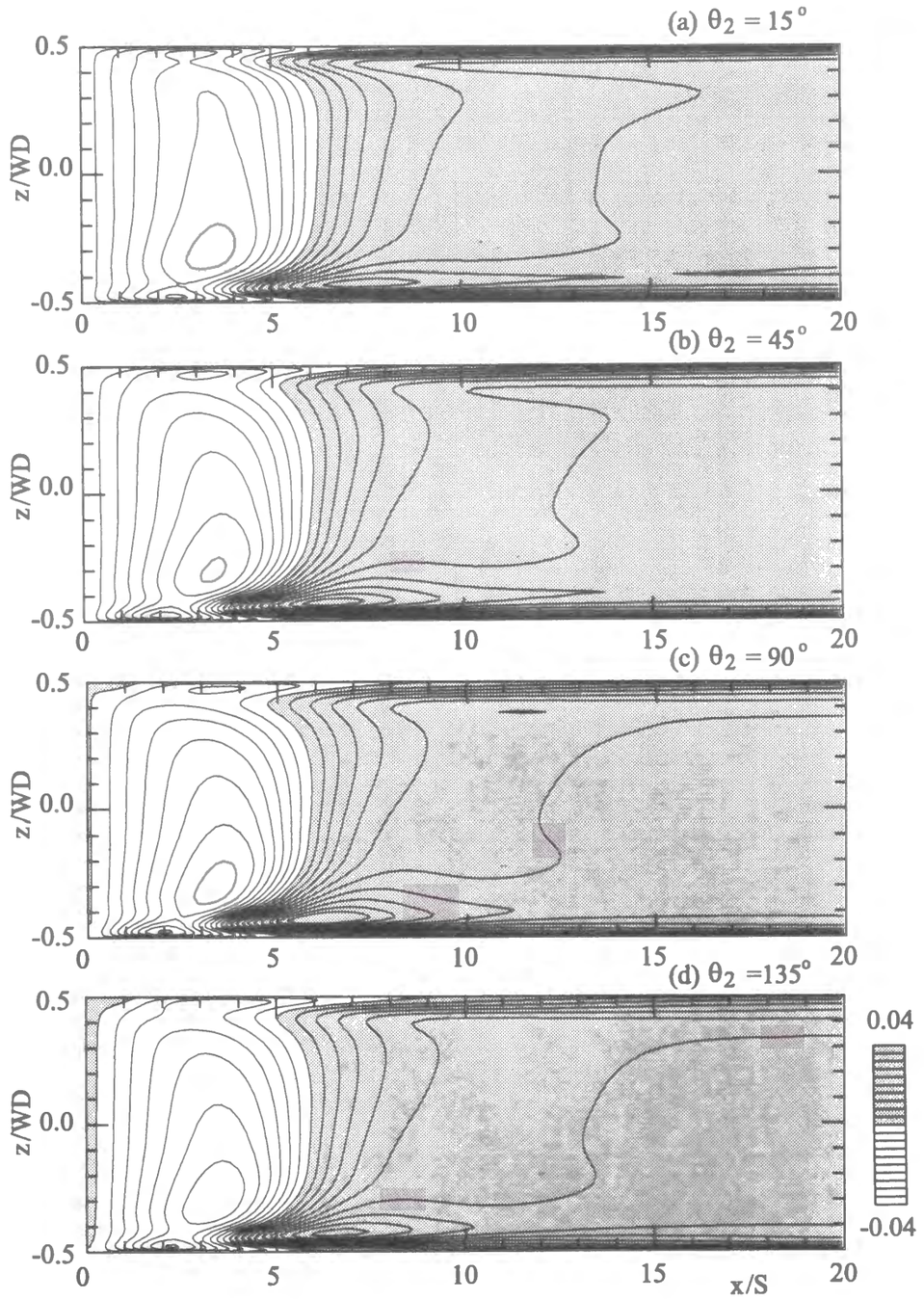

Figure 5.16: C_f contours on the heated wall.

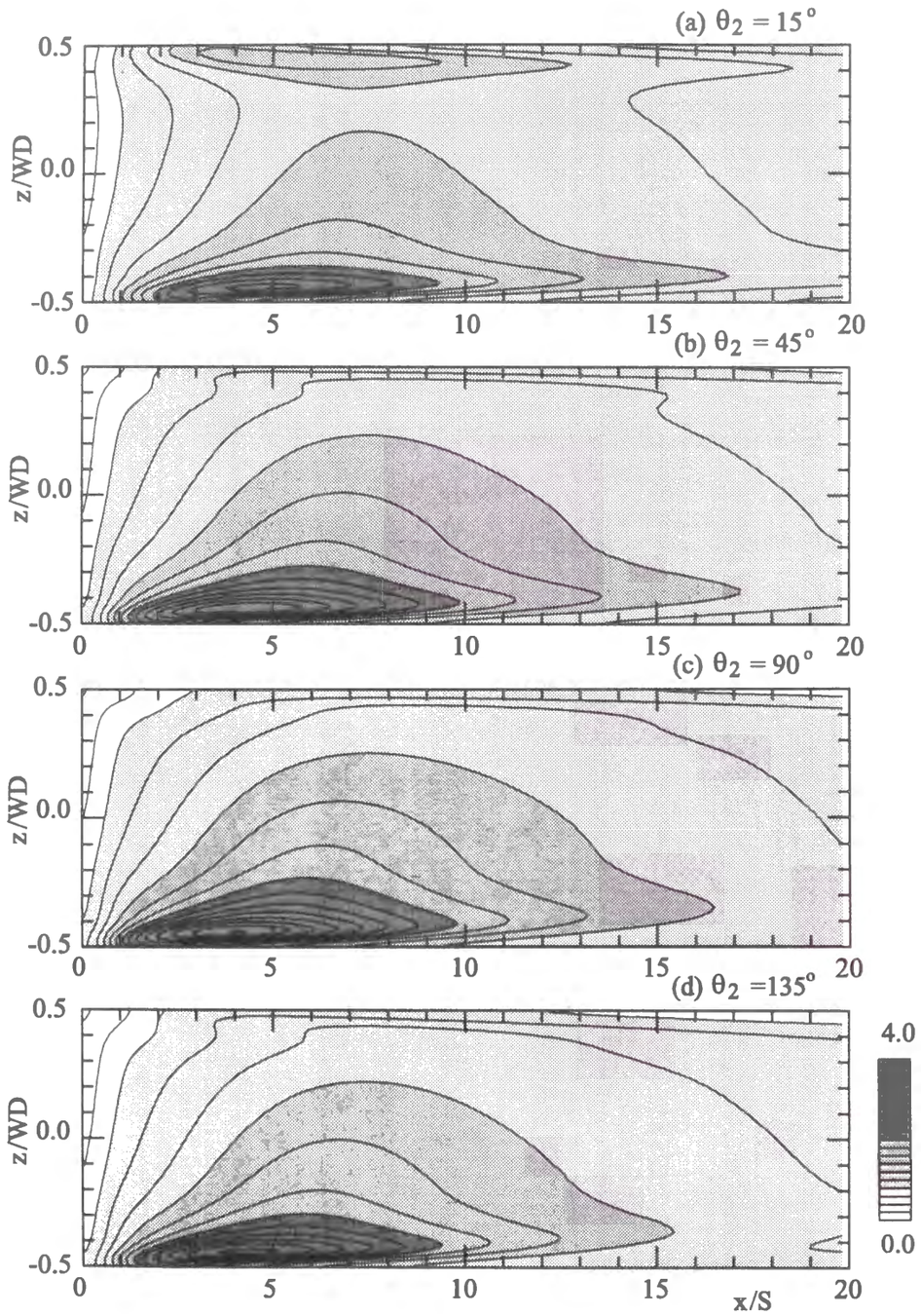

Figure 5.17: Nu contours on the heated wall.

Figure 5.18 $\sim$ Fig. 5.20 show the effects of θ_2 on the value of Nu_{max} and the streamwise and spanwise locations of the peak Nusselt number. It is seen in Fig. 5.18 and Fig. 5.19 that the maximum Nusselt number,Nu_{max}, appears at the most upstream position in the case θ_2=90° and takes the highest value. Figure 5.20 however shows that θ_2 has little effect on the spanwise position of the maximum Nusselt number.

It was shown in Chapter 3 that for the pure forced convection case the maximum Nusselt number is obtained at two positions near the side walls symmetrically located with respect to the centerline. This was because of the downwash flow which symmetrically exist at such spanwise positions. The downwash flow brings relatively cooler fluid to near the heated bottom wall, causing the temperature gradient large and consequently Nu high there. Therefore it would be natural to think that the effects of the rolling angle θ_2 on the downwash flow should be related to the spanwise asymmetry of the Nusselt number distribution observed in the Fig. 5.17.

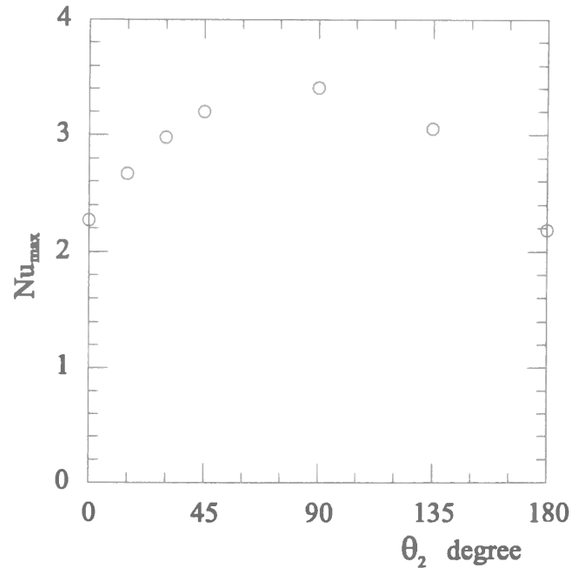

Figure 5.18: Effect of θ_2 on Nu_{max}.

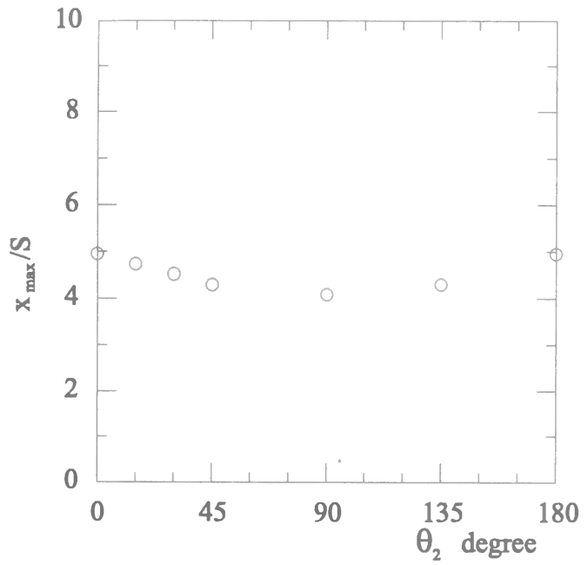

Figure 5.19: Effect of θ_2 on the streamwise position of Nu_{max}.

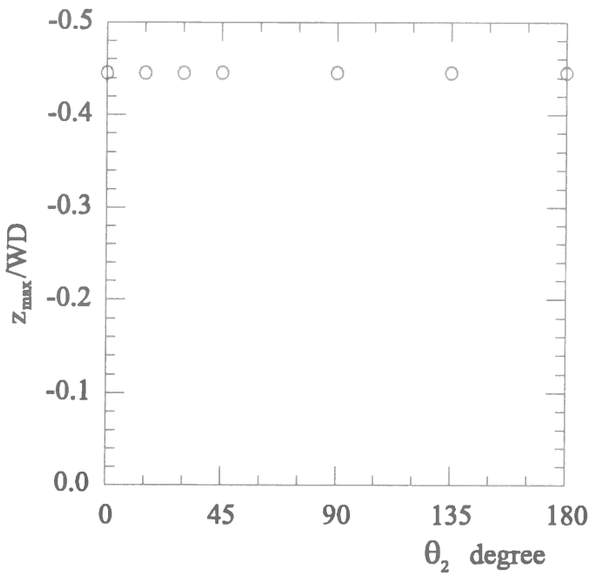

Figure 5.20: Effect of θ_2 on the spanwise position of Nu_{max}.

In order to discuss the three-dimensionality of the flow and thermal fields more in detail, velocity field in a y-z cross-section of the duct is examined at six different streamwise locations for the case of θ_2=90°. Velocity vector of the cross-sectional secondary flow and contour of the streamwise velocity U in the three streamwise cross-sectional planes are shown in Fig. 5.21. The shaded areas here correspond to the region where U velocity is positive. Figure 5.22, on the other hand, shows contours of the fluid temperature. The gray tone level correspond to the value of the fluid temperature. The upper side wall at $z/WD = 0.5$ is drawn on the left hand side of the paper in Fig. 5.21 and Fig. 5.22. The left hand side of these figures is higher than the right hand side.

At the location $x/S = 0.5$, as is observed in Fig. 5.22, temperature contour already shows asymmetry. In the region of $0 < y/S < 1$, where small velocity is expected to exist, the velocity vectors show that fluid flows upward. It is seen in Fig. 5.21 that U contour protrudes toward the heated wall at positions around $|z/WD| = 0.45$ at the location $x/S = 4.0$. This is caused by the downwash flow directed toward the heated wall observed at such spanwise positions. However, comparison of the velocity vectors at such spanwise positions shows that the downwash flow at $z/WD = -0.45$ is obviously more prominent than that at $z/WD = 0.45$. The temperature contours show that relatively cooler fluid approaches the heated wall at positions around $z/WD = -0.45$. This is effective to keep the wall temperature lower, therefore, to result in higher Nusselt number there. However, this low temperature region is not observed at the position around $z/WD = 0.45$. At the location $x/S = 15.0$, no prominent secondary flow in y-z plane is observed. Yet a careful observation suggests that there exists a large scale flow rotation. Fluid near the heated wall is directed upward (to the left side in the figures) while it is directed downward (to the right side in the figures) near the opposite unheated wall.

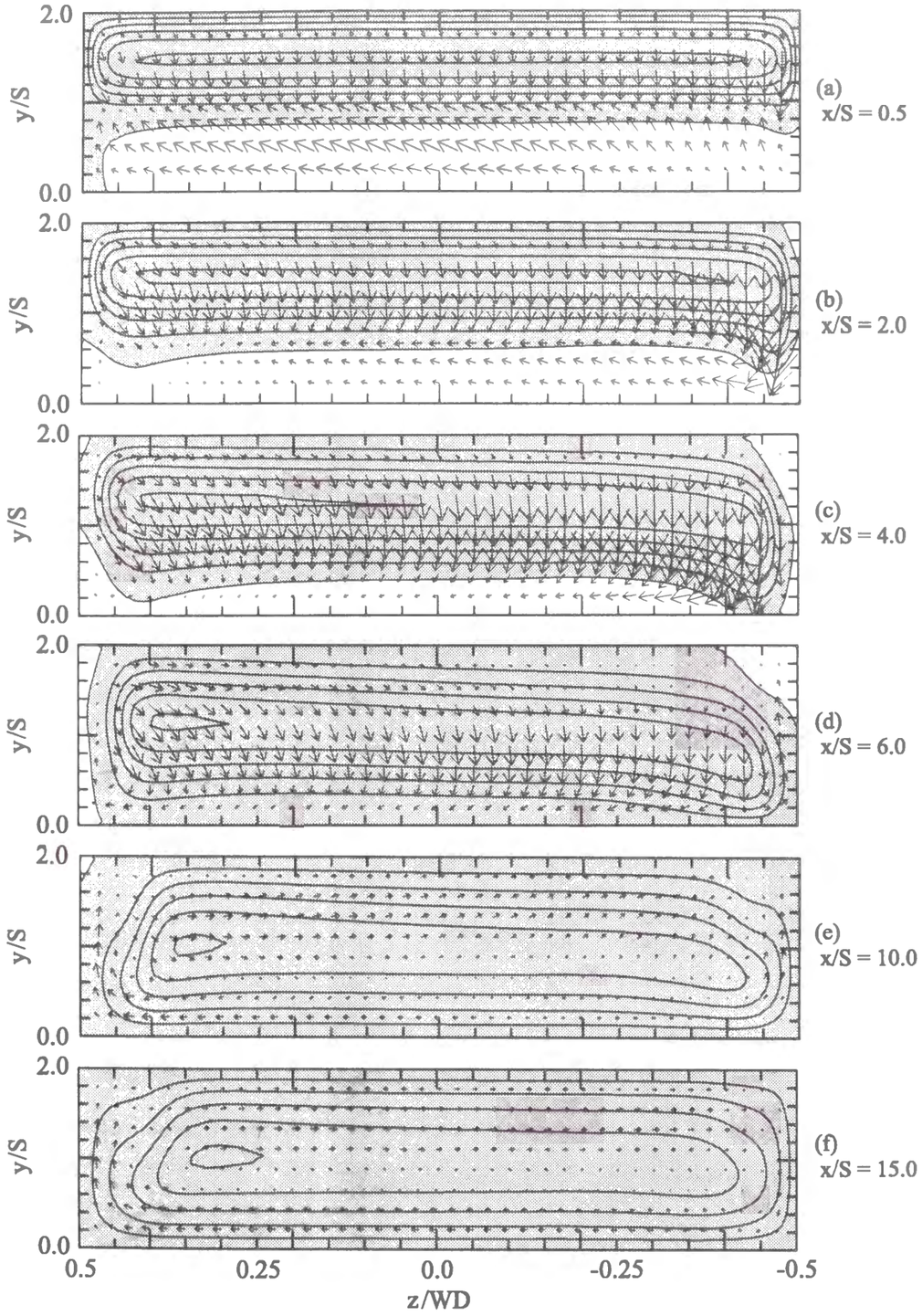

Figure 5.21: U contours and V-W vector plots.

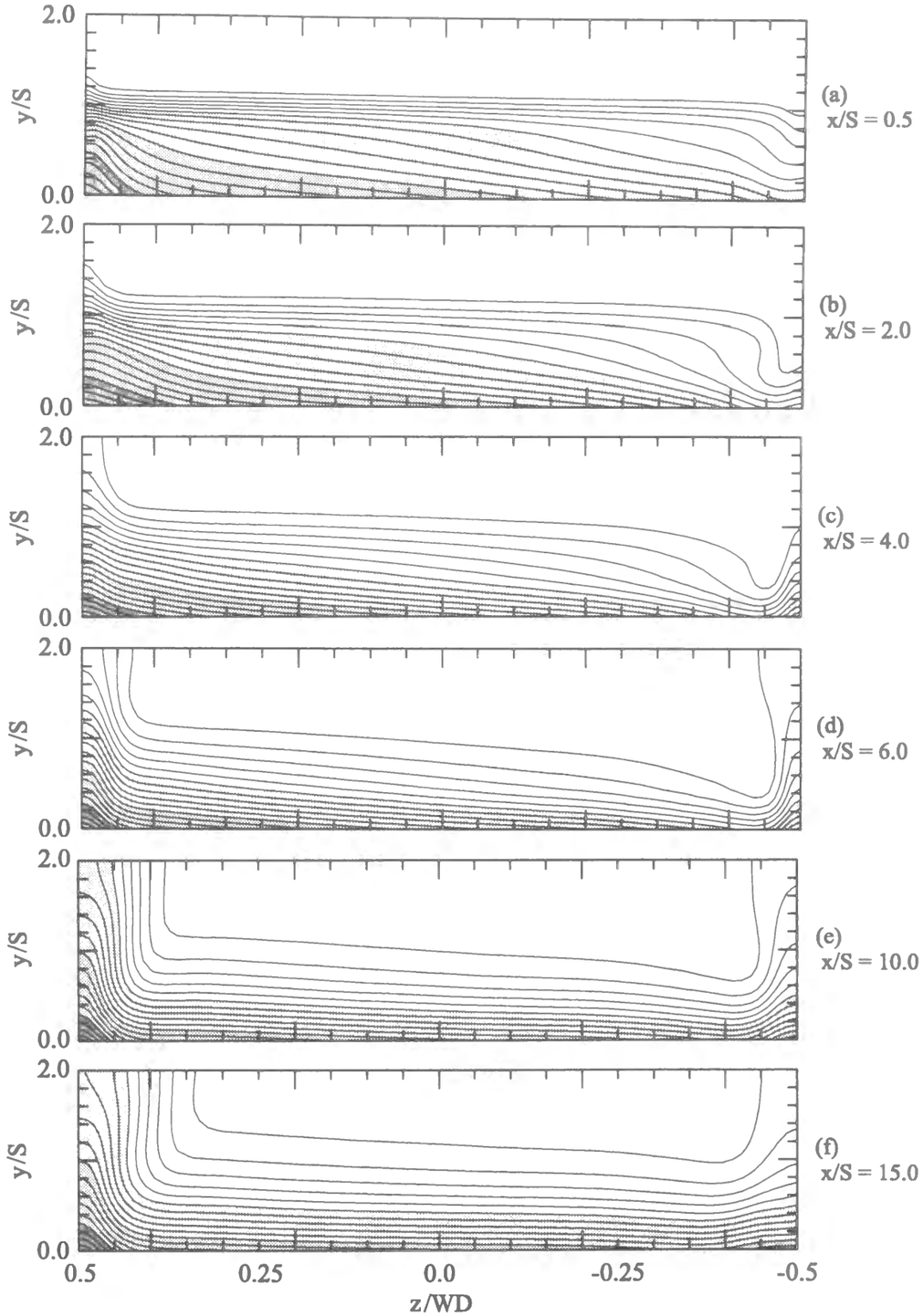

Figure 5.22: Temperature contours.

5.4 Conclusions

3-D numerical simulations have been carried out for mixed convective flows over a backward-facing step in a duct to study the effects of two inclination angles, the pitch angle and the rolling angle. The following conclusions were obtained.

(1) Both of pitch angle and rolling angle significantly affect the flow and thermal fields. The positions of x_r, x_p and x_s on the centerline of the heated wall shift with θ_1.

(2) When θ_1 is changed keeping θ_2 to be zero degree, positions of the maximum Nusselt numbers are symmetrically obtained at the positions on the heated wall near the two side walls, similar to the cases of pure forced convection. The value of maximum Nusselt number and its position are affected by the value of θ_1. The maximum Nusselt number appears at the most upstream position in the case θ_1=0° and takes the highest value. Buoyancy effects seems to be relatively small in the cases of horizontal flows, especially for the flow and thermal fields downstream the reattachment point.

(3) When θ_2 is changed keeping θ_1 to be 90 degrees, the flow and thermal fields become asymmetric about the duct centerline. The downwash flow directed toward the heated wall is prominent only near the lower side wall, resulting only one prominent peak of Nusselt number, Nu_{max}, there. The maximum Nusselt number appears at the most upstream position in the case θ_2=90° and takes the highest value. However θ_2 has little effect on the spanwise position of the maximum Nusselt number.

References

[1] Hong B.,Armaly, B.F. and Chen, T.S., *Laminar Mixed Convection in a Duct with a Backward-Facing Step: the Effects of Inclination Angle and Prandtl Number* , Int.J.Heat Mass Trans., vol.36-12, pp.3059-3067 (1993).

[2] Patankar, S.V., Ramadhyani, S. and Sparrow, E.M., *Effect of Circumferentially Nonuniform Heating on Laminar Combined Convection in a Horizontal Tube*, Trans.ASME: J.Heat Trans., Vol. 100, pp.63-70, (1978).

[3] Shah, R.K. and London, A.L., *Laminar Forced Convection in Ducts*, (1978), Academic Press.

[4] Lin J.T.,Armaly, B.F. and Chen, T.S., *Mixed Convection in Buoyancy-Assisting, Vertical Backward-Facing Step Flows*, Int.J.Heat Mass Trans., Vol.33-10, pp. 2121-2132, (1990).

[5] Abu-Mulaweh, H.I., Armaly, B.F. and Chen, T.S., *Measurements in Buoyancy-Opposing Laminar Flow over a Vertical Backward-Facing Step*, Trans.ASME: J.Heat Trans., Vol.116, pp. 247-249, (1994).

Chapter 6

The Effects of Aspect Ratio on Turbulent Flows over a Backward-Facing Step

6.1 Introduction

Previous chapters have basically dealt with laminar flows over a backward-facing step, taking into account the recent requirement for compact heat exchanger, where relatively low Reynolds number flows are expected to appear. However, there is no doubt that turbulent flows are widely used in many engineering devices. Because of its importance, flow separation and reattachment phenomena in turbulent flows have been studied by many researchers. Especially the backward-facing step flow was intensively investigated as a typical problem of this category. Turbulent flows over a backward-facing step have also played a central role in benchmarking the performance of turbulent models for separating and reattaching flows.

However all numerical works documented in the literature so far practically ignored the influence of side walls on the turbulent flow over a backward-facing step, assuming that the flow is two-dimensional. To what extent such two-dimensional simulations are relevant and accurate in predicting the actual three-dimensional flow is still unknown. Therefore,

it would be useful and important to carry out a full three-dimensional computation to investigate the three-dimensional effects on a supposedly two-dimensional flow and to verify the two-dimensional assumptions. de Brederode and Bradshaw [1] studied the effects of small aspect ratios on the general features of the 'external' flow ($ER \approx 1$) downstream of a backward-facing step. Their conclusion was that the side wall effects on the flow along the centerplane were negligible for aspect ratios (AR) greater than 10.

This chapter aims at studying the turbulent flows over a backward-facing step in a rectangular duct. Three-dimensional numerical simulations are carried out to study their three-dimensional structures of the flow and thermal fields. Two types of turbulent models are tested with the basic computational code described in Chapter 2.

6.2 Computational Conditions

6.2.1 Computational Domain

Figure 6.1 schematically illustrates the computational domain presently adopted for three-dimensional computations. Two-dimensional computations are carried out in a plane where $z/WD = 0.0$. The expansion ratio, $ER = H/(H - S)$, is kept constant at 2. The computational domain is set to cover $-5 \leq x/S \leq 30$ in the streamwise direction, where S is the step height.

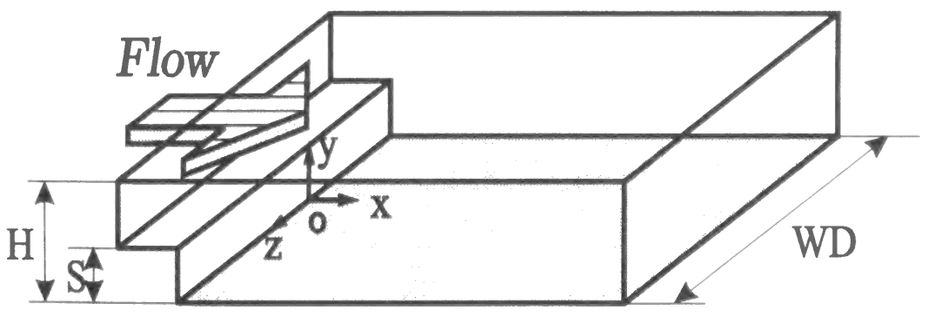

Figure 6.1: Computational domain.

6.2.2 Governing Equations

Because turbulence consists of random fluctuations of the various flow properties, a statistical approach is often adopted. The procedure introduced by Reynolds (1895) in which all quantities are expressed as the sum of mean and fluctuating parts is usually employed. Using this averaging concept, the following time-averaged form of governing equations are obtained:

$$\frac{D\rho}{Dt} = 0 \tag{6.1}$$

$$\frac{D\rho U_i}{Dt} = -\frac{\partial P}{\partial x_i} + \frac{\partial}{\partial x_j}\left(\mu\frac{\partial U_i}{\partial x_j} - \rho\overline{u_i u_j}\right) \tag{6.2}$$

$$\frac{D\rho T}{Dt} = \frac{\partial}{\partial x_j}\left(\frac{\mu}{Pr}\frac{\partial T}{\partial x_j} - \rho\overline{u_i\theta}\right) \tag{6.3}$$

Here, U_i and T are the time-averaged velocity component and temperature respectively. As can be seen from the equations above, the time-averaging process leads to the appearance of momentum fluxes, that act as apparent stresses ($-\rho\overline{u_i u_j}$, Reynolds stress) in Eq. (6.2), and heat flux components ($\overline{u_i\theta}$, turbulent heat flux) associated with the turbulent motion in Eq. (6.3). Equations for these quantities include additional unknown quantities. This illustrates the issue of closure, which is commonly handled through turbulence modeling.

6.2.3 Turbulent Models

The $k - \varepsilon$ model used in the present study can be classified under the group of Eddy Viscosity Models (EVM's) which is based on the Boussinesq's eddy viscosity concept. Following Boussinesq (1877), the EVM represents the effective turbulent shear stress as

$$-\rho\overline{u_i u_j} = \mu_t\left(\frac{\partial U_i}{\partial x_j} + \frac{\partial U_j}{\partial x_i}\right) - \frac{2}{3}\rho k\delta_{ij} \tag{6.4}$$

where μ_t is the eddy viscosity. The standard $k - \varepsilon$ model (high Reynolds number version) employs two transport equations for, k, the turbulent kinetic energy and its viscous dissipation rate, ε, respectively. The eddy viscosity is then represented by

$$\mu_t = \rho C_\mu \frac{k^2}{\varepsilon} \tag{6.5}$$

where the adopted length scale is $l = k^{3/2}/\varepsilon$, the dissipation length scale, and the velocity scale $k^{1/2}$, the velocity scale of energy containing eddies. C_μ is a scalar constant in an isotropic expression of eddy viscosity.

The standard $k-\varepsilon$ model has achieved notable success in predicting a wide range of flows related with industrial engineering applications and is still the most widely used and validated turbulence model. The high Reynolds number version mentioned here was originally devised for fully turbulent flows remote from the walls and hence cannot be applied to near-wall regions characterized by viscosity effects. Instead, wall functions are usually employed to specify the boundary condition at a position remote from the wall in place of the no-slip wall boundary condition given at the wall. However, the application of wall function is restricted to situations where a universal law (i.e. law of the wall) exists. Thus, the wall functions and high Reynolds number turbulence model cannot properly evaluate the separation of flows.

To take into account such viscous effects, Jones and Launder [2] devised a low Reynolds number version of $k-\varepsilon$ model by using the turbulent Reynolds number, R_t, as well as introducing some additional modeled terms. Actually, Launder and Sharma [3] 'retuned' the model's closure constants which are presently used by many researchers. The modeled equations of this well-known Launder-Sharma model (LS model) are as follows:

$$\frac{D\rho k}{Dt} = \frac{\partial}{\partial x_j}\left\{\left(\mu + \frac{\mu_t}{\sigma_k}\right)\frac{\partial k}{\partial x_j}\right\} + P_k - \rho\left(\tilde{\varepsilon} + D\right) \tag{6.6}$$

$$\frac{D\rho\tilde{\varepsilon}}{Dt} = \frac{\partial}{\partial x_j}\left\{\left(\mu + \frac{\mu_t}{\sigma_\varepsilon}\right)\frac{\partial \tilde{\varepsilon}}{\partial x_j}\right\} + \frac{\tilde{\varepsilon}}{k}\left(C_{\varepsilon 1} f_1 P_k - C_{\varepsilon 2}\rho f_2 \tilde{\varepsilon}\right) + E \tag{6.7}$$

where

$$P_k = -\rho\overline{u_i u_j}\frac{\partial U_i}{\partial x_j} = \frac{1}{2}\mu_t\left(\frac{\partial U_i}{\partial x_j} + \frac{\partial U_j}{\partial x_i}\right)^2 ,$$

$$D = 2\nu\left(\frac{\partial\sqrt{k}}{\partial x_j}\right)^2 ,$$

$$\varepsilon = \tilde{\varepsilon} + 2\nu\left(\frac{\partial\sqrt{k}}{\partial x_j}\right)^2 ,$$

$$E = 2\nu\mu_t\left(\frac{\partial^2 U_i}{\partial x_j \partial x_l}\right)^2 ,$$

$$f_1 = 1.0 \ , \ f_2 = 1 - 0.3exp\left(-\tilde{R}_t^{\,2}\right) \ , \ C_{\varepsilon 1} = 1.14$$

$$C_{\varepsilon 2} = 1.92 \ , \ \sigma_\varepsilon = 1.3, \ , \ \sigma_k = 1.0$$

Eddy viscosity is expressed as,

$$\mu_t = \rho C_\mu f_\mu \frac{k^2}{\tilde{\varepsilon}} \quad \text{and} \tag{6.8}$$

$$f_\mu = \exp\left(\frac{-3.4}{\left(1 + \tilde{R}_t/50\right)^2}\right) \ , \ C_\mu = 0.09$$

where

$$\tilde{R}_t = \frac{\rho k^{\frac{1}{2}}\ k^{\frac{3}{2}}/\tilde{\varepsilon}}{\mu} = \frac{\rho k^2}{\mu\tilde{\varepsilon}}$$

The quantity $\tilde{\varepsilon}$ here can be interpreted as the isotropic part of the dissipation, and solving an equation for $\tilde{\varepsilon}$ simplifies the wall boundary condition of the equation for dissipation rate since $\tilde{\varepsilon} = 0$ at the wall. An extended three-dimensional form of the k and $\tilde{\varepsilon}$ equations are described in the Appendix. The extended form of the momentum equations are also included there for reference purposes.

LS model + Yap Correction

The LS model described above has been used to predict a wide range of parallel flows satisfactorily well. However, one of its main defects is that it gives far too large near-wall length-scales in impinging or recirculating flows. As a remedy to this, Yap [4] introduced an extra source term, Y_ε, (Yap correction) into the dissipation equation:

$$Y_\varepsilon = max\left[0.83\left(\frac{k^{3/2}}{2.5\tilde{\varepsilon}y_n}-1\right)\left(\frac{k^{3/2}}{2.5\tilde{\varepsilon}y_n}\right)^2\frac{\tilde{\varepsilon}^2}{k},0\right] \tag{6.9}$$

Here, y_n refers to the normal distance from the wall. The main idea that Yap adopted is that if the predicted dissipation length-scale is much larger than the prescribed local equilibrium one, the additional source term could act to control and reduce the length-scale. The Yap correction is regarded as a powerful measure to reduce near-wall turbulent length-scale in a separated flow, particularly near the flow reattachment point around where the maximum heat-transfer occurs [5]. The modified LS model combined with the Yap correction term will be tested in the present study.

CSL model (2-eq. NLEVM)

Models like the LS model are classified as linear eddy viscosity models (hereafter referred as LEVM). It is known that such conventional LEVM's have severe defects in predicting swirl, stagnation and recirculation of flows, streamline curvature effects, flows in duct with secondary motions, three-dimensional flows and flows with boundary-layer separation etc. And for wall heat transfer, it is generally the normal stress perpendicular to the surface that can play quite an important role. LEVM's can present the normal stress only under the assumption of isotropy of normal stresses. These problems are the result of the crude assumptions adopted in the modeling.

Such shortcomings of LEVM's can be reduced by using a non-linear EVM (hereafter referred as NLEVM) approach recently proposed by several researchers and investigators. With a NLEVM approach, a more appropriate functionals of the Reynolds stress tensor is

achieved without introducing any additional differential equations. It is assumed that the Boussinesq approximation is the leading term to appear in the functionals.

Many quadratic stress-strain relations have been proposed in recent years to extend the applicability of LEVM's at modest computational cost. However, comparison shows that none achieves much greater width of applicability. The UMIST group recently proposed a new non-linear model (Craft, Suga and Launder) [6], hereafter referred as CSL model, in which strain and vorticity tensors to the cubic level are retained. Comparisons over a range of complex shear flows have shown that the new model performs consistently better than any LEVM's in capturing effects of streamline curvature with certain degrees of accuracy.

The newly proposed model is actually the result of several modifications and improvements made to the LS model. In order to improve predictions obtained by EVM's, the UMIST group introduced sensitivity to the strain and vorticity invariants in modeling C_μ and the viscous source term of the ε equation. A non-linear $k-\varepsilon$ EVM, including cubic products of the velocity gradient tensors, was then developed. Most of the existing $k-\varepsilon$ non-linear EVM's include up to the quadratic terms in the stress-strain relation, although quadratic terms do not have any effect on the mean velocity of swirling flows or flows with streamline curvature. It was found that inclusion of higher order (cubic) terms was essential to capture the characteristics of these flows [6].

The modeled terms and closure coefficients recommended by the UMIST group are documented below:

$$\begin{aligned}\rho\overline{u_iu_j} &= \frac{2}{3}k\rho\delta_{ij}-\mu_tS_{ij}\\ &+c_1\mu_t\frac{k}{\tilde{\varepsilon}}\left(S_{ik}S_{kj}-\frac{1}{3}S_{kl}S_{kl}\delta_{ij}\right)\\ &+c_2\mu_t\frac{k}{\tilde{\varepsilon}}\left(\Omega_{ik}S_{kj}+\Omega_{jk}S_{ki}\right)\\ &+c_3\mu_t\frac{k}{\tilde{\varepsilon}}\left(\Omega_{ik}\Omega_{jk}-\frac{1}{3}\Omega_{lk}\Omega_{lk}\delta_{ij}\right)\\ &+c_4\mu_t(\frac{k}{\tilde{\varepsilon}})^2\left(S_{ki}\Omega_{lj}+S_{kj}\Omega_{li}\right)S_{kl}\end{aligned}$$

$$
\begin{aligned}
&+c_5\mu_t(\frac{k}{\tilde{\varepsilon}})^2\left(\Omega_{il}\Omega_{lm}S_{mj}+S_{il}\Omega_{lm}\Omega_{mj}-\frac{2}{3}S_{lm}\Omega_{mn}\Omega_{nl}\delta_{ij}\right)\\
&+c_6\mu_t(\frac{k}{\tilde{\varepsilon}})^2 S_{ij}S_{kl}S_{kl}\\
&+c_7\mu_t(\frac{k}{\tilde{\varepsilon}})^2\Omega_{ki}\Omega_{kj}\Omega_{kl}
\end{aligned}
\tag{6.10}
$$

$$
\begin{aligned}
\text{where}\quad S_{ij} &= \left(\frac{\partial U_i}{\partial x_j}+\frac{\partial U_j}{\partial x_i}\right)\ ,\quad \Omega_{ij}=\left(\frac{\partial U_i}{\partial x_j}-\frac{\partial U_j}{\partial x_i}\right)\\
\tilde{S} &= \frac{k}{\tilde{\varepsilon}}\sqrt{S_{ij}S_{ij}/2}\ ,\quad \tilde{\Omega}=\frac{k}{\tilde{\varepsilon}}\sqrt{\Omega_{ij}\Omega_{ij}/2}\\
\mu_t &= \rho C_\mu f_\mu \frac{k^2}{\tilde{\varepsilon}}
\end{aligned}
$$

Table 6.1: Model Coefficients for 2 Eq.-NLEVM

	c_1	c_2	c_3	c_4	c_5	c_6	c_7
2-eq. NLEVM	-0.1	0.1	0.26	$-10{C_\mu}^2$	0	$-5{C_\mu}^2$	$5{C_\mu}^2$

Table 6.2: Model functions for 2 Eq.-NLEVM

C_μ	f_μ	η
$\frac{0.3\left[1-exp\{-0.36exp(0.75\eta)\}\right]}{1+0.35\eta^{1.5}}$	$1-exp\left\{-(\frac{\tilde{R}_t}{90})^{1/2}-(\frac{\tilde{R}_t}{400})^2\right\}$	$max(\tilde{S},\tilde{\Omega})$

$\tilde{\varepsilon}$-equation

$$
\frac{D\rho\tilde{\varepsilon}}{Dt} = \frac{\partial}{\partial x_j}\left\{\left(\mu+\frac{\mu_t}{1.3}\right)\frac{\partial\tilde{\varepsilon}}{\partial x_j}\right\}+c_{\varepsilon1}P_k\frac{\tilde{\varepsilon}}{k}-\rho c_{\varepsilon2}\frac{\tilde{\varepsilon}^2}{k}+P_{\varepsilon3}+\rho Y_\varepsilon
$$

Table 6.3: Model Terms/Coefficients for $\tilde{\varepsilon}$ equation

$c_{\varepsilon1}$	$c_{\varepsilon2}$	$P_{\varepsilon3}$
1.14	$1.92\left\{1-0.3exp(-{\tilde{R}_t}^2)\right\}$	$0.0022\frac{\tilde{S}\mu_t k^2}{\tilde{\varepsilon}}\left(\frac{\partial^2 U_i}{\partial x_k\partial x_l}\right)^2,\ \tilde{R}_t\le 250$

Y_ε
$max\left[0.83\left(\frac{k^{3/2}}{2.5\tilde{\varepsilon}y_n}-1\right)\left(\frac{k^{3/2}}{2.5\tilde{\varepsilon}y_n}\right)^2\frac{\tilde{\varepsilon}^2}{k},0\right]$

Full expressions of Eq. (6.10) for each specific combination of i and j are included in the Appendix.

6.2.4 Turbulent Heat Flux Model

In direct analogy between the turbulent heat transport and momentum transport, the turbulent heat flux is often assumed to be proportional to the temperature gradient, i.e.

$$
\overline{u_i\theta} = -\alpha_t\frac{\partial T}{\partial x_i} \tag{6.11}
$$

where α_t is the turbulent thermal diffusivity. Like μ_t, α_t is not a fluid property but depends on the state of turbulence. The Reynolds analogy between heat transport and momentum transport suggests that α_t is closely related to μ_t,

$$
\alpha_t = \frac{\mu_t}{\rho Pr_t} \tag{6.12}
$$

where Pr_t is the turbulent Prandtl number. For gaseous fluids, this value is assumed to be constant taking the value of 0.9. This value is used in the present study.

6.2.5 Boundary Conditions

In order to assume the inlet profiles as close as possible to the actual ones, preliminary computations were first carried out for a duct flow employing the same turbulence model as the one described above. The obtained results are then used as the inlet conditions at the upstream boundary ($x/S=-5$). Boundary layer thickness is set equal to $\delta/S\simeq 0.16$ at the inlet. All variables except for temperature are set equal to zero at all wall surfaces. The wall downstream of the step is assumed to be heated at a uniform heat flux, while all other walls are treated thermally adiabatic. Streamwise gradients of all quantities at the duct exit are set to be zero. The location of the outlet is selected at $x/S=30$ far away from the step so that zero streamwise change of the variables can be assumed without any serious toleration.

6.2.6 Computational Conditions

There are various principal parameters that affect the flow past a backward-facing step. Eaton and Johnston [7] identified five main independent parameters in their review paper on subsonic turbulent flow reattachment, namely, (i) initial boundary-layer state, (ii) the initial boundary layer thickness, (iii) freestream turbulence, (iv) pressure gradient, (v) aspect ratio.

The present study is undertaken mainly to investigate the three-dimensionalityof such a flow. To validate and to assess the computational procedures and the adopted models used in the present work, 2-D computations are first carried out to compare with the experimental and DNS results previously reported in the literatures. Computational conditions for these calculations will be described in the relevant sections and will not be described here. The 3-D simulations performed in the present work are carried out under the conditions to be as close as to that of the flow field studied by Papadopoulos [8]. The flow studied by Papadopoulos had a Reynolds number of 26,500. The Reynolds number is based on the freestream mean velocity at the inlet, U_{ref} and step height,S. To simulate the same flow at the same Reynolds number, a large number of grid points with very fine, densely concentrated grids near the wall should be required. This necessitates large computing costs and would not be very economical. Therefore, a Reynolds number of 5,200 is chosen instead. An average number of grid points of approximately $140 \times 60 \times 70$ is employed in the present study employing the LS + Yap model. Computation was found to persistently diverge when the same number of grid points was used with the CSL model. A coarser mesh of about $100 \times 40 \times 40$ is then adopted to cope with this problem. 3-D computations are carried out for two different values of the aspect ratio,$AR = 4$ and 12. One is greater than 10 and the other smaller than 10 the aspect ratio suggested by de Brederode and Bradshaw [1]. The computational conditions are summarized below.

- Reynolds number, $Re = \frac{U_{ref}S}{\nu} = 5,200$
- Boundary layer thickness at the inlet i.e $\delta/S \simeq 0.16$ at $x/S = -5$

- Expansion Ratio, $ER = \frac{H}{H-S} = 2$
- Aspect Ratio, $AR = \frac{WD}{S} = 4$ and 12

In addition to the above, mean skin friction coefficient, mean Stanton number and mean Nusselt number are defined as below:

$$\text{Mean skin friction coefficient}, C_f = \tau_w / \left(\rho U_{ref}^2/2\right) \tag{6.13}$$

$$\text{Mean Stanton number}, St = \frac{q_w}{[\rho C_P U_{ref}(T_w - T_{in})]} \tag{6.14}$$

$$\text{Mean Nusselt number}, Nu = \frac{q_w S}{\lambda(T_w - T_{in})} \tag{6.15}$$

τ_w, q_w, T_w and T_{in} used here refer to the time mean values of the wall shear stress, wall heat flux, wall temperature and inlet temperature respectively.

6.3 Results and Discussion

6.3.1 Model Assessment

As the first step, two-dimensional computations are carried out to see the performance of the models adopted. The results are then compared with the experimental and DNS results reported in the literatures. LS model calculations are also carried out for comparison purposes. The experimental results of Jovic and Driver [9] are selected in the first comparison with the flow field computations. Results of the direct numerical simulation by Le, Moin and Kim [10] case are also available for this particular and can be used as the additional data available for model validation and assessment. As for the thermal field, the experimental data of Vogel and Eaton [11] are compared next with the calculated results in the present study. The experiment was performed at constant heat flux condition at the bottom wall. Experimental and computational conditions of the cases mentioned here are summarized in Table 6.4.

Table 6.4 : Experimental and DNS conditions and results

	ER	Re_S	Inlet Condition , δ/S	x_r/S
1. Jovic and Driver (1995) [9] [Exp.]	1.2	5000	1.2	6.00
2. Le *et al* (1993) [10] [DNS]	1.2	5100	1.0	6.00
3. Vogel and Eaton (1985) [11] [Exp.]	1.25	28000	1.1	6.67

Grid-independent tests were carried out for all three models and the mesh size stated below were judged to be sufficiently fine to give reasonable results. It was also confirmed that the first grid point from the bottom wall was located at $y^+ \approx 1.0$ for all cases.

Flow field

The solution domain adopted in this two-dimensional computation covers the region from $10S$ prior to the step and to $32S$ downstream from the step. The presently used mesh has 160 x 83 grid cells. In order to achieve the inlet profiles as close as possible to the experimental and DNS conditions, a preliminary computation is first carried out for a channel flow with uniform inlet conditions. The results obtained at a streamwise location where the computed results well correspond with the inlet experimental conditions i.e. $\delta/S \approx 1.2$ (δ : boundary layer thickness), are used as the inlet conditions at $x/S = -10$ for the two-dimensional backstep flow computations. It was expected that steady-state results would be obtained for all the three computations. However, it was not possible to arrive at a steady-state solution for the case employing the CSL model. The calculated flow became unsteady, exhibiting a periodic, purely harmonic vortex formation. Such unsteadiness of the flow was also observed in the experiment of Jonhston [12] and also in the computation by Lasher [13]. Figure 6.2 shows the time trace of U monitored at two locations. Clearly the flow can be considered periodic. Time averaged results will be shown in the figures hereafter for the CSL cases.

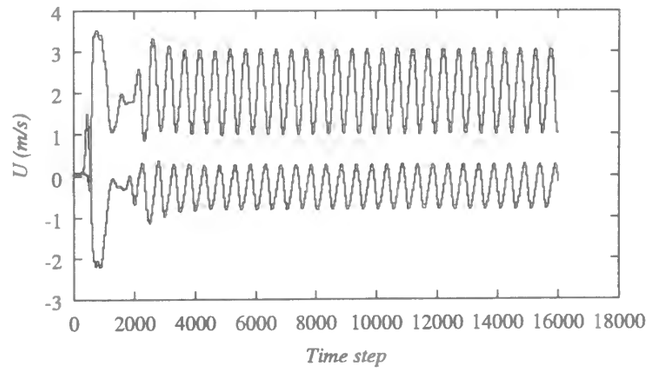

Figure 6.2: Time trace of U monitored at 2 locations within the recirculation region (CSL model)

A few selected comparisons of the performance of the three models with experimental and DNS results are shown in Fig. 6.3 and Fig. 6.4. U_{ref} used in normalization refers to the inlet freestream mean velocity. Comparison for the mean skin friction coefficient, C_f is shown in Fig. 6.3 while Fig. 6.4 compares the predictions of mean streamwise velocity, Reynolds normal stresses and Reynolds shear stress. Since different models give different mean reattachment lengths, x_r, a normalized streamwise distance, X^* is used in Fig. 6.4. X^* used here is defined as $(x - x_r)/x_r$, where x is the streamwise distance and x_r, the mean reattachment length obtained with each model. The mean reattachment point is defined as a location where the skin friction coefficient change its sign from negative to positive. The mean reattachment length,x_r, predicted using the three models is $4.26S$ with the original LS model, $6.02S$ with the LS + Yap model and $7.60S$ for the CSL model. Since it was impossible to obtain steady-state solutions with the CSL model, the time-averaged value is used. It is clear from Fig. 6.3 that the mean reattachment length is significantly overpredicted with the CSL model. In contrast, the LS + Yap model shows excellent agreement on the reattachment length with the DNS data. The LS model however considerably underpredicts the reattachment length by approximately 29% as is expected. In Fig. 6.4 it can be seen that the presently calculated mean streamwise velocity, U, streamwise component of the Reynolds normal stress, u' and Reynolds shear stress, $\overline{uv}$ with the experimental and DNS data counterparts are generally quite good for both LS + Yap and CSL models. The non-linear CSL model reproduces the best transverse component of the Reynolds normal stress, v' agreeing rather well with the experimental profile too. In contrast, both the LS model and the LS + Yap model overpredict v'. This is due to the inherent isotropic nature of the models.

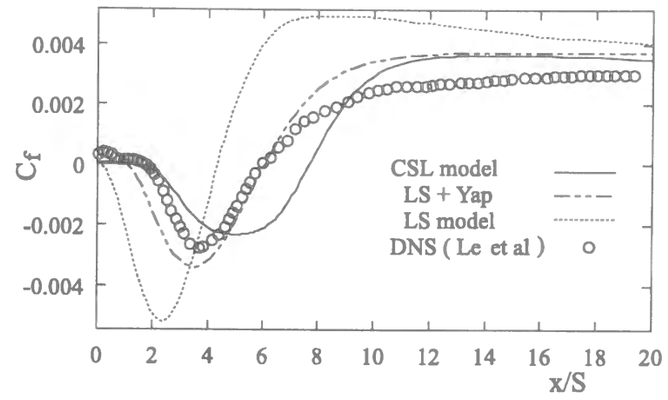

Figure 6.3: Mean skin-friction coefficient downstream of the step

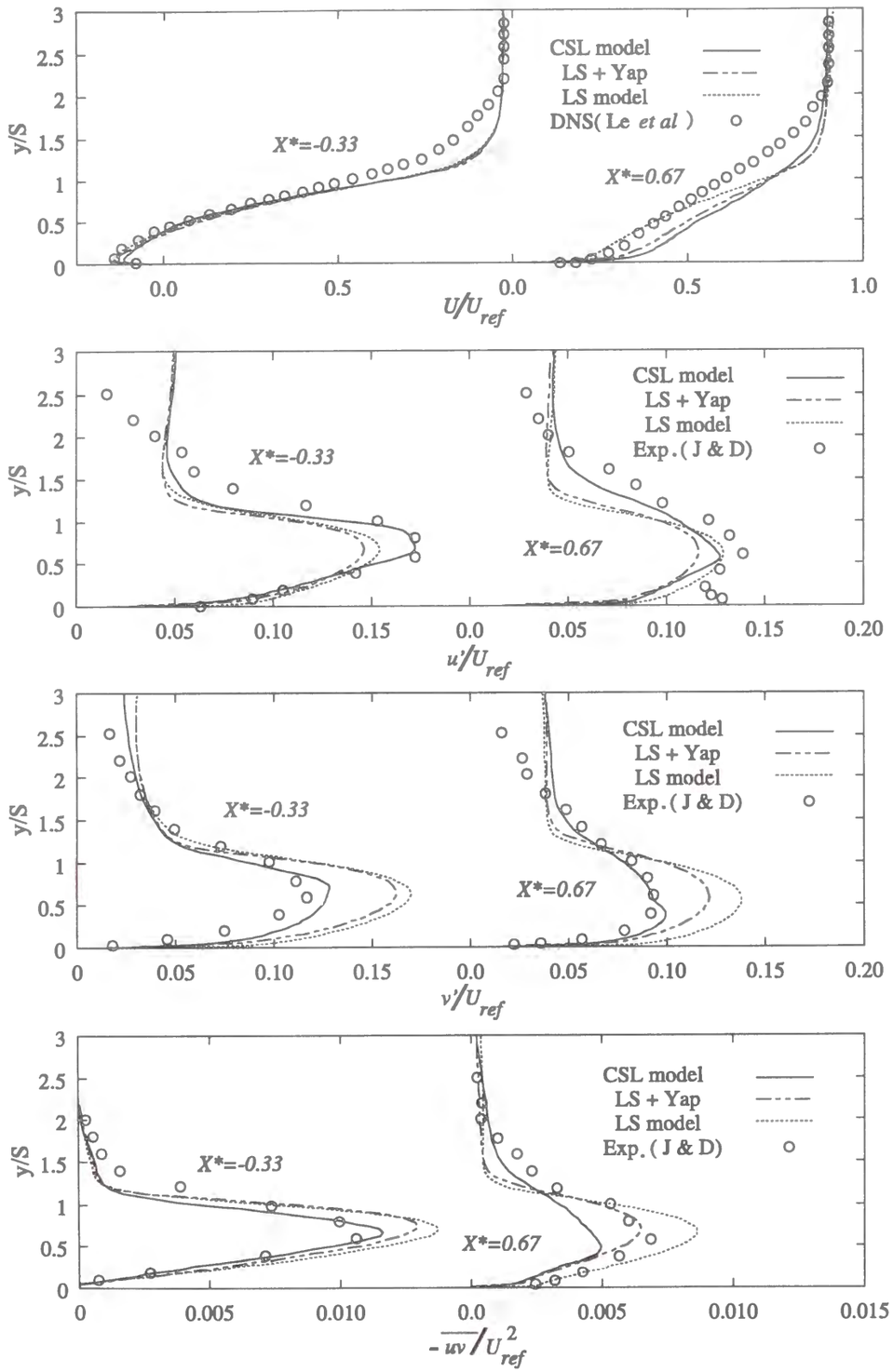

Figure 6.4: Comparison of the three models with experimental data of Jovic & Driver (J & D) and DNS data of Le *et al*, $(X^* = \frac{x-x_r}{x_r})$

Thermal field

The inlet and outlet of the computational domain are located $5S$ upstream and $30S$ downstream of the step for the following thermal field computation. The mesh used has 189 x 120 grid cells for all three models.

For the thermal field predictions, it is clear from Fig. 6.5 that the LS model over-predicts the mean Stanton number,St by a factor of approximately three and this reconfirms the conclusion drawn in the previous studies by other researchers [5] employing the LS model. The Yap correction term, regarded as a powerful measure to reduce near-wall turbulent length scale in a separated flow, in particular near the flow reattachment point where the maximum heat transfer occurs, is able to offer remarkable improvements over the original LS model, although it still suffers from slight overprediction. Among the three models, the CSL model offers the best predictions of thermal quantities. A better prediction of heat transfer from a wall using the CSL model seems to be related to a better prediction of v' observed earlier. It is believed that heat transfer is generally closely associated to the normal stress component perpendicular to the surface, i.e. v'.

Results obtained from all the three models also show that the turbulent heat transfer coefficient reaches a maximum value in the reattachment region. The approximate maximum Stanton number position predicted by the LS + Yap model is $6.0S$ while the same position is estimated to be at $8.0S$ with the CSL model. Interestingly, the CSL model predicts the point of maximum heat transfer coefficient slightly downstream of the mean reattachment point while the LS + Yap model predicts the same point to be slightly upstream. For axisymmetric separating and reattaching flows, Kang [14,15], Suzuki [16] reported that the maximum heat transfer position was located upstream of the reattachment point.

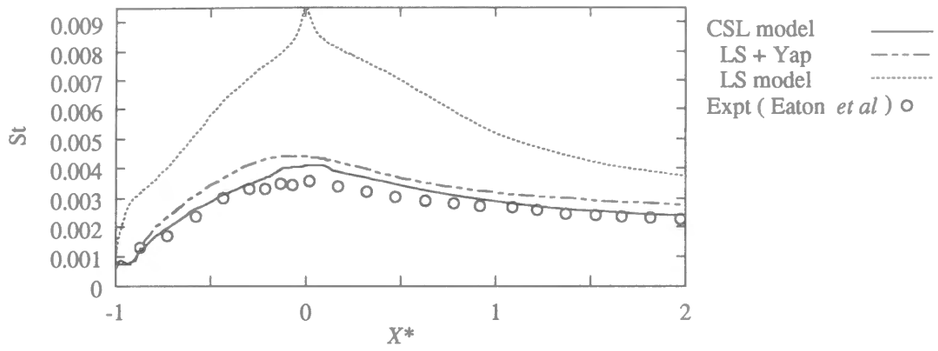

Figure 6.5: Mean Stanton number profile

Through the two-dimensional simulation results described above, it is found that the LS + Yap model gives a very good prediction of the mean reattachment length,x_r, within approximately 3% accuracy when compared with experimental or DNS data, while the CSL model tends to predict a longer x_r by about 15%. Although both models are capable to reproduce mean streamwise velocity profiles, there are differences in the predictions of Reynolds stresses between the two models. It seems that a better prediction of v' can be achieved using the CSL model, which is probably the reason for the better prediction of the Stanton number profile by the CSL model compared with the LS + Yap model. The LS + Yap model predicts the position of the maximum heat transfer coefficient to be located upstream the reattachment point while the CSL model predicts otherwise.

6.3.2 Comparison between 2-D and 3-D Simulation Results

3-D computations respectively using the LS + Yap model and the CSL model are now performed at an aspect ratio (AR) of 12, a value greater than 10, the value suggested by de Brederode and Bradshaw [1] to be large enough to acquire two-dimensional nature of the flow in the central part of the duct. Therefore, the quantities along the centerline calculated in three-dimensional computation can be compared with the 2-D computation results. A total grid number of $100 \times 40 \times 45$ is allocated in the computational domain. The

first grid point from the bottom wall is located at $y^+ \approx 3.5$. It should be noted here that all 3-D computation results to be presented hereafter are all time mean values averaged over an arbitrary long period of time. The 2-D simulations discussed above were actually performed at the same computational conditions with the grid size employed in the x-y plane of the 3-D computations.

Comparison of C_f distribution

The LS + Yap model predicts exactly the same reattachment length of $7.93S$ for both 2-D and 3-D simulations. This is also in good agreement with the experimental value of $8.2S$ [8]. The corresponding experiment was carried out at a Reynolds number approximately five times higher. This may explain the slightly longer reattachment length observed in the experiment. The present CSL model predicts a longer reattachment length of $9.55S$ for both 2-D and 3-D calculations. Reattachment length predicted in both of 2-D and 3-D computations described here are summarized in Table 6.5.

Table 6.5 : Mean reattachment lengths.

	2-D	3-D
LS + Yap model	$7.93S$	$7.93S$
CSL model	$9.55S$	$9.55S$
Experiment of Papadopoulos		$8.2S$ ($AR > 10$)

Velocities Comparison

Figures 6.6 and 6.7 compare mean velocity and fluctuation quantities obtained from 2-D computations at various streamwise locations and the centerplane counterparts of 3-D computations with the LS + Yap model and the CSL model respectively. U_{ref} in these figures refers to the inlet freestream mean velocity. The experimental results of Papadopoulos [8] for the case of $AR = 12$ are also included in these figures for comparison. The normalized streamwise distance,X^*, is used here. X^* is defined as $(x - x_r)/x_r$, where x is the streamwise distance and x_r the mean reattachment length. Negative values of

X^* indicate locations within the recirculation region while its positive values represent positions downstream the recirculation region.

It can be observed that the results obtained from 2-D simulations agree quite well with the values obtained from 3-D simulations carried out with the respective models in the centerplane. Especially the mean streamwise velocity profiles obtained by 2-D and 3-D simulations are almost identical to each other at all streamwise locations. However, slight differences can be seen between the two cases performed with different turbulence models both on the velocity fluctuation intensities and the Reynolds shear stresses. It seems that 2-D simulation has a tendency to predict turbulent fluctuation quantities higher than that of the 3-D one within the recirculating region. These tendency agrees with the trends suggested by Berbee [17] based on their experimental results that a 2-D simulation may accurately predict the mean velocity field, but that the calculated turbulence intensity will be too high.

Quantitative agreements with the experimental counterparts cannot be obtained for the Reynolds stresses with either of the model. This is probably be due to the difference in the Reynolds number between the experiment and the present computations. The experiment was carried out at a Reynolds number approximately five times larger than that of the present simulations.

It is confirmed that the results obtained from both 2-D and 3-D simulations agree satisfactory with each other if the aspect ratio is large enough ($AR > 10$). In particular, exactly the same mean reattachment lengths are predicted both in the 2-D and 3-D simulations with either of CSL and LS + Yap models. This suggests that three-dimensional effects are minor in the central region of the duct for the cases of large aspect ratios.

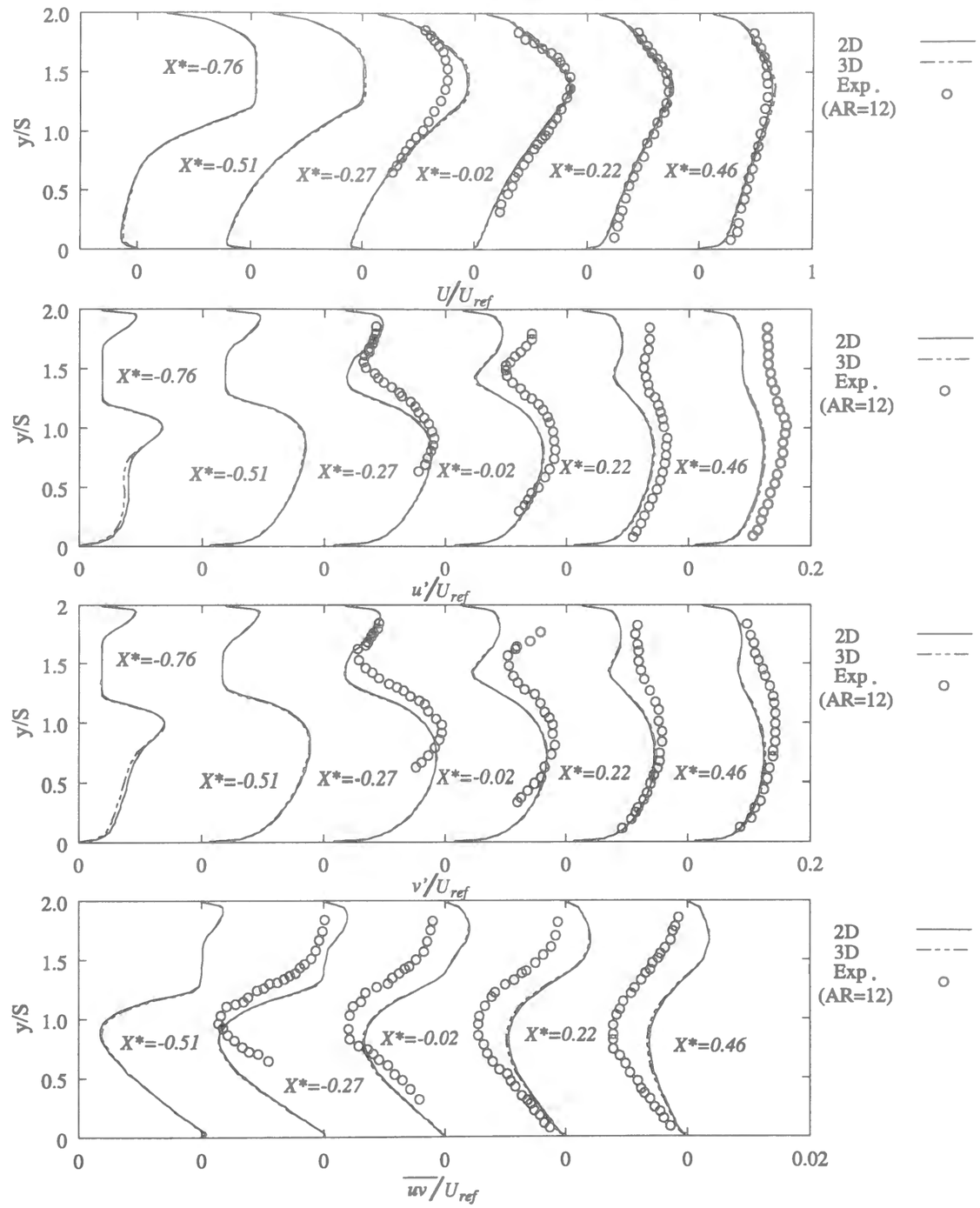

Figure 6.6: Comparison between 2-D and 3-D ($AR = 12$) simulations for mean streamwise velocity, velocity fluctuation intensities and Reynolds shear stress (LS + Yap model)

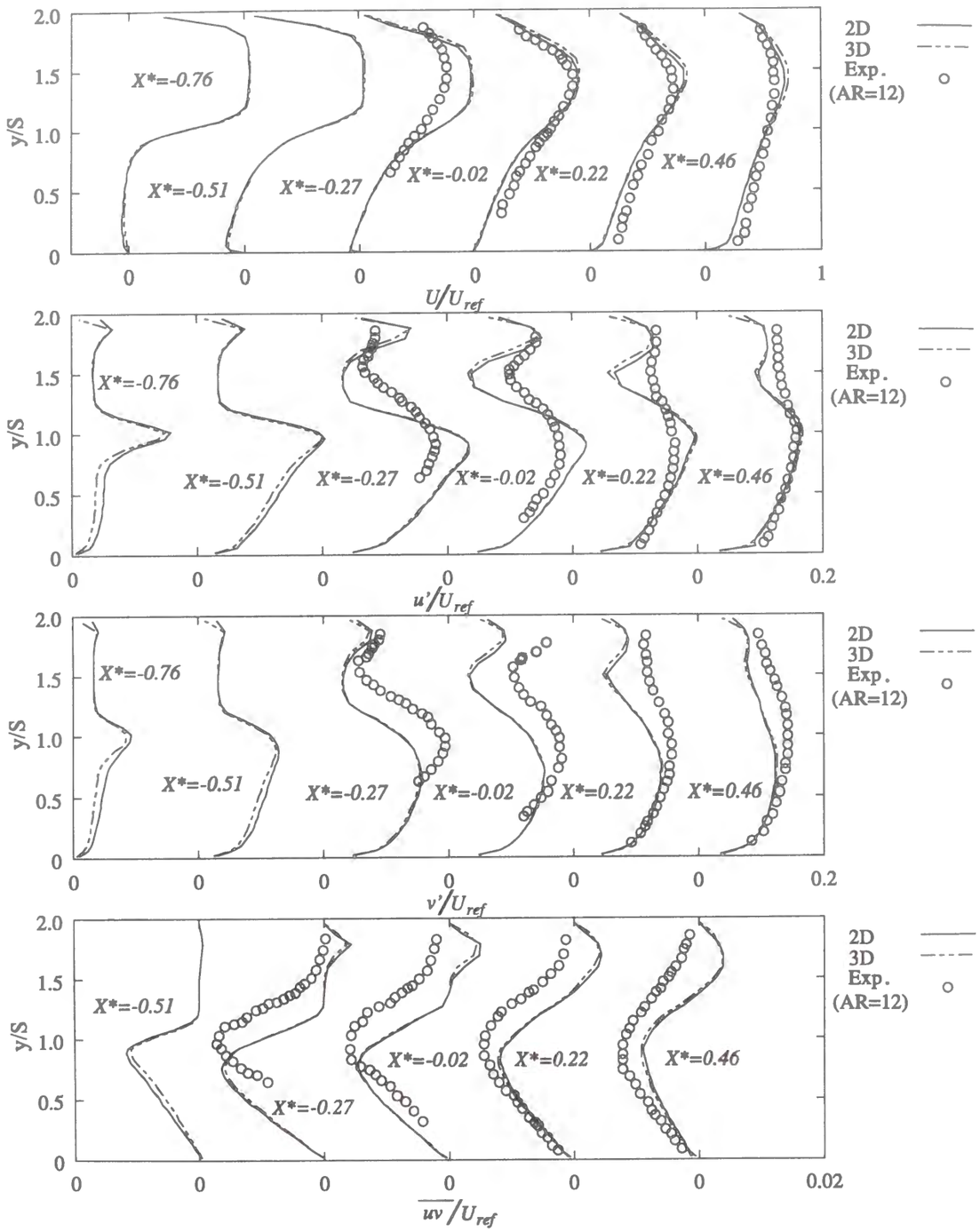

Figure 6.7: Comparison between 2-D and 3-D ($AR = 12$) simulations for mean streamwise velocity, velocity fluctuation intensities and Reynolds shear stress (CSL model)

6.3.3 Effect of Aspect Ratio

Three-dimensional simulations are performed adopting two aspect ratios, 12 and 4, both with the LS + Yap model and the CSL model in order to gain a deeper understanding of the three-dimensional side wall effects on the separating turbulent flow structure.

Centerplane Integral Flow Parameters, Heat Transfer Characteristics and Velocities

The centerplane mean skin friction coefficient, C_f downstream of the step for the two aspect ratios are shown in Fig. 6.8. An evident difference between the two aspect ratios can be observed in the region around one to two step height downstream the bottom corner of the step. A small but clear peak of C_f is obtained in this region for the smaller aspect ratio 4 with either of the two models. This suggests the appearance of a relatively stronger forward flow in the secondary recirculation region as the aspect ratio decreases. The secondary recirculation region mentioned here is a recirculating flow region which appears at the corner of the step, inside of the main recirculation zone but has an opposite sign of vorticity. A relatively weaker reversed flow is however predicted in the main recirculation region for the smaller aspect ratio 4. Predicted mean reattachment lengths, x_r for the two aspect ratios are tabulated in Table 6.6. LS + Yap model shows quantitatively better agreement with the experimental data. Mean reattachment length is predicted to be smaller for the smaller aspect ratio with the CSL model. This is consistent with the reported experimental observations [8] [1]. Contrary, the LS + Yap model predicts a slightly larger mean reattachment length for the smaller aspect ratio.

Table 6.6 : Mean reattachment lengths along centerline

	AR=12	AR=4
LS + Yap model	$7.93S$	$8.00S$
CSL model	$9.55S$	$9.00S$
Experiment of Papadopoulos	$8.20S$	$8.05S$

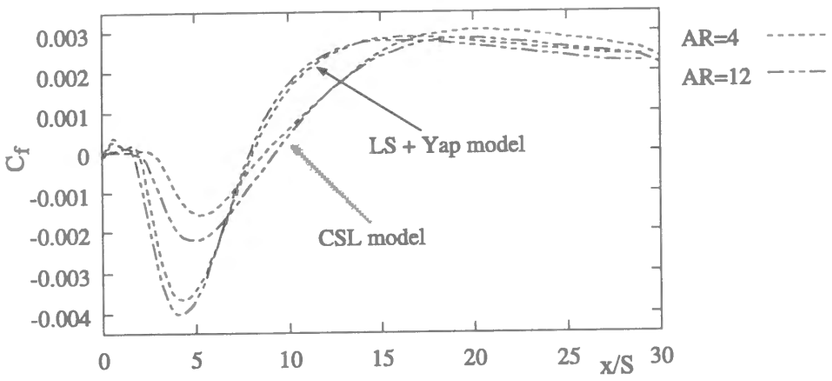

Figure 6.8: Centerplane mean skin friction coefficient

Figures 6.9 and 6.10 illustrate the profiles of the centerplane mean streamwise velocity, streamwise and transverse components of the normal Reynolds stresses and the Reynolds shear stress for the two aspect ratios studied.

The results obtained with the LS + Yap model are presented in Fig. 6.9 and the results with the CSL model in Fig. 6.10.

The general shapes of the various profiles obtained with the tested models are similar to each other. For the mean streamwise velocity, it is observed that the velocity recovery is relatively slower for the larger aspect ratio AR. The distributions of the turbulent intensities, u' and v', show maxima around the locations where maximum mean shear rate is observed and in contrast, minimum values of u' and v' are obtained at locations where the mean streamwise velocity gradient is zero (at $y/S > 1.0$). The distributions of Reynolds shear stress, $\overline{uv}$ also show maximum around the location of maximum velocity gradient $\frac{\partial U}{\partial y}$.

Quantitative comparisons of the various quantities illustrated in Fig. 6.9 and Fig. 6.10 with the experimental data of Papadopoulos reveal that the LS + Yap model works better than the CSL model. However, it is shown in Fig. 6.9 that the effect of the aspect ratio on all centerplane profiles shown here seems to be quite moderate when LS + Yap model is used. In particular, the predicted distributions of u' and v' are almost identical to each other. This should be the case since the model (LS + Yap model) adopted here assumed

isotropic normal stresses.

On the other hand, it is shown in Fig. 6.10 that the value of the aspect ratio considerably affects the centerplane profiles when CSL model is used. Quantitative agreement with the experimental data may not be good but qualitatively, the present CSL model is able to capture the differences between the two aspect ratios. This is particularly so in the regions $0.0 < y/S < 1.5$, where slight difference observed between the predicted turbulence fluctuation intensities agrees quite well with the experimental data. As for the Reynolds shear stress, the CSL model predicts a smaller $\overline{uv}$ for smaller aspect ratio. This trend is also consistent with the experimental data.

Because the main objective of this chapter is to study the three dimensional side wall effects on the flow and thermal fields, the CSL model, which could reflect the effects of aspect ratio, seems to be more appropriate to discuss the three dimensionality. Therefore the results obtained from the CSL model are carefully examined hereafter.

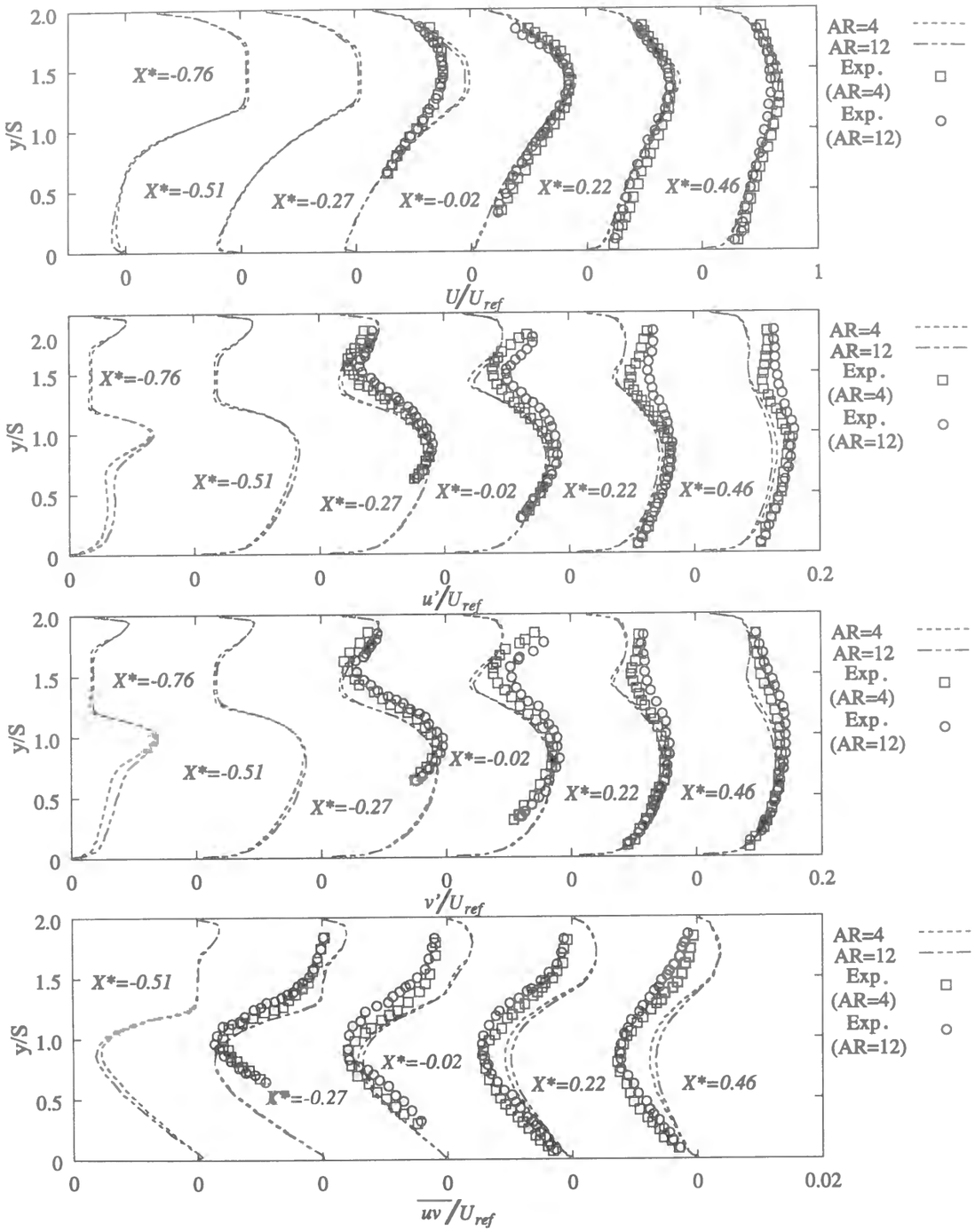

Figure 6.9: Effect of aspect ratio on mean streamwise velocity, velocity fluctuation intensities and Reynolds shear stress (LS + Yap model)

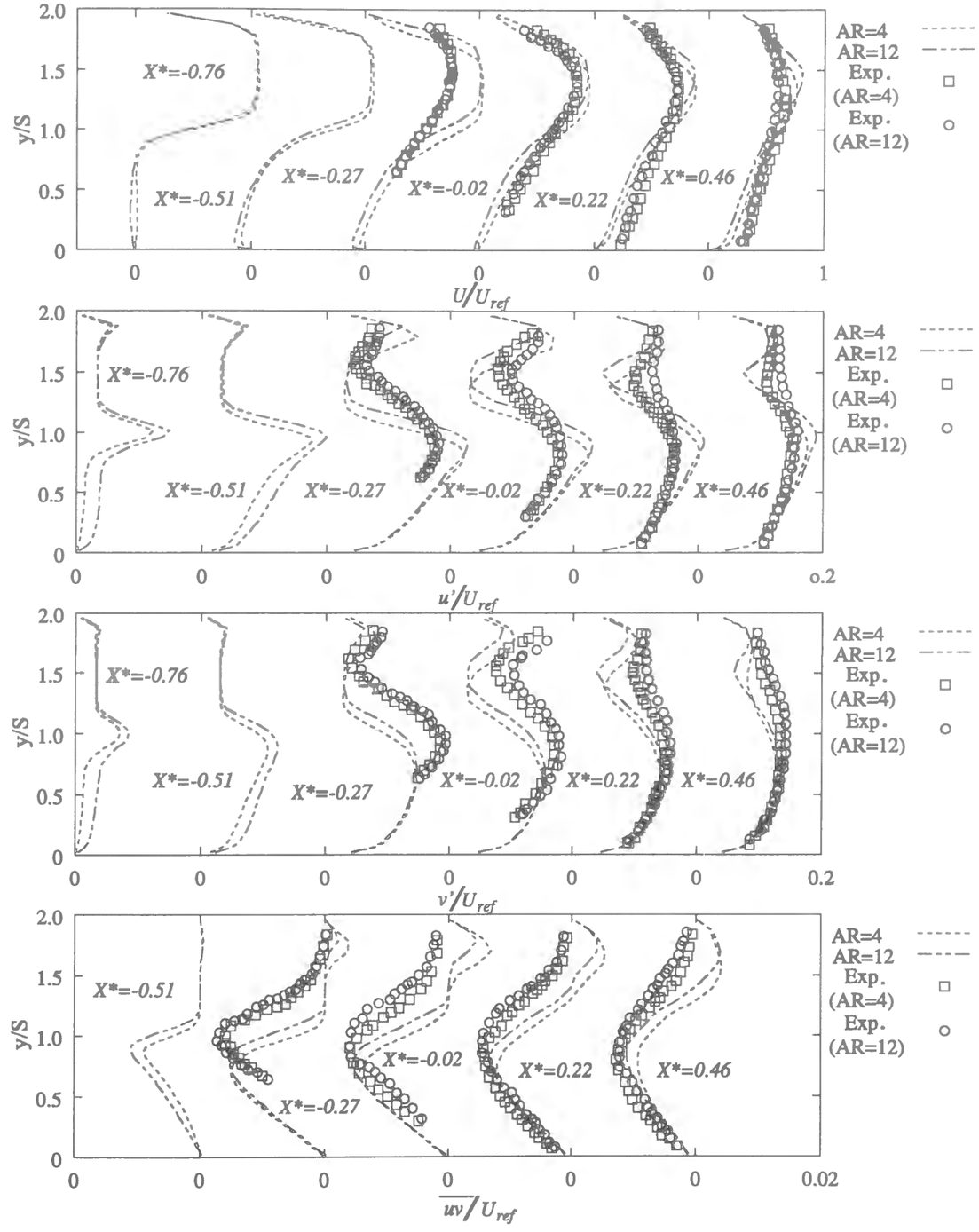

Figure 6.10: Effect of aspect ratio on mean streamwise velocity, velocity fluctuation intensities and Reynolds shear stress (CSL model)

The mean skin friction coefficient,C_f, and the mean Nusselt number,Nu, contours on the heated bottom wall for the two different aspect ratios are illustrated in Fig. 6.11 and Fig. 6.12. In Fig. 6.11 the shaded area corresponds to the region where the skin friction coefficient is positive. As for Fig. 6.12, gray tone levels correspond to the level of Nusselt number. Darker tone means higher Nusselt number. Slight asymmetry about the duct centerline is observed in these figures. The main cause of this asymmetry could be insufficient averaging time.

For the case of $AR = 12$, the two-dimensional zone, where contours of both C_f and Nu are parallel to the z-axis, can be observed around the duct center region, while no such region can be seen for the case of $AR = 4$. When $AR = 4$ spanwise non-uniformity of C_f and Nu around the centerplane is particularly prominent in the downstream region after the flow reattachment (x/S >9.00). High Nu area widely expands in the region of $5 < x/S < 15$ in both cases of smaller and larger aspect rations. Three peaks of Nu are observed in the case of $AR = 4$ around $x/S \approx 10$, one in the duct center region and two near the side walls. In the case of $AR = 12$, two pairs of peaks are symmetrically observed around $x/S \approx 10$ at $|z/WD| \simeq 0.3$ and 0.45. However these peaks are less distinct compared to those observed in the laminar flow cases shown in Chapter 3. The distribution patterns of both C_f and Nu are quite complicated in the region immediately after the step ($0 < x/S < 2$).

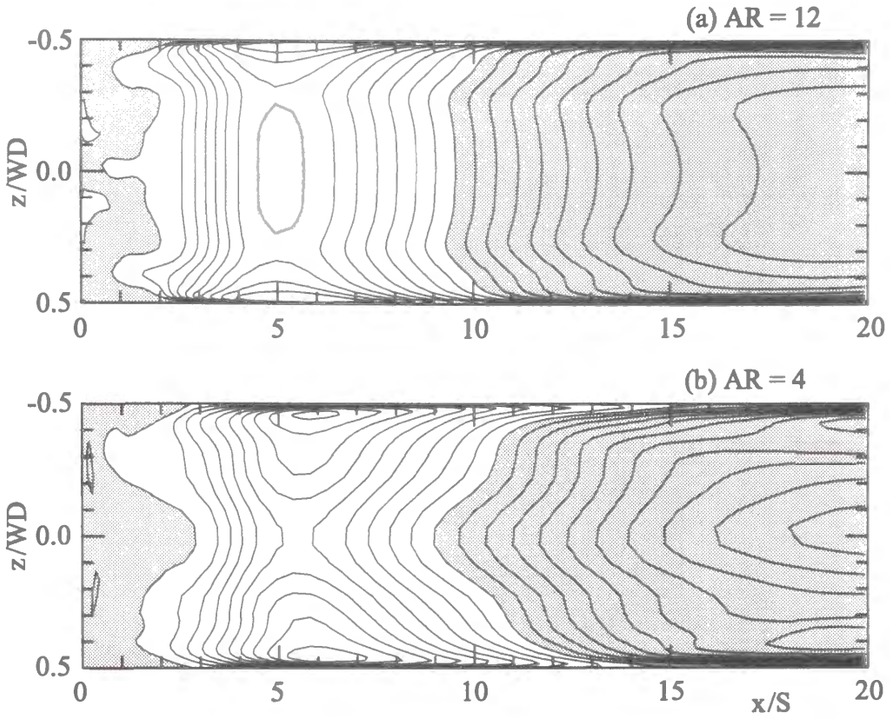

Figure 6.11: Mean skin friction coefficient contour on the bottom wall.

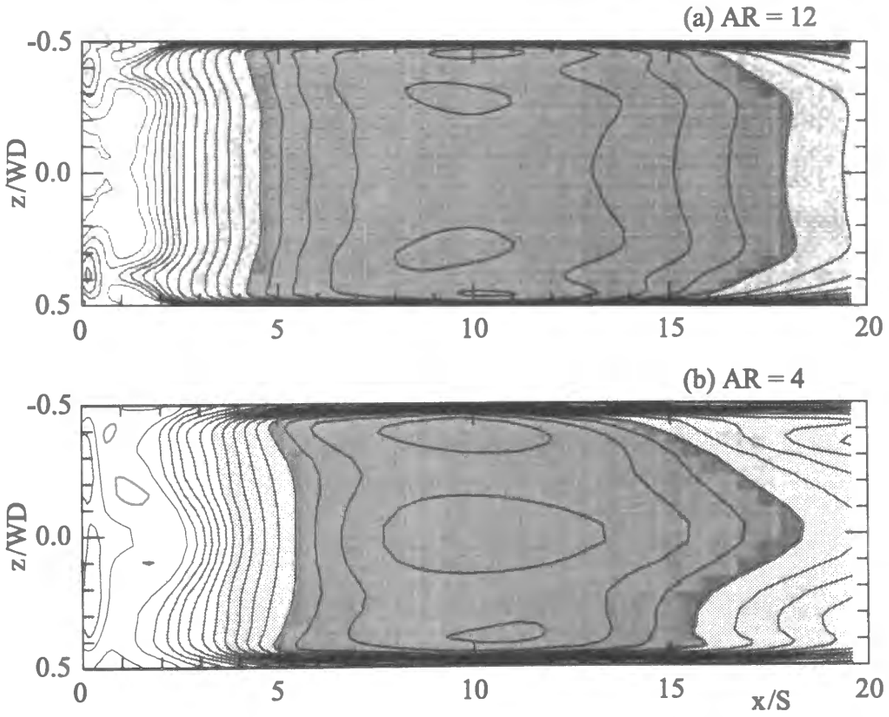

Figure 6.12: Mean Nusselt number contour on the bottom wall.

In the laminar flow cases discussed in Chapter 3, two distinct peaks in Nu distribution were symmetrically obtained near both side walls due to the downwash flows directed toward the heated wall at such spanwise positions. In turbulent flows, heat transfer can be enhanced as the effects of turbulence. Figure 6.13, 6.14 and 6.15 show the distributions of velocity fluctuation intensities,u' and v', and turbulent heat flux,$\overline{v\theta}$, near the heated wall ($y/S = 0.02$) respectively. Gray tone level correspond to the level of each value. The distribution patterns of these figures look similar to each other. For any illustrated quantity, a peak is observed around $x/S \simeq 9$ and $z/WD \simeq 0$ in the case of $AR = 4$ while two peaks are symmetrically observed in the case of $AR = 12$ around $x/S \simeq 9$ and $|z/WD| \simeq 0.3$. High turbulence intensities and high turbulent heat flux are expected at such positions. The positions of these peaks are located roughly close to the positions of peak Nu in Fig. 6.12, suggesting that heat transfer enhancement due to the turbulence is one of the cause for the Nu peaks at such positions. The positions of the peak $\overline{v\theta}$, however, do not exactly match the positions of peak Nu. Peak Nu are always obtained slightly downstream of the positions of peak $\overline{v\theta}$. Considering that the positions of peak Nu are also close to the positions of reattachment point in Fig. cslconcf, time averaged flow structure also plays an important role to induce the Nu peaks at such positions.

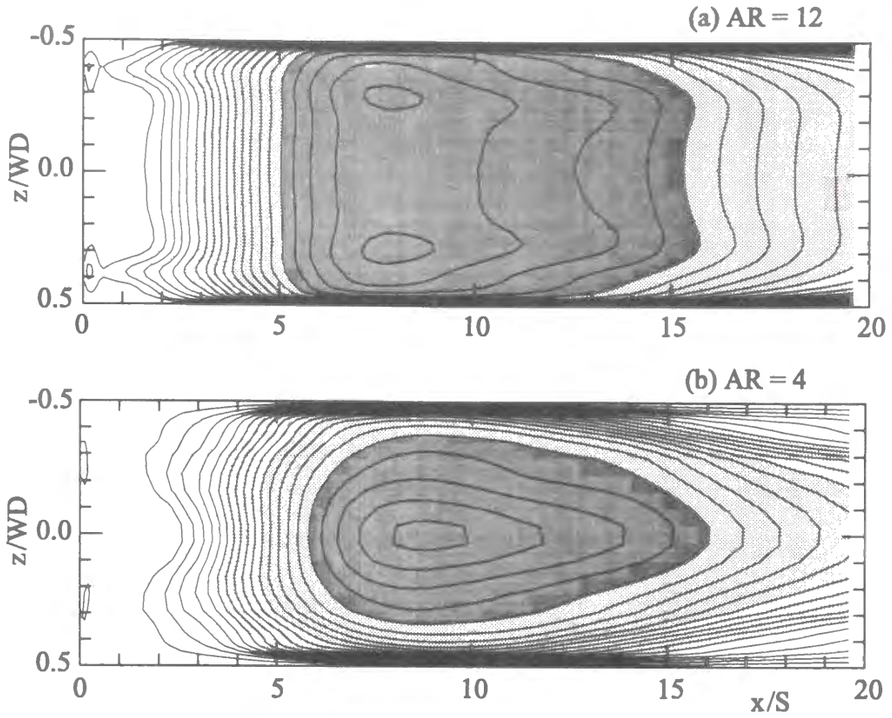

Figure 6.13: u' contours near the bottom wall.

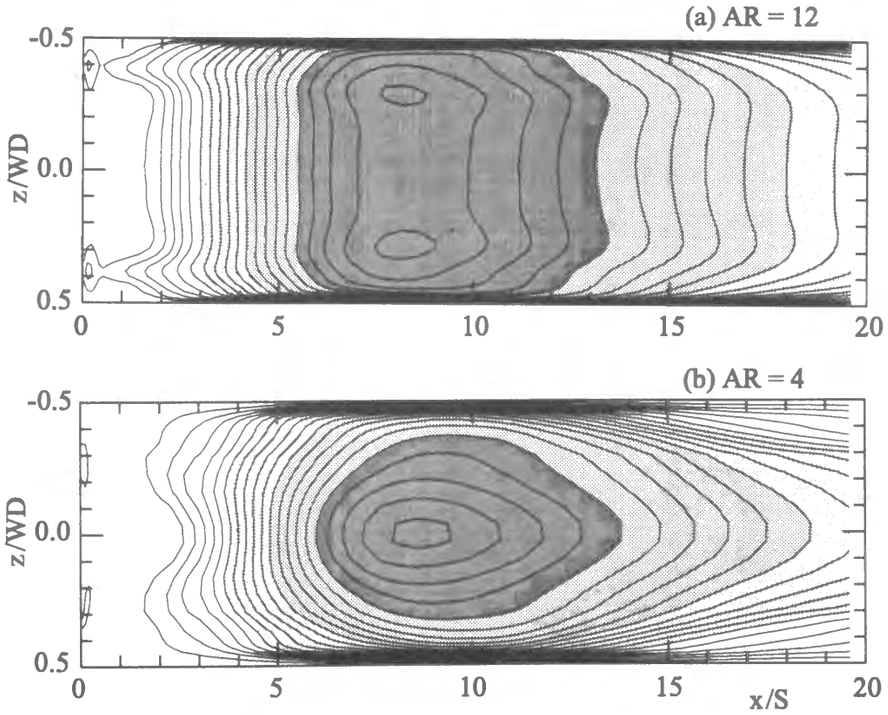

Figure 6.14: v'contours near the bottom wall.

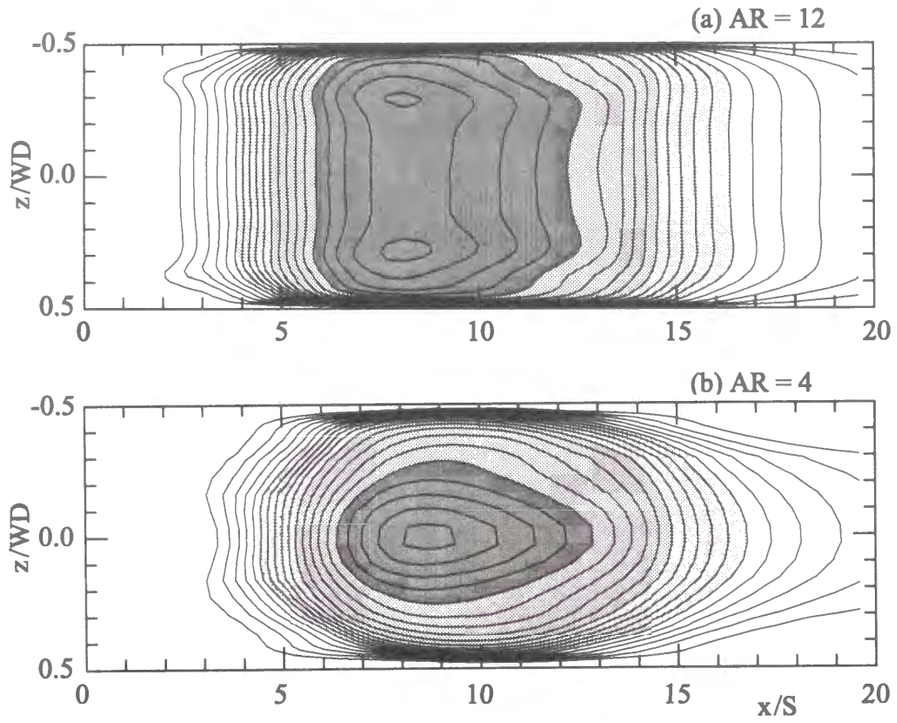

Figure 6.15: $\overline{v\theta}$ contours near the bottom wall.

Velocity-vector maps in two x-z planes immediately after the step are shown in Fig. 6.16 for the two aspect ratios. It can be seen in Fig. 6.16 that there exist two pairs of counter rotating eddies whose axes are normal to the bottom wall.

In the case of AR=12, these eddies, confined in the corners formed by the step and the side walls, are slightly weaker and are situated at positions around $|z/WD|$=0.45 and $|z/WD|$=0.3. In the duct central region, there exists a zone where fluid is almost stagnant. This confirms that two-dimensionality can be assumed in the central portion of the duct where spanwise uniformity of the velocity field is observed near the bottom wall.

In the case of AR=4, the velocity vector maps look slightly more complex. Nevertheless, a pair of counter rotating eddies can still be observed at $|z/WD|$=0.2. An eddy can be also seen at z/WD=–0.4. Another eddy having opposite rotation to pair with this one is expected to exist at a position around z/WD=0.4. However, no such distinct eddy can be observed in Fig. 6.16. The main cause of this could be insufficient averaging time. It means anyway that hierarchy of unsteadiness exists in the calculated flow behind a backward-facing step and that the life of wall-normal vortex behind the step is quite long. It is also seen in this figure that a relatively strong forward flow is generated in the central portion of the bottom wall under the influence of these eddies. It is clear that two-dimensionality does not hold in this region for the case of AR=4.

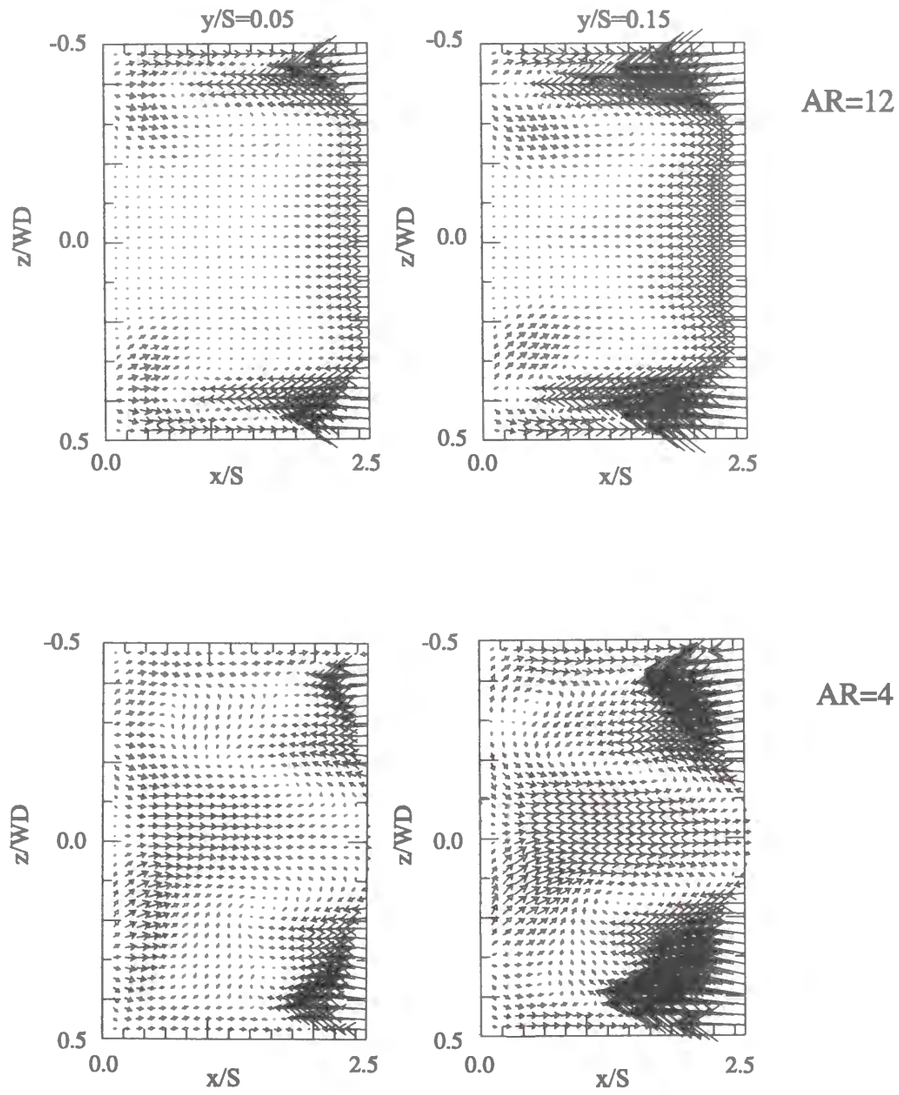

Figure 6.16: U-W vector plot in the secondary recirculation region.

A near wall flow model immediately after the step was proposed based on results of the surface visualization for different aspect ratios by Papadopoulos [8] and it is reproduced in Fig. 6.17. According to Papadopoulos [8], the nearly dead flow zone on the bottom wall immediately after the step is dominated by a pair of primary eddies situated near the side walls, whose axes are normal to the bottom wall. In between these eddies is yet located another set of counter rotating eddies of even number, which are induced by the motion of the primary eddies. The number of such secondary eddies depends on the aspect ratio. The sense of rotation of the eddies predicted by the present simulations matches basically that obtained from the surface visualization results.

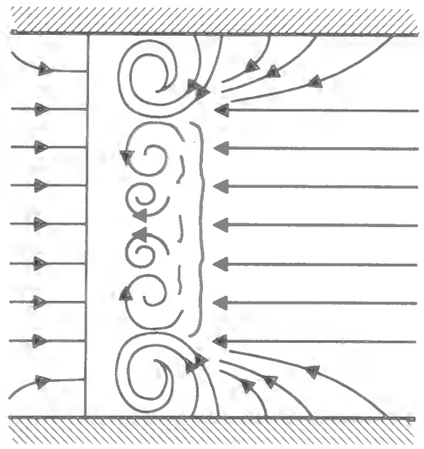

Figure 6.17: Near wall flow model in the secondary recirculation region (Papadopoulos [8])

Contours of streamwise velocity U in several cross-sections are shown in Fig. 6.18 and Fig. 6.20 respectively for the cases of AR=4 and AR=12. In the figures, cross-sectional flow pattern is also shown in the form of velocity vector maps. Figures 6.19 and 6.21 illustrate the temperature contours in the corresponding cross-sections of the respective cases of AR=4 and AR=12. Namely, the cross sectional velocity field and the temperature contours are presented in sequence for each respective case of aspect ratio in these figures. White areas are used to indicate negative U regions in the cross sectional velocity field plots while shaded areas correspond to positive U regions. As for the temperature contour plots, the level of the gray tone corresponds to the temperature levels. In other words, darker the tone is, the higher the temperature.

For both of the aspect ratios AR=4 and 12, longitudinal vortices or stream-aligned vortices are formed after the step edge near the both side walls at the height from the bottom wall of $y/S \approx 1.0$. These vortices are more distinctively observed for the smaller aspect ratio at the streamwise position slightly downstream of the step $x/S = 1.5$ near side walls $|z/WD| = 0.42$ (Fig. 6.20(b)). Further downstream after $x/S = 8$, these streamwise vortices are no longer noticeable. Instead, they seem to have transformed to a downwash flow which generates inward flow near the bottom wall. Comparing Figures 6.18 and 6.20, such inward flows seem to be relatively stronger when aspect ratio is smaller. Moreover, secondary flows of this nature persist even at the locations considerably downstream for example at $x/S = 18$. Again, such feature is more prominent for the smaller aspect ratio. The existence of such secondary flows (streamwise vortices and downwash flow) also explain the characteristic feature of the temperature contour observed in Figures 6.19 and 6.21. The relatively stronger downwash flow even at the downstream locations $x/S = 18$ for the smaller aspect ratio is depicted by temperature contours protruding toward the bottom wall near the two side-bottom corner regions ($|z/WD| \simeq 0.43$). The existence of such downwash flow is also the cause of higher Nusselt number being observed near the side walls at $|z/WD| \simeq 0.4$ as can be seen in Fig. 6.12. In addition to such streamwise vortices and downwash flows, corner eddies can also be observed near the corners of the

rectangular duct for both aspect ratios. Such vortex motion is again more distinct in the case of AR=4. Secondary motion of this type is believed to be turbulence-induced one, arising owing to differences between turbulent normal stresses [18].

Papadopoulos [8], from their surface visualization experimental results, postulated that the structure near the side walls is dominated by two streamwise vortices each originating at the junction of the step edge and reported that such secondary motion is the principal cause producing the non-uniform spanwise flow structure. It is also reported [8] that the decrease in the centerplane reattachment length for the smaller aspect ratio is related to the existence of such secondary flows. The present computational findings seem to be consistent with the experimental observations.

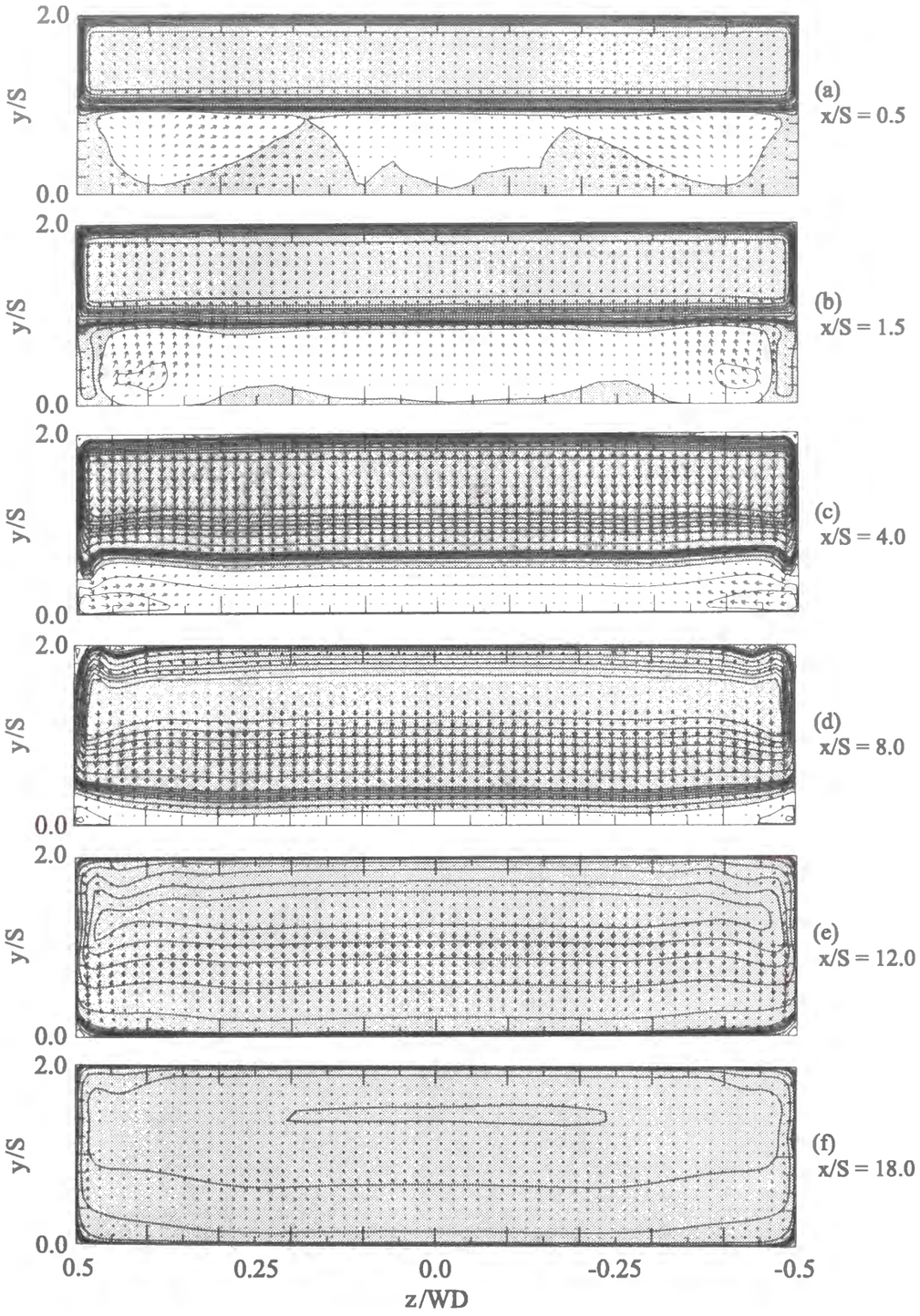

Figure 6.18: U contours and $V - W$ vector plot at various streamwise-locations (AR=12)

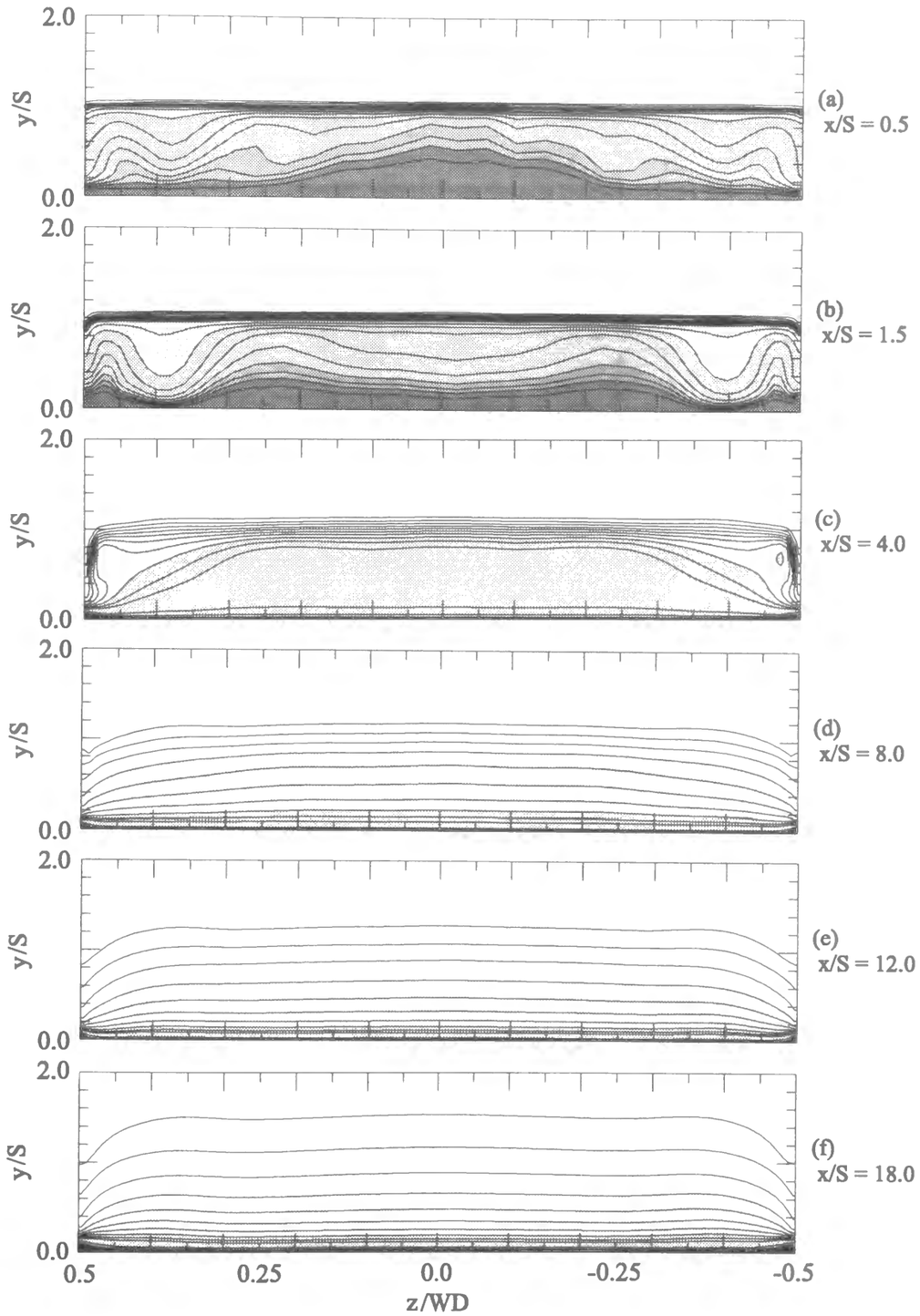

Figure 6.19: Temperature contours at various streamwise-locations (AR=12)

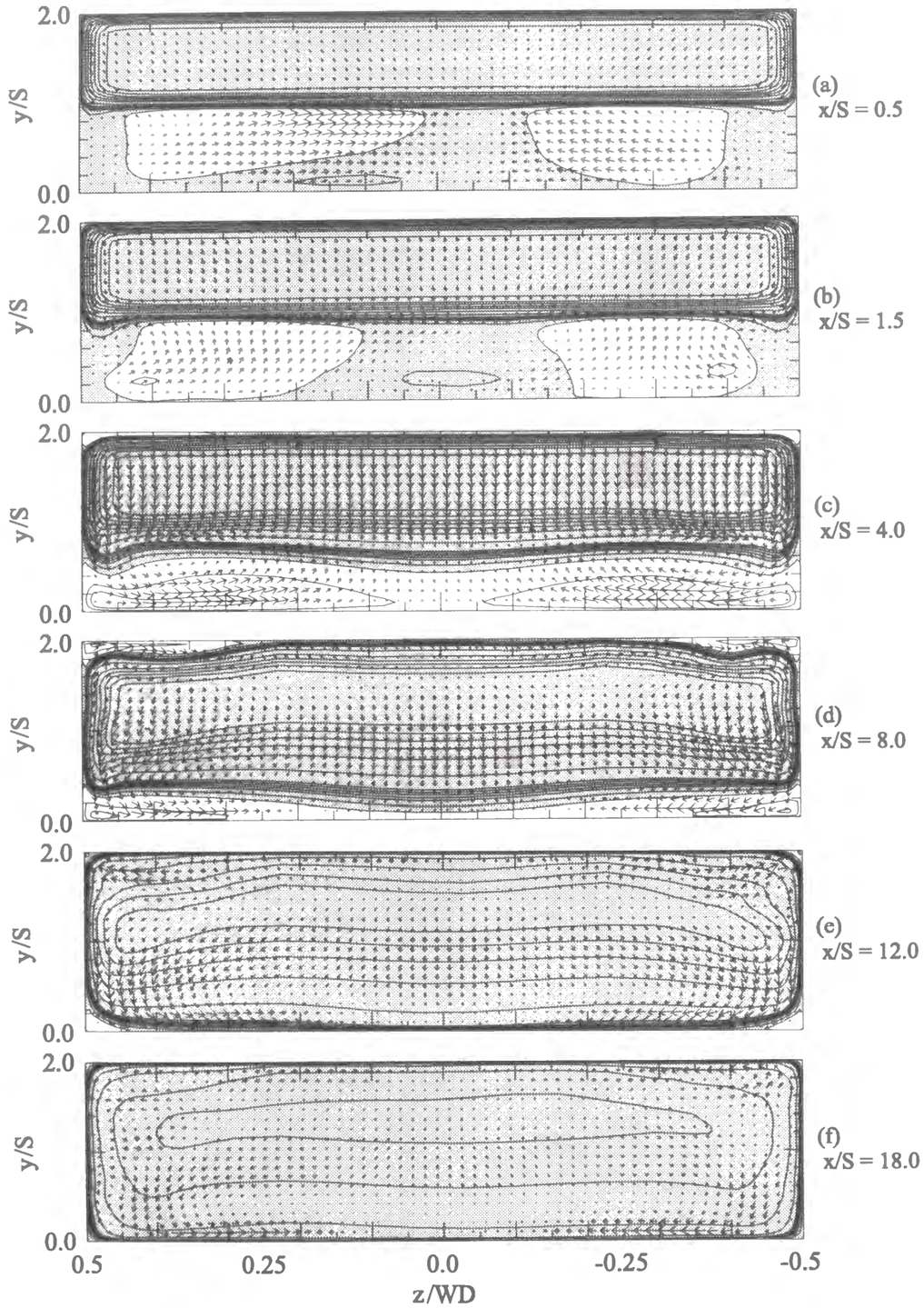

Figure 6.20: U contours and $V - W$ vector plot at various streamwise-locations (AR=4)

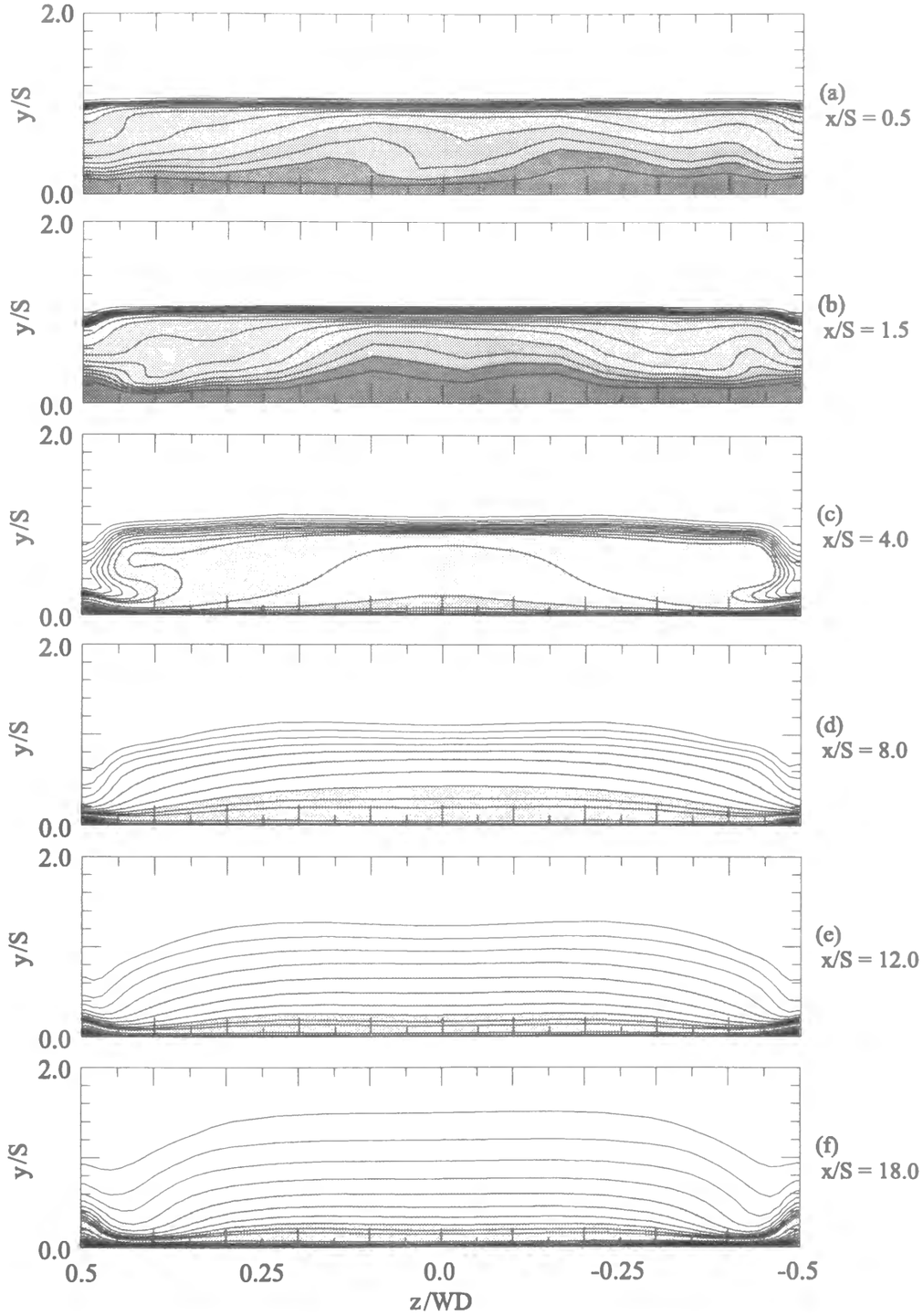

Figure 6.21: Temperature contours at various streamwise-locations (AR=4)

6.4 Conclusions

Two- and three-dimensional simulations were performed for turbulent flows over a backward-facing step. Two types of turbulent models were introduced into the computation code described in Chapter 2. The computations were carried out for two different aspect ratios (AR=4 and 12) in 3-D simulation to investigate three-dimensionality of the flow and thermal fields. The following conclusions were obtained:

(1) The results obtained by 2-D simulations show that both the LS + Yap model and the CSL model are capable to reproduce mean streamwise velocity profiles. LS + Yap model gives a better prediction of the reattachment length if compared with experimental or DNS data, while CSL model gives a better prediction of v', probably resulting a better prediction of the Stanton number profile.

(2) When the aspect ratio,AR, in 3-D simulations is 12, the statistical quantities calculated in the centerplane agree satisfactory with the results obtained by 2-D simulations for both the LS + Yap model and the CSL model.

(3) Quantitative comparisons of statistical quantities made with the experimental data show that the LS + Yap model gives slightly better agreement in the statistical quantities calculated in the centerplane than the more complex CSL model. However, qualitatively, the CSL model gives a better description of the physics of the flow when three-dimensional effects become important.

Following (3), three-dimensionality of flow and thermal fields were studied through the numerical results which were mainly obtained using CSL model.

(4) In the case of $AR = 12$, the two-dimensional region is observed around the duct center region, while no such region is seen in the case of $AR = 4$. The general belief that two-dimensionality along the centerplane can be assumed for backward-facing step flows with an aspect ratio greater than 10 is tolerably correct.

(5) High Nu region is observed over the streamwise positions of $5 < x/S < 15$ for both of the aspect ratios. Those high Nu regions are obtained not only as the result of heat

transfer enhancement due to the turbulence, but also as the result of the downwash flow, similar to the laminar flow cases discussed in Chapter 3.

(6) Transverse counter rotating eddies are observed in the relatively low velocity region right after the step, resulting the highly three-dimensional flow and thermal field there. This is more prominent for the smaller aspect ratio(AR=4).

References

[1] Brederode, V. de, and Bradshaw, P., *Three-Dimensional Flow in Nominally Two-Dimensional Separation Bubbles; I. Flow Behind a Rearward-Facing Step*, Imperial College of Science and Technology, Aero Report 72-19, (1972).

[2] Jones W.P. and Launder B.E. , *The Prediction of Laminarization with a Two-Equation Model of Turbulence* , Int.J. Heat Mass Transfer, vol.15, pp.301-314 (1972).

[3] Launder B.E. & Sharma B.I., Letters in Heat and Mass Transfer Vol.1, pp. 131-138, (1974).

[4] Yap, C.R., *Turbulent Heat and Momentum Transfer in Recirculating and Impinging Flows*, PhD Thesis, Faculty of Technology, University of Manchester, (1987).

[5] Launder B.E. , *On the Computation of Convective Heat Transfer in Complex Turbulent Flows*, J. Heat Transfer, Vol. 110, pp. 1112-1128, (1988).

[6] Suga K., *Development and Application of a Non-linear Eddy Viscosity Model Sensitised to Stress and Strain Invariants*, UMIST, Dept of Mechanical Engineering, Report TFD/95/11, (1995).

[7] Eaton J.K. and Johnston J.P. , *A Review of Research on Subsonic Turbulent Flow Reattachment*, AIAA Journal, Vol 19, no. 9, pp. 1093-1100 , (1981).

[8] Papadopoulos G. , Ötügen M. V. , *Separating and Reattaching Flow Structure in a Suddenly Expanding Rectangular Duct*, Journal of Fluids Engineering, Vol.117, pp. 17-23, (1995).

[9] Jovic. S and Driver. D.M, *Reynolds Number Effects on the Skin Friction in Separated Flows Behind a Backward-Facing Step*, Exp. Fluids Vol 8, no. 6, pp. 464-467, (1995).

[10] Le H. , Moin P. , and Kim J. , *Direct Numerical Simulation of Turbulent Flow Over a Backward-Facing Step*, Proceedings of The 9th International Symposium on Turbulent Shear Flows, pp. 13.2.1-13.2.5, (1993).

[11] Vogel J.C. and Eaton J.K. , *Combined Heat Transfer and Fluid Dynamic Measurements Downstream of a Backward-Facing Step*, J. Heat Transfer, Vol 107, pp. 922-929, (1985).

[12] Eaton, J.K., and Johnston, J.P., *Low-Frequency Unsteadiness of a Reattaching Turbulent Shear Layer*, Proceedings of The 3rd International Symposium on Turbulent Shear Flows, Davis, Calif., (1981).

[13] Lasher, W.C. and Taulbee, D.B., *On the Computation of Turbulent Back-Step Flow*, Int. J. Heat and Fluid Flow, Vol.13, pp 30-40, (1992).

[14] Kang Y. , Suzuki K. , Sato T. and Nishino J. , *Numerical and Experimental Study on a Confined Jet*, Trans. JSME B, 49-443, pp. 1513-1520, (1983), (in Japanese).

[15] Kang Y. , Nishino J. , Suzuki K. and Sato T. , *Application of Flow and Surface Temperature Visualization Techniques to a Study of Heat Transfer in Recirculating Flow Regions*, Flow Visualization, pp. 77-81, Hemishpere, (1982).

[16] Suzuki K. , Suga K. , Oshikawa Y. , Lee C.G. , *LDV Measurements of Turbulence and Test of Turbulence Models in a Recirculating Flow*, Trans. JSME B, 53-496, pp. 3639-3647, (1987).

[17] Berbee, J.B., and Ellzey, J.L., *The Effect of Aspect Ratio on the Flow over a Rearward-Facing Step*, Exp. Fluids, Vol. 7, pp.447-452, (1989).

[18] Speziale C.G. , *On Non-linear $k-l$ and $k-\varepsilon$ Models of Turbulence*, J. Fluid Mech., Vol. 178, pp 459-475, (1987).

Chapter 7

Rarefaction Effects on a Microscale Backward-Facing Step Flow

7.1 Introduction

Advances in microfabrication technology enable now the manufacturing of micro engineering devices such as micro heat exchanger [1] and Micro Electro Mechanical Systems (MEMS) [2]. Flows in such micro devices cannot be treated as one of continuum. The characteristic length of these devices that governs the momentum and energy transfer in these devices are often comparable to the molecular mean free path of the fluid (gas). In order to improve the performance of such micro devices, it is important to have a clear idea about the related flow and thermal phenomena. In normal scale, it is known that separation and reattachment of flows are important phenomena affecting the efficiency of heat exchangers and are sometimes intentionally used for heat transfer enhancement, although they cause pressure drop and related energy loss. As one of the simplest geometry to generate separation and reattachment of flows, a great attention has been paid to a backward-facing step flow and heat transfer. 2-D and 3-D numerical simulations for flows over a backward-facing step in a normal scale rectangular duct were thus carried out and their results were presented in the previous chapters. In micro scale flow geometry, however, there are only few investigations on this flow separation and reattachment phenomena, in

spite of the recent increasing interests in production of high-performance microscale devices. Recently, Beskok and Karniadakis [3] have performed 2-D numerical computations for backward-facing step flows in the slip flow regime and proposed the continuum-based slip models, which are capable of predicting the basic physics of backward-facing step flows.

In this chapter, both 2-D and 3-D numerical simulations are performed for flows over a backward-facing step in a microscale rectangular duct. The main objective of this study is to investigate the effects of rarefaction (the velocity slip and temperature jump conditions) on the microscale flows with separation and reattachment phenomena. The pressure variation along the flow is usually quite large in microscale flows. The compressibility of the working fluid may play an important role in such cases. Therefore, effect of compressibility is also taken into account in addition to the rarefaction effects.

7.2 Computational Conditions

When the characteristic length of the domain geometry is comparable to the mean free path of the fluid (gas), the fluid does not behave as continuum. The effects of rarefaction have to be considered in this case. The level of rarefaction can be evaluated by Knudsen number,Kn, which is defined as the ratio between the mean free path of the molecules,l, and the characteristic length of the geometry,L.

$$Kn = \frac{l}{L} \tag{7.1}$$

As the value of Kn is increased, the rarefaction effects become more important. The gas flows can be classified as follows [4]. When Kn is less than 10^{-3} the fluid can be considered as a continuum, while Kn is larger than 10 it is considered as a free molecular flow. A rarefied flow is the flow which Kn is between 10^{-3} and 10. In that regime, a further classification is commonly used: Slip flow regime $10^{-3} \leq Kn \leq 0.1$ and transition regime $0.1 \leq Kn \leq 10$. This chapter focuses on microscale flows in the slip flow regime.

7.2.1 Computational Domain

Figure 7.1 schematically illustrates the computational domain adopted for three-dimensional computations. The aspect ratio,$AR = WD/S$, and the expansion ratio,$ER = H/(H-S)$, are kept constant at 8 and 2 respectively in this chapter. The computational domain is set to cover the streamwise positions of -8 $\leq x/S \leq$ 26 , where S is the step height. The origin of the coordinate system is located at the center of the bottom line of the backward-facing wall. x-coordinate is set for the streamwise direction, y for the transverse direction and z for the spanwise direction. 2-D computations are conducted in the plane where z=0.

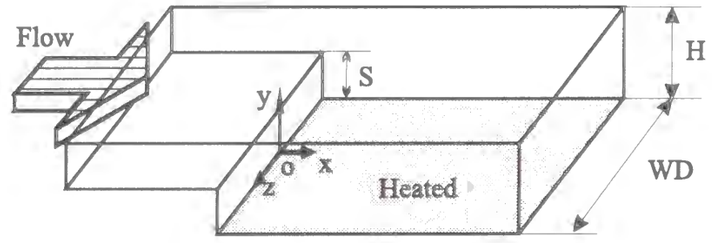

Figure 7.1: Computational domain.

7.2.2 Governing Equations

The characteristic length of the geometry in this chapter is the duct height downstream of the step,H. Knudsen number,Kn_o, based on the duct outlet condition is set in the range where the flow can be considered in slip flow regime. That is $10^{-3} < l_o/H < 0.1$ where l_o is the mean free path of the molecule at the duct outlet. In slip flow regime, the velocity and temperature fields can be determined from Navier-Stokes equation and energy equation if velocity slip and temperature jump conditions at the walls are taken into account [5]. The following steady Navier-Stokes and energy equations are solved numerically together with the continuity equation using the finite difference method.

Continuity equation

$$\frac{\partial}{\partial x}(\rho U) + \frac{\partial}{\partial y}(\rho V) + \frac{\partial}{\partial z}(\rho W) = 0 \tag{7.2}$$

Navier-Stokes equations

$$\frac{\partial}{\partial x}(\rho U^2)+\frac{\partial}{\partial y}(\rho VU)+\frac{\partial}{\partial z}(\rho WU)$$
$$= -\frac{\partial P}{\partial x}+\frac{\partial}{\partial x}\left(\mu\frac{\partial U}{\partial x}\right)+\frac{\partial}{\partial y}\left(\mu\frac{\partial U}{\partial y}\right)+\frac{\partial}{\partial z}\left(\mu\frac{\partial U}{\partial z}\right) \quad (7.3)$$

$$\frac{\partial}{\partial x}(\rho UV)+\frac{\partial}{\partial y}(\rho V^2)+\frac{\partial}{\partial z}(\rho WV)$$
$$= -\frac{\partial P}{\partial y}+\frac{\partial}{\partial x}\left(\mu\frac{\partial V}{\partial x}\right)+\frac{\partial}{\partial y}\left(\mu\frac{\partial V}{\partial y}\right)+\frac{\partial}{\partial z}\left(\mu\frac{\partial V}{\partial z}\right) \quad (7.4)$$

$$\frac{\partial}{\partial x}(\rho UW)+\frac{\partial}{\partial y}(\rho VW)+\frac{\partial}{\partial z}(\rho W^2)$$
$$= -\frac{\partial P}{\partial z}+\frac{\partial}{\partial x}\left(\mu\frac{\partial W}{\partial x}\right)+\frac{\partial}{\partial y}\left(\mu\frac{\partial W}{\partial y}\right)+\frac{\partial}{\partial z}\left(\mu\frac{\partial W}{\partial z}\right) \quad (7.5)$$

Energy equation

$$\frac{\partial}{\partial x}(\rho Uh)+\frac{\partial}{\partial y}(\rho Vh)+\frac{\partial}{\partial z}(\rho Wh)$$
$$= \frac{\partial}{\partial x}\left(\frac{\lambda}{C_P}\frac{\partial h}{\partial x}\right)+\frac{\partial}{\partial y}\left(\frac{\lambda}{C_P}\frac{\partial h}{\partial y}\right)+\frac{\partial}{\partial z}\left(\frac{\lambda}{C_P}\frac{\partial h}{\partial z}\right)+U\frac{\partial P}{\partial x}+V\frac{\partial P}{\partial y}+W\frac{\partial P}{\partial z} \quad (7.6)$$

where x,y and z are the streamwise, transverse and spanwise directions respectively. The symbols U,V,W,P and h denote the fluid velocity components in the x,y and z directions, pressure and enthalpy, respectively, while ρ,μ,λ and C_P stand for the fluid density, viscosity, thermal conductivity and specific heat, respectively. The properties of the working fluid (Nitrogen) are assumed to be constant when the fluid is assumed to be incompressible. When fluid compressibility is taken into account, the local fluid density (ρ) in the momentum and energy equations is determined from local temperature and local pressure following the ideal gas assumption, ($P = \rho RT$). The pressure correction equation in the SIMPLE algorithm is derived from the continuity equation as described in Chapter 2. The local fluid density in the continuity equation is also determined in the same way in the compressible flow computations. The last three terms in the energy equation (7.6) are the pressure work terms. They are taken into account only in the compressible flow computations.

7.2.3 Boundary Conditions

At the upstream boundary, inlet flow is assumed to have uniform profiles for both velocity (U_{in}) and temperature (T_{in}). The duct bottom wall downstream of the step is maintained at a uniform temperature (T_w) higher than the inlet flow temperature. The top wall ($y/S = 2.0$), the bottom wall upstream of the step ($y/S = 1.0$, $x/S < 0$), the backward-facing step wall and the side walls in the 3-D computation cases are assumed to be thermally adiabatic. Thermal creep effect is neglected in the present study. The temperature difference between T_w and T_{in} should be small so that the assumption of constant fluid properties for the incompressible flow calculations is legitimate. $T_w - T_{in}$ is kept constant at 5 K throughout this study. The exit pressure is set to 101,325Pa (1atm) in all the studied cases.

Velocity Slip and Temperature Jump Conditions

The velocity slip and temperature jump conditions at the walls have to be taken into account in slip flow regime [6]. Figure 7.2 schematically illustrates the tangential velocity near the wall. s in this figure is the imaginary surface located very close to the wall where the velocity slip and temperature jump occur.

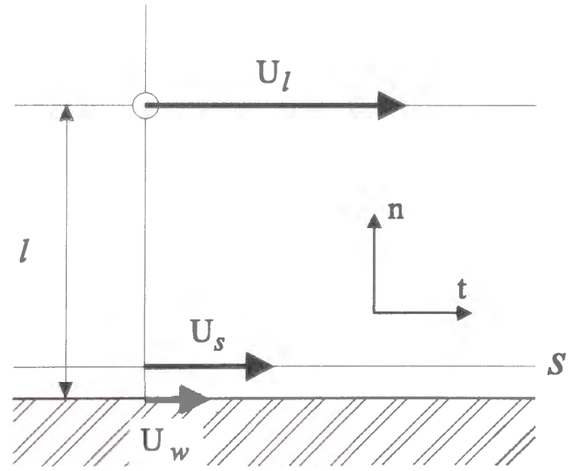

Figure 7.2: Sketch of the slip velocity near the wall.

Here, the following two assumptions are taken:

1. Half of the molecules passing through surface s are coming from the layer of gas one mean path away from the surface with an average tangential velocity of U_l while the other half of the molecules are reflected from the wall.

2. σ_v $(0 \leq \sigma_v \leq 1)$ of the molecules are reflected from the wall diffusively with an average tangential velocity of U_w while (1-σ_v) of the molecules are reflected from the wall specularly with an average tangential velocity of U_l.

Then the following slip velocity U_s is obtained [4].

$$U_s = \frac{1}{2}(U_l + (1-\sigma_v)U_l + \sigma_v U_w) \tag{7.7}$$

Expanding U_l in terms of U_s, using Taylor series expansion, results in:

$$U_s - U_w = \frac{2-\sigma_v}{\sigma_v}\{Kn(\frac{\partial U}{\partial n})_s + \frac{Kn^2}{2}(\frac{\partial^2 U}{\partial n^2})_s + \frac{Kn^3}{6}(\frac{\partial^3 U}{\partial n^3})_s + \cdots\} \tag{7.8}$$

Note that

$$U_s - U_w = \frac{2-\sigma_v}{\sigma_v}\{Kn(\frac{\partial U}{\partial n})_s\} \tag{7.9}$$

is Maxwell's first order slip boundary condition. Being analogous to the equation(7.8), the temperature jump condition can be written [3]:

$$T_s - T_w = \frac{2-\sigma_T}{\sigma_T}[\frac{2\gamma}{\gamma+1}]\frac{1}{Pr}\{Kn(\frac{\partial T}{\partial n})_s + \frac{Kn^2}{2}(\frac{\partial^2 T}{\partial n^2})_s + \frac{Kn^3}{6}(\frac{\partial^3 T}{\partial n^3})_s + \cdots\} \tag{7.10}$$

Recognizing the Taylor series expansion of T_l about T_s, this equation can be written as follows:

$$T_s = \frac{\frac{(2-\sigma_T)}{Pr}\frac{2\gamma}{(\gamma+1)}T_l + \sigma_T T_w}{\sigma_T + \frac{(2-\sigma_T)}{Pr}\frac{2\gamma}{\gamma+1}} \tag{7.11}$$

In the early stage of the present study, Maxwell's first order velocity slip condition (Eq. (7.9)) was adopted as the velocity boundary condition at the wall. However, it turned out that the Navier-Stokes solution with the Maxwell's velocity slip condition could become numerically unstable as reported by Beskok [4]. Therefore, the equation (7.7) and (7.11) proposed by Beskok [3,4] are adopted in the present computation as the velocity slip condition and the temperature jump condition respectively. The velocity accommodation coefficient,σ_v, and the temperature accommodation coefficient,σ_T, are basically kept constant at 1.0 and 0.85 respectively [7]. Velocity slip condition is used at all wall surfaces and temperature jump condition is used at the heated wall. U_w is set equal to zero in the present study.

7.2.4 Computational Conditions

The main interests in the present study are the effects of the velocity slip and temperature jump conditions on the microscale flow with separation and reattachment and its related thermal field. Effect of compressibility is also expected to be of some importance for this flow [8]. Therefore, the following three types of computational code were prepared in order to investigate these effects.

Code (I-N):Incompressible flow with no-slip and no-temperature jump conditions
Code (I-S):Incompressible flow with slip and temperature jump conditions
Code (C-S):Compressible flow with slip and temperature jump conditions

A comparison of results between (I-N) and (I-S) is expected to reveal the effects of rarefaction (velocity slip and temperature jump conditions), while the effects of compressibility could be discussed through a comparison between (I-S) and (C-S). Calculations are carried out for several cases with different Reynolds number, Knudsen number, which is based on the duct outlet condition, and velocity accommodation coefficient,σ_v. Close attention is paid to the distribution patterns of both the skin friction coefficient and the Nusselt number on the heated wall. These characteristic values are defined as below:

$$\text{Reynolds number}, Re = \frac{U_o H}{\nu} \tag{7.12}$$

$$\text{Knudsen number}, Kn_o = \frac{l_o}{H} \tag{7.13}$$

$$\text{Skin friction coefficient}, C_f = \frac{2\tau_w}{\rho U_o^2} \tag{7.14}$$

$$\text{Nusselt number}, Nu = \frac{q_w S}{\lambda(T_w - T_{in})} \tag{7.15}$$

$l_o, \tau_w, q_w, T_w, T_{in}$ and U_o used here refer to the values of the mean free path of the molecule at the outlet, wall shear stress, wall heat flux, wall temperature, inlet temperature and the cross-sectional mean velocity at the outlet, respectively.

7.3 Results and Discussion

In order to obtain the general idea about the microscale backward-facing step flows in the slip flow regime, the effects of the rarefaction and the compressibility are studied. As a first step, 2-D simulations have been carried out over a Reynolds number range of $0.1 \leq Re \leq 35$, while keeping the outlet Knudsen number,Kn_o, and the velocity accommodation coefficient,σ_v constant at 0.013 and 1.0 respectively. Validity of incompressibility assumption is also discussed.

The effect of Reynolds number,Re, on reattachment length,x_r, at a constant outlet Knudsen number,$Kn_o = 0.013$ is shown in Fig. 7.3. Figure 7.3(b) is a partial enlarged view over a Reynolds number range of $0 \leq Re \leq 6$ of Fig. 7.3(a). The reattachment point in this study is defined as the point at which the skin friction coefficient changes its sign from negative to positive value. In incompressible flow cases, the values of x_r increase linearly with the increase of Re. A comparison between the (I-N) cases and the (I-S) cases shows that x_r is always predicted upstream in (I-S) cases than in (I-N) cases for the same value of Re. Figure 7.3(b) shows that x_r of the (C-S) cases match x_r of the (I-S) cases only at a very low Reynolds number ($Re \leq 1$), indicating that the incompressible flow assumption may be valid only at such low Re. It can be also seen in Fig. 7.3 that x_r increases non-linearly with Re in the (C-S) cases, as reported by Beskok and Karniadakis [3]. For $Re > 15$, deviation of x_r of (C-S) cases from that of (I-S) cases is a little more pronounced.

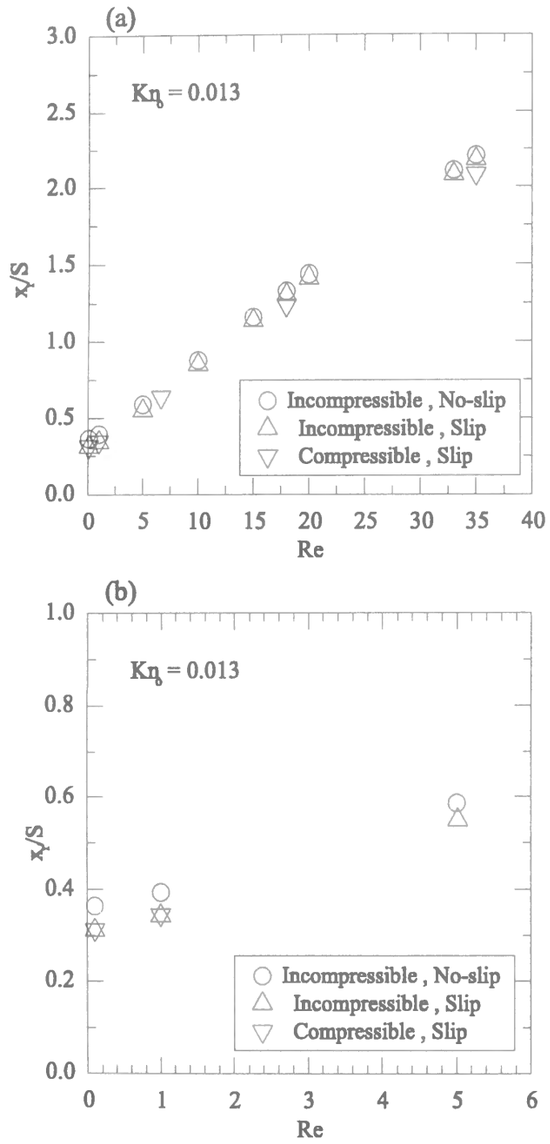

Figure 7.3: Effect of Re on Reattachment length.

The distributions of both skin friction coefficient,C_f, and Nusselt number,Nu, simultaneously computed on the heated wall are shown in Fig. 7.4 for three different values of Re. In each figure, the results for all (I-N),(I-S) and (C-S) cases are plotted. It can be observed in Fig. 7.4 that the absolute values of C_f in (I-S) cases are generally smaller than those in the (I-N) cases. This is due to the velocity slip at the wall. The C_f in the (C-S) case is even smaller than that of the case (I-S) at $Re = 18$. But it should be kept in mind that the value of C_f in the (C-S) case continuously increase as it flows downstream due to the flow acceleration, while C_f in the (I-S) case keeps a constant value in the developed flow region ($x/S > 5$). The values of C_f for the case (I-S) and case (C-S) at $Re = 18$ come closer to each other at positions near the duct outlet ($x/S = 26$). The distribution patterns of Nu for the both cases (I-N) and (I-S) are identical at any Re. The effects of the temperature jump as well as the effects of flow modification due to the velocity slip on the thermal field seem to be negligible under the conditions of the present study. On the other hand, higher Nu are predicted for the (C-S) case both at $Re = 1$ and $Re = 18$. This implies that incompressibility assumption can only be valid at Re as low as 0.1 under the present conditions. The inlet to outlet pressure ratio at $Re = 0.1$ was only 1.01. It should be noted that the flow is almost a creep flow at $Re = 0.1$. The flow separation does not occur at the step corner but a small recirculation region is formed at the step corner formed by the backward-facing wall and the heated wall.

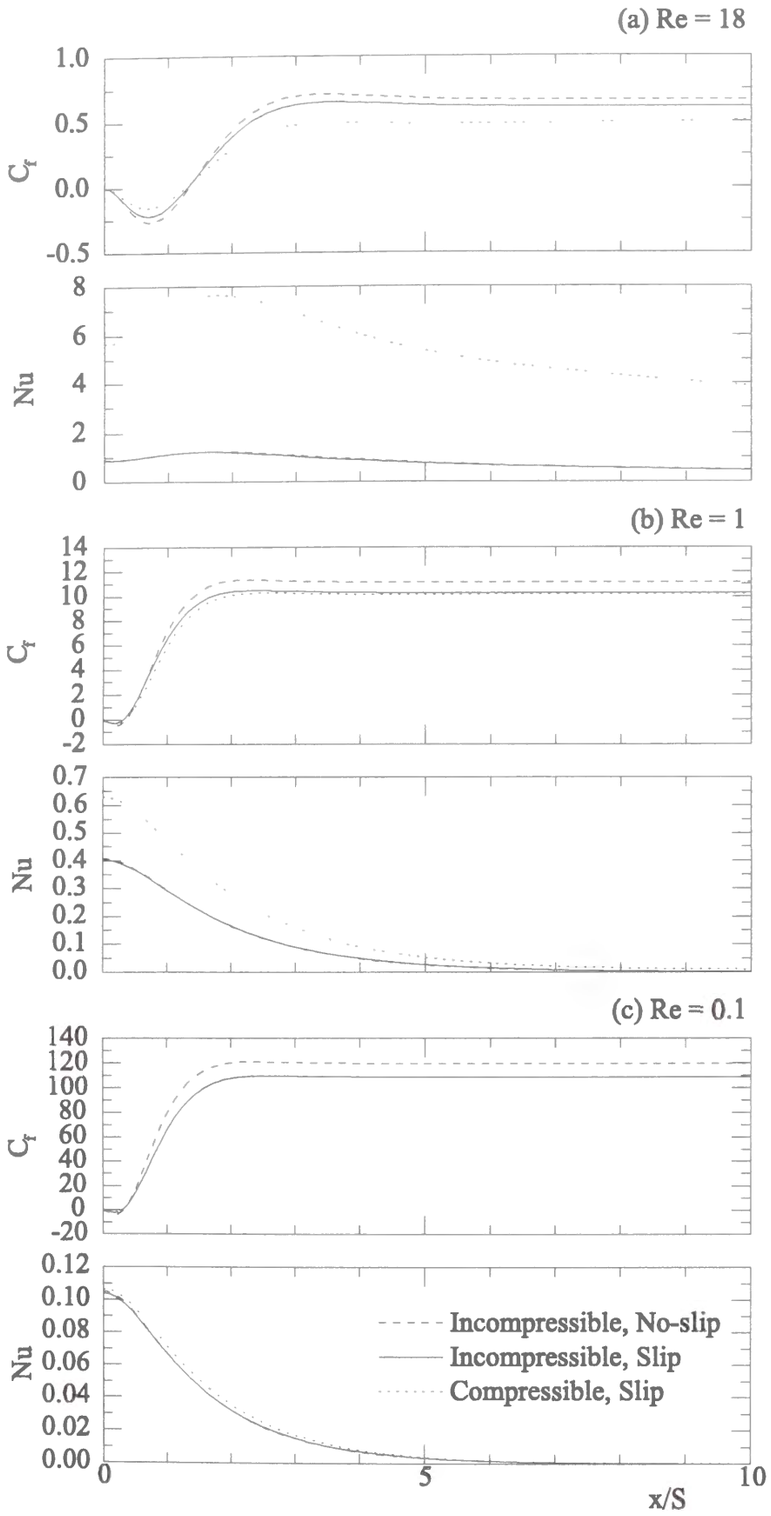

Figure 7.4: C_f and Nu distribution on the heated wall(2-D).

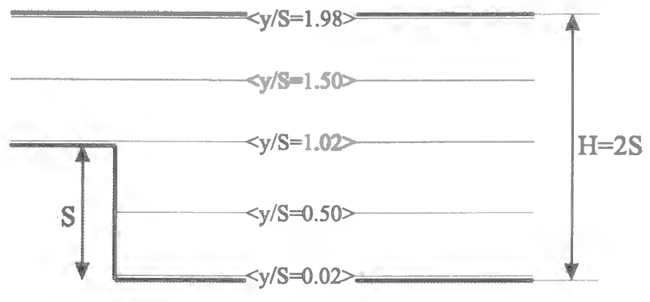

Figure 7.5: Monitoring locations.

Since the effects of both rarefaction and compressibility are clearly observed in Fig. 7.3 and Fig. 7.4 at $Re = 18$, details of the flow and thermal fields at this Reynolds number will be discussed. Figures 7.6, 7.7 and 7.8 present, respectively, the normalized pressure, streamwise velocity and the temperature distributions along x-direction at five different y locations for three different cases (I-N), (I-S) and (C-S). These y locations are schematically illustrated in Fig. 7.5. P_o in Fig. 7.6 and c_o in Fig. 7.7 are the pressure and the sound speed at the duct outlet, respectively.

In Fig. 7.6, all the three patterns of pressure distribution are similar to one another. Pressure changes almost linearly in the streamwise direction except for the near step region ($-1 < x/S < 4$). Although it is reported that the pressure distribution becomes non-linear in straight microchannels [9], only slight deviation from linearity can be observed in the case (C-S) in the regions $x/S < -1$ and $4 < x/S$ in the present study. A significant pressure drop is observed at the step location ($x/S = 0$) along $y/S = 1.02$. It can be seen in Fig. 7.6 that the pressure drop is always largest in the (I-N) case, reflecting its relatively high skin friction coefficient shown in Fig. 7.4.

In Fig. 7.7 and Fig. 7.8, a significant difference can be observed between the incompressible cases (I-N) (I-S) and the compressible case (C-S). In the incompressible flow cases,

change of streamwise velocity occurs only near step region ($-2 < x/S < 8$). As for the other regions ($x/S < -2, 8 < x/S$), the value of streamwise velocity at each y/S location is found to be constant, where fully developed flow is expected to exist. In the compressible flow case, on the other hand, flow accelerates together with the decrease of the pressure, even in the regions $x/S < -2$ and $8 < x/S$ where flow is free from the separation and reattachment effect. In Fig. 7.8(c), a drastic temperature decrease can be observed in the entrance section ($x/S < 0$) where flow is passing between two thermally adiabatic walls. Conversion of thermal energy into kinetic energy is clearly observed in this entrance section. This results in the decrease of main flow temperature toward the downstream, and consequently a larger temperature gradient at the heated wall. This explains the higher local Nusselt number in the (C-S) case as found in Fig. 7.4.

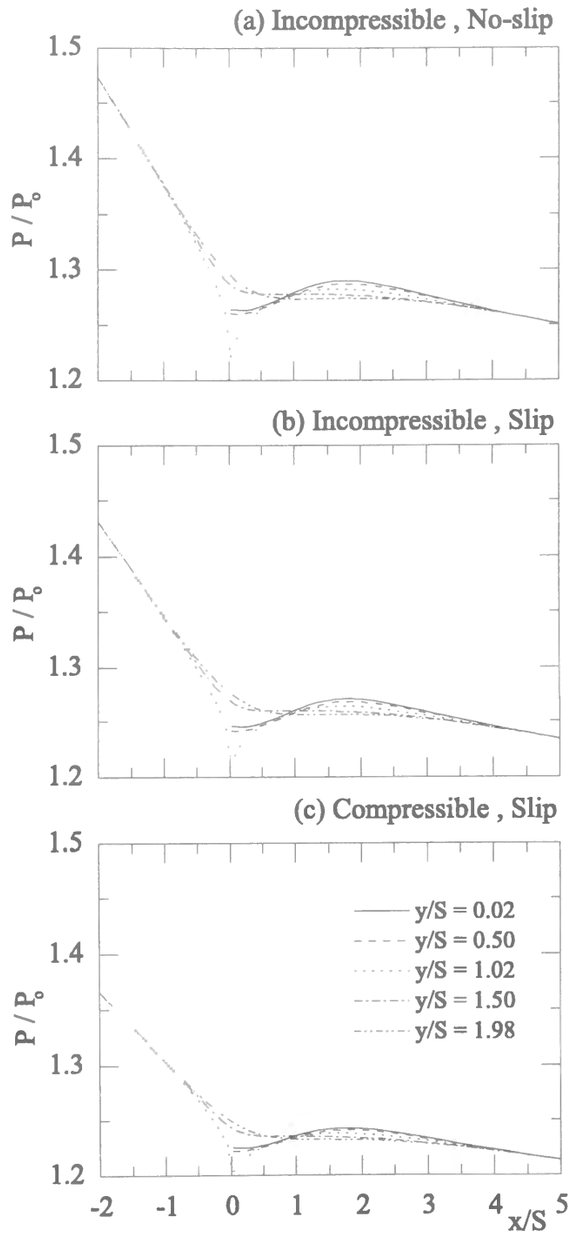

Figure 7.6: Pressure at several y locations($Re = 18$,2-D).

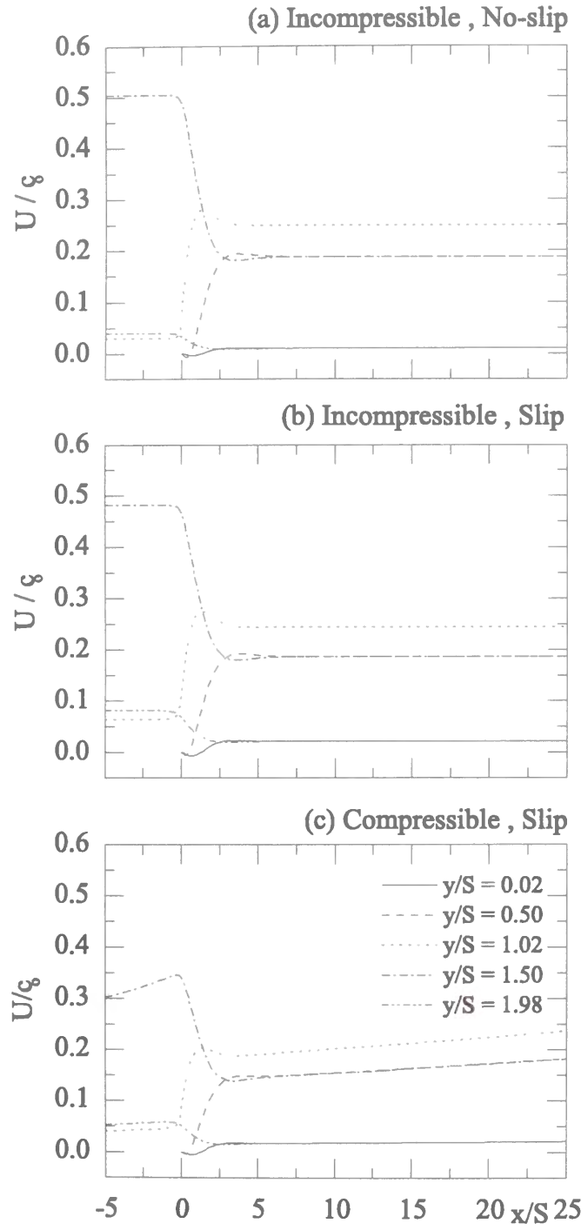

Figure 7.7: Streamwise velocity at several y locations($Re = 18$,2-D).

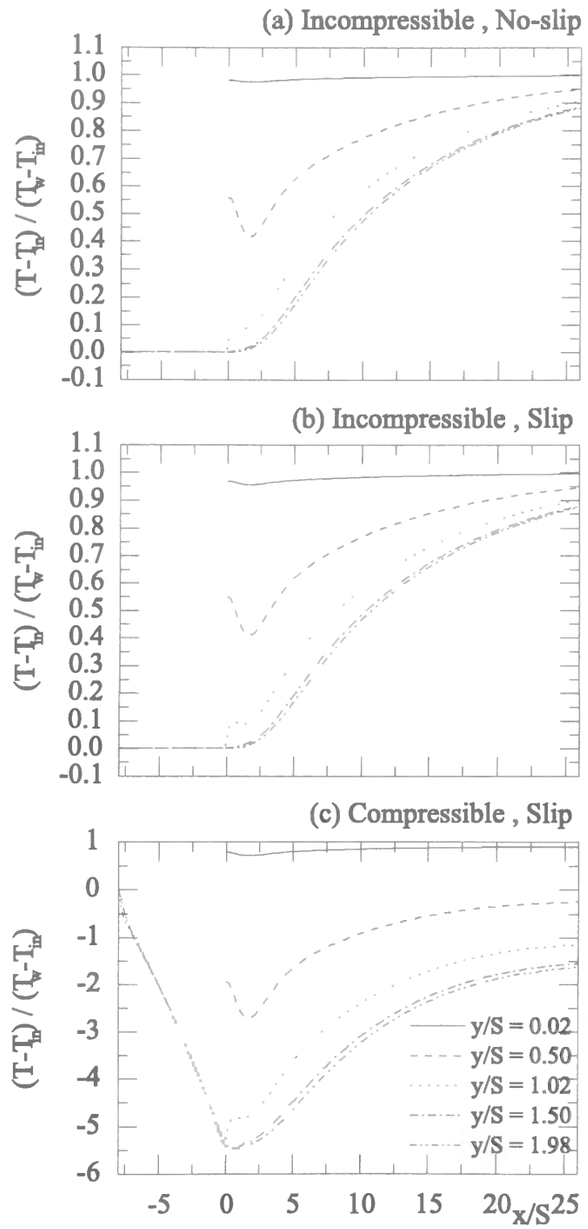

Figure 7.8: Temperature at several y locations($Re = 18$,2-D).

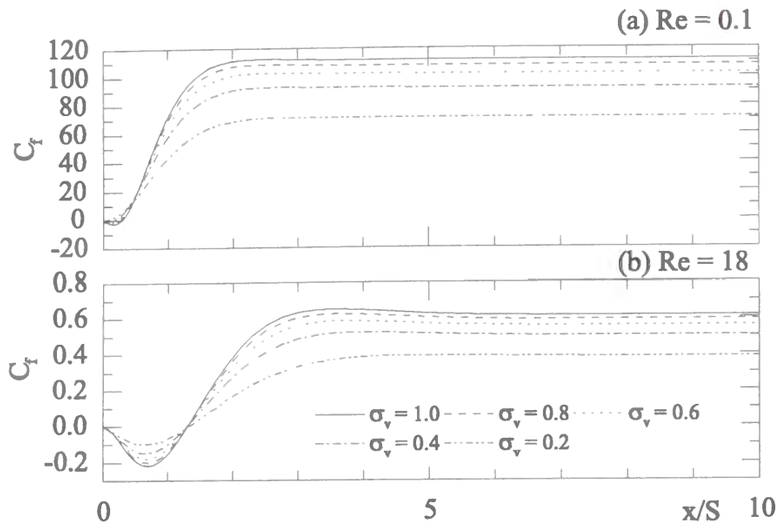

Figure 7.9: Effect of σ_v on C_f distribution(2-D).

In the above discussion, the velocity accommodation coefficient,σ_v and the outlet Knudsen number,Kn_o, have been kept constant at 1.0 and 0.013 respectively. The effect of σ_v and Kn_o are studied through 2-D simulations. Figure 7.9 shows the skin friction coefficient distribution at $Kn_o = 0.013$ for different accommodation coefficient,σ_v. Computations were carried out under incompressible assumption to focus on the effect of the accommodation coefficient. It was found that the position of reattachment point ($C_f = 0$) was not affected by the value of σ_v. The absolute value of skin friction coefficient at any streamwise location reduces monotonically with a decrease of σ_v, corresponding to larger slip velocity,U_s, defined at equation (7.7).

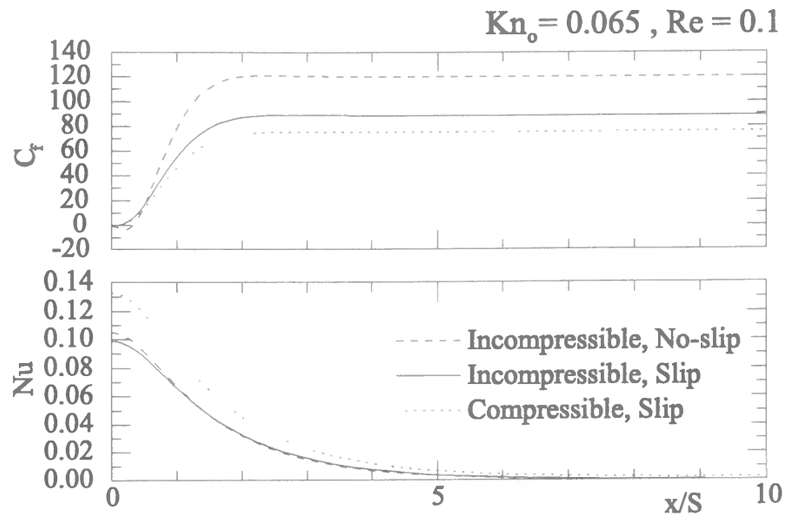

Figure 7.10: Effect of Kn_o on C_f and Nu distribution(2-D).

Figure 7.10 shows both the skin friction coefficient and Nusselt number distributions at $Re = 0.1$ and $Kn_o = 0.065$ for the cases (I-N), (I-S) and (C-S). A comparison between Fig. 7.10 and Fig. 7.4(c) reveals the influence of outlet Knudsen number,Kn_o. It is confirmed from the present results that the rarefaction effects become more important as Kn_o becomes larger. The decrease of C_f due to the slip condition is more prominent in Fig. 7.10 than in Fig. 7.4(c). Nu distribution in (I-S) case also shows slight deviation from that of (I-N) case at positions $0 \leq x/S < 2$ as is found in Fig. 7.10, which cannot be seen in Fig. 7.4. It can be seen in Fig. 7.10 that both C_f and Nu from the case (C-S) do not match those of the case (I-S), indicating that incompressible assumption is no longer valid. The inlet to outlet pressure ratio in the (C-S) case was only 1.11. The limit of Re where the incompressible assumption is valid becomes smaller as Kn_o increases.

The effects of rarefaction and compressibility on a backward-facing step flow have been so far discussed, only through 2-D simulations. It is reported in previous chapters that innegligible three dimensionality of flows could arise in a normal scale backward-facing step flow due to the existence of the side walls. To author's knowledge, there are only few investigations about the three dimensionality of microscale backward-facing step flows. Therefore, 3-D simulations are performed for the cases of (I-N), (I-S) and (C-S) at $Re = 18$ and $Kn_o = 0.013$ to see if any three dimensional flow and thermal structure can be observed. Figure 7.11 shows the Nusselt number contours on the heated wall. The gray tone level correspond to the level of Nusselt number. Thicker tone shows higher Nu. The distribution patterns of two incompressible cases are similar to each other. It indicates that the effect of rarefaction on heat transfer is small under the present condition. In the compressible case (C-S), Nu is larger over wide streamwise region downstream of the step as a result of conversion of thermal energy into kinetic energy observed in above 2-D simulations. It should be noted that Nu especially remains larger along the duct centerline in (C-S) case. The flow acceleration is expected to be more prominent around duct center region away from the side walls. The maximum Nusselt number, Nu_{max} appears near both side walls, not on the centerline of the bottom wall, in all the cases studied above. The locations and values of Nu_{max} in each case are summarized in Table 7.1.

Table 7.1 Locations and values of $Nu_{max}(Re = 18)$.

Code	x_{max}/S	$\lvert z_{max}/WD \rvert$	Nu_{max}
(I-N)	1.8	0.27	1.27
(I-S)	1.8	0.27	1.25
(C-S)	1.8	0.32	8.09

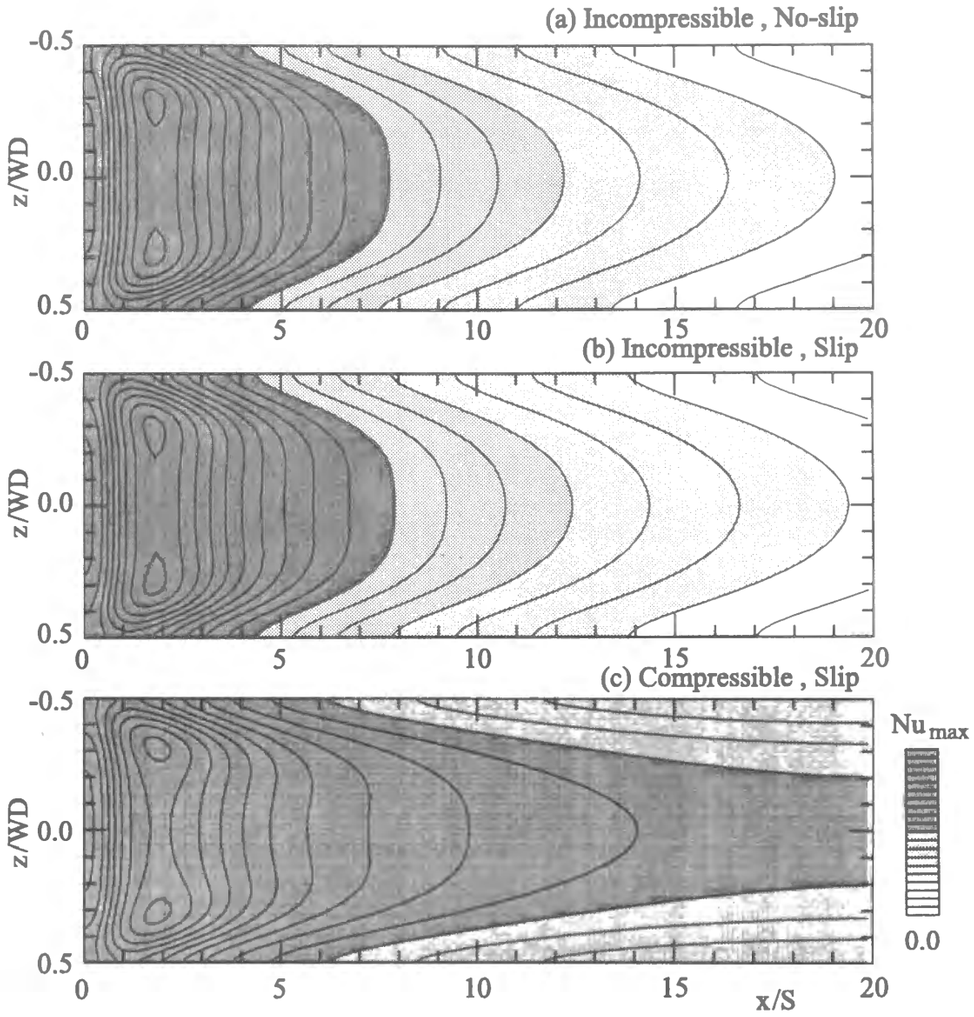

Figure 7.11: Nu contours on the heated wall($Re = 18$,3-D).

7.4 Conclusions

2-D and 3-D numerical computations were carried out for flows over a backward-facing step in a microscale duct to study the effects of rarefaction and compressibility. This chapter focused on the microscale flows in the slip flow regime. The following conclusions were obtained.

(1) Incompressible flow assumption is valid only at a Reynolds number as low as 0.1 for $Kn_o = 0.013$ under the conditions adopted in this study. The incompressible limit of Re becomes lower as Kn_o increases.

(2) The absolute value of skin friction coefficient is reduced when the velocity slip at the wall is taken into account. This effect is more prominent for a lager Knudsen number and/or a smaller accommodation coefficient. No significant effects of temperature jump condition on Nu distribution are observed under the conditions adopted in this study. When the compressibility effect is taken into account, Nu increases due to the lowering of fluid temperature caused by the conversion of thermal energy into kinetic energy. The effect of the velocity slip condition and thermal jump condition on the heat transfer is found to be relatively minor comparing to the effect of compressibility.

(3) In 3-D simulations, the maximum Nusselt number is obtained at two positions near the side walls symmetrically located with respect to the duct centerline, not on the centerline of the duct. This is similar to the results for the normal scale backstep flow. Higher Nu region is widely observed on the heated wall in the (C-S) case due to the compressibility effect mentioned in (2). No additional three-dimensional structure due to rarefaction and/or compressibility is observed.

References

[1] Tuckerman, D. B. and Pease, R. F. W., *High-Performance Heat Sinking for VLSI* , IEEE Electron Device Letters, Vol.EDL-2, No.5, pp.126-129 (1981).

[2] Ho, C.M. and Tai, Y.C., *Review: MEMS and its Applications for Flow Control*, J. Fluid Eng., vol.118, pp.437-447 (1996).

[3] Beskok, A. and Karniadakis, G. E., *Modeling Separation in Rarefied Gas Flows*, AIAA 97-1883 (1997).

[4] Beskok, A., Karniadakis, G. E. and Trimmer, W., *Rarefaction and Compressibility Effects in Gas Microflows*, J. Fluids Engineering, Vol.118, pp.448-456 (1996).

[5] Arkilic, E. B., Breuer, K. S. and Schmidt, M. A., *Gaseous Flow in Microchannels*, ASME Application of Microfabrication to Fluid Mechanics, FED-Vol. 197, pp.57-66 (1994).

[6] Schaaf, S.A. and Chambre, P.L., *Flow of Rarefied Gases*, (1961), Princeton University Press.

[7] Saxena, S.C. and Joshi, R.K., *Thermal Accommodation and Adsorption Coefficients of Gasses*, Vol.1,2, Series Editors Y.S. Touloukian, C.Y. Ho, McGraw-Hill/CINDAS Data Series on Material Properties, (1981), McGraw-Hill.

[8] Guo, Z.Y. and Wu, X.B., *Friction Factor and Nusselt Number of Gas Flow in Smooth Microtubes*, Proc. of the Symposium on Molecular and Micro Heat Transfer in Materials Processing and Other Applications, pp.66-73 (1996).

[9] Pong, K.C., Ho, C.M., Liu, J. and Tai, Y.C., *Non-linear Pressure Distribution in Uniform Microchannels*, ASME Application of Microfabrication to Fluid Mechanics, FED-Vol.197, pp.51-56 (1994).

Chapter 8

Conclusions

8.1 Conclusions

This study aims at investigating details of the flow structures and the related heat transfer characteristics of flows over a backward-facing step in a rectangular duct in a wide range of Reynolds number. Two- and three-dimensional numerical computations were performed for backward-facing step flows and heat transfer. The major findings are summarized below.

In Chapter 2, the fundamental procedure of numerical simulation adopted in the present study has been outlined. The governing equations were discretised using Finite-Volume Method. Staggered grid arrangement was employed as the grid system. Non-uniform grid system was employed whereby grid points were allocated densely near the walls in order to save the computational time. Fifth-order upwind scheme and fourth-order central scheme were used as the finite difference methods or the convection and diffusion terms respectively. The obtained fully implicit forms of the equations were solved, using SIMPLE algorithm for the computation of pressure. The details of the boundary conditions are described in each chapter.

Chapter 3 presented the results of three-dimensional numerical simulations performed for the laminar flows over a backward-facing step in a rectangular duct. It was found that an aspect ratio of as large as AR=16 is needed at least to secure two-dimensional region

in the central part of the duct at Re=250. In the case of constant aspect ratio, the area of the two-dimensional region becomes larger, as Re number is decreased. It is also found that the maximum Nusselt number on the bottom wall is obtained at two positions near the side walls located symmetrically with respect to the duct centerline, and not on the centerline in all the cases studied here. This is due to the downwash flow directed toward the bottom wall near the both side walls. The value of maximum Nusselt number increases with an increase of the aspect ratio and/or Re number. Spiral motion of the fluid particles starting from the vicinity of a side wall was observed in the recirculating flow region behind the step. This spiral fluid motion approaches toward the center of the duct because of the spanwise pressure non-uniformity decreasing toward the centerline.

Chapter 4 presented the effects of buoyancy on the flow and thermal fields over a backward-facing step. 2-D and 3-D numerical computations were carried out for mixed convective upward flows under the conditions such that the flow remains steady if buoyancy is being neglected. The following conclusions were obtained. It was found through 2-D simulations that both of the reattachment point and the peak Nusselt number point move upstream as the modified Richardson number,Ri^*, increases, while the secondary recirculation region, formed at the corner of the step becomes larger in size. The main recirculation region detaches from the heated wall at Ri^*=0.12. The peak Nusselt number point always appear downstream of the reattachment point and the distance between them increases as Ri^* increases. The results of 3-D simulations have shown that maximum Nusselt number positions on the heated wall are located symmetrically with respect to the duct centerline near the side walls, in a similar manner to the cases of pure forced convection and their positions shift upstream as Ri^* increases. There also exists an inward flow near the bottom wall right after the step, where flow is directed toward the center of the duct. Such flow becomes more intensive as Ri^* increases. Three-dimensionality of the flow and thermal fields related to this inward flow right after the step becomes prominent when $Ri^* > 0.06$ at $Re = 125$.

Chapter 5 presented the results of 3-D numerical simulations performed for mixed con-

vective flows over a backward-facing step in a duct to study the effects of two inclination angles, the pitch angle θ_1 and the rolling angle θ_2. The positions of reattachment point, peak Nusselt number point and the downstream size of secondary recirculation region on the centerline of the heated wall move with the change of θ_1. The positions of the maximum Nusselt numbers are symmetrically obtained at the positions on the heated wall near the two side walls, similar to the cases of pure forced convection. The value of maximum Nusselt number and its position are affected by the value of θ_1. Buoyancy effects seems to be relatively small in the cases of horizontal flows. When θ_2 is changed, on the other hand, the flow and thermal fields become asymmetric about the duct centerline. The downwash flow directed toward the heated wall is prominent only near the lower side wall, resulting only one Nu_{max} there.

Chapter 6 presented the results of 2-D and 3-D simulations performed for turbulent flows over a backward-facing step. Two types of turbulent models, Launder-Sharma model with Yap correction and non-linear eddy viscosity model by Craft, Suga and Launder, were introduced. The computations were carried out for two different aspect ratios (AR=4 and 12) in 3-D simulation to investigate three-dimensionality of the flow and thermal fields. The results obtained by 2-D simulations show that both the LS + Yap model and the CSL model are capable to reproduce mean streamwise velocity profiles. Quantitative comparisons of statistical quantities made with the experimental data show that the LS + Yap model gives slightly better agreement in the statistical quantities calculated in the centerplane than the more complex CSL model. However, qualitatively, the CSL model gives a better description of the physics of the flow when 3-D effects become important. The general belief that two-dimensionality along the centerplane can be assumed for backstep flows with an aspect ratio greater than 10 is tolerably correct. High Nu region is observed over the streamwise positions of $5 < x/S < 15$ for both of the aspect ratios. Those high Nu regions are obtained not only as the result of heat transfer enhancement due to the turbulence, but also as the result of the downwash flow, similar to the laminar flow cases discussed in Chapter 3. Transverse counter rotating eddies are observed in the relatively low velocity

region right after the step, resulting the highly three-dimensional flow and thermal field there.

Chapter 7 presented the results of 2-D and 3-D numerical computations performed for flows over a backward-facing step in a microscale duct to study the effects of rarefaction (velocity slip condition and thermal jump condition) and compressibility. Incompressible flow assumption is valid only at a Reynolds number as low as 0.1 for $Kn_o = 0.013$ under the conditions adopted in this study. The incompressible limit of Re becomes lower as Kn_o increases. The absolute value of skin friction coefficient is reduced when the velocity slip at the wall is taken into account. This effect is more prominent for a lager Knudsen number and/or a smaller accommodation coefficient. When the compressibility effect is taken into account, Nu increases due to the lowering of fluid temperature caused by the conversion of thermal energy into kinetic energy. The effect of the rarefaction on the heat transfer is relatively minor comparing to the effect of compressibility. In 3-D simulations, the maximum Nusselt number is obtained at two positions near the side walls symmetrically located with respect to the duct centerline, similar to the results for the normal scale backstep flow. Higher Nu region is widely observed on the heated wall in the case in which compressibility effect is taken into account. No additional three-dimensional structure due to rarefaction and/or compressibility is observed.

8.2 Suggestions for the future work

Three-dimensional flow and thermal structures of flows over a backward-facing step were the major interests and have been discussed through the results of numerical computations in this thesis. It was found that there were conditions under which the three-dimensionality could play an important role in terms of heat transfer enhancement in both laminar and turbulent flow cases. Nevertheless, as is described in Chapter 1, many of the investigation available today were carried out under two-dimensional assumption. Therefore, it would be worthwhile to perform an accurate and reliable measurement for three-dimensional flow and thermal fields, especially near side walls after the step where flow structure was expected

to be very different from the flow at the duct center region even at a relatively large aspect ratio.

Intensive and continuous efforts have been made by many researchers to develop turbulent models. The CSL model, which is one of the latest models, was found to give a good description of the physics of the flow when 3-D effects become important. However it seems the results of the simulations with CSL model are still not satisfactory if compared quantitatively with experimental data. A further development of the turbulent model is desired for three-dimensional flows with separation and reattachment phenomena.

The investigation for the microscale flows with separation and reattachment phenomena is still on its early stage and there are only few data available. Intensive numerical investigations on this problem are desired. Great difficulties are expected in the experimental approach for this problem because of the extremely small duct size, some experimental data, which reflect the effect of the flow separation and reattachment phenomena, are desired.

Appendix

Launder-Sharma model

x-momentum equation

$$\begin{aligned}\frac{\partial \rho U}{\partial t}+\frac{\partial \rho UU}{\partial x}+\frac{\partial \rho VU}{\partial y}+\frac{\partial \rho WU}{\partial z} &= \frac{\partial P}{\partial x}-\frac{\partial}{\partial x}\left(\frac{2}{3}k\rho\right)\\ &+\frac{\partial}{\partial x}\left(\left(\mu_t+\mu\right)\frac{\partial U}{\partial x}\right)+\frac{\partial}{\partial y}\left(\left(\mu_t+\mu\right)\frac{\partial U}{\partial y}\right)+\frac{\partial}{\partial z}\left(\left(\mu_t+\mu\right)\frac{\partial U}{\partial z}\right)\\ &+\frac{\partial}{\partial x}\left(\mu_t\frac{\partial U}{\partial x}\right)+\frac{\partial}{\partial y}\left(\mu_t\frac{\partial V}{\partial x}\right)+\frac{\partial}{\partial z}\left(\mu_t\frac{\partial W}{\partial x}\right)\end{aligned}$$

y-momentum equation

$$\begin{aligned}\frac{\partial \rho V}{\partial t}+\frac{\partial \rho UV}{\partial x}+\frac{\partial \rho VV}{\partial y}+\frac{\partial \rho WV}{\partial z} &= -\frac{\partial P}{\partial y}-\frac{\partial}{\partial y}\left(\frac{2}{3}k\rho\right)\\ &+\frac{\partial}{\partial x}\left(\left(\mu_t+\mu\right)\frac{\partial V}{\partial x}\right)+\frac{\partial}{\partial y}\left(\left(\mu_t+\mu\right)\frac{\partial V}{\partial y}\right)+\frac{\partial}{\partial z}\left(\left(\mu_t+\mu\right)\frac{\partial V}{\partial z}\right)\\ &+\frac{\partial}{\partial x}\left(\mu_t\frac{\partial U}{\partial y}\right)+\frac{\partial}{\partial y}\left(\mu_t\frac{\partial V}{\partial y}\right)+\frac{\partial}{\partial z}\left(\mu_t\frac{\partial W}{\partial y}\right)\end{aligned}$$

z-momentum equation

$$\begin{aligned}\frac{\partial \rho W}{\partial t}+\frac{\partial \rho UW}{\partial x}+\frac{\partial \rho VW}{\partial y}+\frac{\partial \rho WW}{\partial z} &= -\frac{\partial P}{\partial z}-\frac{\partial}{\partial z}\left(\frac{2}{3}k\rho\right)\\ &+\frac{\partial}{\partial x}\left(\left(\mu_t+\mu\right)\frac{\partial W}{\partial x}\right)+\frac{\partial}{\partial y}\left(\left(\mu_t+\mu\right)\frac{\partial W}{\partial y}\right)+\frac{\partial}{\partial z}\left(\left(\mu_t+\mu\right)\frac{\partial W}{\partial z}\right)\\ &+\frac{\partial}{\partial x}\left(\mu_t\frac{\partial U}{\partial z}\right)+\frac{\partial}{\partial y}\left(\mu_t\frac{\partial V}{\partial z}\right)+\frac{\partial}{\partial z}\left(\mu_t\frac{\partial W}{\partial z}\right)\end{aligned}$$

k-equation

$$\begin{aligned}\frac{\partial \rho k}{\partial t}+\frac{\partial \rho Uk}{\partial x}+\frac{\partial \rho Vk}{\partial y}+\frac{\partial \rho Wk}{\partial z} &= \frac{\partial}{\partial x}\left(\left(\frac{\mu_t}{\sigma_k}+\mu\right)\frac{\partial k}{\partial x}\right)+\frac{\partial}{\partial y}\left(\left(\frac{\mu_t}{\sigma_k}+\mu\right)\frac{\partial k}{\partial y}\right)+\frac{\partial}{\partial z}\left(\left(\frac{\mu_t}{\sigma_k}+\mu\right)\frac{\partial k}{\partial z}\right)\\ &+\mu_t\left\{2\left(\frac{\partial U}{\partial x}\right)^2+2\left(\frac{\partial V}{\partial y}\right)^2+2\left(\frac{\partial W}{\partial z}\right)^2\right.\\ &\left.+\left(\frac{\partial U}{\partial y}+\frac{\partial V}{\partial x}\right)^2+\left(\frac{\partial V}{\partial z}+\frac{\partial W}{\partial y}\right)^2+\left(\frac{\partial W}{\partial x}+\frac{\partial U}{\partial z}\right)^2\right\}\\ &-2\mu\left[\left(\frac{\partial\sqrt{k}}{\partial x}\right)^2+\left(\frac{\partial\sqrt{k}}{\partial y}\right)^2+\left(\frac{\partial\sqrt{k}}{\partial z}\right)^2\right]\\ &-\rho\tilde{\varepsilon}\end{aligned}$$

$\tilde{\varepsilon}$-equation

$$
\begin{aligned}
\frac{\partial \rho\tilde{\varepsilon}}{\partial t}+\frac{\partial \rho U\tilde{\varepsilon}}{\partial x}+\frac{\partial \rho V\tilde{\varepsilon}}{\partial y}+\frac{\partial \rho W\tilde{\varepsilon}}{\partial z} &= \frac{\partial}{\partial x}\left(\left(\frac{\mu_t}{\sigma_\varepsilon}+\mu\right)\frac{\partial \tilde{\varepsilon}}{\partial x}\right)+\frac{\partial}{\partial y}\left(\left(\frac{\mu_t}{\sigma_\varepsilon}+\mu\right)\frac{\partial \tilde{\varepsilon}}{\partial y}\right)+\frac{\partial}{\partial z}\left(\left(\frac{\mu_t}{\sigma_\varepsilon}+\mu\right)\frac{\partial \tilde{\varepsilon}}{\partial z}\right)\\
&+C_{\varepsilon 1}f_1\frac{\tilde{\varepsilon}}{k}\mu_t\left\{2\left(\frac{\partial U}{\partial x}\right)^2+2\left(\frac{\partial V}{\partial y}\right)^2+2\left(\frac{\partial W}{\partial z}\right)^2\right.\\
&\left.+\left(\frac{\partial U}{\partial y}+\frac{\partial V}{\partial x}\right)^2+\left(\frac{\partial V}{\partial z}+\frac{\partial W}{\partial y}\right)^2+\left(\frac{\partial W}{\partial x}+\frac{\partial U}{\partial z}\right)^2\right\}\\
&-C_{\varepsilon 2}\rho f_2\frac{\tilde{\varepsilon}^2}{k}\\
&+2\nu\mu_t\left\{\left(\frac{\partial^2 U}{\partial x^2}\right)^2+\left(\frac{\partial^2 V}{\partial y^2}\right)^2+\left(\frac{\partial^2 W}{\partial z^2}\right)^2\right.\\
&+\left(\frac{\partial^2 U}{\partial y^2}\right)^2+\left(\frac{\partial^2 U}{\partial z^2}\right)^2+\left(\frac{\partial^2 V}{\partial x^2}\right)^2+\left(\frac{\partial^2 V}{\partial z^2}\right)^2+\left(\frac{\partial^2 W}{\partial x^2}\right)^2+\left(\frac{\partial^2 W}{\partial y^2}\right)^2\\
&+2\left(\frac{\partial^2 U}{\partial x\partial y}\right)^2+2\left(\frac{\partial^2 U}{\partial y\partial z}\right)^2+2\left(\frac{\partial^2 U}{\partial x\partial z}\right)^2\\
&+2\left(\frac{\partial^2 V}{\partial y\partial z}\right)^2+2\left(\frac{\partial^2 V}{\partial z\partial x}\right)^2+2\left(\frac{\partial^2 V}{\partial x\partial y}\right)^2\\
&+2\left(\frac{\partial^2 W}{\partial z\partial x}\right)^2+2\left(\frac{\partial^2 W}{\partial x\partial y}\right)^2+2\left(\frac{\partial^2 W}{\partial y\partial z}\right)^2\Bigg\}
\end{aligned}
$$

Craft-Suga-Launder model (2 Eq-NLEVM)

$$
\begin{aligned}
\rho\overline{uu} &= \frac{2}{3}k\rho-\mu_t S_{11}\\
&+c_1\mu_t\frac{k}{\tilde{\varepsilon}}\left({S_{11}}^2+{S_{12}}^2+{S_{13}}^2-\frac{1}{3}S_{ij}S_{ij}\right)\\
&+2c_2\mu_t\frac{k}{\tilde{\varepsilon}}\left(S_{12}\Omega_{12}+S_{13}\Omega_{13}\right)\\
&+c_3\mu_t\frac{k}{\tilde{\varepsilon}}\left({\Omega_{12}}^2+{\Omega_{13}}^2-\frac{1}{3}\Omega_{ij}\Omega_{ij}\right)\\
&-2c_4\mu_t(\frac{k}{\tilde{\varepsilon}})^2\quad\left(S_{11}S_{12}\Omega_{12}+S_{11}S_{13}\Omega_{13}+S_{12}S_{22}\Omega_{12}\right.\\
&\quad\left.+S_{12}S_{23}\Omega_{13}+S_{13}S_{23}\Omega_{12}+S_{13}S_{33}\Omega_{13}\right)\\
&+c_6\mu_t(\frac{k}{\tilde{\varepsilon}})^2S_{11}S_{ij}S_{ij}\\
&+c_7\mu_t(\frac{k}{\tilde{\varepsilon}})^2S_{11}\Omega_{ij}\Omega_{ij}
\end{aligned}
$$

$$
\begin{aligned}
\rho\overline{uv} &= -\mu_t S_{12}\\
&+c_1\mu_t\frac{k}{\tilde{\varepsilon}}\left(S_{11}S_{12}+S_{12}S_{22}+S_{13}S_{23}\right)\\
&+c_2\mu_t\frac{k}{\tilde{\varepsilon}}\left(-S_{11}\Omega_{12}+S_{22}\Omega_{12}+S_{23}\Omega_{13}+S_{31}\Omega_{23}\right)\\
&+c_3\mu_t\frac{k}{\tilde{\varepsilon}}\left(\Omega_{13}\Omega_{23}\right)\\
&+c_4\mu_t(\frac{k}{\tilde{\varepsilon}})^2\left(S_{11}^2\Omega_{12}-S_{11}S_{13}\Omega_{23}-S_{12}S_{13}\Omega_{13}\right.\\
&\quad-S_{22}^2\Omega_{12}-S_{12}S_{23}\Omega_{23}-S_{22}S_{23}\Omega_{13}\\
&\quad\left.+S_{13}^2\Omega_{12}-S_{23}^2\Omega_{12}-S_{13}S_{33}\Omega_{23}-S_{23}S_{33}\Omega_{13}\right)\\
&+c_6\mu_t(\frac{k}{\tilde{\varepsilon}})^2S_{12}S_{ij}S_{ij}\\
&+c_7\mu_t(\frac{k}{\tilde{\varepsilon}})^2S_{12}\Omega_{ij}\Omega_{ij}
\end{aligned}
$$

$$
\begin{aligned}
\rho\overline{uw} &= -\mu_t S_{13}\\
&+c_1\mu_t\frac{k}{\tilde{\varepsilon}}\left(S_{11}S_{13}+S_{12}S_{23}+S_{13}S_{33}\right)\\
&+c_2\mu_t\frac{k}{\tilde{\varepsilon}}\left(-S_{11}\Omega_{13}+S_{23}\Omega_{12}+S_{12}\Omega_{23}+S_{33}\Omega_{13}\right)\\
&-c_3\mu_t\frac{k}{\tilde{\varepsilon}}\left(\Omega_{12}\Omega_{23}\right)\\
&+c_4\mu_t(\frac{k}{\tilde{\varepsilon}})^2\left(S_{11}^2\Omega_{13}+S_{11}S_{12}\Omega_{23}-S_{12}S_{13}\Omega_{12}\right.\\
&\quad+S_{12}^2\Omega_{13}+S_{12}S_{22}\Omega_{23}-S_{22}S_{23}\Omega_{12}-S_{23}^2\Omega_{13}\\
&\quad\left.+S_{13}S_{23}\Omega_{23}-S_{23}S_{33}\Omega_{12}-S_{33}^2\Omega_{13}\right)
\end{aligned}
$$

$$
\begin{aligned}
&+c_6\mu_t(\frac{k}{\tilde{\varepsilon}})^2 S_{13}S_{ij}S_{ij} \\
&+c_7\mu_t(\frac{k}{\tilde{\varepsilon}})^2 S_{13}\Omega_{ij}\Omega_{ij}
\end{aligned}
$$

$$
\begin{aligned}
\rho\overline{vv} &= \frac{2}{3}k\rho - \mu_t S_{22} \\
&+c_1\mu_t\frac{k}{\tilde{\varepsilon}}\left({S_{22}}^2 + {S_{12}}^2 + {S_{23}}^2 - \frac{1}{3}S_{ij}S_{ij}\right) \\
&-2c_2\mu_t\frac{k}{\tilde{\varepsilon}}\left(S_{12}\Omega_{12} - S_{23}\Omega_{23}\right) \\
&+c_3\mu_t\frac{k}{\tilde{\varepsilon}}\left({\Omega_{12}}^2 + {\Omega_{23}}^2 - \frac{1}{3}\Omega_{ij}\Omega_{ij}\right) \\
&+2c_4\mu_t(\frac{k}{\tilde{\varepsilon}})^2 \quad (S_{11}S_{12}\Omega_{12} - S_{12}S_{13}\Omega_{23} + S_{12}S_{22}\Omega_{12} \\
&\quad -S_{22}S_{23}\Omega_{23} + S_{13}S_{23}\Omega_{12} - S_{23}S_{33}\Omega_{23}) \\
&+c_6\mu_t(\frac{k}{\tilde{\varepsilon}})^2 S_{22}S_{ij}S_{ij} \\
&+c_7\mu_t(\frac{k}{\tilde{\varepsilon}})^2 S_{22}\Omega_{ij}\Omega_{ij}
\end{aligned}
$$

$$
\begin{aligned}
\rho\overline{vu} &= -\mu_t S_{12} \\
&+c_1\mu_t\frac{k}{\tilde{\varepsilon}}\left(S_{11}S_{12} + S_{12}S_{22} + S_{13}S_{23}\right) \\
&+c_2\mu_t\frac{k}{\tilde{\varepsilon}}\left(-S_{11}\Omega_{12} + S_{22}\Omega_{12} + S_{23}\Omega_{13} + S_{31}\Omega_{23}\right) \\
&+c_3\mu_t\frac{k}{\tilde{\varepsilon}}\left(\Omega_{13}\Omega_{23}\right) \\
&+c_4\mu_t(\frac{k}{\tilde{\varepsilon}})^2\left(S_{11}^2\Omega_{12} - S_{11}S_{13}\Omega_{23} - S_{12}S_{13}\Omega_{13}\right. \\
&\quad - S_{22}^2\Omega_{12} - S_{12}S_{23}\Omega_{23} - S_{22}S_{23}\Omega_{13} \\
&\quad \left. + S_{13}^2\Omega_{12} - S_{23}^2\Omega_{12} - S_{13}S_{33}\Omega_{23} - S_{23}S_{33}\Omega_{13}\right) \\
&+c_6\mu_t(\frac{k}{\tilde{\varepsilon}})^2 S_{12}S_{ij}S_{ij} \\
&+c_7\mu_t(\frac{k}{\tilde{\varepsilon}})^2 S_{12}\Omega_{ij}\Omega_{ij}
\end{aligned}
$$

$$
\begin{aligned}
\rho\overline{vw} &= -\mu_t S_{23} \\
&+c_1\mu_t\frac{k}{\tilde{\varepsilon}}\left(S_{12}S_{13} + S_{22}S_{23} + S_{23}S_{33}\right) \\
&+c_2\mu_t\frac{k}{\tilde{\varepsilon}}\left(-S_{13}\Omega_{12} - S_{12}\Omega_{13} - S_{22}\Omega_{23} + S_{33}\Omega_{23}\right) \\
&+c_3\mu_t\frac{k}{\tilde{\varepsilon}}\left(\Omega_{12}\Omega_{13}\right) \\
&+c_4\mu_t(\frac{k}{\tilde{\varepsilon}})^2\left(S_{11}S_{12}\Omega_{13} + S_{11}S_{13}\Omega_{12} + S_{12}^2\Omega_{23} - S_{13}^2\Omega_{23}\right.
\end{aligned}
$$

$$
\begin{aligned}
&\quad + S_{12}S_{22}\Omega_{13} + S_{12}S_{23}\Omega_{12} + S_{22}^2\Omega_{23} \\
&\quad \left. + S_{13}S_{23}\Omega_{13} + S_{13}S_{33}\Omega_{12} - S_{33}^2\Omega_{23}\right) \\
&+c_6\mu_t(\frac{k}{\tilde{\varepsilon}})^2 S_{23}S_{ij}S_{ij} \\
&+c_7\mu_t(\frac{k}{\tilde{\varepsilon}})^2 S_{23}\Omega_{ij}\Omega_{ij}
\end{aligned}
$$

$$
\begin{aligned}
\rho\overline{ww} &= \frac{2}{3}k\rho - \mu_t S_{33} \\
&+c_1\mu_t\frac{k}{\tilde{\varepsilon}}\left({S_{33}}^2 + {S_{13}}^2 + {S_{23}}^2 - \frac{1}{3}S_{ij}S_{ij}\right) \\
&-2c_2\mu_t\frac{k}{\tilde{\varepsilon}}\left(S_{13}\Omega_{13} + S_{23}\Omega_{23}\right) \\
&+c_3\mu_t\frac{k}{\tilde{\varepsilon}}\left({\Omega_{13}}^2 + {\Omega_{23}}^2 - \frac{1}{3}\Omega_{ij}\Omega_{ij}\right) \\
&+2c_4\mu_t(\frac{k}{\tilde{\varepsilon}})^2 \quad (S_{11}S_{13}\Omega_{13} + S_{12}S_{13}\Omega_{23} + S_{12}S_{23}\Omega_{13} \\
&\quad +S_{22}S_{23}\Omega_{23} + S_{13}S_{33}\Omega_{13} - S_{23}S_{33}\Omega_{23}) \\
&+c_6\mu_t(\frac{k}{\tilde{\varepsilon}})^2 S_{33}S_{ij}S_{ij} \\
&+c_7\mu_t(\frac{k}{\tilde{\varepsilon}})^2 S_{33}\Omega_{ij}\Omega_{ij}
\end{aligned}
$$

$$
\overline{ww} = 2k - \overline{uu} - \overline{vv}
$$

$$
\begin{aligned}
\rho\overline{wu} &= -\mu_t S_{13} \\
&+c_1\mu_t\frac{k}{\tilde{\varepsilon}}\left(S_{11}S_{13} + S_{12}S_{23} + S_{13}S_{33}\right) \\
&+c_2\mu_t\frac{k}{\tilde{\varepsilon}}\left(-S_{11}\Omega_{13} + S_{23}\Omega_{12} - S_{12}\Omega_{23} + S_{33}\Omega_{13}\right) \\
&-c_3\mu_t\frac{k}{\tilde{\varepsilon}}\left(\Omega_{12}\Omega_{23}\right) \\
&+c_4\mu_t(\frac{k}{\tilde{\varepsilon}})^2\left(S_{11}^2\Omega_{13} + S_{11}S_{12}\Omega_{23} - S_{12}S_{13}\Omega_{12}\right. \\
&\quad + S_{12}^2\Omega_{13} + S_{12}S_{22}\Omega_{23} - S_{22}S_{23}\Omega_{12} - S_{23}^2\Omega_{13} \\
&\quad \left. + S_{13}S_{23}\Omega_{23} - S_{23}S_{33}\Omega_{12} - S_{33}^2\Omega_{13}\right) \\
&+c_6\mu_t(\frac{k}{\tilde{\varepsilon}})^2 S_{13}S_{ij}S_{ij} \\
&+c_7\mu_t(\frac{k}{\tilde{\varepsilon}})^2 S_{13}\Omega_{ij}\Omega_{ij}
\end{aligned}
$$

$$
\begin{aligned}
\rho\overline{wv} &= \mu_t S_{23} \\
&+c_1\mu_t\frac{k}{\tilde{\varepsilon}}\left(S_{12}S_{13} + S_{22}S_{23} + S_{23}S_{33}\right) \\
&+c_2\mu_t\frac{k}{\tilde{\varepsilon}}\left(-S_{13}\Omega_{12} - S_{12}\Omega_{13} - S_{22}\Omega_{23} + S_{33}\Omega_{23}\right)
\end{aligned}
$$

$$+c_3\mu_t\frac{k}{\tilde{\varepsilon}}\left(\Omega_{12}\Omega_{13}\right)$$
$$+c_4\mu_t(\frac{k}{\tilde{\varepsilon}})^2\Big(S_{11}S_{12}\Omega_{13}+S_{11}S_{13}\Omega_{12}+S_{12}^2\Omega_{23}-S_{13}^2\Omega_{23}$$
$$+S_{12}S_{22}\Omega_{13}+S_{12}S_{23}\Omega_{12}+S_{22}^2\Omega_{23}$$
$$+S_{13}S_{23}\Omega_{13}+S_{13}S_{33}\Omega_{12}-S_{33}^2\Omega_{23}\Big)$$
$$+c_6\mu_t(\frac{k}{\tilde{\varepsilon}})^2S_{23}S_{ij}S_{ij}$$
$$+c_7\mu_t(\frac{k}{\tilde{\varepsilon}})^2S_{23}\Omega_{ij}\Omega_{ij}$$

When these terms are implemented in the momentum equations, the linear terms are treated in the same manner as in the linear LS model and the non-linear $c_1 \sim c_7$ terms are treated as source terms.

Nomenclature

AR	: aspect ratio
a	: coefficients of discretised equation
b	: source term
C	: Courant number
C_f	: skin friction coefficient
C_P	: specific heat capacity at constant pressure
C_p	: wall static pressure coefficient
$C_{\varepsilon 1}$, $C_{\varepsilon 2}$	: coefficients in the $\tilde{\varepsilon}$ equation
C_μ	: coefficient/function in the eddy viscosity formula
c	: speed of sound
$c_1 \sim c_7$	: coefficients in the cubic-stress relation
D	: coefficient of the diffusion term *or* source term in k equation
d	: coefficient for 4th-order central scheme
E	: source term in $\tilde{\varepsilon}$ equation
ER	: expansion ratio
F	: coefficient of the convection term
f	: coefficient for 5th-order upwind scheme
f_μ	: viscous damping function in the eddy viscosity formula
f_1, f_2	: damping functions in the dissipation equation
Gr^*	: modified Grashof number
g	: gravitational acceleration
H	: duct height

h : enthalpy

k : turbulent kinetic energy

Nu : Nusselt number

Nu_{max} : maximum Nusselt number on the heated wall

Nu_p : peak Nusselt number along the centerline of the heated wall

P : pressure

P' : pressure correction

P_k : production by mean strain in the k equation

Pr : Prandtl number

Pr_t : turbulent Prandtl number

q_w : wall heat flux

Re : Reynolds number

Ri^* : modified Richardson number

$\tilde{R}_t$: turbulent Reynolds number

S : step height

S_{ij} : strain tensor

$\tilde{S}$: strain invariants

St : Stanton number

S_ϕ : source term $= S_c + S_p\phi$

T : temperature

T_{in} : inlet temperature

T_w : bottom wall temperature

t : time

U : velocity component in the x direction

U_{ref} : inlet freestream mean velocity

U^* : old streamwise velocity in the computation

u' : intensity of the streamwise fluctuating velocity

$\overline{u_i v_j}$: Reynolds shear stresses

$\overline{u_i \theta}$: turbulent heat flux

u_τ : friction velocity

V : velocity component in the y direction

V^* : old transverse velocity in the computation

v' : intensity of the fluctuating transverse velocity

W : velocity component in the z direction

W^* : old spanwise velocity in the computation

WD : duct width

X^* : normalised streamwise distance

x : streamwise coordinate

x_{max} : streamwise location of the maximum Nusselt number

x_p : streamwise location of peak Nusselt number

x_r : streamwise location of reattachment point

x_s : streamwise size of secondary recirculation region

Y_ε : Yap correction term

y : transverse coordinate

y^+ : $\rho u_\tau y/\mu$

y_n : normal distance from the wall

z : spanwise coordinate

z_{max} : spanwise location of the maximum Nusselt number

Greek Symbols

α_t : turbulent thermal diffusivity

β : Cubic expansion coefficient

Δt : time step

$\Delta x, \Delta y, \Delta z$: grids spacing

δ : boundary layer thickness

δ_{ij} : Kronecker's delta

$\delta x, \delta y, \delta z$: grids spacing

ε : dissipation rate of k

$\tilde{\varepsilon}$: isotropic dissipation rate of k

θ_1 : pitch angle of the duct

θ_2 : rolling angle of the duct

λ : thermal conductivity

μ : fluid viscosity

μ_t : eddy viscosity

ν : kinematic viscosity

ρ : fluid density

σ_T : temperature accommodation coefficient

σ_v : velocity accommodation coefficient

σ_ε : model constant in dissipation equation

τ_w : wall shear stress

ϕ : scalar variable

$\tilde{\Omega}$: vorticity invariants

Ω_{ij} : vorticity tensor, $= \frac{\partial U_i}{\partial x_j} - \frac{\partial U_j}{\partial x_i}$

Subscripts

in : inlet value

w : wall value

max : maximum value

min : minimum value

o : outlet value

E,e,W,w,N,n,S,s,T,b,B,b : face and node values of a control volume

Superscripts

* : guessed value

o : old value

' : correction value